



HAL
open science

Characterization of the long-term mechanical behavior and the durability of polyamide mooring ropes for floating wind turbines

Yoan Chevillotte

► **To cite this version:**

Yoan Chevillotte. Characterization of the long-term mechanical behavior and the durability of polyamide mooring ropes for floating wind turbines. Materials and structures in mechanics [physics.class-ph]. ENSTA Bretagne - École nationale supérieure de techniques avancées Bretagne, 2020. English. NNT: 2020ENTA0011 . tel-03403273

HAL Id: tel-03403273

<https://theses.hal.science/tel-03403273v1>

Submitted on 26 Oct 2021

HAL is a multi-disciplinary open access archive for the deposit and dissemination of scientific research documents, whether they are published or not. The documents may come from teaching and research institutions in France or abroad, or from public or private research centers.

L'archive ouverte pluridisciplinaire **HAL**, est destinée au dépôt et à la diffusion de documents scientifiques de niveau recherche, publiés ou non, émanant des établissements d'enseignement et de recherche français ou étrangers, des laboratoires publics ou privés.

**DOCTORAT
BRETAGNE SCIENCES
LOIRE POUR L'INGENIEUR**



FRANCE
ENERGIES
MARINES



ANR ANR-10-IEED-0006-16



**ENSTA
BRETAGNE**

Ifremer

THESE DE DOCTORAT DE

L'ECOLE NATIONALE SUPERIEURE
DE TECHNIQUES AVANCEES BRETAGNE

ECOLE DOCTORALE N° 602

Sciences pour l'Ingénieur

Spécialité : Mécanique des Solides,
des Matériaux, des structures et des surfaces.

Par

Yoan CHEVILLOTTE

Characterization of the long-term mechanical behavior and the durability of polyamide mooring ropes for floating wind turbines

Thèse présentée et soutenue à Brest, le 19/06/2020

Unité de recherche : Institut de Recherche Dupuy de Lôme, UMR CNRS 6027

Rapporteurs avant soutenance :

Laurent Orgéas Directeur de recherche CNRS, Univ. Grenoble Alpes - CNRS - Grenoble INP
Damien Soulat Professeur des Universités, Gemtex - ENSAIT Roubaix

Composition du Jury :

Président :	Michel Coret	Professeur des Universités, Ecole Centrale de Nantes
Examineurs :	Claudia Marano	Professeur, Politecnico di Milano
	Laurent Orgéas	Directeur de recherche CNRS, Univ. Grenoble Alpes - CNRS - Grenoble INP
	Damien Soulat	Professeur des Universités, Gemtex - ENSAIT Roubaix
Dir. de thèse :	Yann Marco	Maitre de conférences (HDR), IRDL, ENSTA Bretagne
Co-dir. de thèse :	Peter Davies	Dr Ingénieur. HDR, IFREMER LCSM
Encadrant :	Guilhem Bles	Maitre de conférences, IRDL, ENSTA Bretagne

Invité(s)

Sam Weller Dr-Ingénieur, Tension Technology International, Ltd.

Remerciement

Je tiens tout d'abord à remercier particulièrement mon encadrement : Yann Marco, Peter Davies et Guilhem Bles, sans qui ce projet n'aurait pas vu le jour et qui m'ont guidé tout au long de ce travail. Je remercie également les différents partenaires de POLYAMOOD qui ont apporté un plus au projet, en particulier Karel Devos et Michel François pour leur apport technique important.

Je suis très reconnaissant pour l'immense travail des rapporteurs : Laurent Orgeas et Damien Soulat, ainsi que l'implication de tous les membres du jury : Michel Coret, Claudia Marano, Sam Weller qui ont lu avec attention le manuscrit.

Un grand merci également à toutes les personnes du laboratoire de l'ENSTA et l'IFREMER qui m'ont aidé à mettre en place les différentes expérimentations : Frederic Montel, Philippe Godec, Mael Arhant, Didier Penchenat, Bruno et Eric de l'atelier... Ainsi que les autres personnes du centre (doctorant et personnel) pour leurs bonnes humeurs, les discussions intéressantes de la pause thé, et les retours sur les présentations.

Pour finir, je souhaite faire une salutation à ma famille dont une grande partie s'est déplacée pour l'occasion malgré des conditions un peu complexes. A mes amis sudistes pour leur présence et les nombreuses parties de JDR, mes compatriotes de Gloomhaven, mes collègues de bureau ainsi que l'intégralité des membres du BDJeux, lieu qui a été ma deuxième maison à Brest.

Table of content

- 1 Introduction 5
 - 1.1 Context of synthetic fibre rope mooring lines. 5
 - 1.2 Polyamide cables for marine renewable energy applications. 7
 - 1.3 Problem statement 8
 - 1.4 General information on nylon fiber and ropes..... 9
 - 1.5 Difficulties 9
 - 1.6 Summary 13
 - 1.7 References 13
- 2. Constitutive response and behavior law..... 18
 - 2.1. Bibliography 18
 - 2.2. Objective..... 26
 - 2.3. Strategy/Plan..... 28
 - 2.4. Mechanical tests on a 4-ton polyamide wet sub-rope..... 30
 - 2.5. Investigation of the mechanical constitutive characteristics 55
 - 2.6. Constitutive law 68
 - 2.7. Identification method..... 73
 - 2.8. Validation of the constitutive law..... 86
 - 2.9. Conclusion 97
 - 2.10. Reference 100
- 3. Long term creep behavior 105
 - 3.1. Bibliography 105
 - 3.2. Objectives 107
 - 3.3. Creep tests on yarn 107
 - 3.4. Long term creep device 113
 - 3.5. Long term creep tests..... 115
 - 3.6. Comparison between the results on Yarns and on 4-ton ropes..... 122
 - 3.7. Comparison with the multi-creep test..... 124
 - 3.8. Summary 125
 - 3.9. References 126

4. Durability	129
4.1. Context.....	129
4.2. Yarn on Yarn abrasion tests.....	133
4.3. Fatigue tests	139
4.4. Yarn and rope failure mechanisms	158
4.5. Summary.....	161
4.6. References	162
5. An attempt to use a heat build-up measurement protocol to evaluate the fatigue properties of ropes rapidly	167
5.1. Introduction	167
5.2. Evaluating the cyclic dissipated energy from thermal measurement	173
5.3. Heat build-up tests on 4T sub rope	176
5.1. Heat build-up tests on 8T sub rope	186
5.2. Comparison between the 4T and 8T sub-ropes	194
5.3. Summary.....	196
5.4. Reference	197
6. Conclusions and further work	200
6.1. Conclusions	200
6.2. Further work	203
7. Appendix	205

Chapter 1: Introduction

Table of content

1. Introduction.....	5
1.1. Context of synthetic fibre rope mooring lines.....	5
1.2. Polyamide cables for marine renewable energy applications.....	7
1.3. Problem statement	8
1.4. General information on nylon fiber and ropes.....	9
1.4.1. Polyamide 6.....	9
1.1.1 Terminations.....	11
1.4.2. Rope vocabulary and specification	12
1.5. Difficulties	13
1.6. References	13

1.Introduction

This PhD study was performed within the framework of an France Energies Marines project receiving funding from the French national Investments in the Future program called **POLYAMOOR** which responds to the need of industrial developers of EMR technologies to design the future development of cheaper anchoring systems in shallow waters. The French government has initiated an offshore energy production programme (*Rabain, 2019*), and the development of innovative solutions, such as floating wind turbines, is essential to achieve the objectives. Furthermore, near-shore wind turbines have operating limits such as geographic space and population agreement in the Mediterranean Sea, and operability issues in areas further from the coast.

An **advantage** of floating wind power is that it can **overcome water depth limitations, improve acceptability** and provide access to a **larger and more regular wind resource**. These wind turbines are held in position by means of an **anchoring system**. However, the confirmation of the technical and economic interest of floating wind turbines requires the development of innovative and reliable systems to **reduce their costs**.

As the anchoring system and its installation represent a significant part of the cost of electricity, it is essential to optimize mooring solutions.

Moreover, these solutions could also apply to a broad range of other EMR technologies, such as systems using wave and tidal power.

1.1. Context of synthetic fibre rope mooring lines.

Over the past 20 years, polyester fibre (PET, polyethylene terephthalate) mooring lines for floating oil platforms have been developed (*De Pellegrin, 1999; Davies, 2002; Flory, 2004*). These fibers offer good mechanical properties with a modulus of ~ 15 GPa at a reasonable price. They were able to solve some of the issues caused by chain anchoring as production depths increased (such as length and weight of steel chains, its oxidation and the ecological footprint made by the lines dragging on the sea bottom) by changing the way to address the problem.

In fact, it is necessary to install the steel lines in a way which requires a large zone to stabilize the floating platform position: the restraining effort is created by the weight of these lines. This implies long lengths and heavy lines (with rising costs), and ecological issues.

Thanks to their elasticity properties, the synthetic fibre anchor lines technology enables to take up directly the loads required for floating platform station-keeping, with reduced line length (therefore reduced costs)(Figure 1-1). In addition, these stiff and light anchors are easier to install and have excellent mechanical properties.

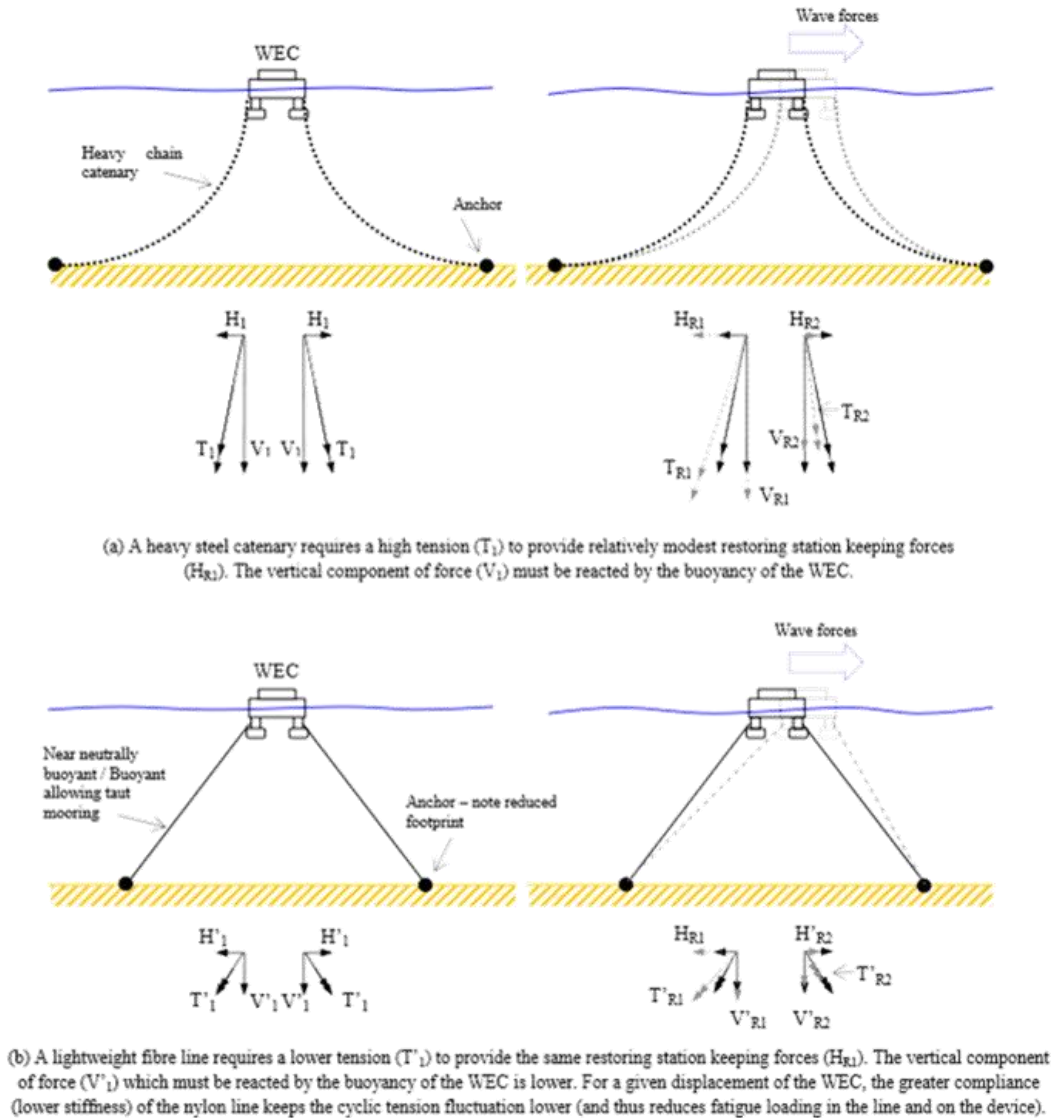


Figure 1-1. Diagram showing the benefits of synthetic rope over chain system (Ridge, 2010).

In order to be accepted by the offshore oil and gas industry these PET fibre ropes **had** to undergo a **major test campaign** in order to demonstrate a fatigue strength equivalent to (or even higher than) that the steel cables they were to replace (*Banfield, 2005*). Other more expensive fibres with higher stiffness (70 GPa or more) exist (aramid, HMPE) to design stiffer anchors. However, when the **movements of the floating**

support are significant, which means the deformation of the line is too important compared to its length (mostly for coastal wind turbines with low depth water), stiff anchor lines cause an increase in the tension of the line that it cannot support without fatigue damage and reduced lifespan. This is precisely the case for many marine renewable energy (MRE) anchors, for which current alternatives are limited and costly.

The mechanical properties of ropes are dictated by the type of fibre, although adjustments can be made by changing the construction parameters (stranding or braiding angles). Fibre ropes are developed hierarchically, as shown in Figure 1-2, and this specificity of "structured" material is a key aspect for these applications (*Lechat, 2007*), as the construction has a significant effect on its behaviour and durability.

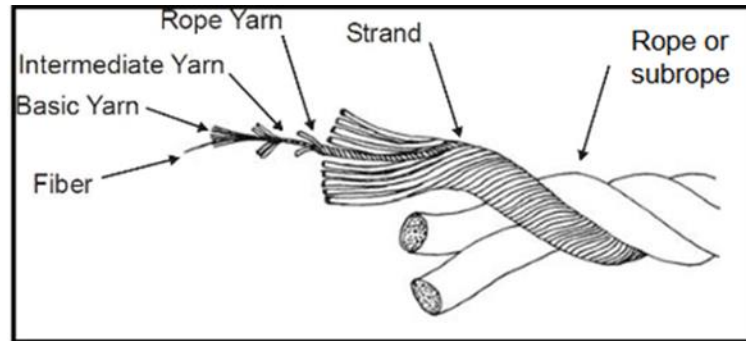


Figure 1-2. Structure of a twisted rope. (Weller, 2013)

1.2. Polyamide cables for marine renewable energy applications.

A recent review presented synthetic cable options for marine renewable energy system anchoring (*Weller, 2015*). For marine renewable energy applications on sites at shallow depths (between 50 and 100 m), in energy environments in the Maritime Public Domain, the search for a **low-cost flexible mooring line is essential**.

The elongation of the lines being schematically the movements of the platform divided by the length of the lines, a specificity of marine renewable energy platforms is the significant elongation of the mooring lines, more important than those of the offshore oil industry (on sites at deeper depths). Steel, in its elasticity range, limits us to a strain of less than 1%, aramids and HMPE to 4%, polyester to 10% and polyamide to 20% of elongation at break. Thus, **polyamide ropes appear to be a potentially attractive technical solution for marine renewable energy platforms**.

Polyamide fibres, or "nylon" (the original brand name), can be of different types (PA6, PA66, PA11, PA12,...) even if PA6 is the most commonly used for ropes. Its modulus of ~ 5 GPa offers a higher elongation than polyester, for an equivalent ultimate tensile strength.

1.3. Problem statement

The first key point is the **validation of the durability of polyamide ropes**. Normative standards exist and provide experimental data on the mechanical and fatigue behaviour of fibres developed for offshore oil and gas. Studies of the fatigue of polyamide ropes are much rarer. Feedback on nylon ropes nowadays exists mainly for hawser and short-term anchoring applications. The service life of these applications does not exceed **1 to 2 years** due to the degradation of properties caused by **internal abrasion** between the rope elements, underlining the importance of fibre coatings. Regarding **permanent anchorage** based on nylon rope, there is **very little data** and the durability of nylon for numbers of loading cycles equivalent to those performed on a system anchored for a period of 20 years has not been documented to date.

The second key point is the qualification and simulation of the mechanical behaviour of these lines. Three time scales are to be considered: the response to in-service stresses (in relation to wave and tides), the long-term evolution of the pre-tension stress (impacted by accidental events such as storm), and the evolution at very long times (creep effect during the whole lifespan of the rope). Behavioural models of commercial numerical simulation codes for the response to in-service stresses are very limited with respect to the complex behaviour of polyamide. The approaches determining the long-term evolution of the pre-tension stress are nowadays very empirical and do not allow to optimize the lengths deployed on site. As part of the Interreg MERiFIC project (Marine Energy in Far Peripheral and Island Communities), IFREMER and the University of Exeter have been working on the behaviour of polyamide at sea (*Weller, 2014; 2015*). They noted a significant change in properties, especially stiffness, after aging. For these three time scales, relevant data and models are currently sorely lacking.

In conclusion, despite the results of some partial studies, we note that there is very little information on which to base the design of a polyamide anchor line for a period of 20 years.

1.4. General information on nylon fiber and ropes

More precise information is given in each chapter, but this section provides a brief, general introduction to the material and ropes that will be studied in the following chapters.

1.4.1. Polyamide 6

Nylon 6 can be described chemically as a semi-crystalline thermoplastic when in fiber form with the following structure:



Figure 1-3. Polyamide 6 chemical structure.

This fiber is highly hydrophilic but commonly used in synthetic rope marine applications as a low-cost material. The crystallinity ratio is around 40% for Nylon and can be schematically represented as shown in Figure 1-4. To describe these fibre materials a specific textile unit is used for the linear density: the tex, which is equivalent to grams per kilometers. This linear density allows us to compare one size of rope to another.

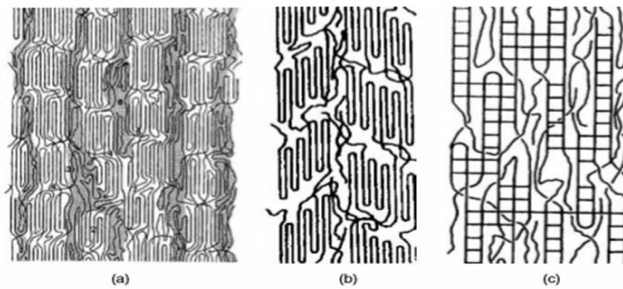


Fig. 2.6 Views of fine structure of nylon fibres. (a) Based on measurements on nylon 6. From Murthy *et al.* (1990). (b) and (c) Schematic views. From Hearle and Greer (1970a, b).

Figure 1-4. Schematic views of microstructure of nylon fibres (McKenna, 2004)

The Nylon yarn used in this study is manufactured by Nexis fibers (reference 1880 f 280) (with a linear mass of 190.5 tex).

One critical property to know is the glass transition temperature (T_g) in the wet and dry states for this material, as when exposed to relative humidity the T_g can be quite close to ambient temperature, as shown below (Figure 1-5) for the same yarn by *Humeau (2017)*. This suggests that the polymer will be in the rubbery state (above the T_g).

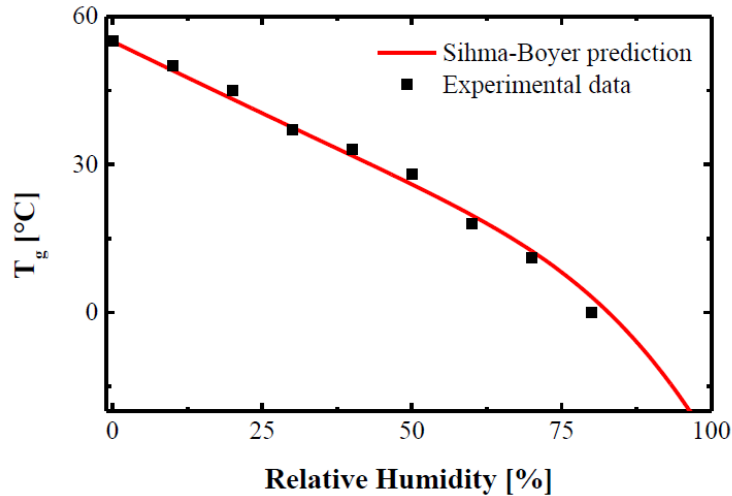


Figure 1-5. Glass transition temperature variation as a function of the relative humidity. (Humeau, 2017)

Humeau (2017) has shown that it is possible to identify the water uptake in Nylon 6 yarns. On the same specimens as those used in our study, he measured a maximal water uptake in fibers of about 10% by weight.

1.4.2. Terminations

Terminations are important for cables, as they transmit the forces and generally limit the breakage of synthetic ropes. The choice of terminations is therefore important. There are several systems for synthetic lines, the main ones are shown in Figure 1-6.

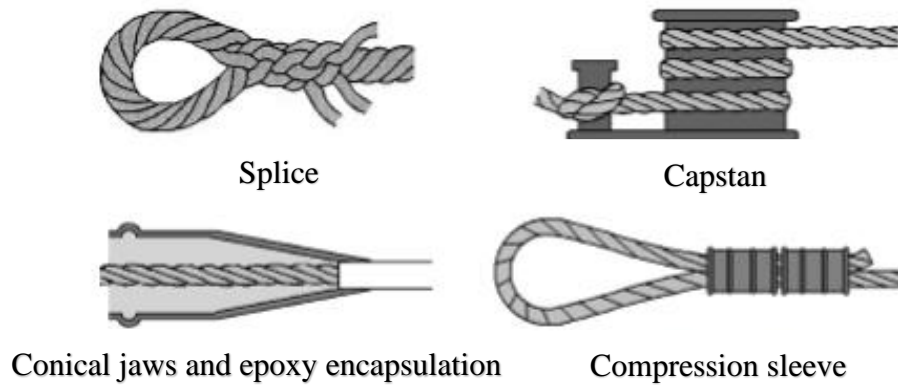


Figure 1-6. Diagram of different methods of terminating synthetic cables (Lechat, 2007).

The eye-splice is usually the most efficient permanent termination and also the most widely used. It has been chosen for our study for all our tests on sub-ropes, as it is the best choice for fatigue loading.

For the capstan, the end of the cable is wrapped several times around a circular part before being fixed by a knot or other fastening system. The winding allows the progressive reduction of friction forces, however the length of the rope on the axis depends on the diameter of the rope and leads to long samples.

For the conical jaw, the end of the cable is placed through a conical part, which is held in place either by resin or with a conical pin. This has the advantage of being a relatively short termination, but induces stress concentrations around the jaws.

The compression sleeves are quite quick and simple to put in place but there is a risk of slipping, abrasion and low strength efficiency.

1.4.2.1. Splices

Splices are usually made by separating the strands from the end of the rope, making a loop with them and inserting them into the structure or braiding these strands within the rope itself. This allows a tightening of the structure under load, which allows a stabilization of the tension in the cable. However, splicing is currently done by hand, requiring time and a qualified user to obtain similar tension in each strand.

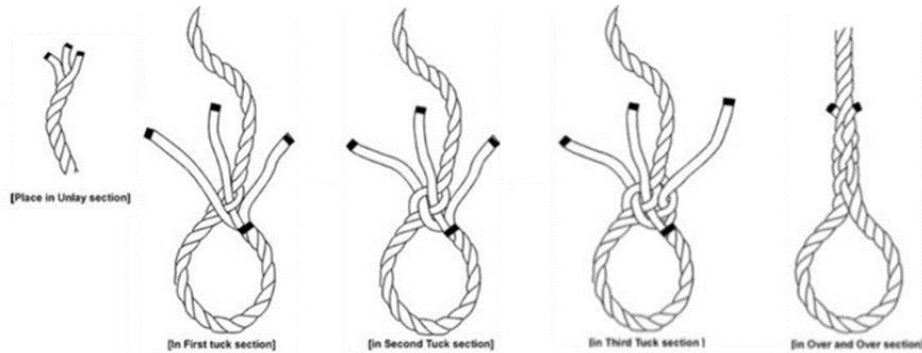


Figure 1-7. Splice construction explanation.

1.4.3. Rope vocabulary and specification

In the context of mooring ropes, a Minimal Breaking Load (MBL) is frequently cited; this is the minimum value that causes the cable to break during testing.

In this document, the load value will usually be presented in N/tex (with the tex being a unit of linear mass commonly used in the textile and cable industry), this allows us to avoid defining the section of the rope, and provides a specific stress which can be used to compare two different sizes of rope.

The strain presented in the manuscript will be the logarithmic strain calculated by the following formula: $\varepsilon = \ln\left(\frac{L}{L_0}\right)$.

1.5. Difficulties

The main difficulties for demonstrating the durability of polyamide ropes and modelling their mechanical behaviour simulation and qualification can be divided in two major scientific and technical issues.

The first issue concerns the complexity of testing the material under realistic environmental conditions (temperature and moisture). **Polyamide is a highly hydrophilic material** and water absorption drastically **alters its glass transition** and therefore its **mechanical properties**. For the targeted applications in the marine environment, this phenomenon is a first-order factor because it means that the operating temperatures will be very close to the glass transition temperature, or even higher. All the **non-linear** components of **behaviour** are therefore expressed, which is a major **difficulty in modeling**. As with fatigue tests, this problem is complicated by the difficulty of transposing characterizations to the scale of the strands for cable characteristics. One of the project's challenges will therefore be to propose a **characterization approach for intermediate scales**, then to apply a modeling of the visco-elasto-plastic response at these scales, and finally to validate the proposed approach at the cable scale.

Secondly the search for a law of **cyclic (fatigue) and creep responses and performances** of a polyamide cable, which is an essential part of the project, requires the characterization of **behaviour at long times** and at ultra-low speeds. Indeed, the high viscosity of these materials cannot be relaxed after one hour of creep testing, nor can they be removed by a slow deformation rate (10^{-5} s^{-1}). However, this behaviour over long periods of time is the main part of the stress of this type of material (*Bles, 2009*) and according to (*Davies, 2000*), and in the case of polyester cables, the most difficult part to model, the remainder being close to a linear viscoelasticity.

1.6. References

Banfield, S.J., Casey, N.F. and Nataraja, R., 2005, January. Durability of polyester deepwater mooring rope. In *Offshore technology conference*. Offshore Technology Conference.

Bles, G., Nowacki, W.K. and Tourabi, A., 2009. Experimental study of the cyclic visco-elasto-plastic behaviour of a polyamide fibre strap. *International Journal of Solids and Structures*, 46(13), pp.2693-2705.

Davies, P., Huard, G., Grosjean, F. and Francois, M., 2000, January. Creep and relaxation of polyester mooring lines. In *Offshore Technology Conference*. Offshore Technology Conference.

Davies, P., François, M., Grosjean, F., Baron, P., Salomon, K. and Trassoudaine, D., 2002, January. Synthetic mooring lines for depths to 3000 meters. In *Offshore Technology Conference*. Offshore Technology Conference.

De Pellegrin, I., 1999, January. Manmade fiber ropes in deepwater mooring applications. In *Offshore Technology Conference*. Offshore Technology Conference.

Flory, J.F., Banfield, S.P. and Petruska, D.J., 2004, January. Defining, measuring, and calculating the properties of fiber rope deepwater mooring lines. In *Offshore Technology Conference*. Offshore Technology Conference.

Kenney, M.C., Mandell, J.F. and McGarry, F.J., 1985. Fatigue behaviour of synthetic fibres, yarns, and ropes. *Journal of materials science*, 20(6), pp.2045-2059.

La Rosa, G. and Risitano, A., 2000. Thermographic methodology for rapid determination of the fatigue limit of materials and mechanical components. *International journal of fatigue*, 22(1), pp.65-73.

Lechat, C., 2007. *Comportement mécanique de fibres et d'assemblages de fibres en polyester pour câbles d'amarrage de plates-formes offshore* (Doctoral dissertation).

Le Saux, V., Marco, Y., Calloch, S., Doudard, C. and Charrier, P., 2010. Fast evaluation of the fatigue lifetime of rubber-like materials based on a heat build-up protocol and micro-tomography measurements. *International Journal of Fatigue*, 32(10), pp.1582-1590.

McKenna, H.A., Hearle, J.W. and O'Hear, N., 2004. *Handbook of fibre rope technology*. Elsevier.

Rabain, A. 2019, 13 Mai. Introduction générale, Scénario énergétiques et conditions de développement des EMR. *Ecole thématique du CNRS, Energies renouvelable*.

Ridge, I.M.L., Banfield, S.J. and Mackay, J., 2010, September. Nylon fibre rope moorings for wave energy converters. In *OCEANS 2010 MTS/IEEE SEATTLE* (pp. 1-10). IEEE.

Weller, S., Davies, P., Johanning, L. and Banfield, S., 2013. Guidance on the use of synthetic fibre ropes for marine energy devices.

Weller, S.D., Davies, P., Vickers, A.W. and Johanning, L., 2014. Synthetic rope responses in the context of load history: Operational performance. *Ocean Engineering*, 83, pp.111-124.

Weller, S.D., Johanning, L., Davies, P. and Banfield, S.J., 2015. Synthetic mooring ropes for marine renewable energy applications. *Renewable energy*, 83, pp.1268-1278.

Weller, S.D., Davies, P., Vickers, A.W. and Johanning, L., 2015. Synthetic rope responses in the context of load history: The influence of aging. *Ocean Engineering*, 96, pp.192-204.

Chapter 2: Constitutive response and behavior law

First, the mechanical behavior of the polyamide sub-rope in water is characterized; its viscoelastic and plastic features are highlighted and measured. To do so, experimental devices are developed in order to perform tensile tests on a 4-ton polyamide sub-rope in water and to measure the strain in the central part of the wet samples. Different loading paths, representative of the service conditions of these ropes, are tested aiming at evaluating different components of the response of the material.

Second, a phenomenological constitutive law for mooring rope elongation behavior is proposed. “Naval Energies”, partner of the Polyamoor project, requires an advanced elongation model for polyamide mooring-line to design future floating wind turbines. An identification method is proposed for each block of the constitutive law; a sequence of 4 stages where each stage is dedicated to one block of the law. This method allows assessment of the relevance of each part in describing the experimental measurements. The proposed law is identified by using the visco-elasto-plastic characterization. The response of this law is then compared with the different characterization tests to assess its viability and limits. The law shows relevant results with respect to the tests, and manages to catch most of the features of the rope behavior.

Keywords: Characterization, Constitutive law, Rope, Nylon, Water, Model.

Table of content

2.	Constitutive response and behavior law.....	18
2.1.	Bibliography.....	18
2.1.1.	Testing machines for wet synthetic ropes.....	18
2.1.2.	Polyamide and water.....	19
2.1.3.	Modeling the behavior of semi-crystalline thermoplastic.....	19
2.1.4.	Towards behavior models of polyamide textile materials.....	20
2.1.5.	Effect of scale and construction.....	24
2.2.	Objective.....	26
2.2.1.	Visco-elasto-plastic characterization of a polyamide twisted rope.....	26
2.2.2.	Constitutive law.....	26
2.2.3.	Direct identification method.....	27
2.2.4.	Implementation of the proposed law into classic FE codes.....	27
2.2.5.	Understanding, effect of scale and construction.....	27
2.3.	Strategy/Plan.....	28
2.4.	Mechanical tests on a 4-ton polyamide wet sub-rope.....	30
2.4.1.	Material and experimental methods.....	30
2.4.2.	Bedding in.....	34
2.4.3.	Tests at different strain rates.....	37
2.4.4.	Cyclic tests with stress-relaxation stages.....	43
2.4.5.	Cyclic tests with multi-creep/recovery.....	51
2.5.	Investigation of the mechanical constitutive characteristics.....	55
2.5.1.	Test selection.....	55
2.5.2.	Dynamic / Short-term elasticity.....	55
2.5.3.	Fully relaxed behavior / Time-independent behavior.....	58
2.5.4.	Plasticity.....	63
2.5.5.	Summary.....	66
2.6.	Constitutive law.....	68
2.6.1.	Discussion and Choices.....	68

2.6.2.	Equations of the constitutive law	72
2.6.3.	Model characteristics.....	72
2.7.	Identification method.....	73
2.7.1.	Dynamic elasticity / Short term elasticity	73
2.7.2.	Slow spring or slow elasticity	75
2.7.3.	Plasticity	77
2.7.4.	Viscosity.....	79
2.8.	Validation of the constitutive law.....	86
2.8.1.	Implementation in a FEM code.....	86
2.8.2.	Cyclic test with multi-relaxation	86
2.8.3.	Monotonous tests at different strain rates.....	91
2.8.4.	Cyclic test with multi-creep/recovery	93
2.9.	Conclusion.....	97
2.10.	Reference	100

2. Constitutive response and behavior law

The Polyamoor project aims to investigate issues that have to be solved for designing and installing floating wind turbines. One of these issues is the understanding of the complex visco-elasto-plastic behavior of polyamide mooring ropes. Until today, floating platforms moored by synthetic lines are usually numerically simulated by assuming that the line behavior is linear elastic in particular situations: for instance, a quasi-static state in calm sea, and a dynamic state due to wave loadings. This is the case for industrial software tools like Ariane (Bureau Veritas) and Deeplines (Principia).

The objective of the present study is to define a constitutive law that could be implemented into time-simulation software tools like Deeplines. That is to say, that one constitutive law should capture all viscoelastic and eventually plastic features of the polyamide rope behavior, in order to simulate a moored floating platform for any loading situation.

Moreover, this constitutive law should be ready to be implemented into Deeplines software tools without needing onerous programming development. So, behavior laws of the integral type that memorize the elongation history from a reference mechanical state are excluded, due to the excessive amount of memory required at each integration point of each finite element of the mooring line model.

2.1. Bibliography

2.1.1. Testing machines for wet synthetic ropes

In order to test synthetic mooring ropes, specialized test machines must be used. These machines are quite rare and expensive. A review from the MERiFIC project (a program to develop marine energy in the North of France and UK) gives some of them in Europe (*Davies, 2012*); for example, there are only about a dozen test machines of 100 ton capacity of greater suitable for rope testing in Europe. Indeed, testing synthetic mooring ropes, especially polyamide ones, requires very long piston strokes. The strokes of classical hydraulic test machines are limited to a few hundred millimeters. Due to the splices required, the length of synthetic textile rope specimens are about 200 times their diameter. The combination of elongations up to 20% with this length-to-diameter ratio makes the classic hydraulic test machines useless for this type of ropes.

These tests are generally performed horizontally, without water for most installations, or with water spraying for laboratories specialized in mooring rope like IFREMER and only a few have the possibility to test ropes fully submerged. Testing rope fully submerged is more complex, time consuming and more costly as it either

needs a box containing a lot of water with watertight joints, or a one-time use special cover around the rope to maintain it fully wetted.

2.1.2. Polyamide and water

The service environment of the ropes under consideration here (for a marine environment), associated with the highly hydrophilic nature of polyamides, raises acute questions of water absorption and the resulting consequences on the mechanical properties and durability.

A first question concerns water diffusion in polyamide, into order to evaluate the absorption and desorption kinetics, the possible gradients induced and the saturation contents. For polyamides, these studies have been conducted for a long time (*Puffr, 1967; Lim, 1999; Reuvers, 2012; Colin, 2014; Broudin, 2015a; 2015b*), and show that the diffusivity of water in the material can be evaluated correctly.

Water sorption in polyamide induces a very significant change in mechanical properties (*Puffr, 1967; Flory, 1988; Launay, 2013*), which is called the "plasticizing effect" (*Merdas, 2002*), and in fatigue resistance (*Kenney, 1985; Bernasconi, 2007*). *Huntley (2016)* shows that after wetting of 1 hour, values of modulus decrease significantly (50-80%) and are totally stabilized in 12 hours.

In the work carried out by (*Launay, 2013*), the authors highlight the changes in the behavior of polyamide when the temperature of the material deviates from its glass transition temperature. But as presented in the first chapter, the glass transition of the material when it is fully saturated in water is below 0°C (*Humeau, 2017*) meaning that for our experiments at around 10 to 20°C, we are on the rubbery plateau and quite far from this value so the result should not be too much affected by the temperature (the value of the laboratory temperature has been marked for each test).

2.1.3. Modeling the behavior of semi-crystalline thermoplastic

The study of the mechanical response of a semi-crystalline thermoplastic such as polyamide is a complex problem which is the subject of various approaches in the literature. A first option is a multi-scale approach (molecular, macromolecular, supramolecular scales) (*Spathis, 1998; Van Dommelen, 2003; Parenteau, 2009*). Nevertheless, in view of the complexity of such a problem (*Fond, 2002*), many authors prefer to work at a larger scale by considering the material as macroscopically homogeneous with possibly the integration of microstructural variables (*Détrez, 2008; Boisot, 2009; Parenteau, 2009; Regrain, 2009*). In the framework of the study of thermoplastic composites, it is the latter type of approach that has been developed and deepened in recent years by the partners of the project (*Launay, 2011; 2013; Bles, 2000; 2002*), by proposing a rich behavior model that can

be used in fatigue design, associated with a robust identification process. Different phenomenological models have also been proposed for the modelling of thermoplastic fibers (*Northolt, 1995; Baltussen, 2001; 2003; 2004; Chailleux, 2003; 2005*).

2.1.4. Towards behavior models of polyamide textile materials

Usually publications dealing with the behavior of synthetic ropes for offshore mooring are of a very applied and technical nature, listing experimental results and empirical observations (*Lechat, 2007*). Moreover, the vast majority of studies deal with polyester fibers. Mechanical behavior of braided nylon rope was investigated by *Bitting (1980; 1985)* using a Zener type of viscoelastic model. But it was not successful enough to cover all the rope properties needed in mooring analysis (*Del Vecchio, 1992*). On polyester, *Del Vecchio (1992)* who characterized yarn, suggested a simple structural model giving a reasonable prediction for one type of rope and passable result for another. These tests were characterized using tensile strength tests, cycling and creep tests.

Dynamic modulus tests are often employed for characterization of rope behavior, and consist of cycling around a fixed value (*Bitting, 1980; 1985*). They experimentally determine an apparent spring constant and hysteresis, then can be treated analytically to calculate the viscoelastic parameters of a three-parameter model of a synthetic line. In the offshore application of cables, the viscoelastic-viscoplastic behavior is thus modelled by a stiffness to be used in mooring system analysis models (*Lechat, 2007*) and should allow three tension loading cases of the mooring lines (static, slow due to second order movements of the platform, dynamic due to platform movements by waves and the dynamic response of the line) to be described (*Banfield, 1998*). However, it is very difficult to reduce the complex behavior of synthetic cables to stiffness (*Weller, 2014; 2015; Vu, 2015; Lechat, 2011; Davies, 2011*) and *Petruska (2005)* thus call into question the procedures for evaluating static stiffness and creep behavior. However, a quasi-static line stiffness was defined at the end of the 1990s, in order to model the viscoelastic response of synthetic ropes under slow variations (several hours or days) in mean tension under the effect of changing weather conditions (*François, 2008*).

François and Davies (2008) formulate the idea that there is a fully relaxed or infinitely slow rate behavior of polyester ropes and approach this behavior by extrapolating their creep and recovery tests to longer times.

In terms of modeling, (*François, 2008*) succinctly proposes a behavior model for polyester rope where the rope deformation is a function of the current tension but also of the maximum tension undergone by the rope in the past. In their model, three strain contributions are summed: one for fully relaxed behavior, one for non-

recoverable permanent strains and finally a deformation with viscoelastic behavior. For a woven strap in PA66, (Bles, 2002) proposes a visco-elasto-plastic model based on the summation of two stresses; the first is that of a time-independent or infinitely slow speed equilibrium behavior of the elastoplastic type and the second is that of a non-linear viscoelastic behavior of the Maxwell type. Later, Bles (2009) has characterized the visco-elasto-plastic cyclic behavior of nylon-fiber woven strap and proposed a different but similar constitutive law implementable into a finite element code for time-domain simulations. Comparison between experimental results and numerical simulations showed good correlation as shown in Figure 2-1 even if some particular visco-elastic phenomena are not captured.

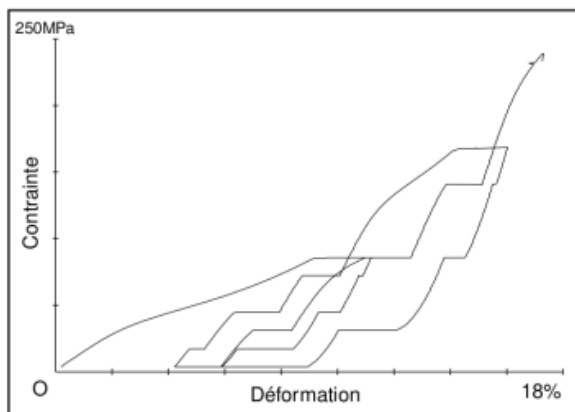


Fig. 12.36 – Essai *Gk14* ($\dot{\sigma} = 6,6 \text{ MPa/s}$) – sangle kaki du groupe A.

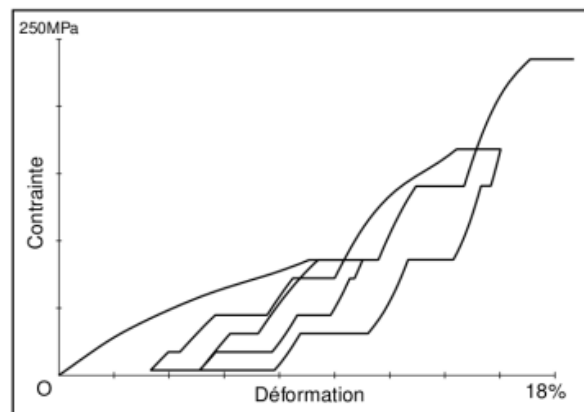


Fig. 12.37 – Simulation de l'essai *Gk14*; modèle de Maxwell avec rebond.

Figure 2-1. Comparison between experimental test (left) and model (right) of Bles (2009).

For coated fabrics, (Dib, 2014) proposed a visco-elasto-plastic model for polyester fibers constituting a coated woven Dacron fabric which showed good agreement with experimental tensile tests on fabric in three directions (warp, weft and at a 45° angle) for various loading paths (monotonic, cyclic, relaxation tension).

Falkenberg et al. (2011; 2018) proposed the SYROPE model, a frequency-domain model consisting “of non-linear characteristics for mean tension and linear stiffness for wave-frequency and low-frequency motions and tensions”. Their mean-tension part is based on curves for loading and unloading as a function of the maximum load experienced by the rope (Figure 2-2). This work provided a rich description of the non-linear visco-elasto-plastic behavior of synthetic ropes but was never formulated by a set of equations nor numerically simulated.

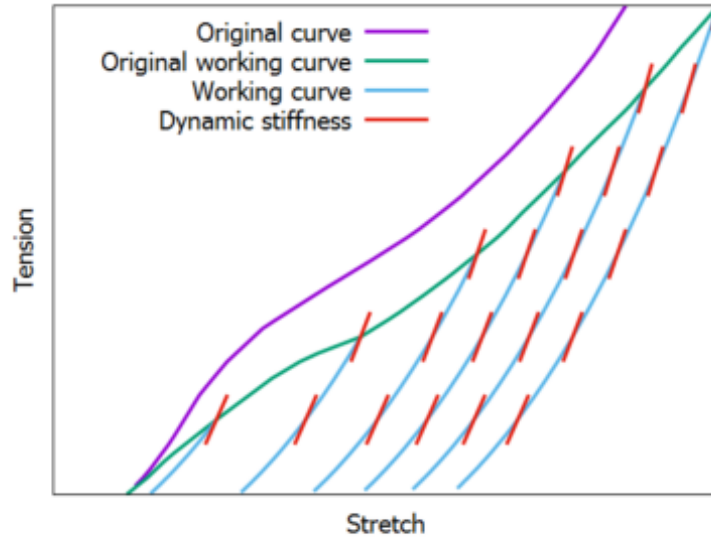


Figure 2-2. The Syrope model (Falkenberg, 2018)

Schapery's visco-elasto-plastic models proposed by *Chailleux (2003;2005)* and *Davies (2003)*, and then followed by *Huang (2014;2015)* can be implemented in finite element codes for time-domain simulation. These models show very good result for creep behavior of the polyester as shown in Figure 2-3, but predictions for quasi-static and dynamic cyclic loading have not been fully shown.

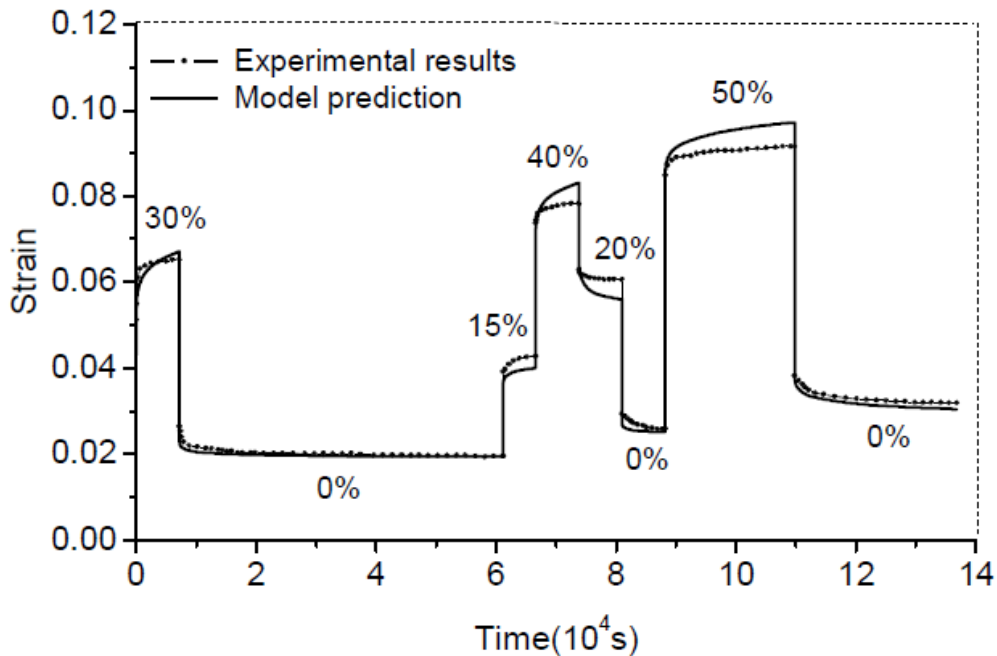


Figure 2-3. Comparison between experimental and simulated creep-recovery test results (Huang, 2014).

Flory (2013) proposed a model for synthetic rope explaining each of the required parts, without putting it into equations nor simulating a rope with it (Figure 2-4).

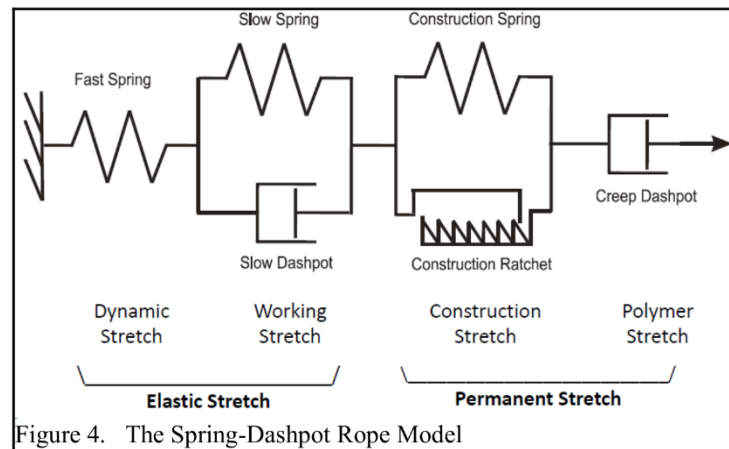


Figure 2-4. Flory (2013) proposal of elements for modeling fiber ropes.

Weller (2018) proposes in his paper a preliminary study on the identification of the individual elements based of the *Flory (2013)* model in order to develop a time domain model capable of representing synthetic rope response. With an initial assessment of several parameter estimation techniques for Nylon rope response (Brute force, Genetic Algorithm, Particle Swarm Optimization, Differential Evolution), this study shows that brute force approaches (both grid search and random) have limited application to synthetic rope response model parameter estimation due to their high computational requirements. And that the agreement between the model and harmonic examples is better than achieving a good fit with an irregular load time series, which is more challenging and likely to require model adaptation.

Some authors have proposed models based on elastic finite element simulations at smaller scales to represent woven structures; for example, a numerical finite element modeling approach applied at the mesoscopic scale of woven fabric. This approach was been proposed ten years ago for woven fabrics used as reinforcement of composite structural pieces for aircraft (*Figure 2-5, Charmetant, 2011; Iwata, 2019*).

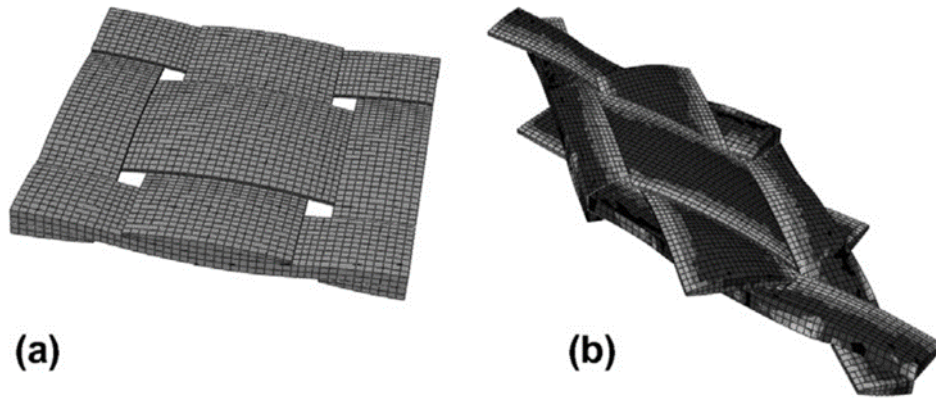


Fig. 10. Unit cell shear simulation: (a) undeformed configuration and (b) deformed configuration.

Figure 2-5. Meso-FE-model of a woven fabric made of 3 fiber bundles or yarns in the warp direction and 3 yarns in the weft directions (Charmetant, 2011).

However, for our topic, this type of approach leads to models with a very large number of degrees of freedom related to the section of the rope. Moreover, the behavior is hyperelastic and does not take into account the viscoelasticity nor plasticity of synthetic ropes, and it seems that neglecting viscosity or slippage between fibers for polyamide does not work very well (*Ghafour, 2019*). So this approach will not be pursued in the present study.

As a summary, published studies on the behavior of synthetic ropes, mainly polyester, showed the following points:

- The behavior includes some non linear elasticities which are different during monotonous tensile loadings and during unloadings.
- The behavior includes viscoelasticity, and the stress relaxation and creep strain time evolution seems to follow a logarithmic function of time.
- The behavior should include plasticity or a permanent deformation that is, to some extent, a function of the maximum tension experienced by the synthetic rope.
- The behavior includes a fully-relaxed time-independent behavior when all viscosities are totally relaxed.

2.1.5. Effect of scale and construction

The construction geometry of a rope has an indisputable effect on its behavior and strength (*Hearle, 1969; Amaniampong, 1992; Rao, 2000; Williams, 2002; Lechat, 2007*), due to the twist angles applied during rope construction. In order to be able to compare the mechanical behavior of ropes of different diameters (different diameter scales), it is necessary to normalize the force by a parameter describing the

cross-sectional size (*Del Vecchio, 1992; Lechat, 2007; Dib, 2014*), usually in tex (g/km). With these parameters, it seems possible to characterize a rope at scale 1 from the mechanical characterization at a reduced scale ("sub-rope"), as shown in the studies of (*François, 2008*) for quasi-static and dynamic stiffness curves and (*Lechat, 2007*) for the creep behavior of polyester filaments and ropes.

Scaling effects have been studied for polyester (*Lechat, 2007; Ghoreishi, 2004*) comparing each element of ropes in terms of rigidity, ultimate tensile strength and creep. Some other studies (*Del Vecchio, 1992*), have tested different scales of a rope but did not show correlations between the different scales. Moreover, the effect of the lay length is only roughly evaluated as "the longer the lay length the higher the rigidity".

2.2. Objective

2.2.1. Visco-elasto-plastic characterization of a polyamide twisted rope

Numerous results in the literature were obtained on polyamide yarns as it is the easiest scale to examine; however, we have very few results for ropes. This is why one of the objectives of the present study is to characterize polyamide twisted sub-ropes under realistic and representative conditions for different loadings. The characterization must be carried out in the strain range from 0 to 12%, with a strain rate between 10^{-5} and 10^{-1} s^{-1} and different types of loadings; cycle, creep, recovery and relaxation.

This characterization must be done with water-saturated sub-ropes which are kept underwater during tests that may last up to two days.

This characterization must make it possible to provide information on all aspects of behaviour in order to be able to propose a law that takes all these aspects into account.

As nothing similar was found in our bibliography research, it seems that such a study has not been performed previously, and as floating wind turbines need this type of characterization to better understand the complex behavior of these polyamide ropes it is a fundamental part of our study.

2.2.2. Constitutive law

Another goal of this project is to provide a behavior law usable for the industrial software employed in designing floating wind turbines. As these simulations are quite long and costly, it must be a phenomenological law, using a small number of internal variables, and be quick to process. And in addition, providing an accurate description of the behavior of the rope for the three time scales of simulation, short term behavior (waves, vibrations ...), mid term (storm, tides ...) and long term (creep).

Few behavior laws have been proposed for synthetic ropes in the published literature, and none for polyamide ropes in water.

The approach proposed in this manuscript will lead to a constitutive law including modeling elements from the literature as *Flory*' (Figure 2-4), *François*, *Davies*, and the Syrope model. The project partner BV has a long experience in the study of the behavior of these synthetic ropes and so the law proposed will also be based on their expertise (*François, 2018*).

2.2.3. Direct identification method

One of the difficulties in modeling polyamide is due to the very viscous behavior of the material. An experimental protocol must be defined to identify intrinsic characteristics of the sample. These experimental protocols must be short enough to be applicable on full scale rope and complex enough to give an accurate description of the material behavior in terms of elasticity and viscosity. The identification processes come from the observation of the material's response, and require a way to separate each component in order to have control over the model.

The identification method proposed here for each block of the law is performed without using an inverse identification approach by an optimization algorithm (*Weller, 2018*). We will try to evaluate in isolation, one by one, the relevance of each element of the model and its performance from the comparison to experimental measurements. This will allow us to validate or question the modeling choices and this will also allow us to give relevant directions of improvement for each block of the law.

2.2.4. Implementation of the proposed law into classic FE codes

First of all, the law must be usable as an engineering tool, as there is a need for a description of the behavior of the rope better than a rigidity model for a mean load value, as used in most software for designing floating wind turbines today.

Then the behavior law will be implanted in a Finite Element code (like Abaqus and/or Deepline).

2.2.5. Understanding, effect of scale and construction

For our study, tests will be performed on small scale samples as they need to be adapted to the laboratory's equipment, to reduce cost, to be easier to make and thus allow more tests to be done. The scale effect is not the main topic of this study, but as the full-scale rope cannot be studied, our evaluation must be made on yarn, rope-yarn or sub-rope. The approach here is to define a characterisation procedure, which will be tested on a similar sub-rope construction to that of the in service rope, and which can then be applied in a future project to the real size rope or sub-rope with a small number of additional tests.

2.3. Strategy/Plan

Before characterizing the rope, some experimental tests were made on yarns to define their break strength (average of 130 Newton), strain and scatter as it is a convenient scale given to study. These results will contribute to understanding the behavior of the material and help designing the subsequent tests on sub-ropes. This part will not be presented in the manuscript as it is not the focus of this chapter. But results can be briefly described as: minimal scatter was found between the stress-strain response of the yarns during tensile tests, but important variation in the breaking strain of yarns was observed (break strain between 16 and 20 % and 0.65 to 0.75 N/tex for break load), and loading below the maximal load seen previously by the yarn does not seem to affect the relaxation behavior. Additionally, it was necessary to verify that the material was almost fully saturated in water before testing. From a previous study (*Humeau, 2017*) on these yarns and from DVS tests, we confirmed the almost fully saturated state of the yarn after 4 hours in water.

To test the stranded rope, a machine with a large cylinder stroke is required, due to the length of the rope and the high breaking strain of the polyamide. The testing machine must also be able to apply complex loading with different tensile speeds. In our case two testing machines were available; the test bench in Ifremer which is mainly used for fatigue test (very busy doing long term test) and limited in its capability to perform high rate loading, and the Servotest machine in Ensta Bretagne.

We chose to use the latter machine. Due to the length of the cylinder stroke it imposed a maximal sample length around 1000 mm, and as the diameter influences the length of the splice, it required a sample with a diameter around 10 mm. The project partner BEXCO provided a sub-rope on a reduced scale similar to the original sub-rope. The vertical setup of this test machine has also some advantages, as the watering of the rope is easier, leading to a better field of vision allowing for the use of camera-based strain measurements. The strain measurement is another key point, because classical extensometers cannot be used due to the presence of water and also due to the torsion strain along the sample. We therefore used a wire strain sensor and a camera as we found that the film of water does not seem to affect the mark detection.

The identification method used will be direct, with no Prony series in our viscoelasticity law, because this requires an optimization algorithm. Usually, the parameters for these laws are found with inverse identification algorithms and are not always accurate when the simulation drifts away from the loading of the characterisation test. So, with a direct identification method we have better control over the law.

No integral type models will be used because the storage of the deformation history cannot be implemented in a code such as Deeplines™. Indeed, integral models use too many variables to be relevant for mooring line finite element models.

Finally, to validate that the behaviour of smaller samples is similar to that of the in service sub-ropes, larger sub-ropes were tested in Ifremer with a similar loading sequence to the one made on the smaller scale samples.

2.4. Mechanical tests on a 4-ton polyamide wet sub-rope

This chapter presents the mechanical characterization that was carried out on 4-ton sub-ropes. The mechanical loadings applied to the ropes are monotonous tensile and several combinations of cycles, relaxations, recovery and creep. A detailed description of these tests and their results are presented.

The 4-ton sub-rope samples are designated as “SR” followed by the number of the manufacture order.

2.4.1. Material and experimental methods

2.4.1.1. Material and sample dimensions

The average diameter of the 4-ton sub-rope is 11.5 mm. The measured Minimal Breaking Load (MBL) is 40 kN, referred to as 4 ton.

This sub-rope is composed of 3 strands with a lay length of 50mm. Each strand is made of 10 twisted rope-yarns. Each rope-yarn is composed of 13 yarns. Additional information on the structure can be found in Table 2-1.

The fiber is a polyamide 6 (PA 6). The coating of the rope is made at the rope yarn scale with a confidential coating process.

	Quantity in the immediate upper scale (line above)	Average diameter (mm)	Linear mass (tex) (g/km)	Lay length (mm)	Z or S twist
Sub-rope 4T	1	11,5	90 000	50	S
Strand	3	9	-	50	Z
Rope-yarn	10	2	2 600	32,26	S
Yarn Nexis type “371”	13	0,27	190,5	-	-
Fiber	280	0,026	-	-	-

Table 2-1. Dimensions and other parameters of the 4-ton sub-rope and its components.

The dimensions of all parts of the sub-rope sample are shown in Figure 2-6.

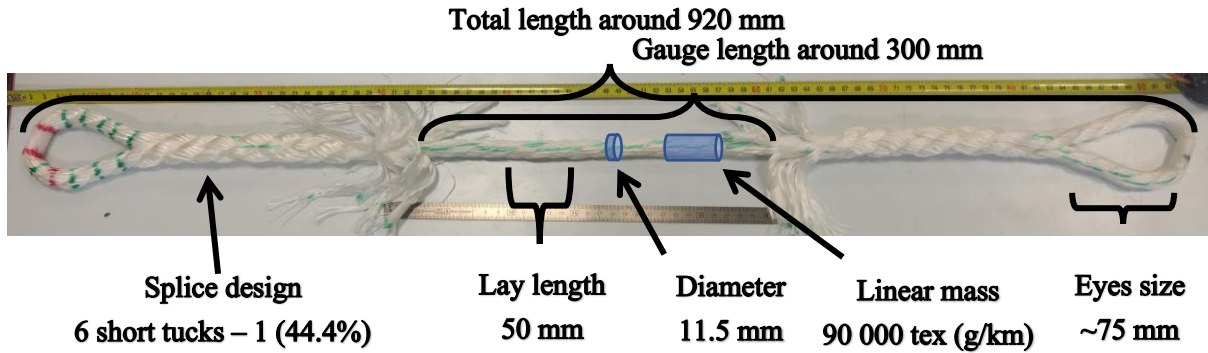


Figure 2-6. The 4-ton sub-rop sample dimensions for mechanical characterization (here SR39 on the picture).

2.4.1.2. Sample preparation

2.4.1.2.1. Splicing

Because of the limited piston stroke of the hydraulic machine, the overall length of the samples is limited. The parameters of the splices have been chosen in order to avoid slippage but to be as short as possible and to get the longest gauge or central length.

We determined from trials and errors that for the characterization test, the splice design would be the following: 6 tucks with the full sub-rop and 1 tuck with 44,4% of each strand.

Splicing requires accurate skills (especially to obtain the same tension in each strand). I made the splices, after receiving a 3-day formation at Bexco, the synthetic rope manufacturer, in Belgium (Figure 2-7).



Figure 2-7. Splicing of a 4 ton sub-rop diameter.

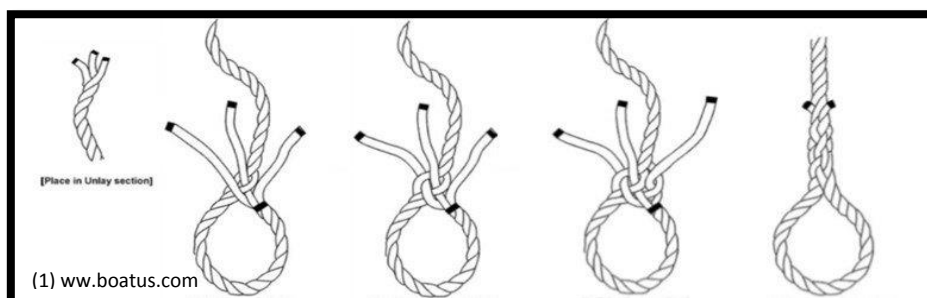


Figure 2-8. Outline of splicing (a) and a 4-ton sub-rop being spliced (b)

2.4.1.2.2. Water diffusion

Before each test, the sub-rope sample was fully immersed in tap water for 10 hours without load, in order to saturate the sample. As shown by *Humeau (2017)* on the same fiber type but without coating, this duration should be highly sufficient. However with the coating, the sorption parameter may change. For this reason a differential vapor sorption (DVS) test (IGAsorp by HidenIsochema) was made on a coated yarn, extracted from a 4-ton sub-rope, to confirm that the watering duration was sufficient: this test has shown a characteristic time to saturation of less than 1 hour, which is largely inferior the to ten hour immersion period. This test was performed on a yarn; one might question if the structure of the sub-rope plays a role in the water diffusion. However the sub-rope is completely unloaded during immersion, leading to large spaces between the yarns; this allows the water to diffuse easily into the yarns. If the rope were loaded and tensioned, it would be a different case.

2.4.1.3. Testing equipment

2.4.1.3.1. Tensile testing machine

A hydraulic machine was employed, designed specially by Servotest for high rate testing at ENSTA Bretagne. It was used in quasi-static tensile mode. Its cylinder stroke is 600 mm in the vertical direction. The maximum displacement speed is 100 millimeters per second for quasi-static tests. At its full capacity, the maximum tensile force is 100 kN at 20 m/s or 200 kN at 10 m/s.



Figure 2-9. Servotest machine used for testing the 4-ton sub-ropes in the mechanical laboratory of ENSTA Bretagne.

2.4.1.3.2. Load cell

The load cell used is a *Hottinger Baldwin Messtechnik*® transducer that has a range of +50 kN and a resolution of 2 mV/V leading to a precision around 10 Newtons.

2.4.1.3.3. Strain measurement in the central part of the rope

The strain has been measured by image correlation; two black 2mm-diameter bungee markers were attached to the rope and tracked by a CCD camera (Retiga 6000 by Q-IMAGING with 6.05 Mega Pixels).

2.4.1.3.4. Jaws and water flow

To connect the rope to the machine, special jaws have been made. The bottom jaw enables a watertight tube to collect the water flowing along the rope and return it to a tank. The loading pin diameter is 35 mm.



Figure 2-10. Bottom jaw of the experimental setup (left), watering system at the top of the sample (middle) and installed sub-rope (right).

Particular attention was paid to the watering of the rope during the test, to prevent drying. As the test will investigate the long-term behavior of the material discrete horizontal sprinklers should be avoided if possible, to prevent drying of the sections between the sprinklers, so a vertical system is more suitable.

A volumetric pump with small flow (around 1 liter/min) brings tap water near the top of the sample, through a spiral-shape pierced tube. This tube is covered by a knitted fabric allowing a homogenous

water flow. This watering system produces a constant and controlled water flow around the sub-rope with a thickness of about 1 mm.

2.4.2. Bedding in

All tests were preceded by the following preloading, called *bedding-in*:

- Loading at 66 Newton/sec (around 10 %MBL/min).
- 1 hour of creep at 0.061 N/tex (around 14 %MBL).
- Unloading at a strain rate of $5 \cdot 10^{-4} \text{ s}^{-1}$.
- 1 hour of recovery at 0.01 N/tex (around 2 %MBL).

This bedding-in sequence was proposed by Bureau Veritas, with the loading rate equivalent to the ISO test, the creep at 14% in MBL being the minimal value to stabilize the rope and the unloading low strain rate chosen to reduce the viscous effects.

This bedding-in allows the stabilization of the structure and hence of the length of the sub-rope. The mechanical state at the end of bedding-in is chosen as a reference state for the subsequent strain measurements. It also allows the specimens to be compared based on the same initial loading history, and to improve the test reproducibility.

In order to understand the benefits and necessity of a bedding-in pre-loading, we also considered the mechanical states reached after the following “manual” procedure, without any bedding-in:

- Manual displacement control of the tensile machine from a fully unloaded sample state to a tensile force of 0.01 N/tex (at these low levels of tension, no automatic servo-control is possible).
- Jaw relative displacement is maintained constant for about 10 minutes; during this time, the black bungee markers and the watering system are put in place.

This procedure was applied before each bedding-in of the tests. After this, the strain measurements were recorded. Figure 2-11 presents the strain measurements at some of these mechanical states after this manual procedure and before the bedding-in. The strain reference is at the end of the bedding-in, so these first strains are negative.

The results show a large scatter in strain and in stress. The stress is not equal to 0.01 N/tex because the behavior includes viscosity and the second stage of the procedure relaxes the stress for about 10 min. The error bar represents the standard

deviation and is around 1 % of strain. Significant variation at low load even when the rope is loaded shows the importance of the bedding in procedure. Indeed, at the of tensile loading, textile materials often show a low increase of stress for a large amount of strain, as the textile structure re-organizes. This particular behavior makes determination of the reference mechanical state for the strain measurements quite delicate. This is not the case for bulk materials like metals for instance.

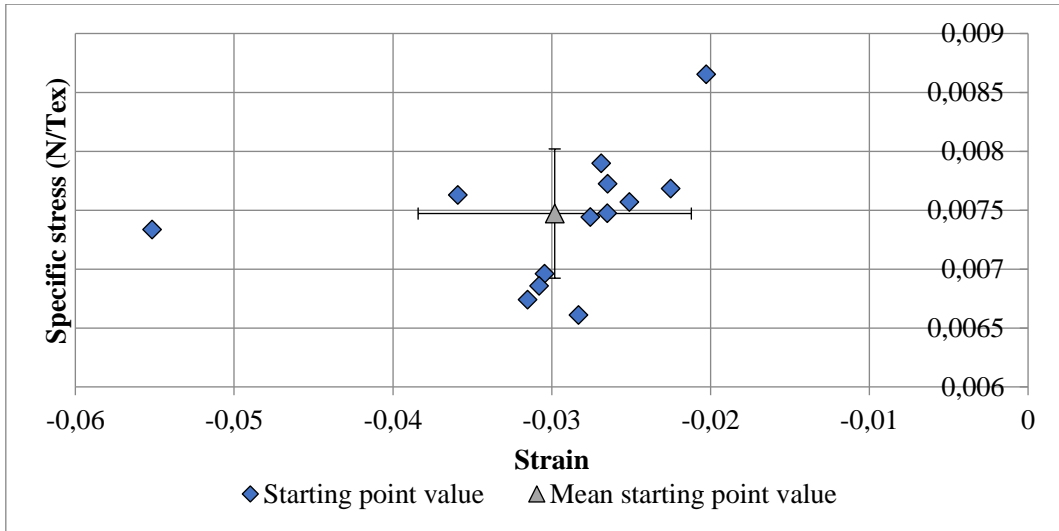


Figure 2-11. Starting positions for some tests made on 4-ton sub-ropes before the bedding-in.

Figure 2-12 presents the stress-strain curve for the bedding-in of sample SR40, that is representative of the other tests. Figure 2-13 presents the stress and strain changes as a function of time.

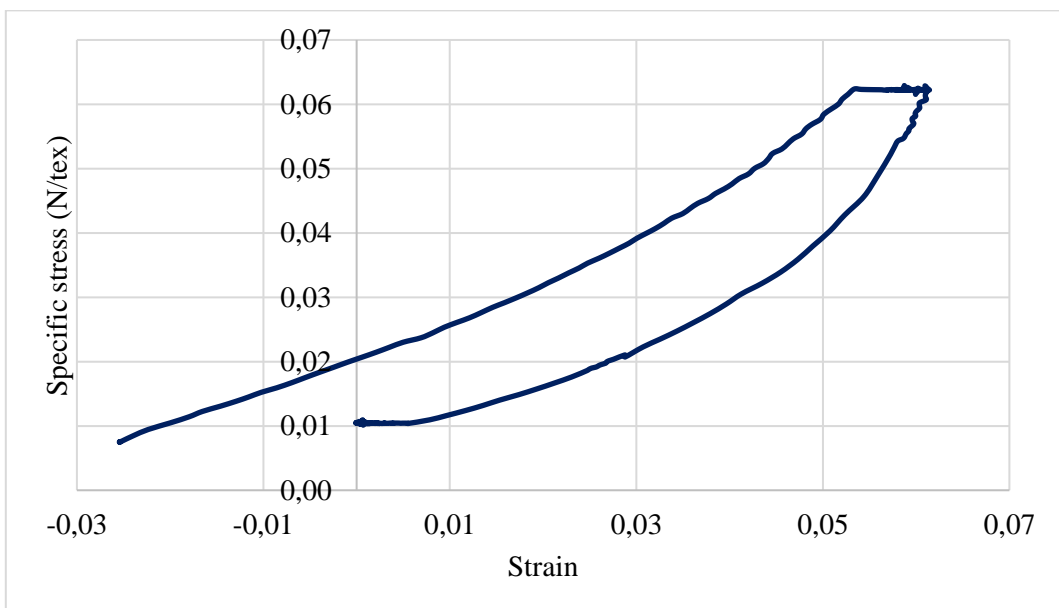


Figure 2-12. Stress-strain curve during a bedding-in preloading (sample SR40).

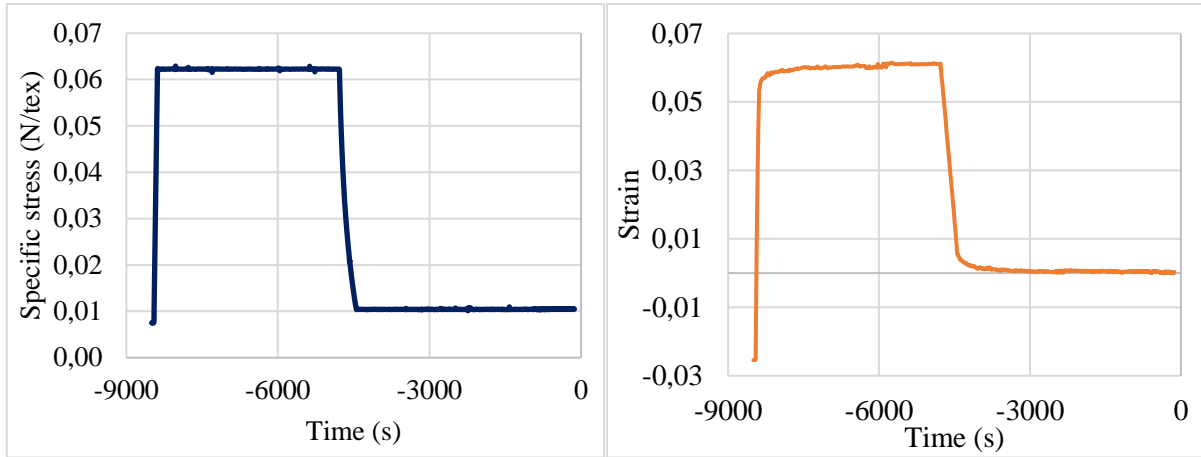


Figure 2-13. Time-evolution of the stress (left) and strain (right) during the bedding-in of sample SR40.

The load control is well respected leading to a more stable strain behavior (after the creep at 0.062 N/tex) between samples, and allowing a reference state to be defined for these tests.

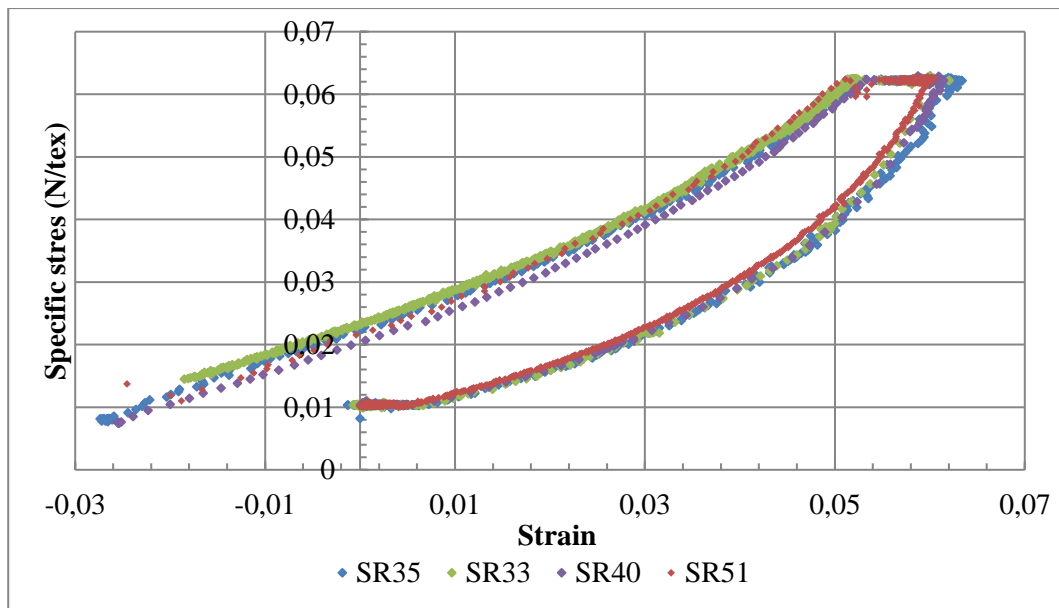


Figure 2-14. Example of scatter for the bedding in.

2.4.3. Tests at different strain rates

Three to five tests were performed for each strain rate from 10^{-5} to 10^{-1} s^{-1} .

2.4.3.1. Procedure

All tests were preceded by the bedding-in sequence described previously in section 2.4.2. The tensile tests were performed with a constant jaw displacement speed leading to an approximately constant strain rate, ranging from 10^{-5} to 10^{-1} s^{-1} , up to a stress value of 0.3 N/tex , corresponding to a force of 27000 N .

Table 2-2 presents the number of specimens tested with the average strain rate and the jaw displacement speed. Figure 2-15 shows some examples of time evolution of the strain during the tests for strain rates of 10^{-4} and 10^{-2} s^{-1} , showing the approximations made on the strain rate.

Number of specimens tested	$\dot{\epsilon} \text{ (s}^{-1}\text{)}$	Displacement speed (mm/s)
3	0.7×10^{-5}	0.008
3	0.7×10^{-4}	0.08
4	0.7×10^{-3}	0.8
4	0.7×10^{-2}	8
5	0.7×10^{-1}	80

Table 2-2. Number of specimens tested by strain rate.

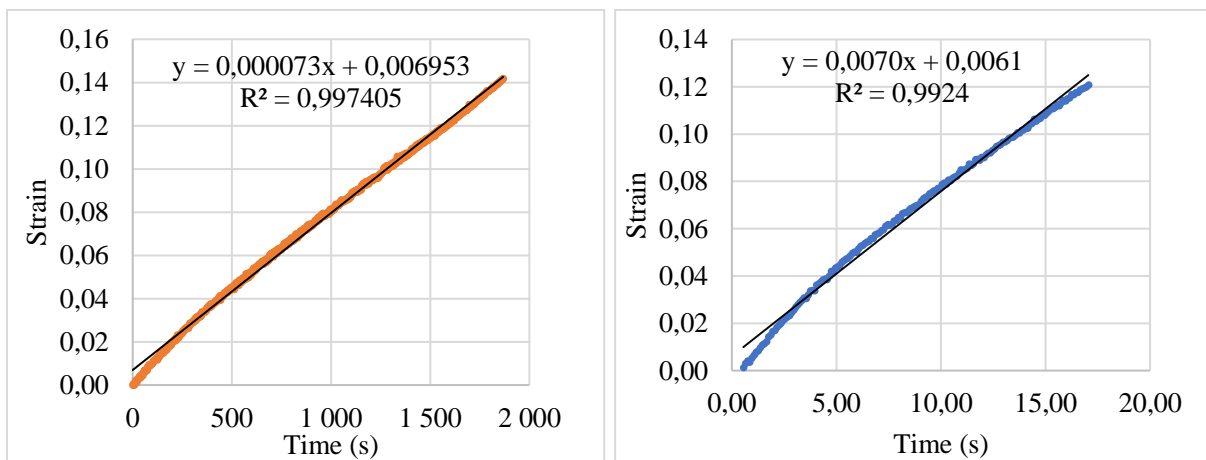
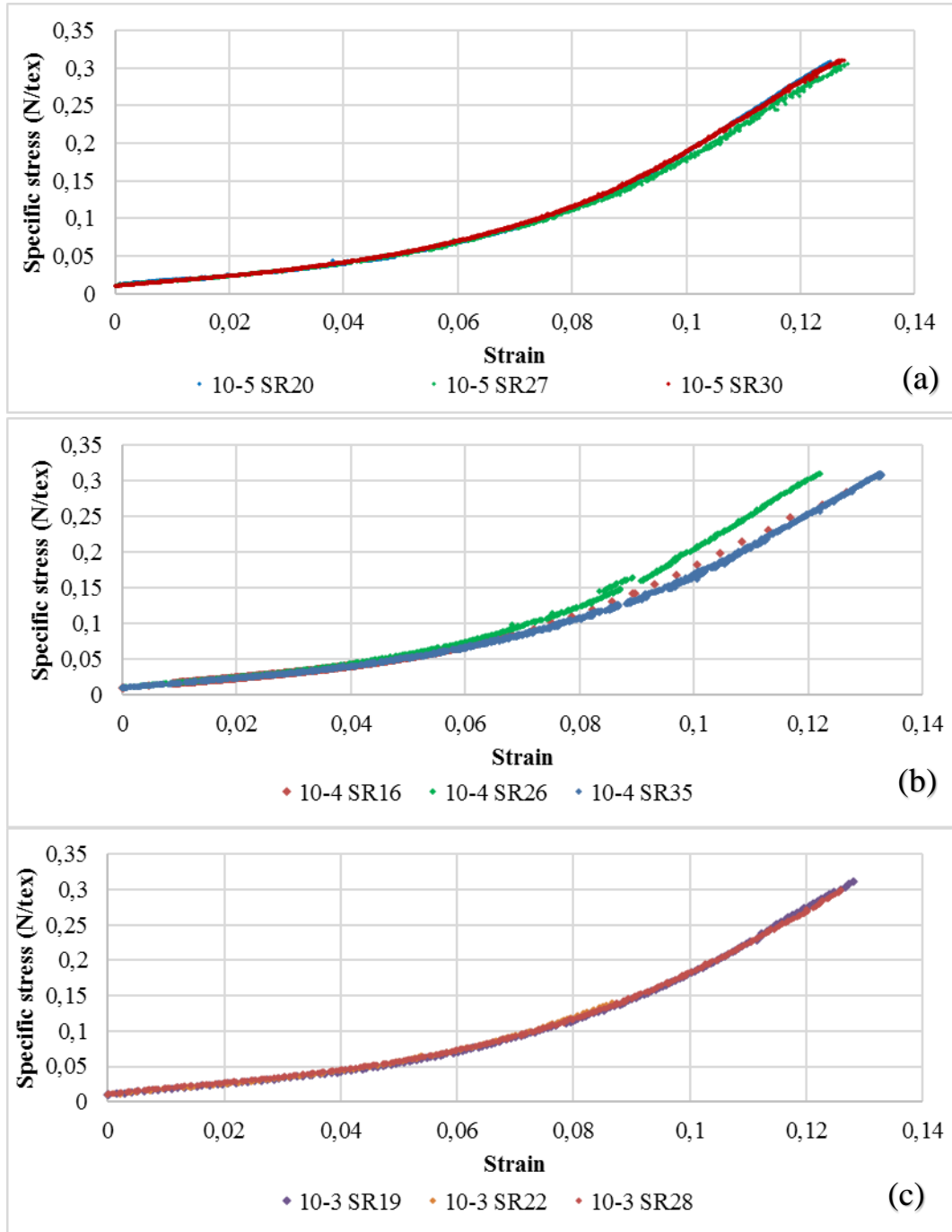


Figure 2-15. Time evolution of the strain for a displacement speed of 0.08 mm/s (left) and 8 mm/s (right).

2.4.3.2. Results

Figure 2-16 shows the results of the different tensile tests at different strain rates. The curves are presented with the specific stress as a function of the logarithmic strain measured by the camera.



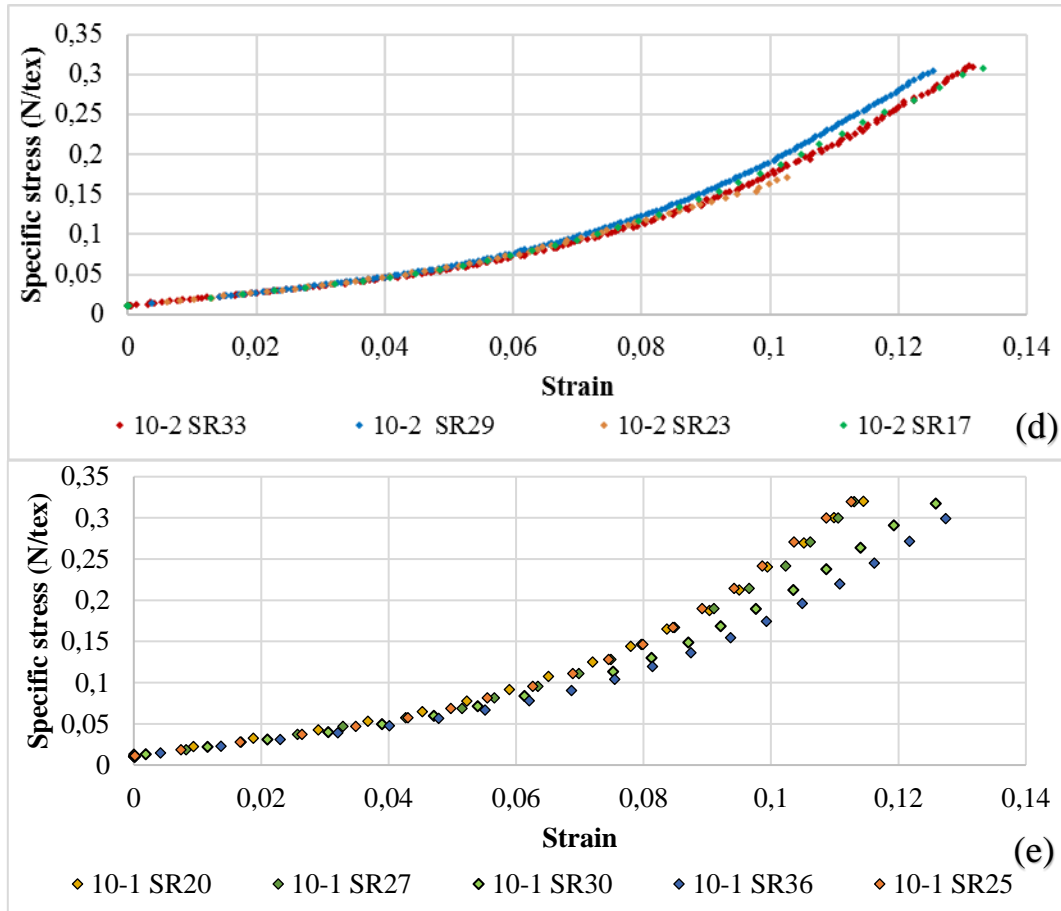


Figure 2-16. Tensile curves for each test at different strain rates ($a=10^{-5}$, $b=10^{-4}$, $c=10^{-3}$, $d=10^{-2}$, $e=10^{-1}$ s $^{-1}$).

These tensile tests show a non-linear stress-strain evolution during monotonous loading. The tensile curves have a characteristic shape with two distinct zones, presenting different slopes in the stress-strain graph. The transition between the two zones is quite gradual. The curve tendencies are similar with a first part from 0% of strain to around 7% where we have a smaller tangent modulus and a second part above 7% where the stiffness increases.

Some tests show a good repeatability (as tests made at a strain rate of 10^{-5} , 10^{-3} and 10^{-2} s $^{-1}$) while others show a large scatter above 7% of strain. It also appears that we need to repeat tests at least three times due to the variability (for tests performed at strain rate of 10^{-4} and 10^{-1} s $^{-1}$).

Tests made on yarn samples usually show a very small scatter. This means that scatter may come from variations in the splices, the structure of the rope or the environment. The lay length is usually controlled during manufacturing and installation before the bedding-in, however a change in the splice can result in a change in the lay length and variations in tensions in the strands.

2.4.3.3. Analysis

The aim of these tests is to characterize the viscoelastic steady state at constant strain rate for the rope behavior. Taking the different strain rate curves, we can generate mean curves for each strain rate with their standard deviation (see Figure 2-17).

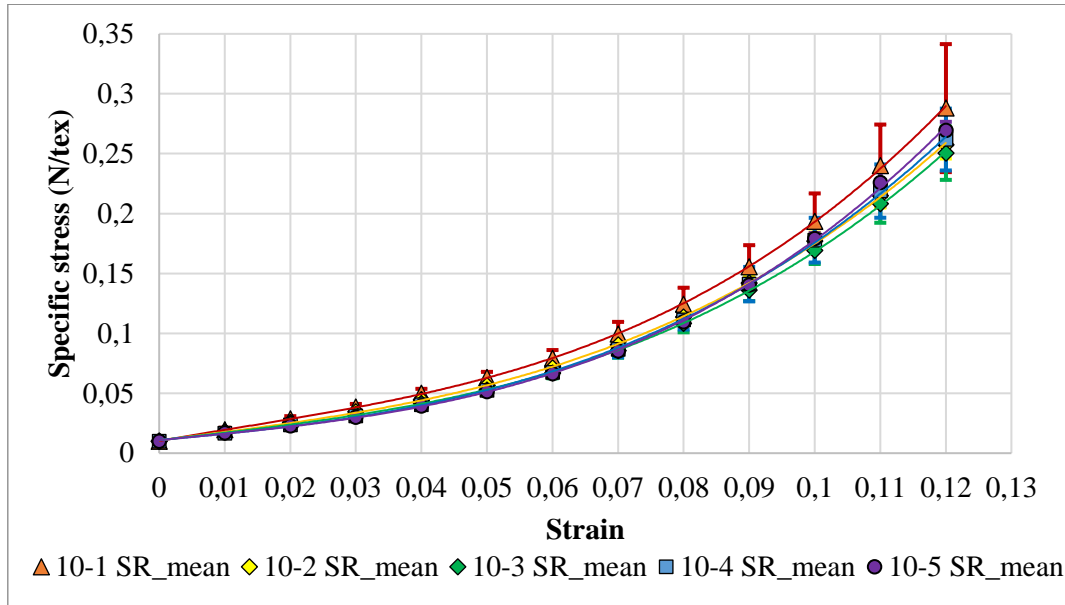


Figure 2-17. Mean tensile curve for each strain rate.

From the mean results, we can see that the higher the strain rate the higher the stress at a given strain value. The tests performed at 10^{-1} s^{-1} are clearly leading to higher stresses in comparison to the others and the test at 10^{-2} s^{-1} is the second highest in stress up to around 9% of strain. After this value of strain, the scatter is too high to draw a conclusion.

As it is quite hard to discern the evolution at lower strains, a different graphical evaluation was made: for each percent of strain; the load measured for different strains is replotted as a function of the strain rate (see Figure 2-18 and Figure 2-19).

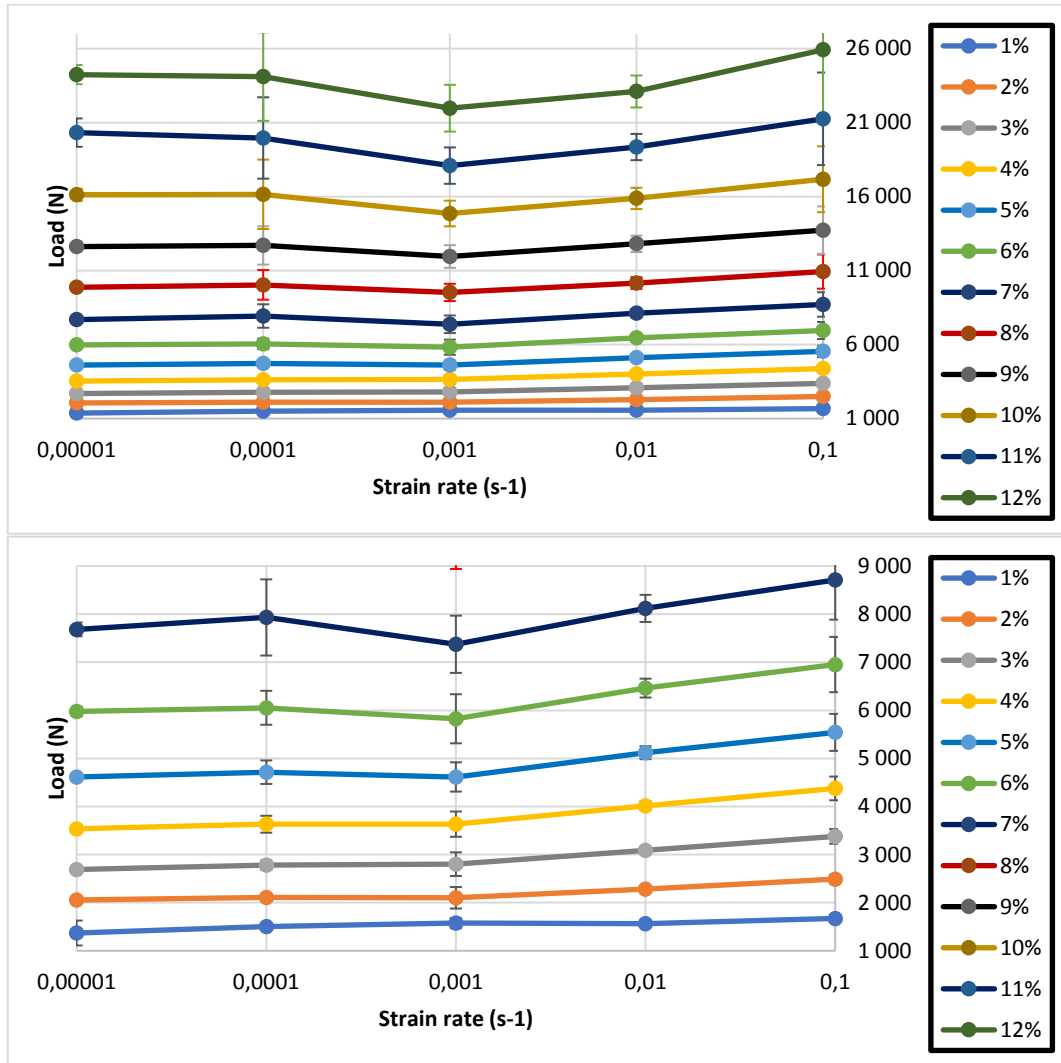


Figure 2-18. Evolution of the load as a function of the strain rate for each percent of strain.

Above 7%, it is difficult to see any trend for the effect of strain rate on the load, so we have only taken the first 7% of strain and plotted the evolution of load ratio as a function of the strain rate (see Figure 2-19).

The load ratio is defined here as the load divided by the load at the lowest strain rate, 10^{-5} s^{-1} .

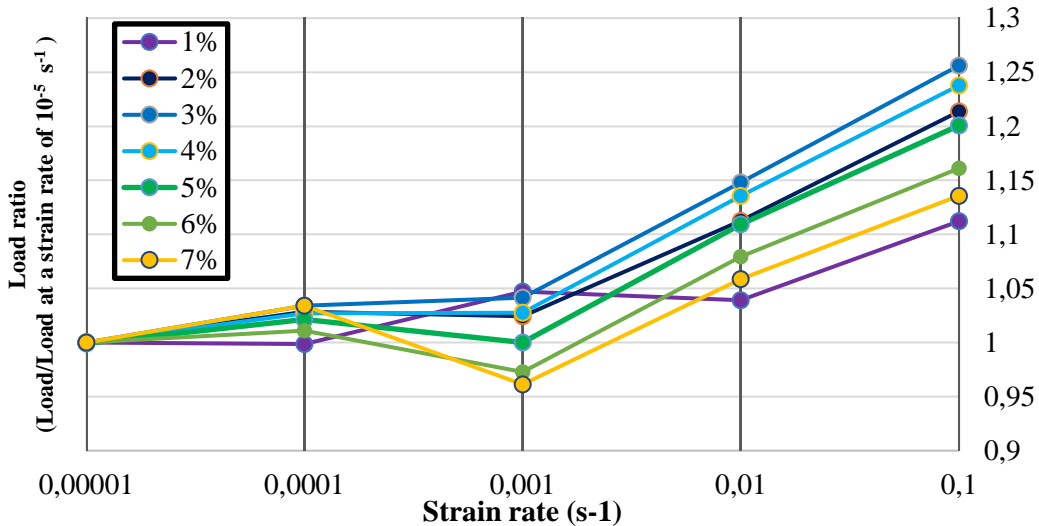


Figure 2-19. Evolution of the load ratio as a function of the strain rate for each percent of strain.

For strain below 7%, it seems that we have two regimes, one with a slow increase and the other one with a linear and much faster increase in load, with the switching point being at around 10^{-3} s^{-1} . The evolution of the fast increase is in fact the same even above 7%.

2.4.3.3.1. Scatter

The evolution of the load ratio as a function of the strain rate is mostly conserved for all strains for strain rates from 10^{-3} to 10^{-1} s^{-1} . However, between 10^{-3} and 10^{-1} s^{-1} the evolution does not make sense, even less so above 7% strain. This influence of the rate on the load is not expected; usually the stress increases when the loading rate increases, according to the classical viscoelasticity theory.

This unexpected rate-dependence may be the response of this PA6 sub-rope to a competition between two phenomena with opposing impacts on the load. For instance, at a high elongation, the flowing water may cool the sub-rope core less than the surface, then an increase of the loading rate could increase the fiber temperature within the sub-rope core, which will reduce the load. This phenomenon could be in competition with the classical viscoelastic effect of the loading rate on the load.

However, this unexpected rate-dependence may also be simply due to scatter in the manufacture of the splices, leading to cases where the stress is not homogeneous and where one strand may be more loaded than the others. The testing environment may also have an effect as the temperature is not controlled, but it was measured (between 18.4°C to 21.3°C) and this variation is quite small.

2.4.4. Cyclic tests with stress-relaxation stages

Four samples have been tested, and the main dimensions are presented in Table 2-3:

Name	Total length (mm)	Useful length (mm)
SR37	920	325
SR38	845	280
SR40	915	355
SR46	1050	320

Table 2-3. Size and useful length of tested specimens.

As a reminder, the splices of the samples are made manually, which explains the variations in lengths.

2.4.4.1. Procedure

All tests are preceded by the bedding-in of section 2.4.2. The cyclic multi-relaxation loading consists of a sequence of load-unload mixed with stress-relaxation stages. These tensile tests have been made under the following conditions:

- A cyclic loading at a strain rate around $0.7 \times 10^{-4} \text{ s}^{-1}$.
- Relaxation of 1 hour (by maintaining the cylinder position) at different strains during the cyclic loading.

Figure 2-19 presents a detailed example of the loading path. At low stress, a recovery stage is performed instead of a stress –relaxation stage; see stage Rc on this figure.

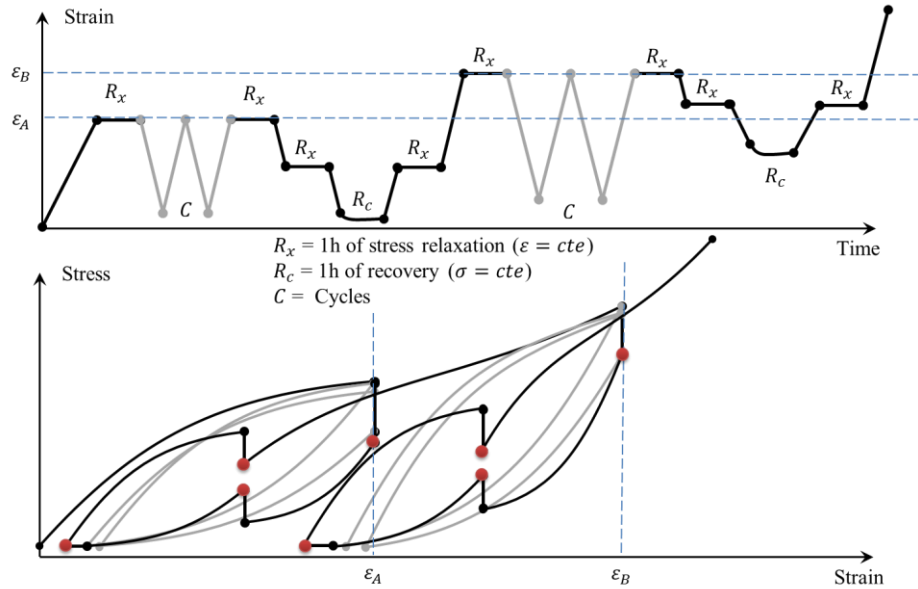


Figure 2-20. Key features of the loading paths of the multi-relaxation tests.

This multi-relaxation loading presents several advantages for characterizing viscoelastic behavior, as it includes cyclic loading, relaxation, recovery and a complex loading history with various maximum loading states. So with one test we can describe most of the elasto-visco-plastic behavior of the material.

In fact, the full test loading path is more complex than is the one presented in Figure 2-20 and is shown the Figure 2-21 below, which shows the test sequence for the sample SR40.

2.4. Mechanical tests on a 4-ton polyamide wet sub-rope

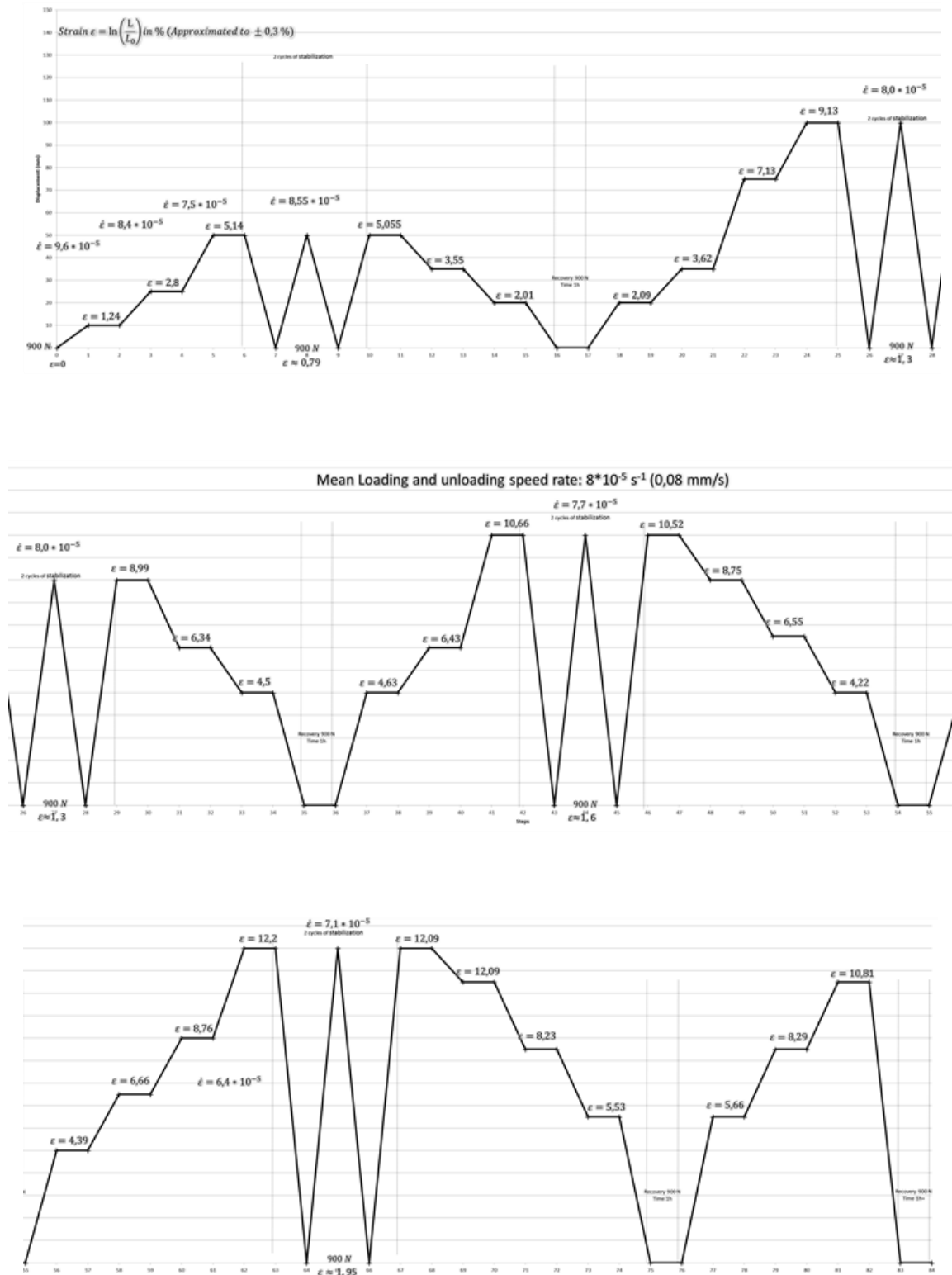


Figure 2-21. Full test description of the different steps of the multi-relaxation test of sample SR40.

Figure 2-22 presents the jaw relative displacement versus time during test SR40. The test duration is around 48h, needing constant supervision. Indeed, the Servotest testing machine had never been used before for a such long-term test. As a result, the intensive use of this machine led to some components failures during some of the tests, meaning that some relaxation stages in the last cycles were missed on samples SR38 and SR46.

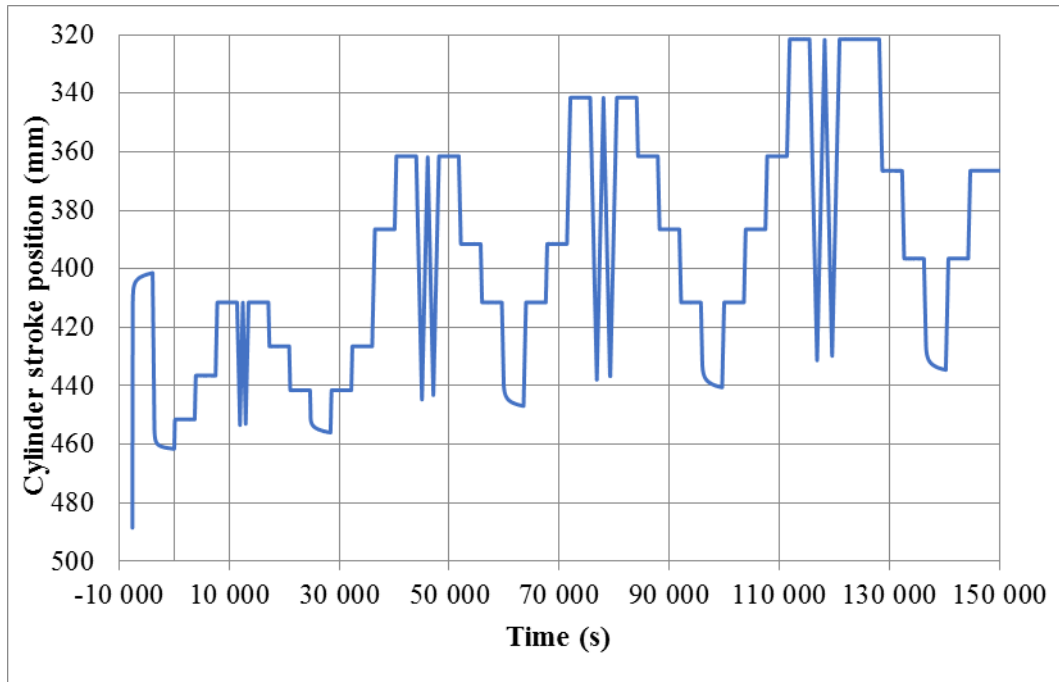


Figure 2-22. Time evolution of the jaw relative displacement during test SR40.

The automatic load servo-control for the load plateau (recovery) was very accurate and the tensile load rate was also fully respected, with smooth transitions between displacement-rate control and load-rate control, during a non-zero tensile load.

2.4.4.2. Results

The first test (SR37) was performed with a slightly different loading from the following ones and allowed the correct jaw displacement to be chosen for the relaxation stages of the three following tests. This test will not be presented here, but it has been used subsequently to validate the numerical simulation results.

Figure 2-23 shows the time evolution of the stress measurement during test SR40.

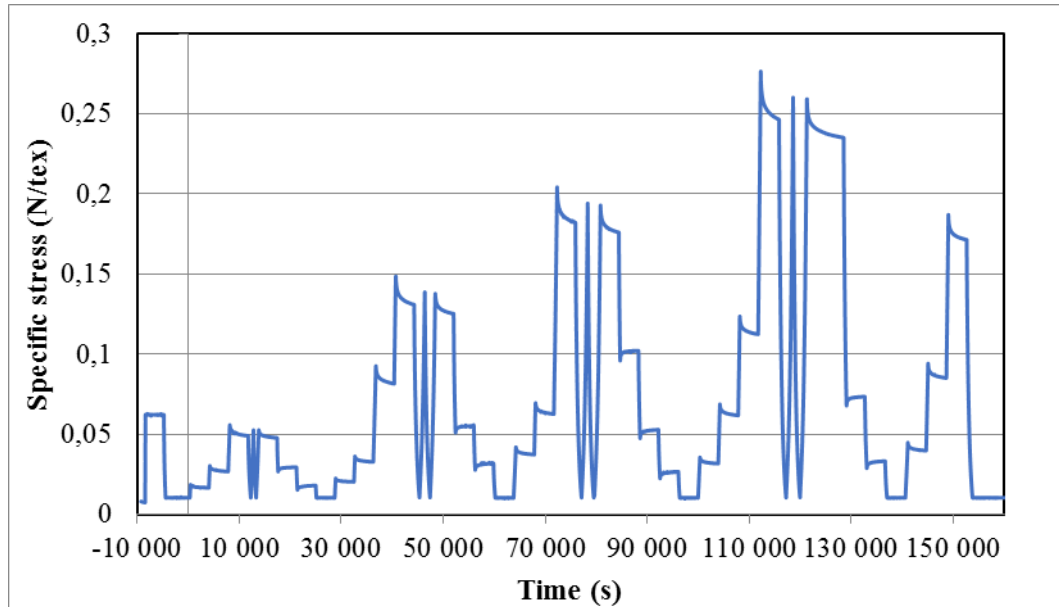


Figure 2-23. Time evolution of the stress during the multi-relaxation test SR40.

Figure 2-24 shows the stress versus strain for test SR40.

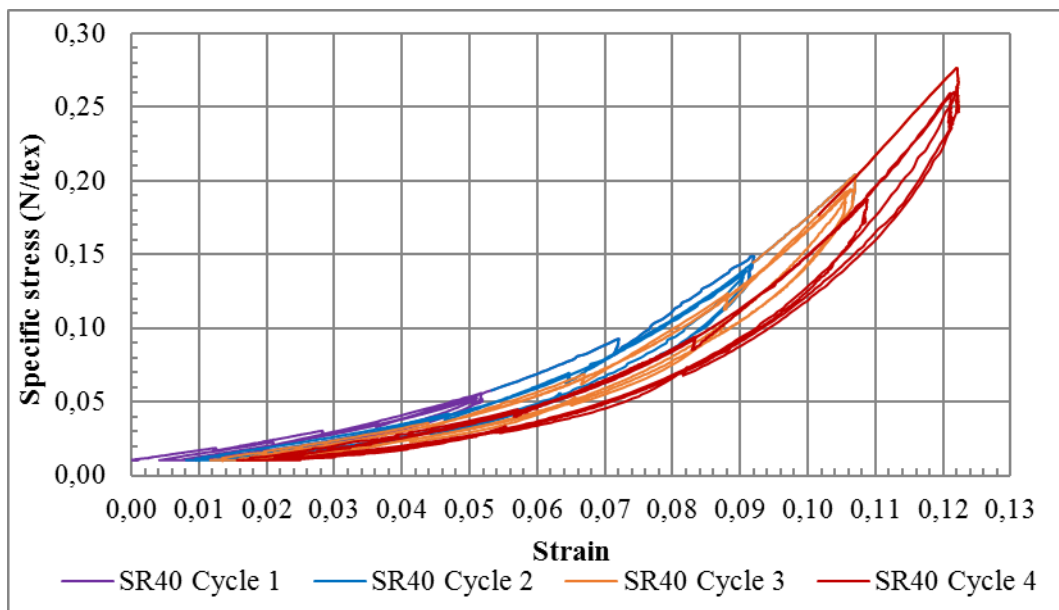
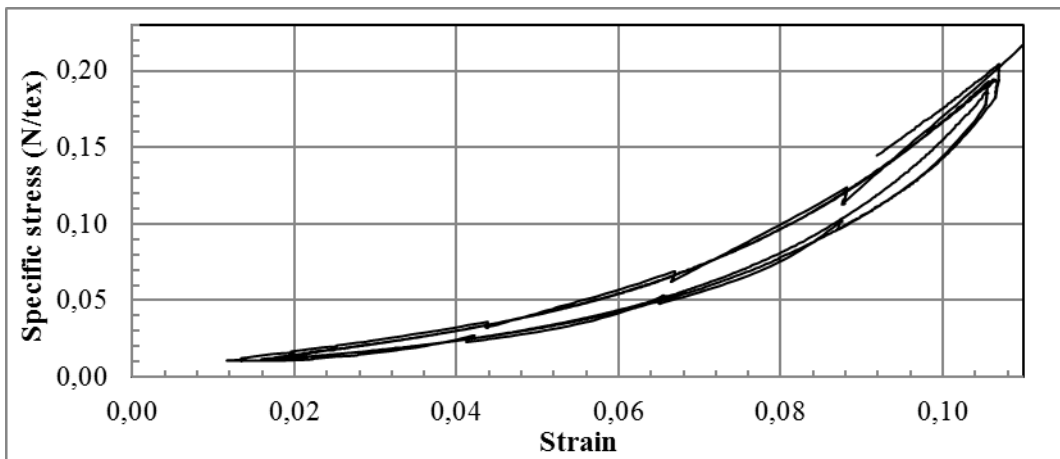
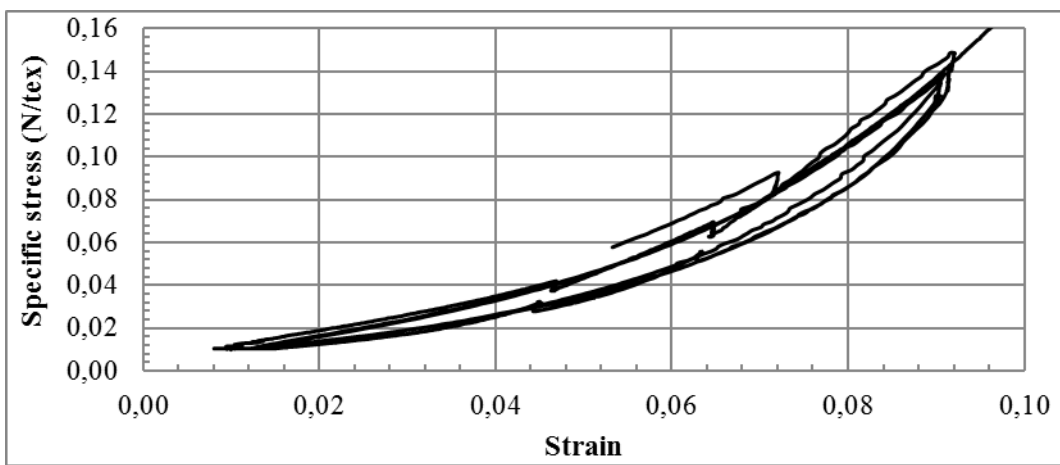
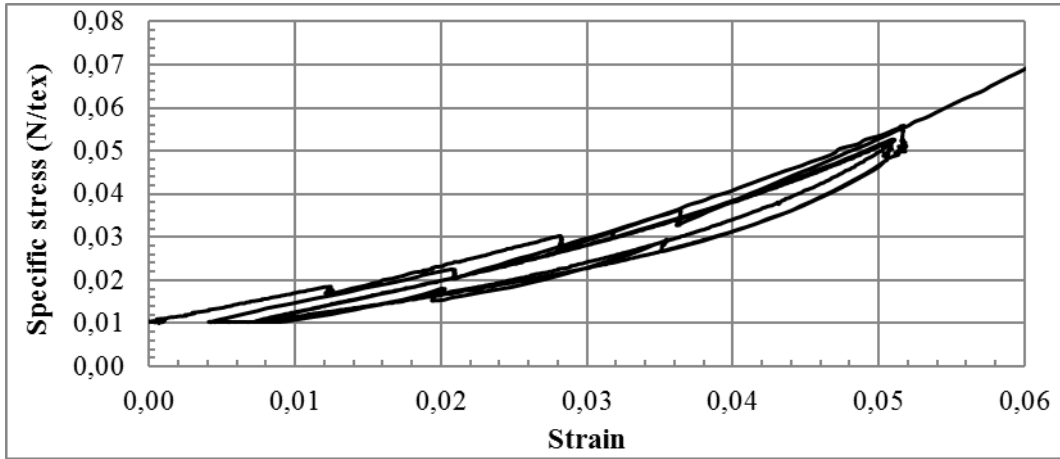


Figure 2-24. Stress versus strain during the multi-relaxation test SR40.

It is quite difficult to examine the details happening in each of these cycles when the entire test is plotted; this is why sections pieces of the test have been separated into different plots in the following Figure 2-25. Comparing the result of the SR40 to other tests a small scatter is observed, similar to those observed for the variable strain rate test. Values of stress at the end of the one hour relaxation are also similar with very little scatter up to 0.1 N/tex (which is around 7 % in strain), and more scatter above this load.



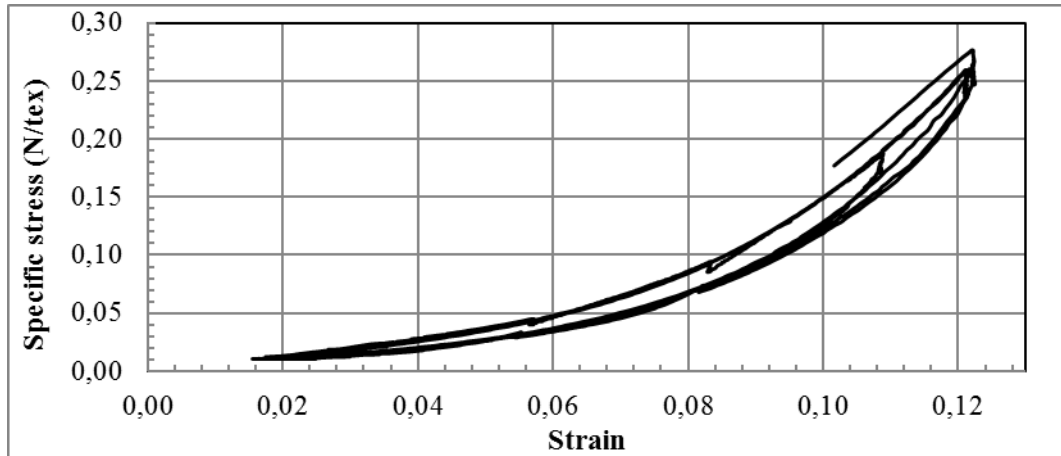


Figure 2-25. Stress versus strain during the multi-relaxation test SR40, separated in four steps.

2.4.4.3. Discussion

The stress relaxation seems to follow a logarithmic function of time (chapter 3); indeed the stress relaxation, plotted on a logarithmic time scale, shows an extended linear evolution (Figure 2-26). Such logarithmic time dependence of stress relaxation or creep strain have often been observed for various polymer materials, and notably for polyester ropes (*François and Davies, 2008*).

If we extrapolate this linear part for greater times, this extrapolation leads to no stabilization of the stress during this relaxation stage, because the logarithmic function trends towards infinity for infinity variables. This is often true for the other relaxation stages.

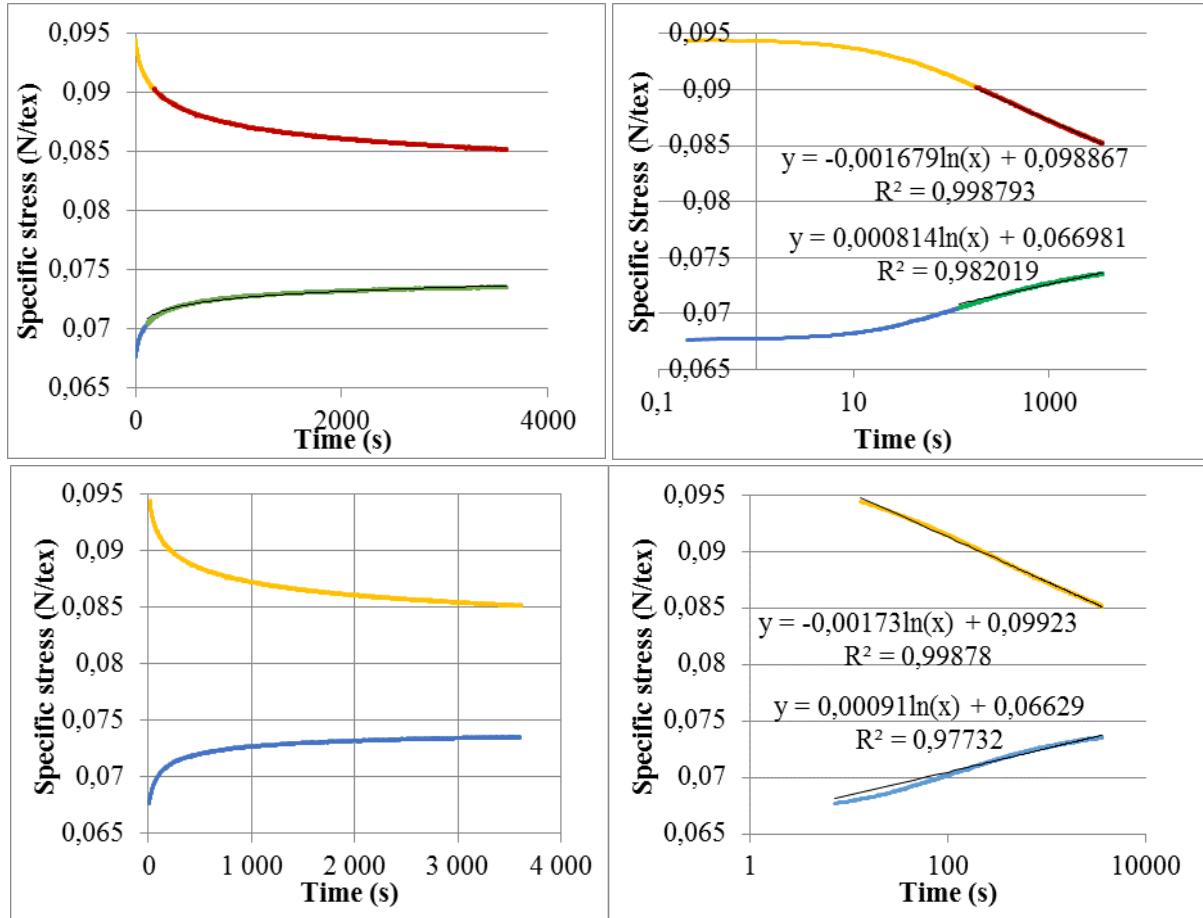


Figure 2-26. Typical time evolution of stress relaxation (left) and in semi log scale (right).

We can also observe that, two relaxations performed at the same strain within a cycle (one performed during the loading phase and the other one during unloading phase) seem to progress to a stabilized value of stress in the middle of the hysteresis loop. As *François and Davies (2008)* proposed, on the basis of the relaxation trends, we can make the hypothesis that the two relaxations, at the same strain, may tend towards a common relaxed stress value which should be approximately at the value where the straight lines are crossing.

From the first cycle and onward, we see that the recovery made after the cycle is insufficient to recover all the strain of our sample, and the higher the load seen, the higher the residual or permanent strain. The maximum permanent strain, occurring after reaching a maximum stress of 0.27 N/tex, is about 2%.

We can also observe that the two opposite relaxations (after loading and unloading with the same maximal load) seem to progress to a stabilized value inside the cycle.

By identifying the time independent value of the relaxation in the cycles, we can plot the evolution of this time independent behavior in all cycles. By plotting the

curve, we observe similar tendencies in the form of the curve of each cycle. So by plotting the value of strain minus the strain value at the end of the recovery of the cycle (i.e. the approximated plastic strain), we have a merging of all the curves to a single main curve, presented in Figure 2-27 for each of the four tests performed.

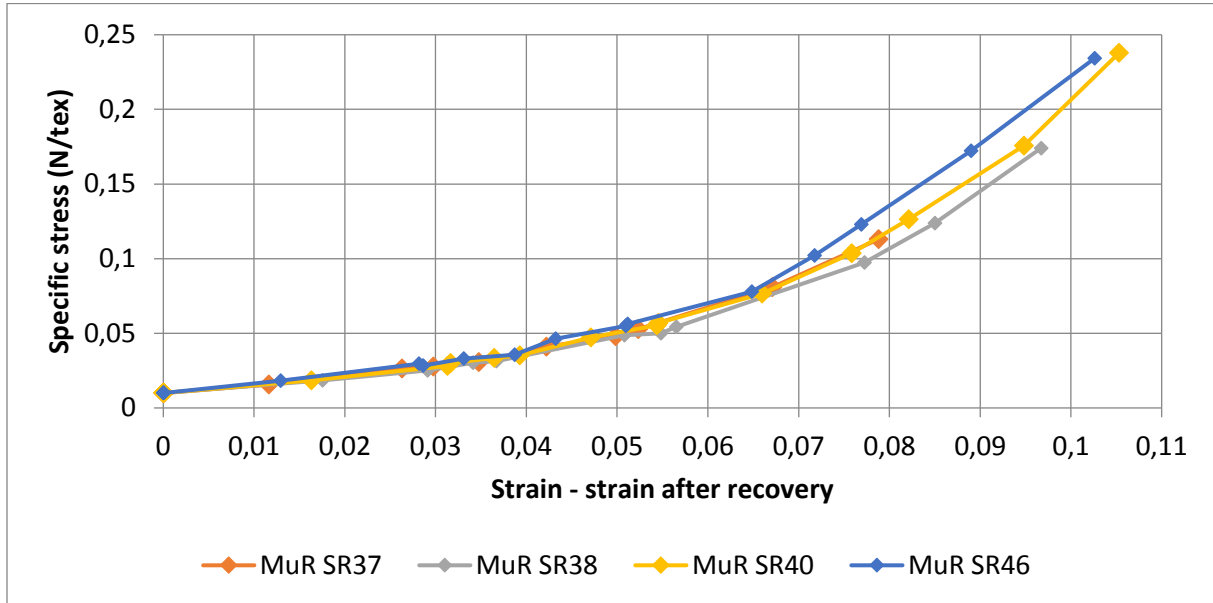


Figure 2-27. Evolution of the time independent behavior in cycles.

2.4.5. Cyclic tests with multi-creep/recovery

Six tests have been performed, named SR47, SR48, SR49, SR50, SR51 and SR52.

2.4.5.1. Procedure

As for the other tests, immersion and bedding-in of the specimens were applied initially. Figure 2-28 presents the loading procedure used. This test consists of 4 batches of 3 cycles with creep and recovery periods at the respective maximal and minimal load of the cycles. This test is load controlled, with a loading speed of 0.001842 N/tex/second which corresponds approximately to a strain rate of 10^{-3} s^{-1} .

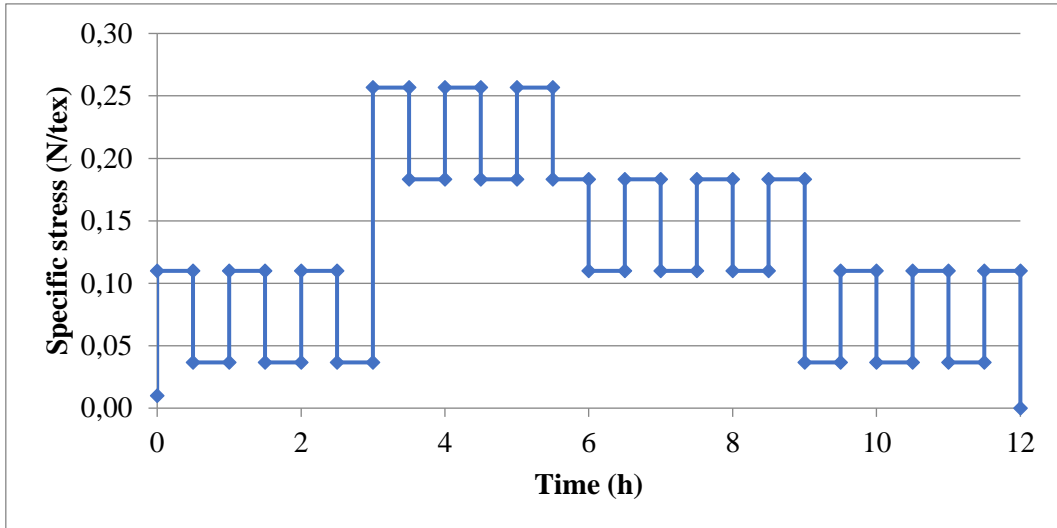


Figure 2-28. Procedure of the multi-creep test at a load rate of $0.001842 \text{ N/tex}\cdot\text{sec}^{-1}$.

The measured load recordings confirmed that the test procedure was respected.

2.4.5.2. Result

Figure 2-29 shows the strain as a function of the time for the test duration.

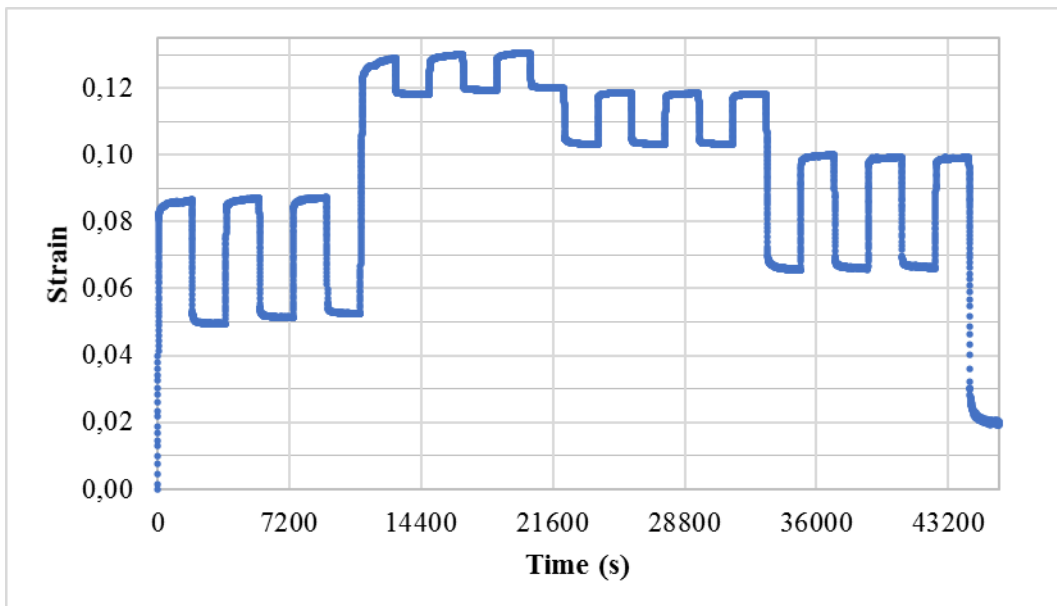


Figure 2-29. Time evolution of the strain during the multi-creep test (SR51).

At the beginning of the test we see a strong increase of the strain, showing the nonlinearity of the material. Each cycle has the same stress amplitude; we have around 4% of strain amplitude for the first block of cycles followed by 1% for the second block (Figure 2-30). During the first block of creep cycles, we also see a stabilization effect with an increase of the minimal strain. Then we see the effect of

the maximal load on the 4th block cycles, leading to stabilized cycles with almost the same strain range as the first batch but shifted by about 2% strain.

Figure 2-30 shows the results of the stress tests as a function of the strain.

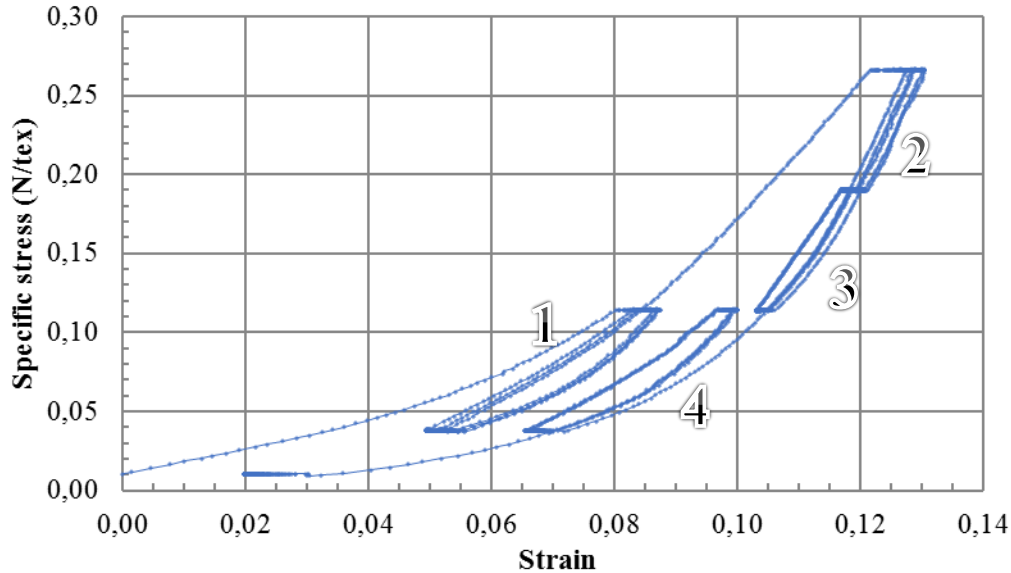


Figure 2-30. Stress versus strain of the multi-creep test (SR51).

With this representation, we see the effect of creep and recovery shifting the curve to the right, to the higher strains. A change in the rigidity within each batch can also be observed, the rigidity increases with the mean load but with no apparent change after a high load in between batches 1 and 4.

A similar test was performed on an 8-ton sub-rope sample; the description of the 8-ton sub-rope sample is presented in Chapter 4.5.2 together with the test details. The 8-ton test was performed with a different bedding-in but including a similar creep step at 0.07 N/tex, before the test. The reference elongation for the strain measurements was taken during the first recovery (after having seen a maximal stress of 0.11 N/tex) at a specific stress of 0.01 N/tex.

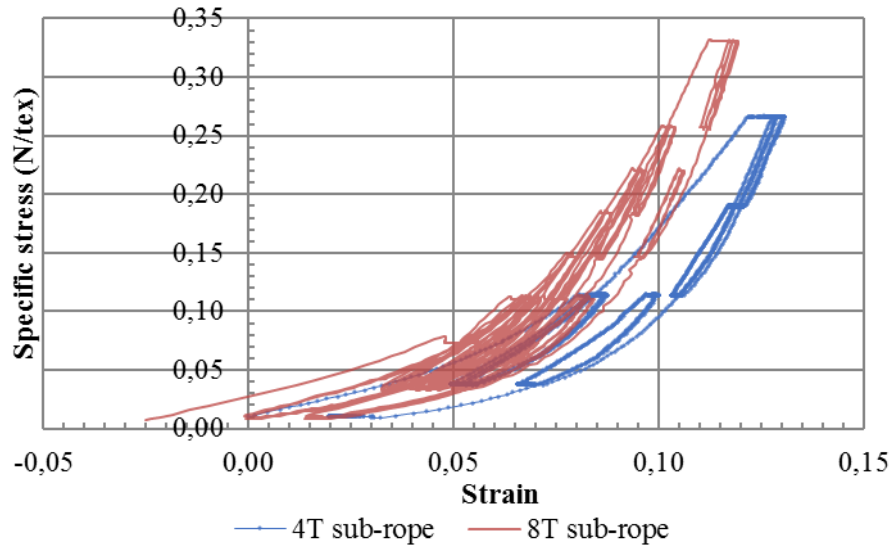


Figure 2-31. Stress versus strain for multi-creep tests on 8-ton and 4-ton sub-ropes.

Figure 2-31 presents a comparison of these tests for the 4-ton and 8-ton sub-ropes. The 8-ton sub-rope is stiffer than the 4-ton; this is probably due to the longer lay length; 50 mm for the 4 ton and longer for the 8 ton. But we observe very similar behaviors between the two sub-ropes in terms of creep, recovery, loading and unloading. This suggests that any mechanical characterization method proposed for the 4-ton sub-rope may be applied to the 8-ton sub-rope.

2.5. Investigation of the mechanical constitutive characteristics

2.5.1. Test selection

To characterize most of the visco-elasto-plastic features of the behavior, we must first define specific loading conditions that allow the features to be revealed. This is why the multi-relaxation test was developed, presenting monotonic loads, relaxations up to a point approaching the relaxed state (by opposite relaxation) and subsequent reloading.

2.5.2. Dynamic / Short-term elasticity

According to the viscoelasticity theory the dynamic or short-term elasticity can be observed at high frequencies, high strain rates or during sudden changes in the loading. We will use this last case; during the re-loadings just after a relaxation, a creep or recovery stage. The tangent modulus just after these stages can be considered as a short-term elastic modulus, as *Bles et al. (2009)* showed on woven polyamide straps.

This elasticity is the fast spring of Flory's element shown previously on Figure 2-4 (*Flory 2013*). This is also the dynamic stiffness of the Syrope model (*Falkenberg, 2018*) (see Figure 2-2).

Figure 2-32 presents the method for the measurement of this short-term elasticity modulus.

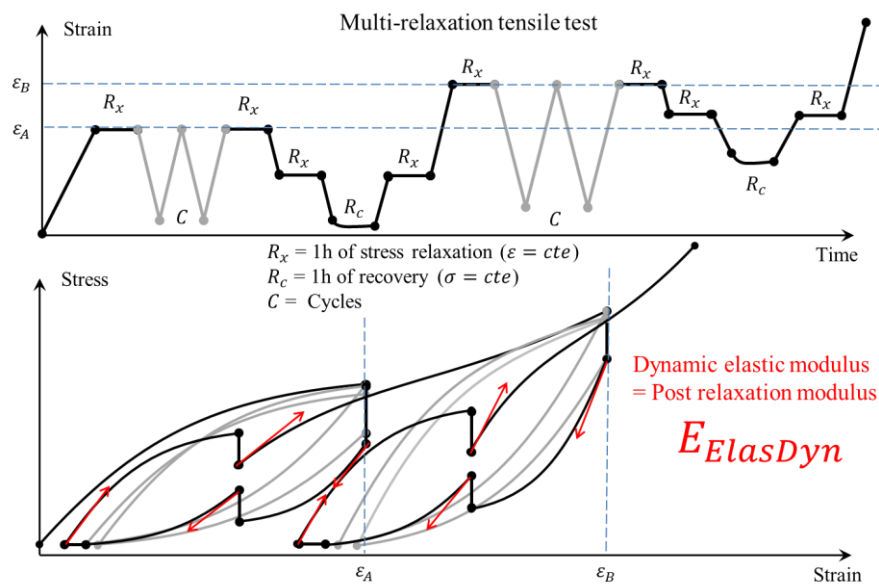


Figure 2-32. Method for measuring the short-term elastic modulus.

A reasonably linear relationship was found between this short-term elastic modulus and the stress, as shown in Figure 2-33, for 4-ton sub-rope samples SR40 and SR48, after all relaxation stages.

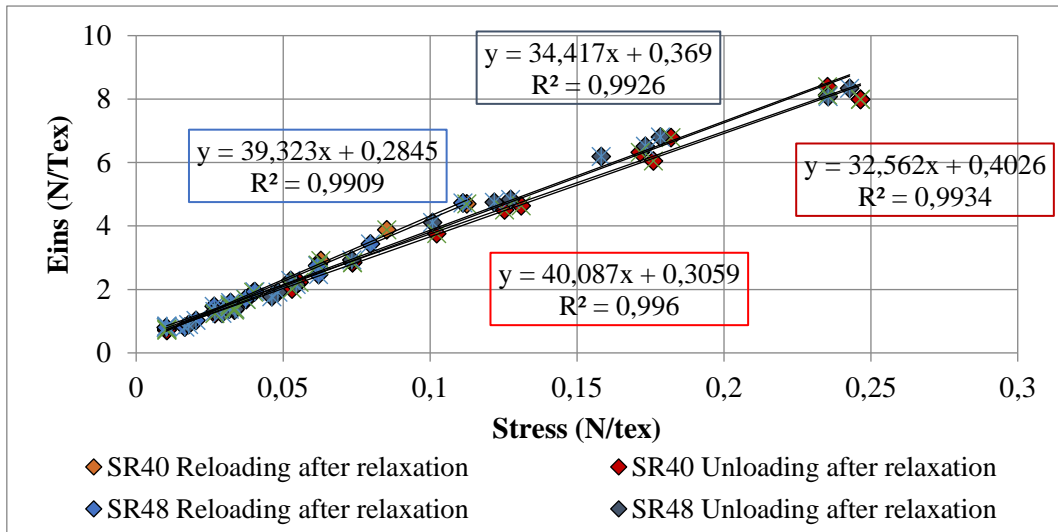


Figure 2-33. Short-term elasticity modulus (E_{ins}) as a function of stress for reloadings and unloadings after relaxation stages.

We can observe a small difference of slopes depending if we are unloading or reloading after a relaxation. However even taking all these values together, the linear relationship seems sufficient to be adopted as a global evaluation with a R^2 of 0.99. *François and Davies (2008)* also found the dynamic stiffness to be linear with the mean load in the case of polyester mooring lines.

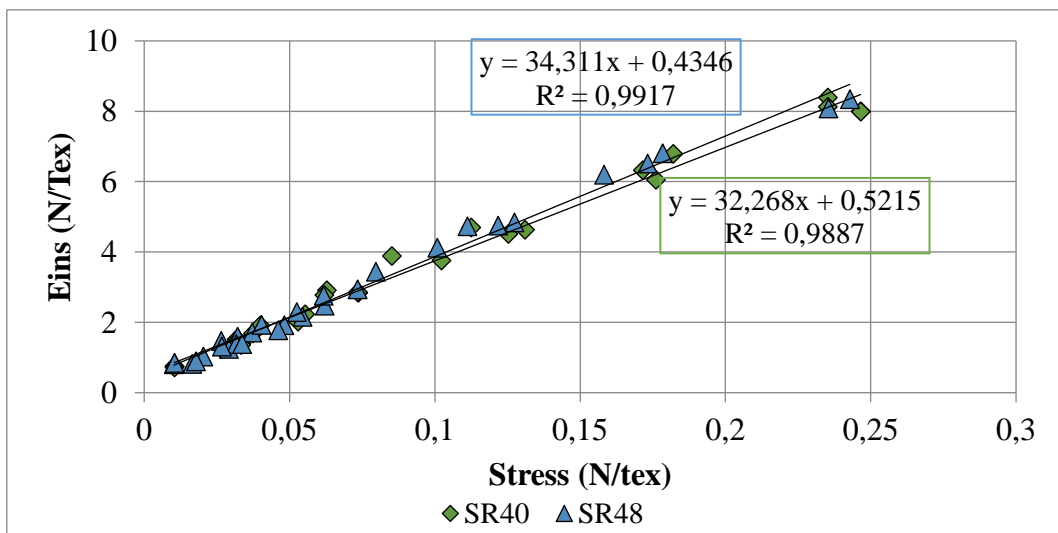


Figure 2-34. Short-term elasticity modulus (E_{ins}) versus stress for 4-ton sub-rope samples SR40 and SR48.

If we assume a linear function between this short-term elastic modulus and the stress as shown by Figure 2-34, we can define a function between stress and strain:

$$\Sigma = \mathbf{i}(\varepsilon)$$

Such that:

$$\mathbf{i}' \circ \mathbf{i}^{-1}(\Sigma) = a * \Sigma + b = E_{ElasDyn} = \frac{d\Sigma}{d\varepsilon}$$

$$\text{or } (\mathbf{i}^{-1})'(\Sigma) = \frac{1}{\mathbf{i}' \circ \mathbf{i}^{-1}(\Sigma)} = \frac{1}{a * \Sigma + b}$$

$$\Rightarrow \mathbf{i}^{-1}(\Sigma) = \frac{\ln(a * \Sigma + b)}{a} + Cte$$

Moreover, if we assume that:

$$0 = \mathbf{i}(0)$$

then:

$$\mathbf{i}^{-1}(0) = 0 = \frac{\ln(b)}{a} + Cte \quad \text{and} \quad Cte = - \frac{\ln(b)}{a}$$

Which leads to the equation:

$$\mathbf{i}^{-1}(\Sigma) = \frac{\ln\left(\frac{a}{b} * \Sigma + 1\right)}{a}$$

Then by inverting the variable, we can determine the function:

$$\mathbf{i}(\varepsilon) = \frac{b}{a} * (e^{a*\varepsilon} - 1)$$

The values of the two parameters are characterized as follows:

$$a = 33.085 /$$

$$b = 0.4849 \text{ N/tex}$$

2.5.3. Fully relaxed behavior / Time-independent behavior

As proposed by *François and Davies (2008)*, a time-independent behavior can be extrapolated from the end of relaxation, creep and recovery stages. We have observed that these stages are not completely relaxed or stabilized after a one hour duration. We propose a method to determine the fully relaxed state by extrapolating them.

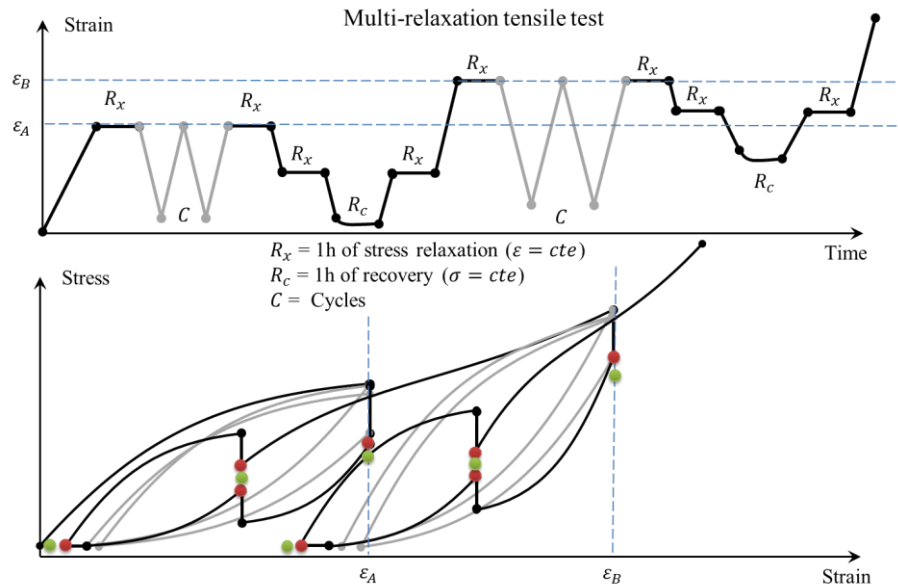


Figure 2-35. Characterization method for the time-independent behavior.

When two relaxations are at the same strain and in the same cycle (one during the loading stage, the other one during the unloading stage), we can define a fully relaxed state by extending the two straight parts of the stress relaxation curves until they cross each other, as shown in Figure 2-36. To do so, we assume, as *François and Davies (2008)* did, that the time evolution is a logarithmic function. The intersection of these lines defines a time, which we call “Creep or Relaxation Stabilization Time” (CRST).

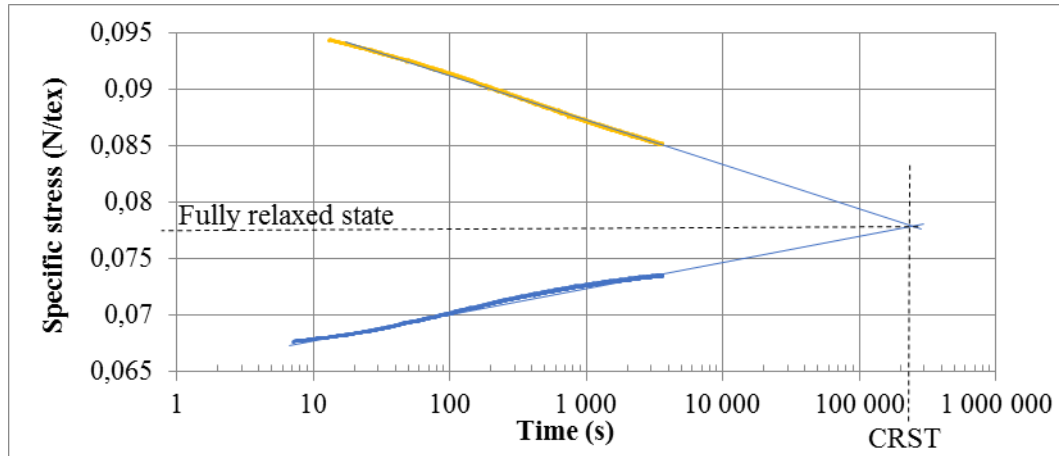


Figure 2-36. Determination of the CRST time.

The relaxation leads to a mean decrease of stress of 15 % after 1h, and a decrease of 19% from the CRST evaluation. For the inverse relaxation, we observe an average of 10% stress increase in the 1 hour of relaxation and a 17% increase with the extrapolated value.

Figure 2-37 presents the result found using the CRST method as a function of the strain. Most of the results follow the same trend with some points being below. The points that are the furthest away from the main trend are usually in the higher cycles (3 or 4, Figure 2-25), but no relation with the plastic strain was found.

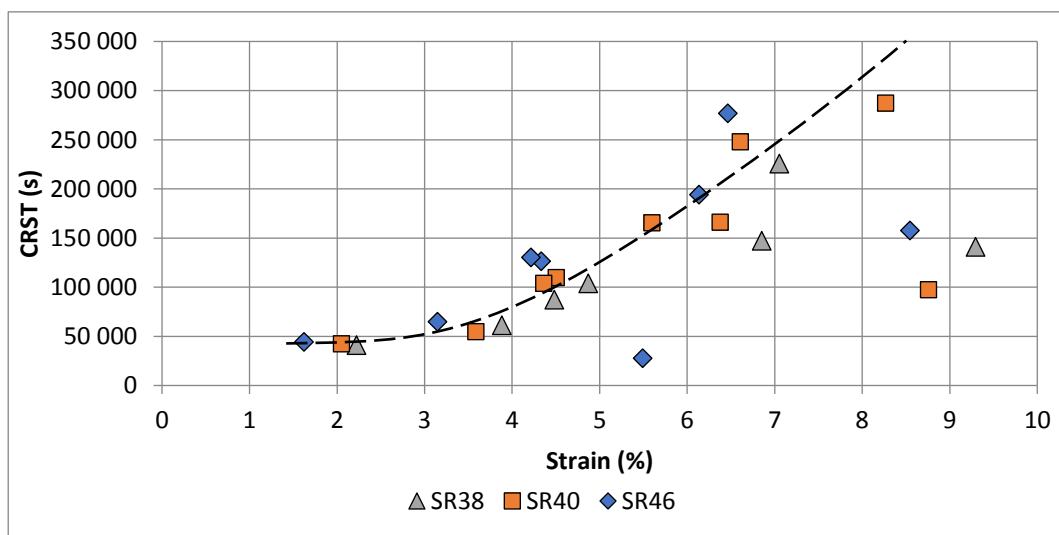


Figure 2-37. Evolution of the CRST time in function of the strain.

For the point on the first loading curve there was no opposite relaxation and recovery, so the mean time found from the preceding method (dashed line in Figure 2-37) was taken and the stress was extrapolate by using a logarithmic fit. The same process was applied to the recoveries, but this time in terms of strain.

Figure 2-38 presents the part of viscosity in the material between the end of relaxation and the fully relaxed extrapolation.

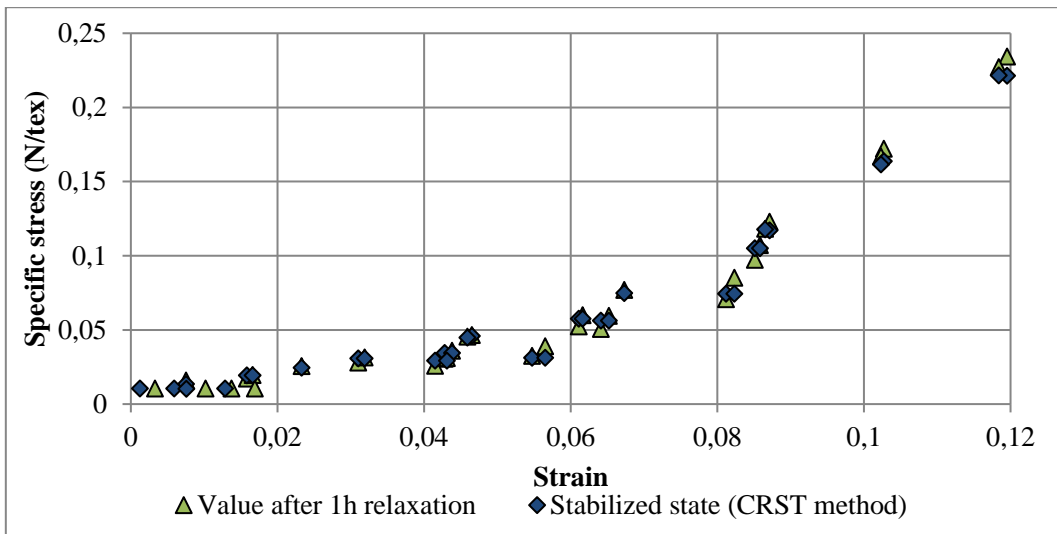


Figure 2-38. Stress versus strain in creep or relaxation after duration of 1 hour and for stabilized state according to the CRST method (on sample SR40).

The values obtained give an approximate value of the fully relaxed or Time-Independent behavior (TIB).

So now that we have an evaluation of the fully relaxed state, we can begin the analysis of the results. Figure 2-39 presents the relaxed result of the mean value for the test SR38, SR40, and SR46.

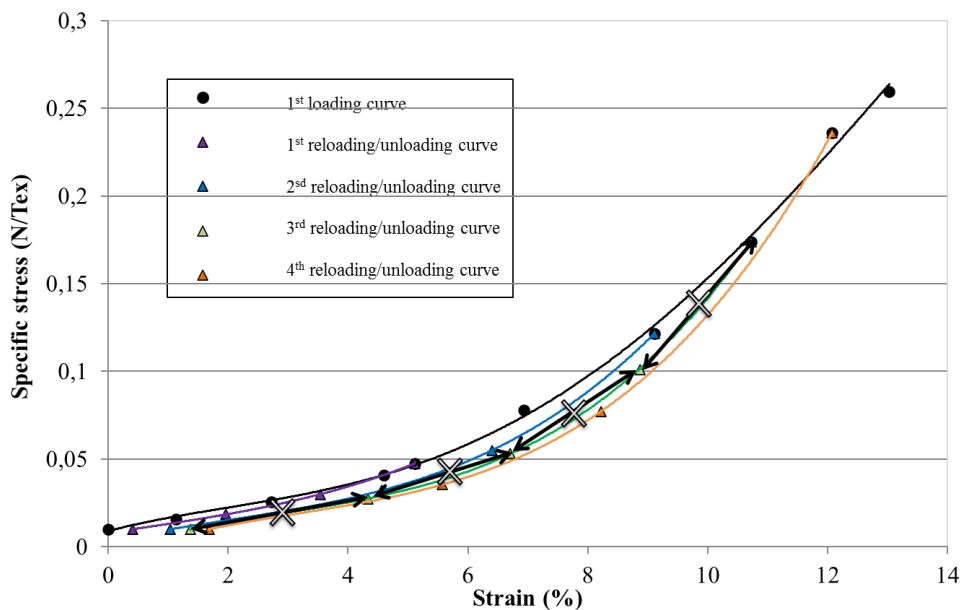


Figure 2-39. Stress versus strain of the time-independent behavior according to the multi-relaxation test.

On this Time-Independent behavior (TIB) plot, we observe that the first loading curve is different from the curves obtained from the unloading-reloading cycles. This TIB is the behavior of Flory's model when we remove all dashpot elements. Only spring and ratchet elements remain, that will produce an elastoplastic behavior (Figure 2-4, *Flory 2013*).

This TIB behavior is the original working curve and working curve of the Syrope model (*Falkenberg, 2018*) (see Figure 2-2); the original working curve corresponds here to the first loading curve of the TIB behavior (in red in Figure 2-40), and the working curve corresponds to the TIB behavior during cycles (in blue in Figure 2-40). In the Syrope model, the blue working curve is shifted horizontally to higher strains as a function of the maximum load, experienced by the rope. This is also similar to an elastoplastic behavior.

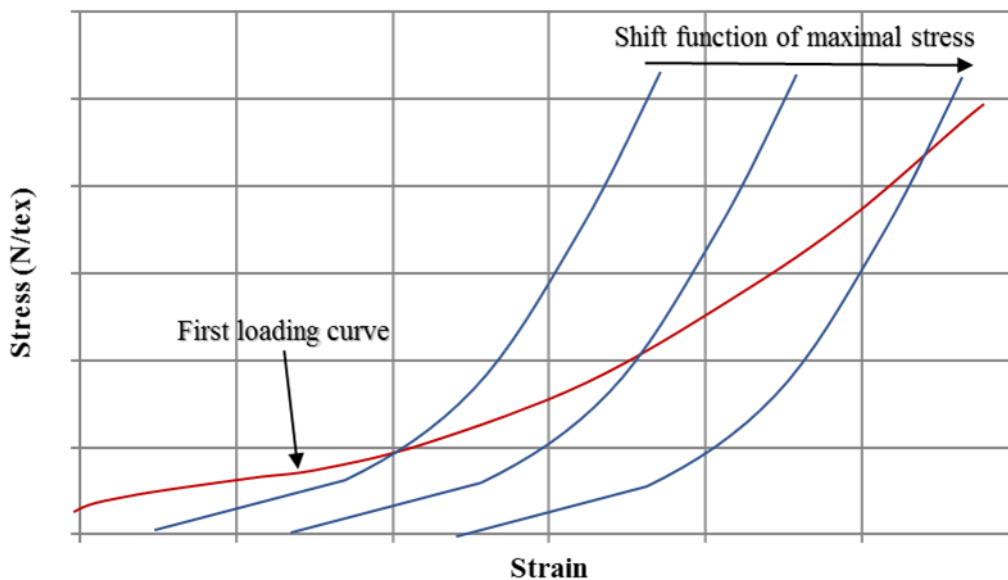


Figure 2-40. Modelling pattern of the time-independent behavior.

For each curve obtained from one cycle, that is to say the TIB behavior during each cycle, we measure the tangent modulus (the arrowed line of Figure 2-39, or the blue line in Figure 2-40); we call this modulus M_{TIB} . On Figure 2-41, this modulus is plotted versus the stress, for all cycles of the test on all tested samples.

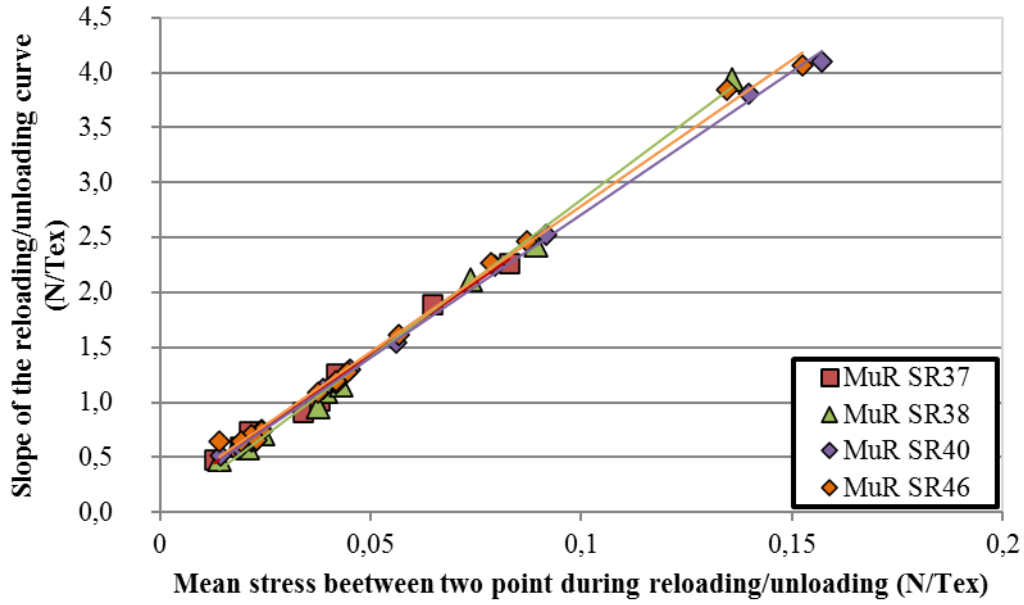


Figure 2-41. Tangent modulus M_{TIB} of the time-independent behavior during cycles as a function of the stress.

From the results presented on Figure 2-41, we observe a linear relationship, for all samples, between the M_{TIB} modulus and the stress:

$$M_{TIB} = c * \Sigma + d$$

François and Davies (2008) found that a quasi-static stiffness, very similar to the concept of the M_{TIB} modulus, is also linear with the mean load.

We can define a relationship between the stress and the strain for the time-independent behavior during cycles, as follows:

$$\Sigma = \mathbf{d}(\varepsilon)$$

Such that:

$$\mathbf{d}' \circ \mathbf{d}^{-1}(\Sigma) = c * \Sigma + d = M_{TIB} = \frac{d\Sigma}{d\varepsilon}$$

$$\text{or } (\mathbf{d}^{-1})'(\Sigma) = \frac{1}{\mathbf{d}' \circ \mathbf{d}^{-1}(\Sigma)} = \frac{1}{c * \Sigma + d}$$

$$\Rightarrow \mathbf{d}^{-1}(\Sigma) = \frac{\ln(c * \Sigma + d)}{c} + Cte$$

Moreover, we assume that:

$$0 = \mathbf{d}(0)$$

then:

$$i^{-1}(0) = 0 = \frac{\ln(d)}{c} + Cte \quad \text{and} \quad Cte = -\frac{\ln(d)}{c}$$

Which leads to the equation:

$$d^{-1}(\Sigma) = \frac{\ln\left(\frac{c}{d} * \Sigma + 1\right)}{c}$$

Then by inverting the variable, we can determine the function:

$$d(\varepsilon) = \frac{d}{c} * (e^{c*\varepsilon} - 1)$$

The values of the two parameters are characterized as follows:

$$c = 26.231 /$$

$$d = 0.0862 \text{ N/tex}$$

As written above, this time-independent behavior is proposed by *Flory (2013)* and *Falkenberg (2018)* to be an elastoplastic behavior. In the next section, we will characterize plasticity from this time-independent behavior.

2.5.4. Plasticity

As proposed by the Syrope model (*Falkenberg 2018*) and by *François and Davies (2008)*, we will assume that the TIB behavior during cycles is shifted horizontally to higher strains, as follows:

$$\Sigma_{TIB} = d(\varepsilon - \varepsilon_p)$$

Where ε_p is a plastic strain, called by *François and Davies (2008)* non-recoverable permanent elongation. And this permanent elongation will increase as a function of the maximum TIB stress Σ_{TIB} as described by Figure 2-42.

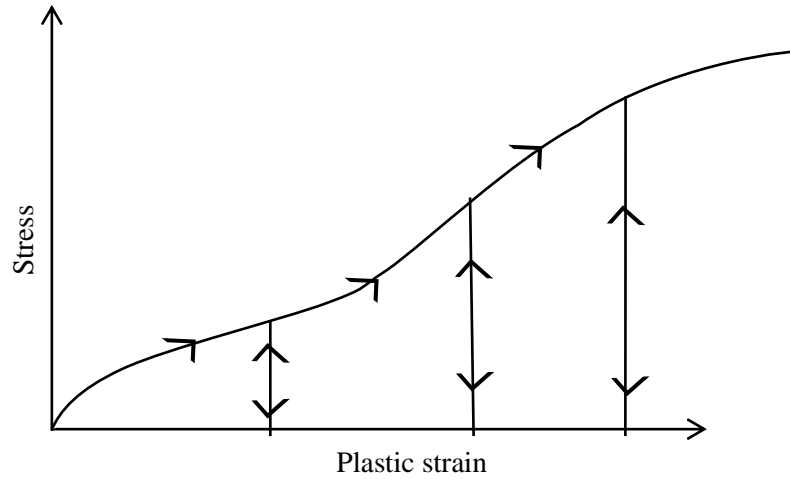


Figure 2-42. Modelling pattern of the plasticity of the time-independent behavior.

Because, in the previous section, we have characterized a function \mathbf{d} , we can calculate this plastic strain from the measured time-independent stress Σ_{TIB} and strain ε , as follows:

$$\varepsilon_p = \varepsilon - \mathbf{d}^{-1}(\Sigma_{TIB})$$

Figure 2-43 shows the TIB stress as a function of this plastic strain for the tests on samples SR40 and SR46.

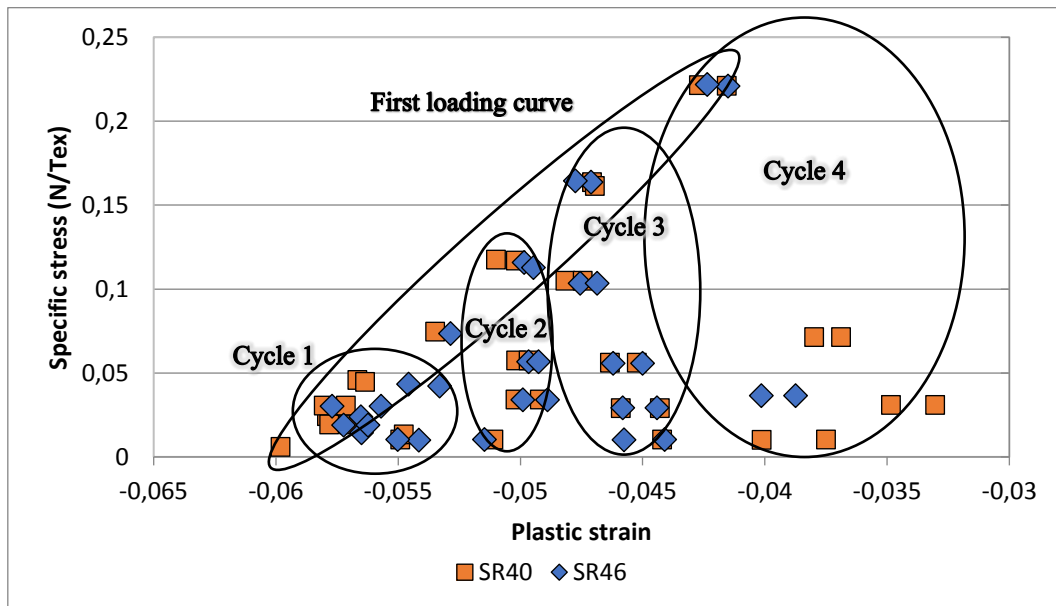


Figure 2-43. Stress versus plastic strain according to the time-independent behavior.

We notice that the plastic strain values remain in a small range ($\approx 2\%$) in our study, by comparison to the total strain which reaches values up to 12-15%.

On Figure 2-43, the evolution of the plastic strain during each cycle is small. So, the modelling pattern described by Figure 2-42 is almost respected.

The curve where the TIB stress is maximum and where the plastic strain increases (first loading curve on Figure 2-43) is quite linear. A function has been fitted to this evolution of maximum TIB stress with the plastic strain, by assuming that negative values for the maximum TIB stress are not relevant:

$$\Sigma_{MAX-TIB} = p(\varepsilon_p) = e * [\tanh(f * \varepsilon_p + h) + 1] \text{ when } \Sigma \text{ is below } e$$

$$\Sigma_{MAX-TIB} = p(\varepsilon_p) = e * [f * \varepsilon_p + h + 1] \text{ when } \Sigma \text{ is above } e$$

This equation allows for a linear relationship between the strain and the maximum TIB stress in most of the test range, while also ensuring that the behavior is coherent with the progressive loading of the rope.

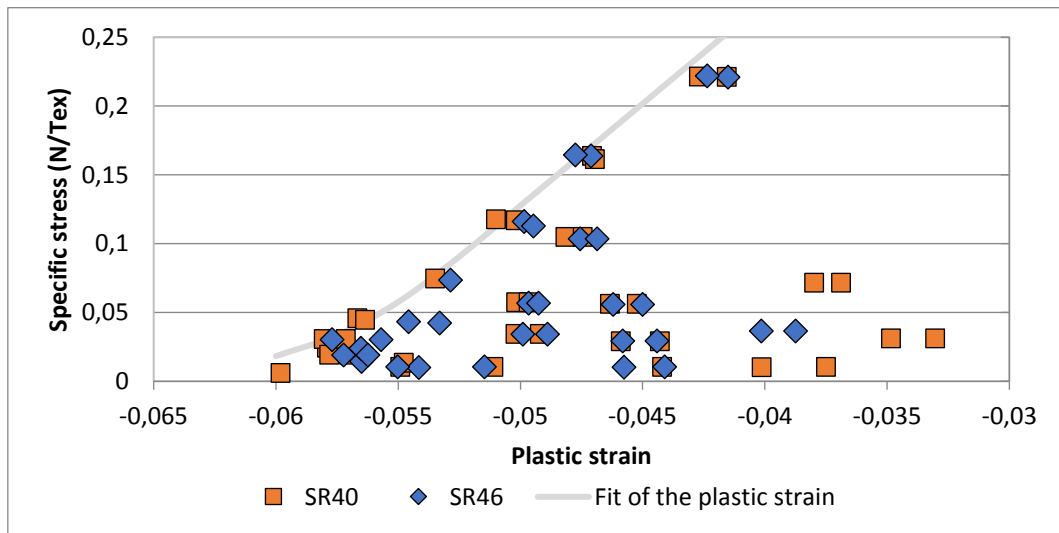


Figure 2-44. Fit of the plastic strain in the first loading curve.

Figure 2-44 shows the fitting function and the experimental points. The values of the optimized three parameters are:

$$e = 0.1134 \text{ N/tex}$$

$$f = 161.7 /$$

$$h = 7.913 /$$

2.5.5. Summary

We have characterized the dynamic elasticity by its modulus as a function of stress as shown Figure 2-45. This dynamic modulus is a linear function of the sub-rope stress. Figure 2-45-b presents the dynamic elasticity behavior characterized by the function i .

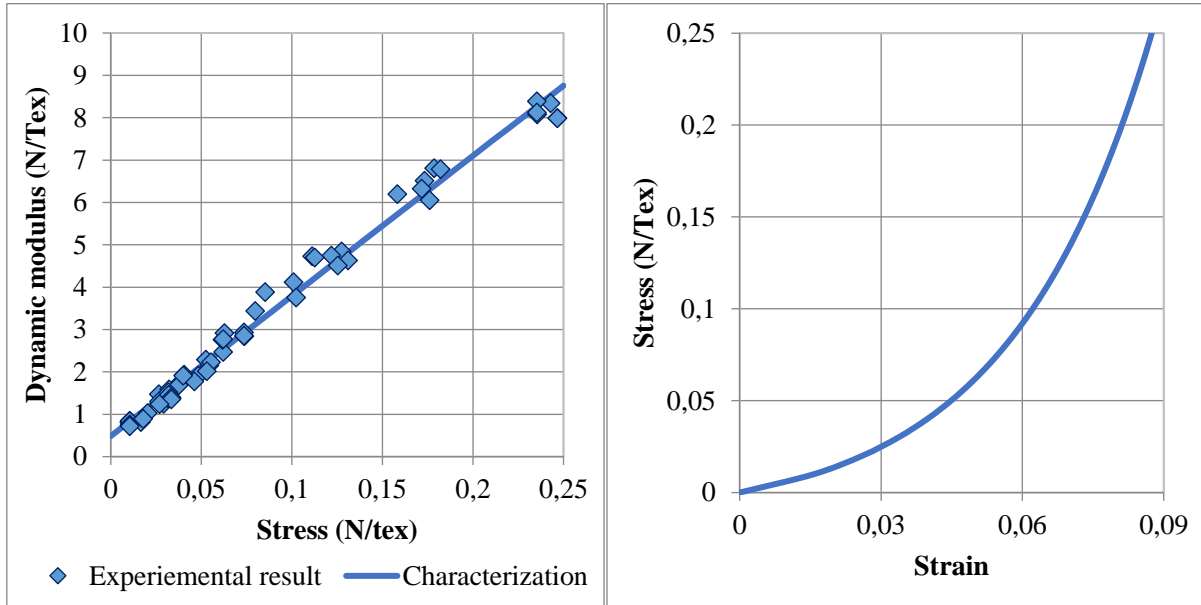


Figure 2-45. Characterization of the dynamic modulus of the 4-ton polyamide sub-rope: (a) modulus versus stress, (b) stress versus strain for the dynamic elasticity.

We have characterized a time-independent behavior (TIB) of the elasto-plastic type illustrated by Figure 2-46. This characterization is built on one function d such that

$$\Sigma_{TIB} = d(\varepsilon - \varepsilon_P)$$

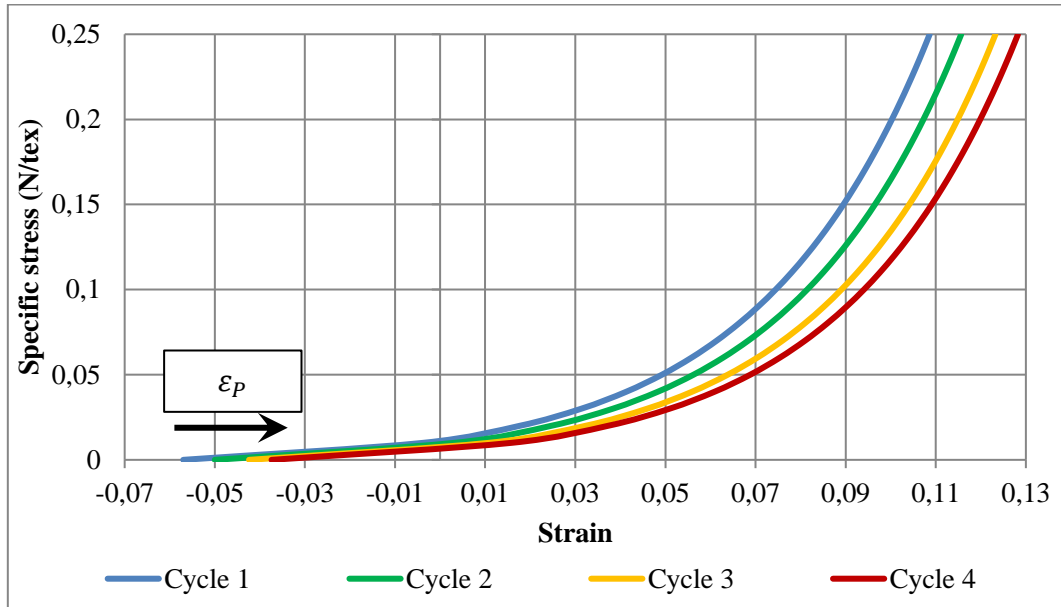


Figure 2-46. Characterization of the time-independent behavior of the 4-ton polyamide sub-rope: stress versus strain.

Figure 2-47 presents the characterized plasticity behavior. This characterization is based on one function p , such that if the stress is lower than the value $p(\epsilon_P)$, the plastic strain remains constant, and the plastic strain increases only if the stress is equal to $p(\epsilon_P)$.

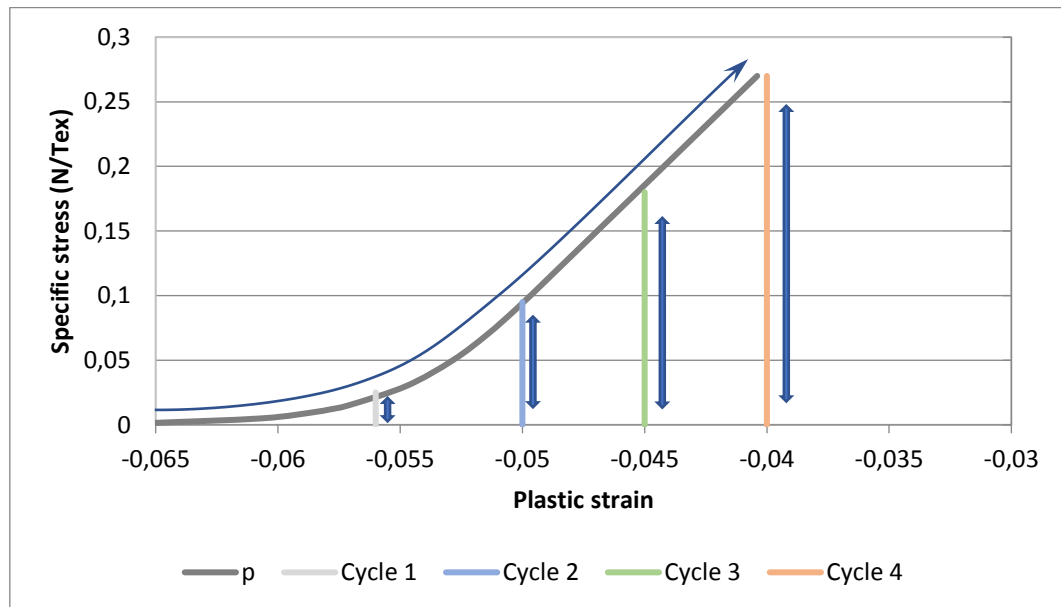


Figure 2-47. Characterization of the plasticity behavior of the 4-ton polyamide sub-rope: stress versus plastic strain.

2.6. Constitutive law

The proposed behavior law is based on Flory's proposal (Figure 2-48), and also on the expertise of Michel François from Bureau Veritas.

2.6.1. Discussion and Choices

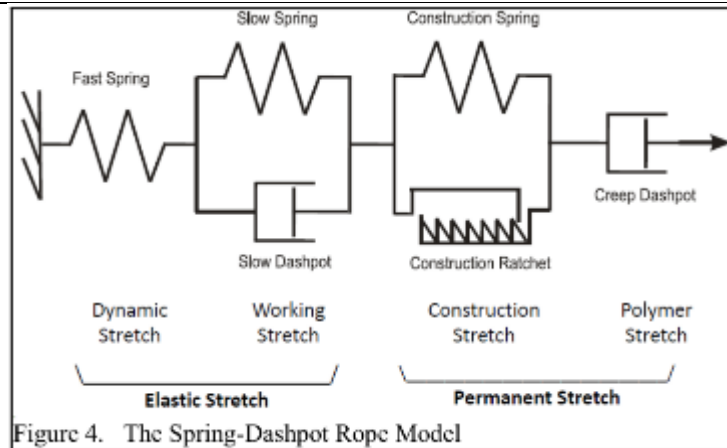


Figure 2-48. Flory (2013) proposal of elements for modeling fiber ropes.

Flory's rope model is recalled in Figure 2-48. As *François and Davies (2008)* did, we will assume first that all creep loading stabilizes at a non-infinite strain, that is to say, there exists a non-zero behavior reached at the stabilization of all creep and relaxation loadings. In viscoelasticity theory, this type of material is called *solid* and not *fluid*. According to this assumption, the *creep dashpot* of Flory's model has to be removed. Figure 2-49 shows the resulting model.

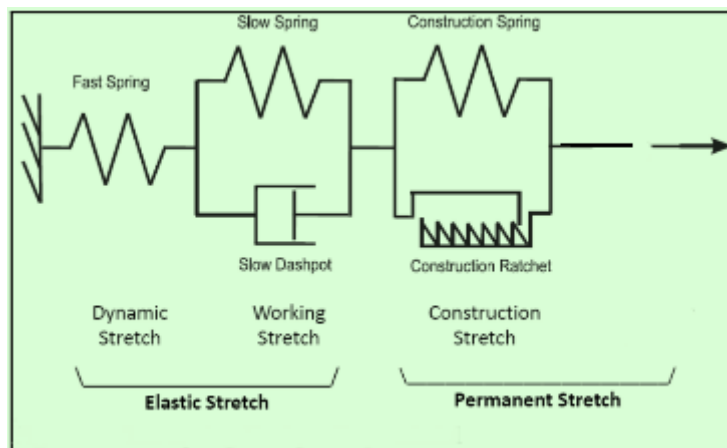


Figure 2-49. Step 1 in the proposition of the constitutive law.

In the characterization section, we have observed that the dynamic elasticity modulus is a linear function of stress and is not impacted by the history of the loading

path; indeed this observed linear function was the same when the stress is after a first, second or third unloading, or after any reloading. Let us consider the model (Figure 2-49) in the case of dynamic loadings; for that we replace the dashpot by a rigid link as shown by Figure 2-50.

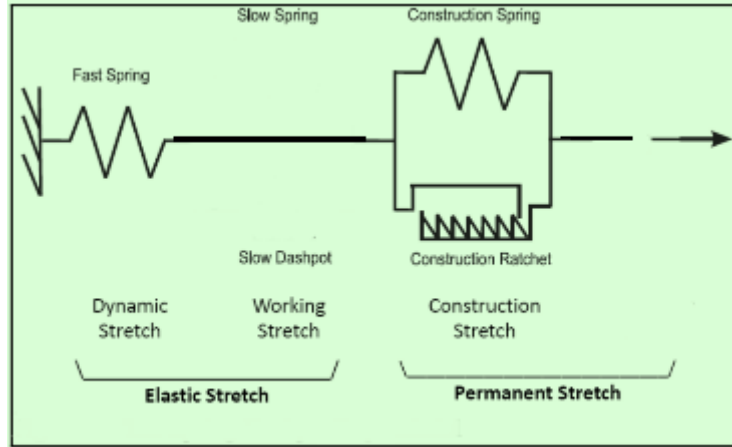


Figure 2-50. Dynamic behavior of step 1 in the proposition of the constitutive law.

This model has an elasto-plastic behavior, and its tangent modulus is dependent on the sliding or non-sliding of the *construction ratchet*. This leads to a dynamic modulus dependent on the history of the loading, which is not in agreement with the experimental observations we have made on the 4-ton sub-rope. To avoid this issue, we modified the step-1 model for the one shown in Figure 2-51, and called *step-2* model.

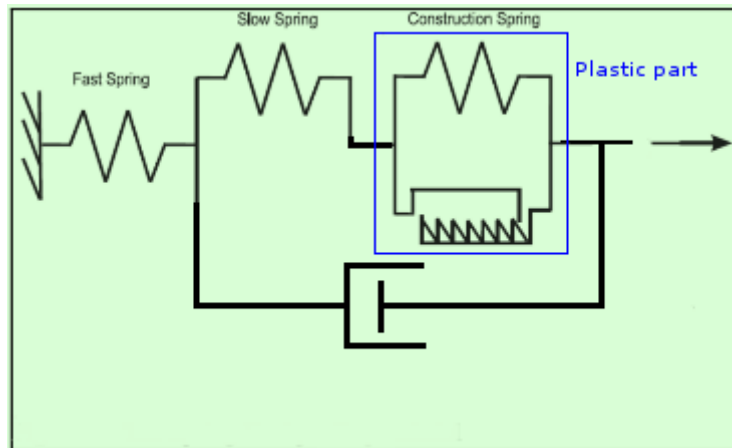


Figure 2-51. Step 2 in the proposition of the constitutive law.

For the sake of simplicity, the plastic part on Figure 2-51 can be replaced by a non-linear ratchet element, without any change in behavior. This non-linear ratchet element follows a behavior shown in Figure 2-42; the non-linear feature describes the

curve of maximum stress where the plastic strain increases. Then we obtain the *step-3* and final model, given by Figure 2-52.

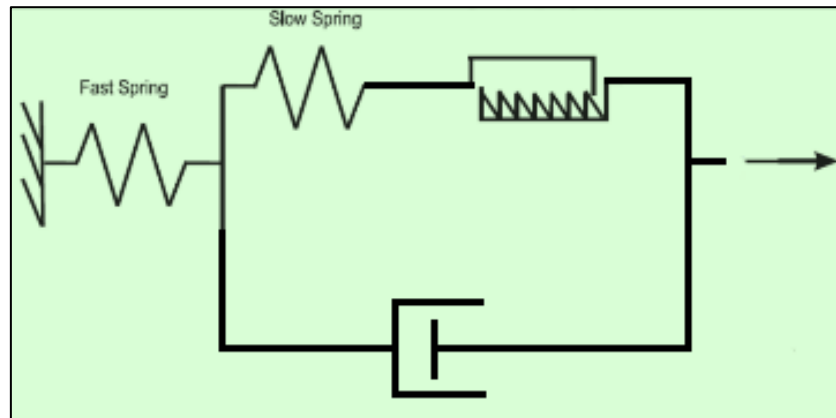


Figure 2-52. Step 3 and final step in the proposition of the constitutive law.

As *François and Davies (2008)* did, we assumed a non-zero fully relaxed or infinitely slow speed behavior. During the mechanical characterization, we observed a dynamic elasticity modulus independent of the loading history. Starting from Flory's model, and taking into account these two points, we propose the behavior model of Figure 2-52.

Moreover, this model is in agreement with the Syrope model (*Falkenberg, 2018*); the *dynamic stiffness* is the Fast Spring of the proposed model; the *original working curve* and *working curves* can be modeled by the Fast Spring, Slow Spring and the non-linear ratchet elements of the proposed model.

Bureau Veritas (Michel François) proposed the following behavior for the viscosity element (Dashpot) of the proposed model:

$$\Sigma = W_2 \sinh^{-1} \left(\frac{\dot{\epsilon}}{W_1} \right)$$

Where Σ and $\dot{\epsilon}$ are respectively the stress and the strain rate of the viscosity element. W_1 and W_2 are parameters. This viscous behavior is relevant for predicting the stress relaxation and creep strain for polyester ropes, which follow a logarithmic time evolution.

Figure 2-53 presents the different elements of the model and some useful parameters.

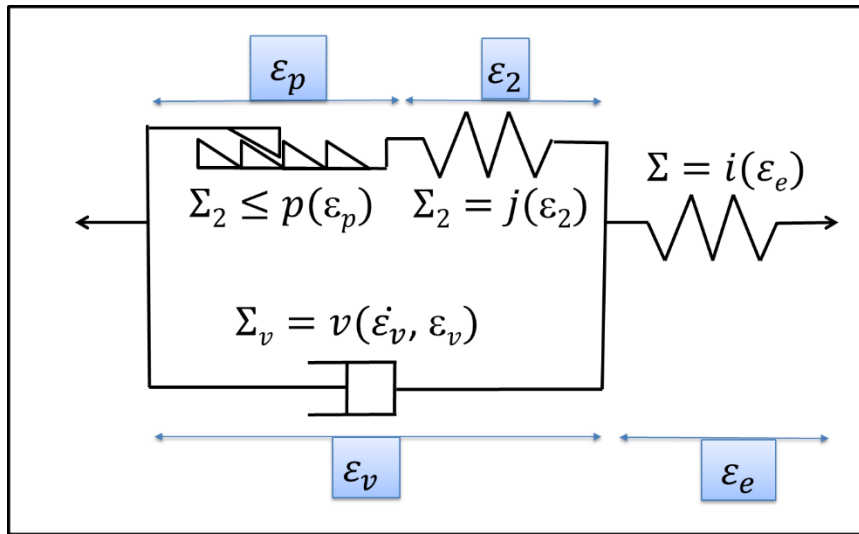


Figure 2-53. The proposed constitutive law.

Our elasto-visco-plastic model can be divided into several parts, a viscous part (called v) and a time-independent part (i , j and p). In the time-independent part, we find a part including the instantaneous elasticity (i), another spring (j) and a part including the plastic part of the model (p) (which takes into account the structure and plasticity of the material).

In order to get a wide applicability of this law to predict various material behaviors, we chose non-linear elasticity and non-linear ratchet elements; by means of the functions $i(\epsilon_e)$, $j(\epsilon_2)$ and $p(\epsilon_p)$. Moreover, the non-linear function $v(\dot{\epsilon}_v, \epsilon_v)$ of the viscosity element will be $\Sigma = W_2 \sinh^{-1}\left(\frac{\dot{\epsilon}}{W_1}\right)$, where the parameters W_1 and W_2 may be functions of the viscous strain ϵ_v .

2.6.2. Equations of the constitutive law

The constitutive law is defined by the nine following equations:

$$\varepsilon = \varepsilon_v + \varepsilon_e \ ; \ \Sigma = i(\varepsilon_e)$$

With ε the total strain, ε_v the strain of the viscous part, ε_e the strain of the dynamic elasticity, Σ the global stress.

$$\Sigma = \Sigma_2 + \Sigma_v \ ; \ \Sigma_2 = j(\varepsilon_2)$$

With Σ_v the stress in the viscous part, and Σ_2 the stress in the plastic part and ε_2 the strain of spring j.

$$\varepsilon_v = \varepsilon_2 + \varepsilon_p \ ; \ \Sigma_v = v(\dot{\varepsilon}_v, \varepsilon_v)$$

With ε_p the plastic strain, such that the classic Kühn-Tucker equations are always satisfied:

$$\Sigma_2 \leq \mathbf{p}(\varepsilon_p) \ ; \ \varepsilon_p \geq 0 \ ; \ \dot{\varepsilon}_p \cdot [\Sigma_2 - \mathbf{p}(\varepsilon_p)] = 0$$

2.6.3. Model characteristics

This model presents some particular properties:

- The plastic evolution of the model is permanent, i.e. non-recoverable, as we chose to define the plastic properties by a ratchet. Once stabilized and for a stress below the maximal stress seen previously by the ratchet, we have no evolution of the plastic strain.
- The model possesses a memory defined by the damping part and the plastic strain.
- Viscosity is represented around a behavior defined by the time-independent part.

2.7. Identification method

This section presents the method and the results of the identification of the constitutive law parameters.

2.7.1. Dynamic elasticity / Short term elasticity

The part called dynamic elasticity or short-term elasticity is represented in the model by the fast spring "i" (Figure 2-54). This can be observed at high frequency, high strain rate or in our case, in the very short term after a relaxation.

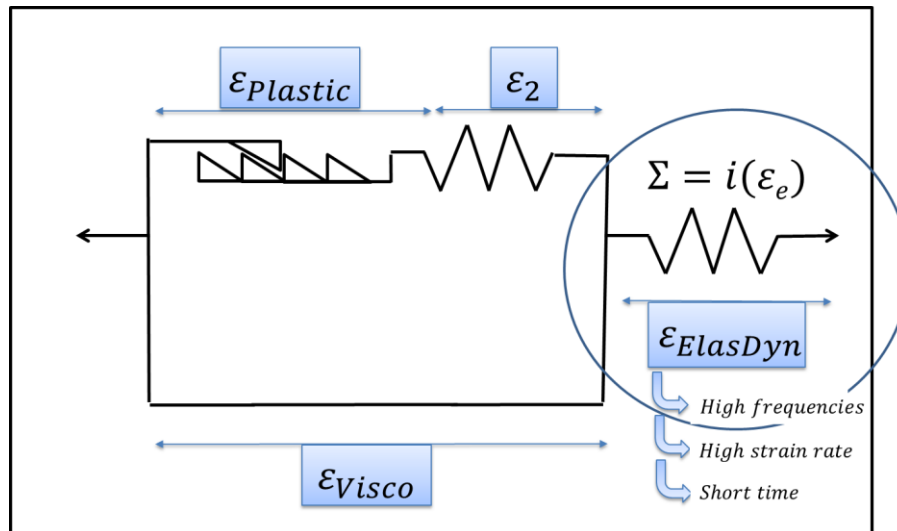


Figure 2-54. Short-term elasticity or dynamic behavior of the constitutive law.

After a relaxation, reloading is done with a fairly high slope. This slope increases with the deformation and is representative of the spring called **i**.

The identification of this dynamic part of the model is made thanks to the characterization of the dynamic elasticity, presented in section 2.5.2. Indeed, the function $i(\varepsilon_e)$ of the model is equal to the characterized function i , as follows:

$$i(\varepsilon_e) = \frac{b}{a} * (e^{a*\varepsilon_e} - 1)$$

where the two identified parameters are:

$$a = 33.0852 /$$

$$b = 0.484869 \text{ N/tex}$$

We may assess the relevance of this dynamic part of the constitutive law by comparing the experimental data to the linear regression lines on Figure 2-34.

Figure 2-55 presents the experimental results between the stress and the viscous strain calculated as :

$$\varepsilon_v = \varepsilon - \mathbf{i}^{-1}(\Sigma)$$

according to the equations of the model.

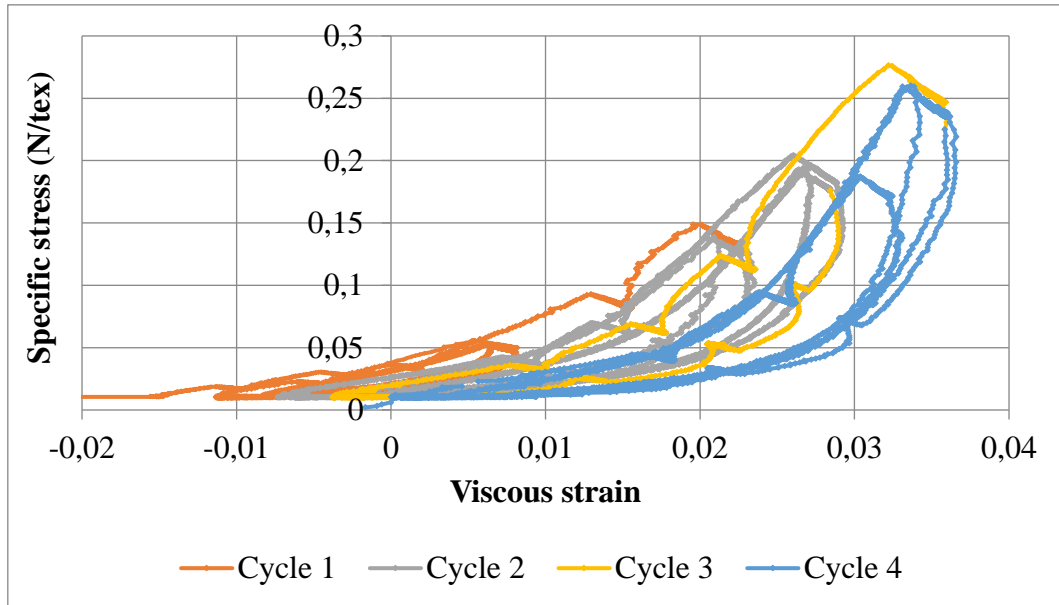


Figure 2-55. Time-independent stress versus viscosity strain; experimental results modified according to the identification of dynamic elasticity (from the test on sample SR40 in section 2.4.4).

On this diagram of stress versus viscous strain, the cycles are much more open at higher load, and the relaxation stages are not at a constant viscous strain.

2.7.2. Slow spring or slow elasticity

Figure 2-56 presents the time-independent behavior of the constitutive law.

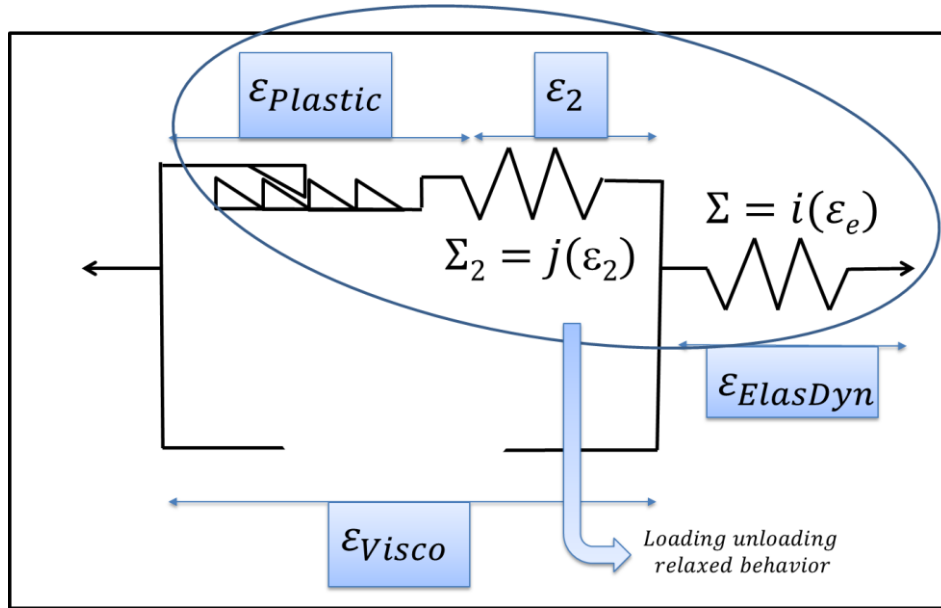


Figure 2-56. Time-independent behavior of the constitutive law.

The time-independent behavior of the model can be written:

$$\begin{aligned}\varepsilon_v &\sim 0 \quad ; \quad \Sigma_v = 0 = v(0, \varepsilon_v) \\ \Sigma &= \Sigma_2 + 0 \quad ; \quad \Sigma = \Sigma_2 = j(\varepsilon_2) \\ \varepsilon &= \varepsilon_e + \varepsilon_2 + \varepsilon_p \quad ; \quad \Sigma = i(\varepsilon_e)\end{aligned}$$

Then,

$$\varepsilon - \varepsilon_p = i^{-1}(\Sigma) + j^{-1}(\Sigma)$$

In the case of a constant plastic strain, that is to say:

$$\Sigma_2 < p(\varepsilon_p) \quad ; \quad \dot{\varepsilon}_p = 0$$

The time-independent behavior (TIB) of the constitutive law is the one characterized by the tangent modulus M_{TIB} during cycles, as shown in section 2.5.5, and was characterized as

$$\Sigma_{TIB} = \mathbf{d}(\varepsilon - \varepsilon_p)$$

This is equivalent to:

$$\varepsilon - \varepsilon_p = \mathbf{d}^{-1}(\Sigma_{TIB})$$

So, the identification of function $\mathbf{j}(\varepsilon_2)$ of the model is done by the method of section o, that leads to:

$$\mathbf{d}(x) = \frac{d}{c} * (e^{c*x} - 1)$$

Where the two identified parameters are:

$$c = 26.231 /$$

$$d = 0.0861586 \text{ N/tex}$$

And, satisfying the following relationship:

$$\mathbf{d}^{-1}(\Sigma) = \mathbf{i}^{-1}(\Sigma) + \mathbf{j}^{-1}(\Sigma)$$

Then, the function $\mathbf{j}(\varepsilon_2)$ is identified by its inverse function:

$$\mathbf{j}^{-1}(\Sigma) = \frac{\ln\left(\frac{c}{d} * \Sigma + 1\right)}{c} - \mathbf{i}^{-1}(\Sigma) = \frac{\ln\left(\frac{c}{d} * \Sigma + 1\right)}{c} - \frac{\ln\left(\frac{a}{b} * \Sigma + 1\right)}{a}$$

Which means that we have to numerically invert this function in the mooring time-simulation software tools.

We may assess the relevance of this slow elasticity of the constitutive law by comparing the experimental measurements to the linear regression lines on Figure 2-37.

Figure 2-57 presents the experimental results between the TIB stress and the plastic strain calculated as:

$$\varepsilon_p = \varepsilon - \mathbf{i}^{-1}(\Sigma) - \mathbf{j}^{-1}(\Sigma) = \varepsilon - \mathbf{d}^{-1}(\Sigma)$$

according to the equations of the model. This figure presents the evolution of the plastic strain during the test, with an increase of the plastic strain during the first loading curve and then almost no evolution during cycles made at a lower stress.

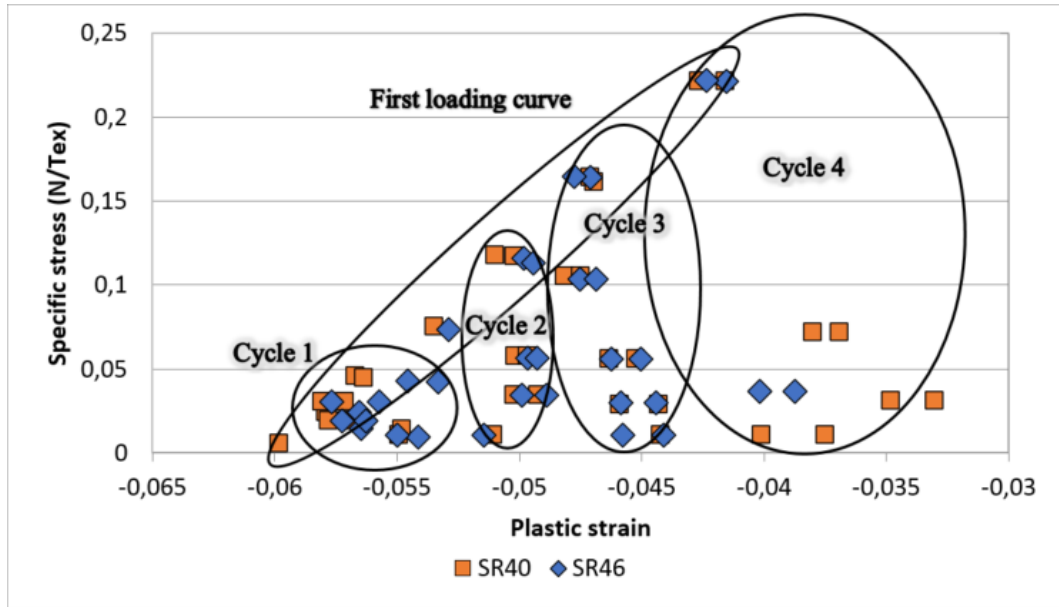


Figure 2-57. Time-independent stress versus the plastic strain; experimental results modified according to the identification of dynamic and slow elasticities.

2.7.3. Plasticity

Figure 2-58 presents a schematic view of the behavior of the non-linear ratchet element of the model. The curve, where the plastic strain increases and where the stress is maximum, is defined by the model equations, as follows:

$$\Sigma_2 \leq p(\varepsilon_p)$$

For the identification of this function $p(\varepsilon_p)$, we applied the method of section 2.5.4 on the experimental data of Figure 2-57:

$$p(\varepsilon_p) = e * [\tanh(f * \varepsilon_p + h) + 1]$$

Where the three identified parameters are:

$$e = 0.1134 \text{ N/tex}$$

$$f = 161.7 /$$

$$h = 7.913 /$$

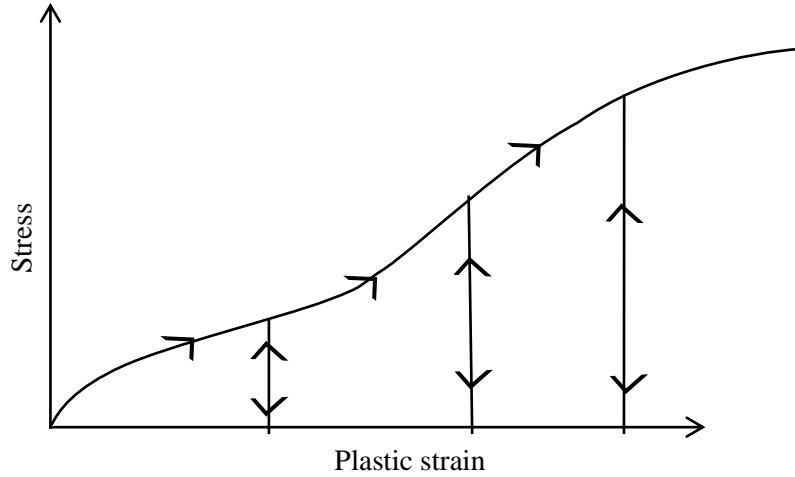


Figure 2-58. Behavior of the plasticity part of the constitutive law; non-linear ratchet element.

We may assess the relevance of the elasto-plastic block of the constitutive law by comparing the experimental data to the identified function $\mathbf{p}(\varepsilon_p)$ on Figure 2-43, and by comparing the stress-plastic strain cycles of Figure 2-57 to vertical unloadings-reloadings at constant plastic strain.

Figure 2-58 presents the experimental results of sample-SR40 test, but only the monotonic increasing plastic strain were kept. These data correspond to the *first loading curve* on Figure 2-57.

According to the equations of the law, in this case of

$$\dot{\varepsilon}_p > 0$$

the Σ_2 stress and the plastic strain satisfy the following relation:

$$\Sigma_2 = \mathbf{p}(\varepsilon_p)$$

Moreover, these selected experimental data were analysed to obtain the viscous stress and the viscous strain, as follows:

$$\varepsilon_v = \varepsilon - \mathbf{i}^{-1}(\Sigma)$$

$$\Sigma_v = \Sigma - \Sigma_2 = \Sigma - \mathbf{k}(\varepsilon_v)$$

Where function \mathbf{k} is defined by its inverse, as follows:

$$\mathbf{k}^{-1}(\mathbf{x}) = \mathbf{p}^{-1}(\mathbf{x}) + \mathbf{j}^{-1}(\mathbf{x})$$

according to the equations of the model; In the case of $\dot{\varepsilon}_p > 0$:

$$\Sigma_2 = \mathbf{p}(\varepsilon_p) = \mathbf{p}(\varepsilon_v - \varepsilon_2) = \mathbf{p}(\varepsilon_v - \mathbf{j}^{-1}(\Sigma_2))$$

Which is equivalent to

$$\varepsilon_v = \mathbf{p}^{-1}(\Sigma_2) + \mathbf{j}^{-1}(\Sigma_2) = \mathbf{k}^{-1}(\Sigma_2)$$

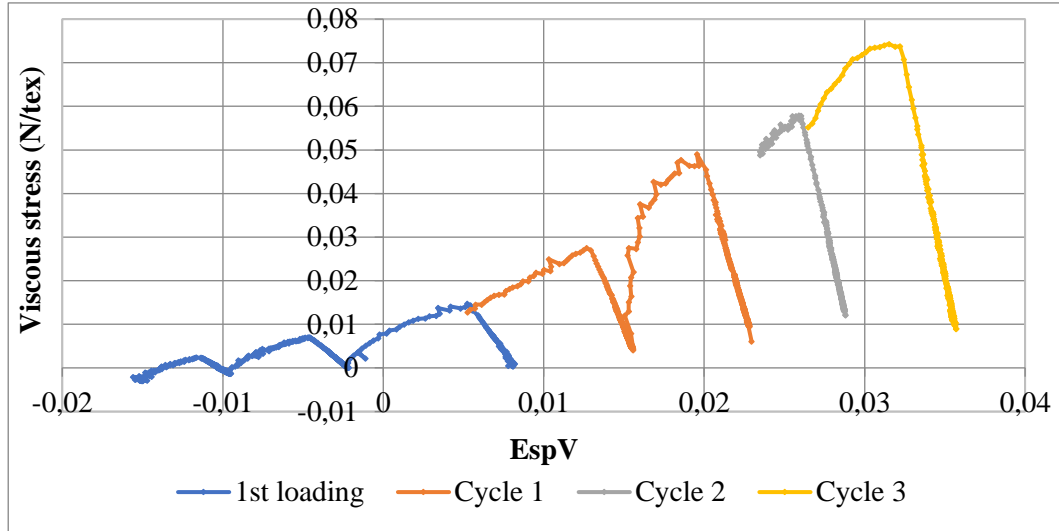


Figure 2-59. Viscous stress versus viscous strain of test on sample SR40: experimental results modified according to the identification of dynamic and slow elasticities and the non-linear ratchet element.

2.7.4. Viscosity

The viscosity is identified on the stress relaxations of the experimental data of Figure 2-59.

For each of the seven relaxation stages, a linear regression is applied between the viscous stress and the viscous strain (Figure 2-59):

$$\Sigma_v = -r \cdot \varepsilon_v + q$$

This linear relation and the chosen viscosity behavior

$$\Sigma_v = W_2 \sinh^{-1}\left(\frac{\dot{\varepsilon}_v}{W_1}\right)$$

lead to the following differential equation:

$$\dot{\varepsilon}_v = W_1 \sinh\left(\frac{-r \cdot \varepsilon_v + q}{W_2}\right)$$

This equation is resolved analytically:

$$\Sigma_v(t) = 2W_2 \cdot \tanh^{-1} \left[\tanh \left(\frac{\Sigma_v(t_0)}{2W_2} \right) \cdot \exp \left(\frac{-rW_1(t - t_0)}{W_2} \right) \right]$$

For each of the seven relaxation stages, a set of parameters (W_1, W_2) is identified on the experimental data by a non-linear least-squares Marquardt-Levenberg algorithm. The parameters obtained are given by the circles on Figure 2-60 and Figure 2-61.

Values of parameters W_1 do not show any clear correlation with the viscous strain. Thus, we decided to choose a constant value; this value is the average of the identified ones. This average value is illustrated by the squares on Figure 2-60:

$$W_1 = 1.83656 \times 10^{-7} s^{-1}$$

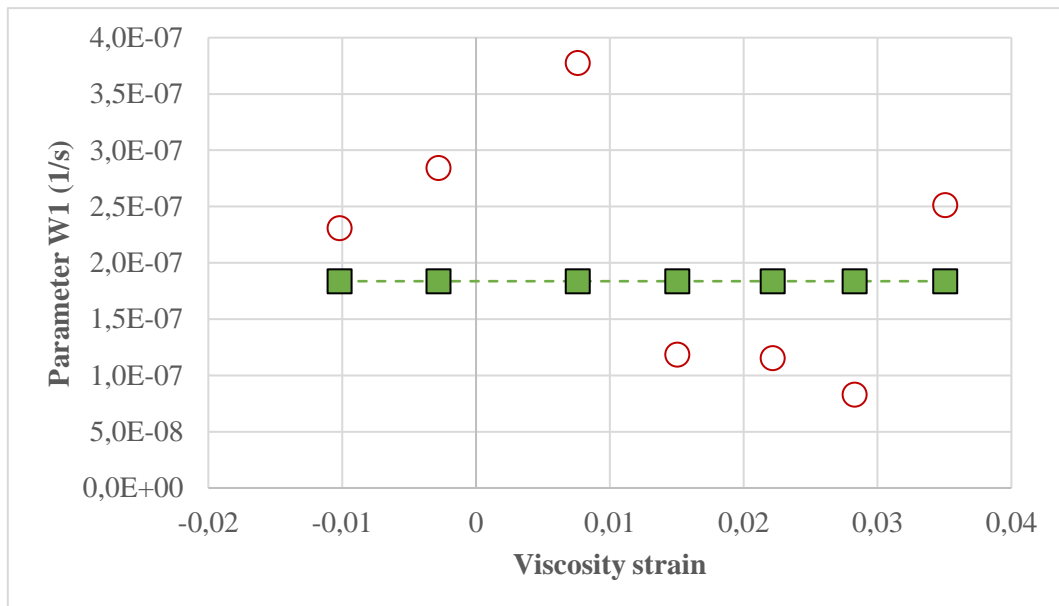


Figure 2-60. Identified parameter W_1 versus viscous strain; (circle) identified for each relaxation (square) average value of the identified “circle” values.

Then, by fixing parameter W_1 to this average value, parameter W_2 is again identified by the same process. Figure 2-61 shows these identified values by square symbols.

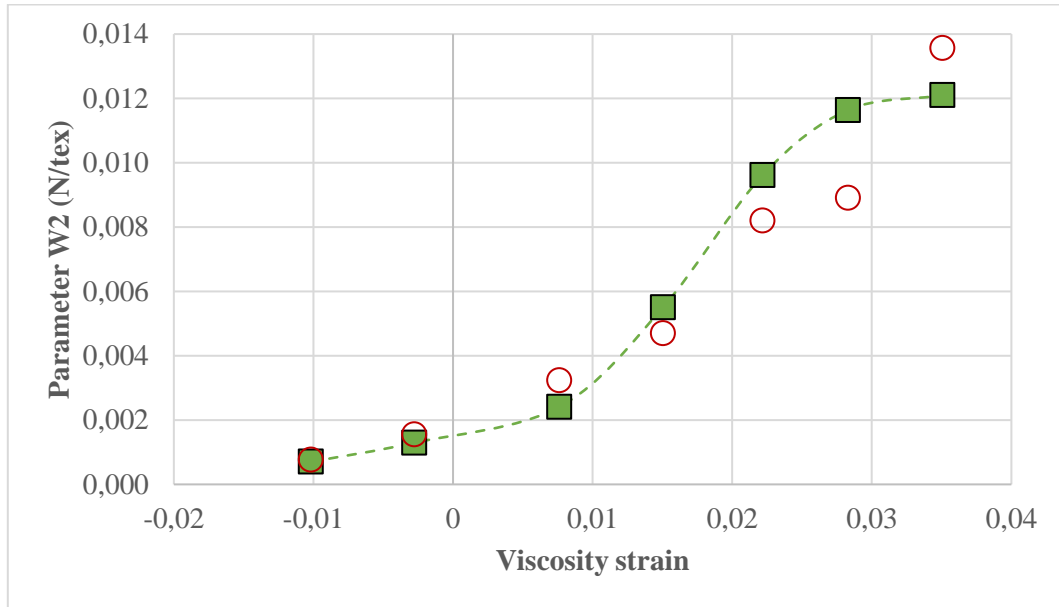


Figure 2-61. Identified parameter W_2 versus viscous strain; (circle) identified with the “circle” W_1 values of Figure 2-60; (square) identified with a constant parameter W_1 chosen as the average value (squares on Figure 2-60).

Parameter W_2 is assumed to be a function of the viscous strain, as follows:

$$\text{if } \varepsilon_v \geq a_{W_2} \text{ then } W_2(\varepsilon_v) = b_{W_2} \cdot \tan^{-1} \left(\frac{d_{W_2}(\varepsilon_v - a_{W_2})}{b_{W_2}} \right) + c_{W_2}$$

$$\text{if } \varepsilon_v < a_{W_2} \text{ then } W_2(\varepsilon_v) = \frac{2c_{W_2}}{\pi} \cdot \tan^{-1} \left(\frac{d_{W_2}(\varepsilon_v - a_{W_2})}{\frac{2c_{W_2}}{\pi}} \right) + c_{W_2}$$

Parameters $(a_{W_2}, b_{W_2}, c_{W_2}, d_{W_2})$ are identified by a non-linear least-squares Marquardt-Levenberg algorithm:

$$a_{W_2} = 0.0163408 /$$

$$b_{W_2} = 0.00482934 \text{ N/tex}$$

$$c_{W_2} = 0.00636687 \text{ N/tex}$$

$$d_{W_2} = 0.692185 \text{ N/tex}$$

The identified function of $W_2(\varepsilon_v)$ is given in Figure 2-62.

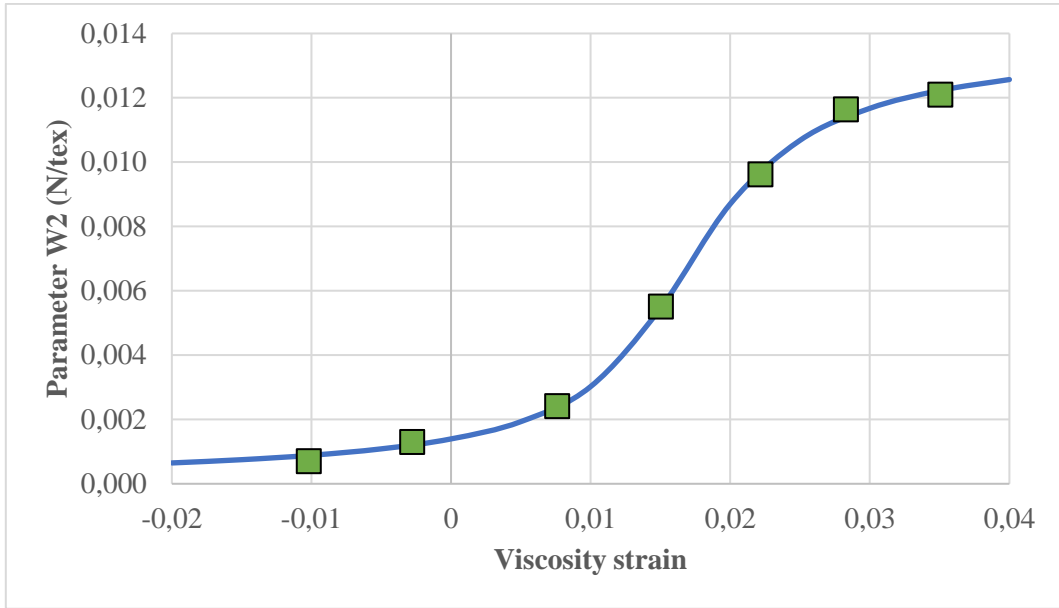


Figure 2-62. Identified parameter W2 versus viscous strain; (square) identified values on each relaxation stages; (line) identified function of W2.

This identified viscosity element was simulated during the relaxation stages of the experimental data of Figure 2-59, by a Runge-Kutta algorithm of 4th order. The following figures give a comparison between the experimental data and the simulation of the identified viscosity element of the constitutive law.

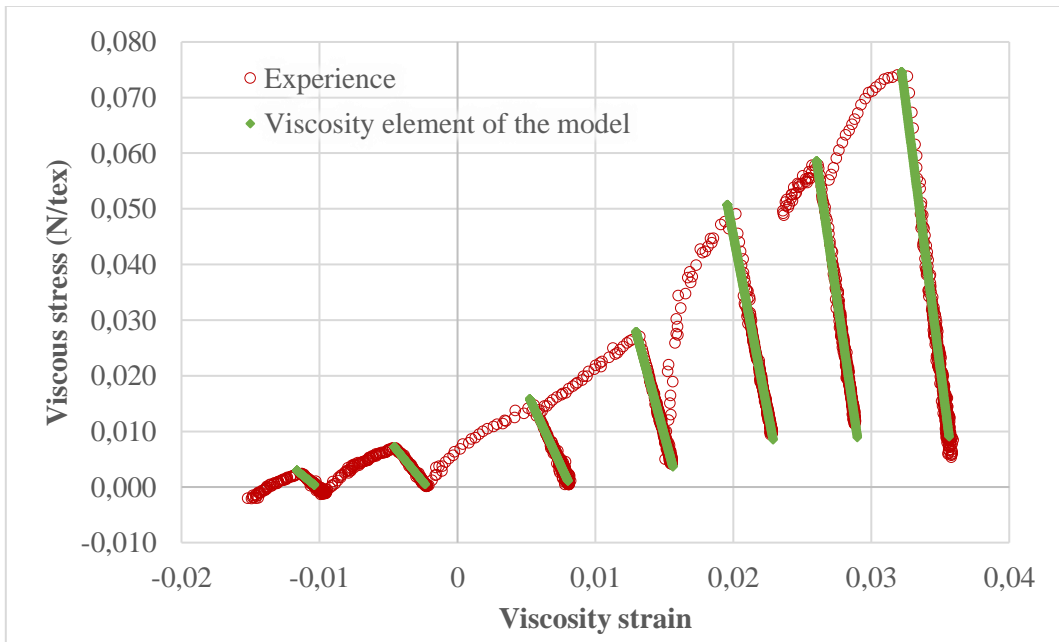


Figure 2-63. Viscous stress versus viscous strain; (red) experimental data (green) simulation of the viscosity element of the constitutive law.

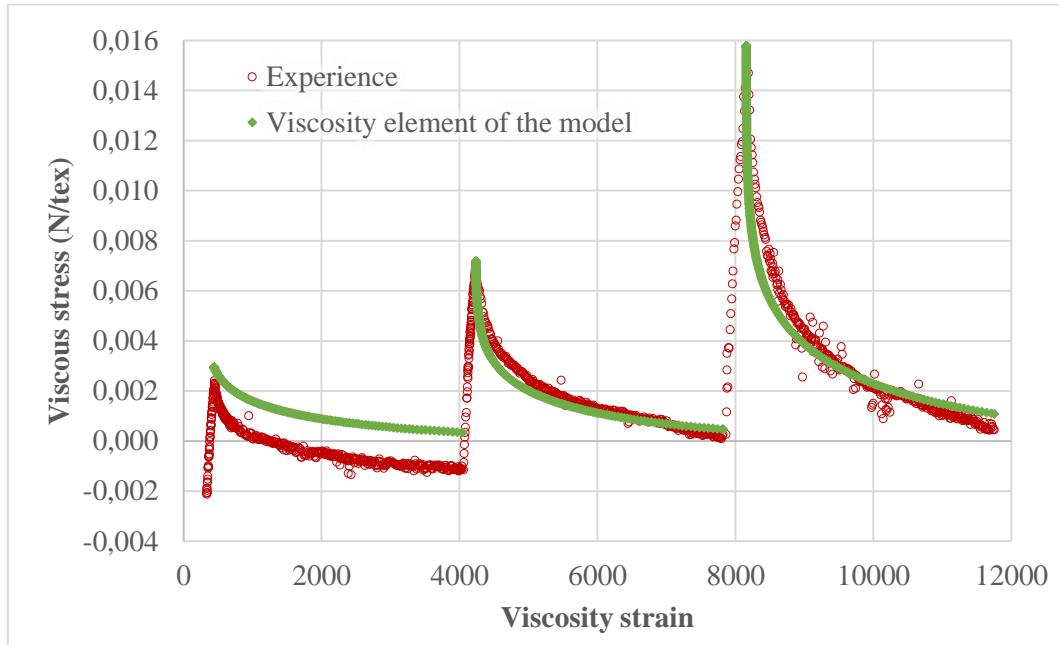


Figure 2-64. Viscous stress versus time of the 3 first relaxations; (red) experimental data (green) simulation of the viscosity element of the constitutive law.

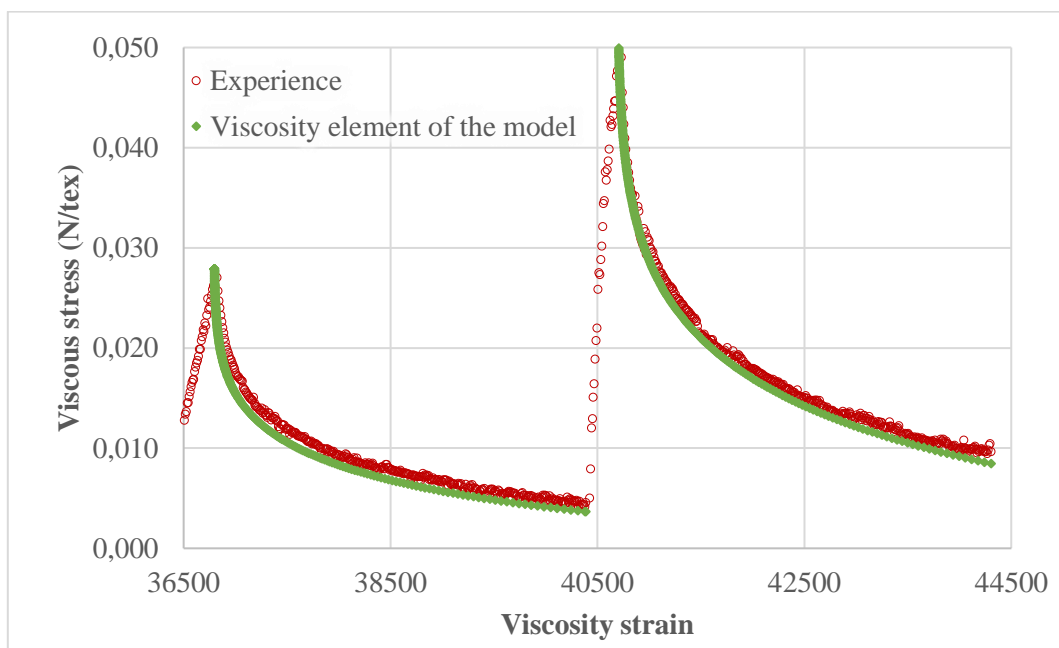


Figure 2-65. Viscous stress versus time of relaxations 4 and 5; (red) experimental data (green) simulation of the viscosity element of the constitutive law.

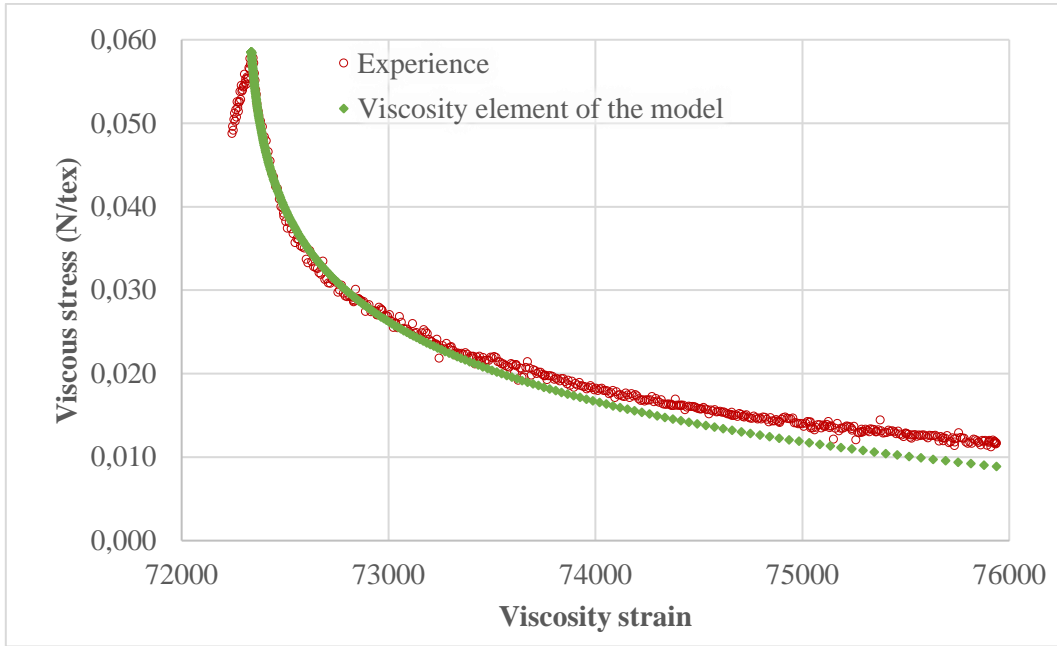


Figure 2-66. Viscous stress versus time of relaxation 6; (red) experimental data (green) simulation of the viscosity element of the constitutive law.

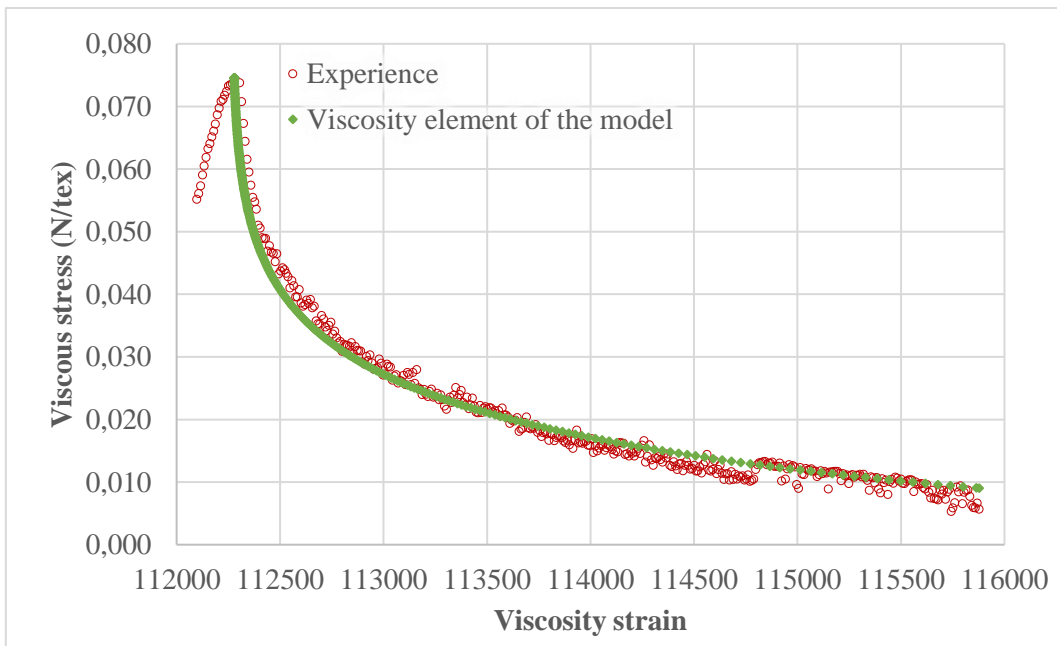


Figure 2-67. Viscous stress versus time of relaxation 7; (red) experimental data (green) simulation of the viscosity element of the constitutive law.

Comparison between the experimental data and the simulation of the identified viscosity element of the constitutive law show a good description of the behavior for all relaxation except the first one, where the stress is over estimated (because the stress was negative). For the relaxations 2 and 3, the predicted decrease in stress is quicker in the first part of the relaxation and slower in the second part. For the

relaxation 4 and 5, the model gives almost the same behavior with the simulated value slightly below the experimental one. Lastly for relaxation 6 and 7, we have overlapping values as for the relaxations 2 and 3.

2.8. Validation of the constitutive law

In this chapter we will simulate the tests presented in chapter 0 and compare the predictions to the experimental results.

2.8.1. Implementation in a FEM code

The constitutive law was implemented in a Fortran user routine of the commercial finite-element structure analysis code Abaqus-Standard. The element type is a one-dimensional truss element (in a three-dimensional space), for which only compression and tensile loads are available. The FEM code gives the time evolution of the finite element strain. The constitutive law has to calculate the corresponding stress response.

Two internal variables are used in the model: the viscosity and plastic strains. So, the simulation of mooring lines with this constitutive law does not require a large amount of memory (RAM).

Some law functions are inverted numerically by a Newton-Raphson algorithm. The time differential equation of the viscous strain is discretized according to a Euler implicit type and solved by a Newton-Raphson algorithm, depending on two modes; one when the plastic strain is constant (viscoelastic mode), and the other when it increases (visco-elasto-plastic mode).

The numerical simulations performed have proved the robustness of the Jacobian ratio, necessary for a structure equilibrium algorithm of the Newton-Raphson type, as classically. None of the Newton-Raphson algorithms of the implementation failed during the simulations.

2.8.2. Cyclic test with multi-relaxation

The identification has been made on this first test, so the test results should fit the simulation well. However, as the viscous parameter has been identified only on the first loading sequence of the test, some differences could be expected in the cycle if the viscosity is different during unloading, reloading or in the plastic regime.

Figure 2-68 presents the experimental evolution of strain with time for the sample-SR40 and its numerical simulation. This evolution is an input of the numerical simulation, except for the recovery stages, where the sub-rope force is maintained constant.

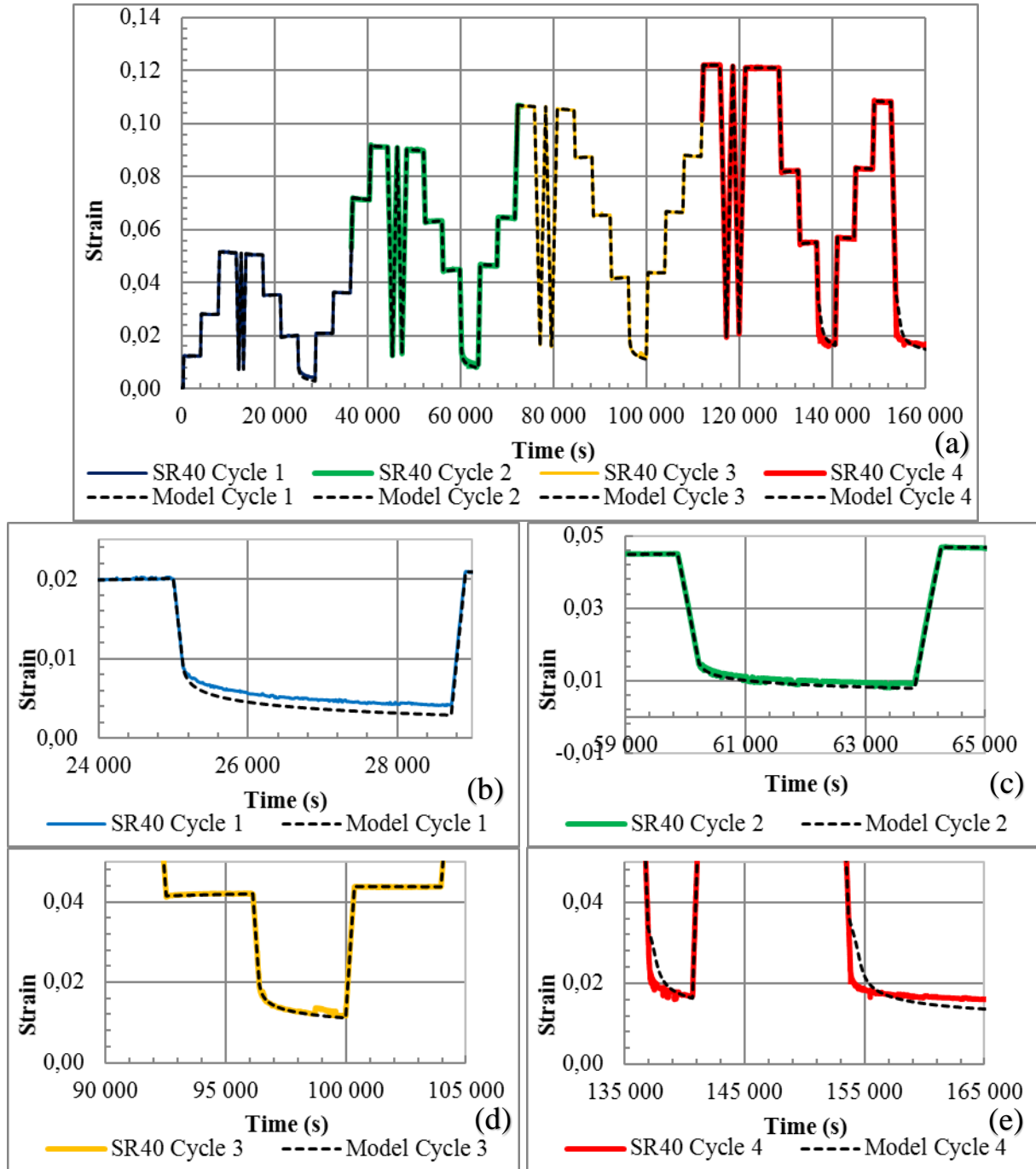


Figure 2-68. Time evolution of strain for test SR40 and the constitutive law (a), with zoom on recoveries (b,c,d,e).

The simulation is in good agreement with the recovery strains. Some differences exist for the two last recovery stages; the final strain is almost correct, but the kinetics are different from the experimental results.

Figure 2-69 presents the time evolution of the stress of the experience and the simulation. The values are quite close, but with some differences during relaxations.

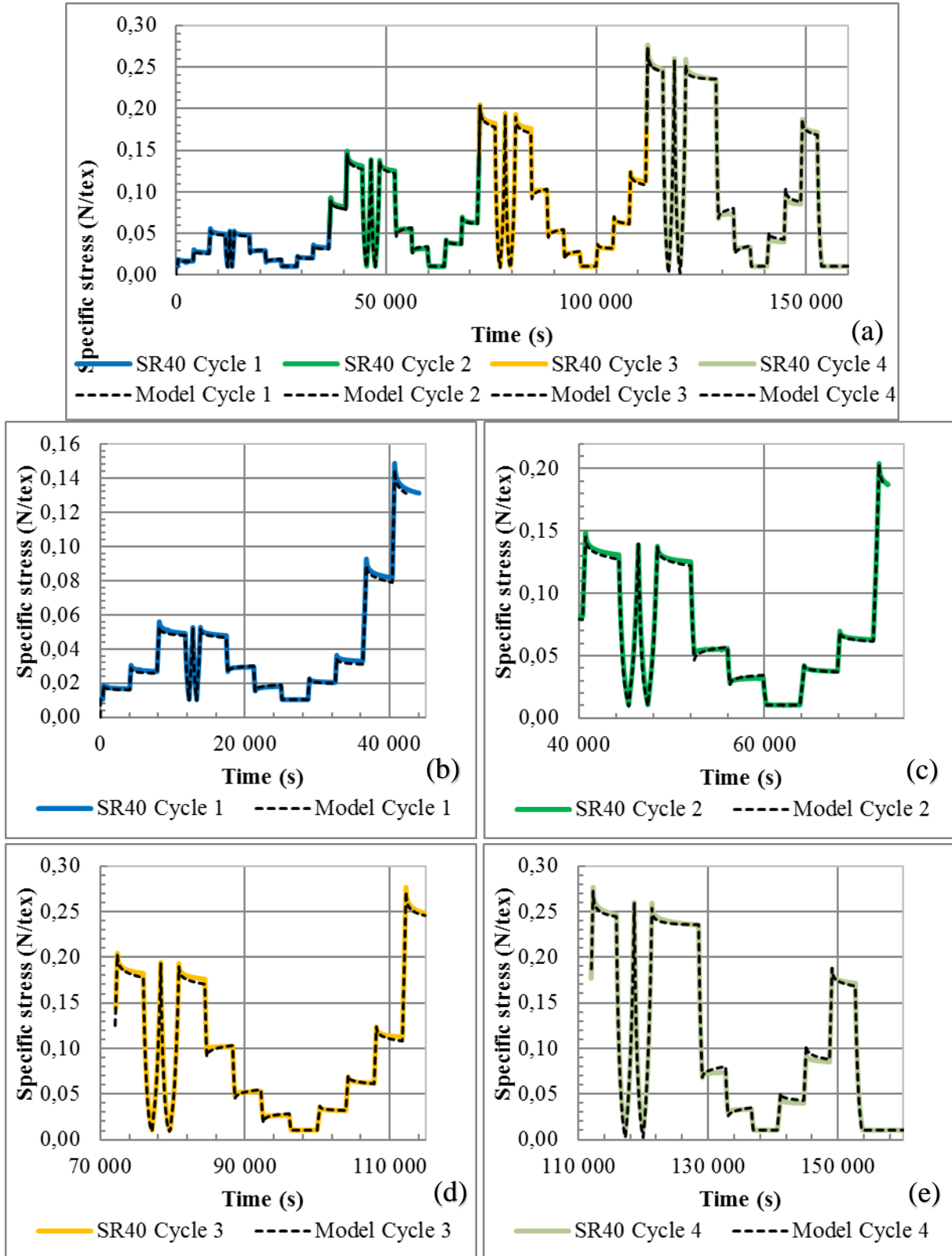


Figure 2-69. Time-evolution of stress for the test SR40 and the model (a), and zoom (b,c,d,e).

The comparison of the strain-stress curves is given by Figure 2-70. To get a better idea of the differences between the tests and the numerical simulation, each cycle is drawn separately in Figure 2-71.

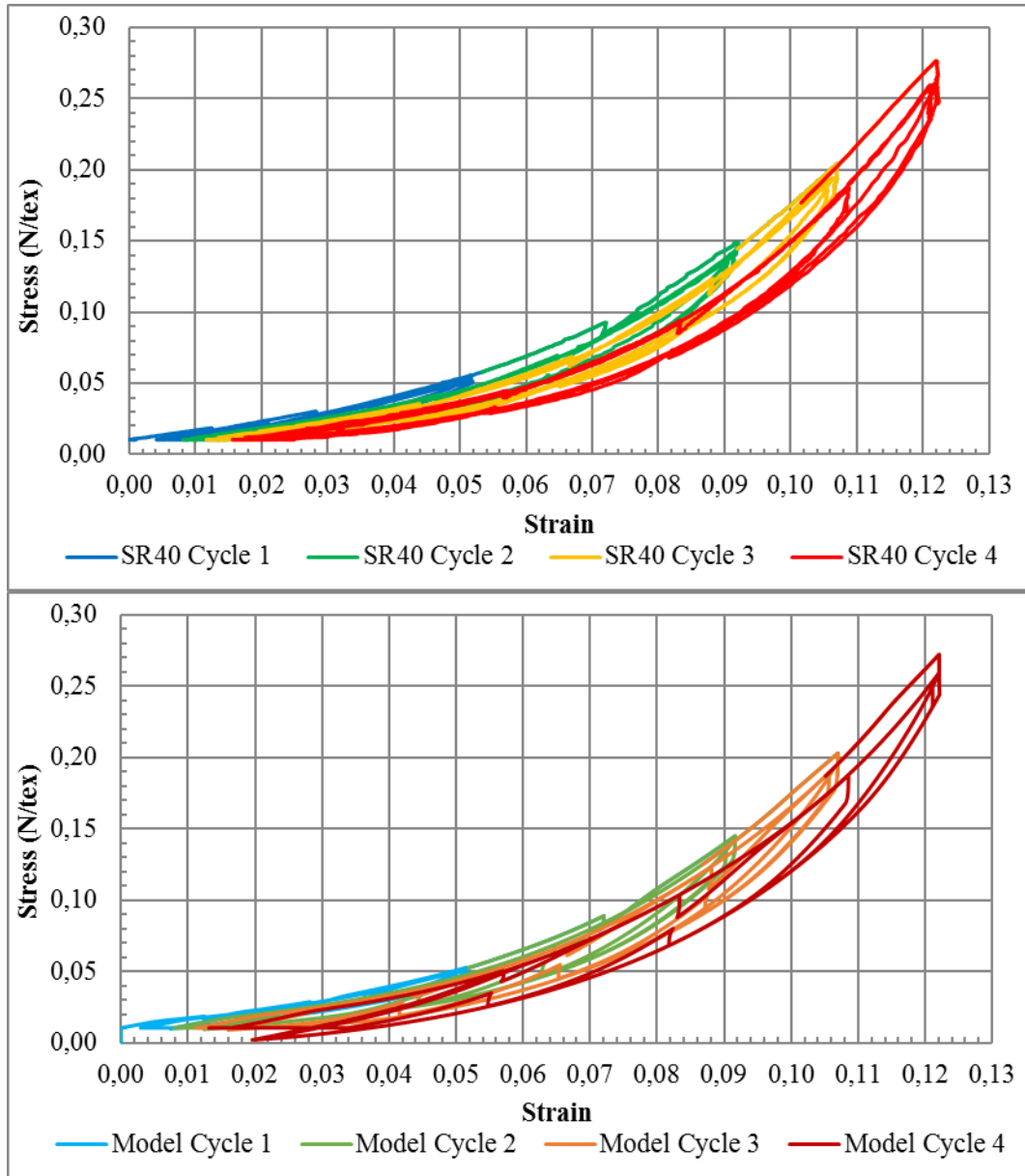


Figure 2-70. Comparison between experience and model, for the multi-relaxation test, stress vs strain.

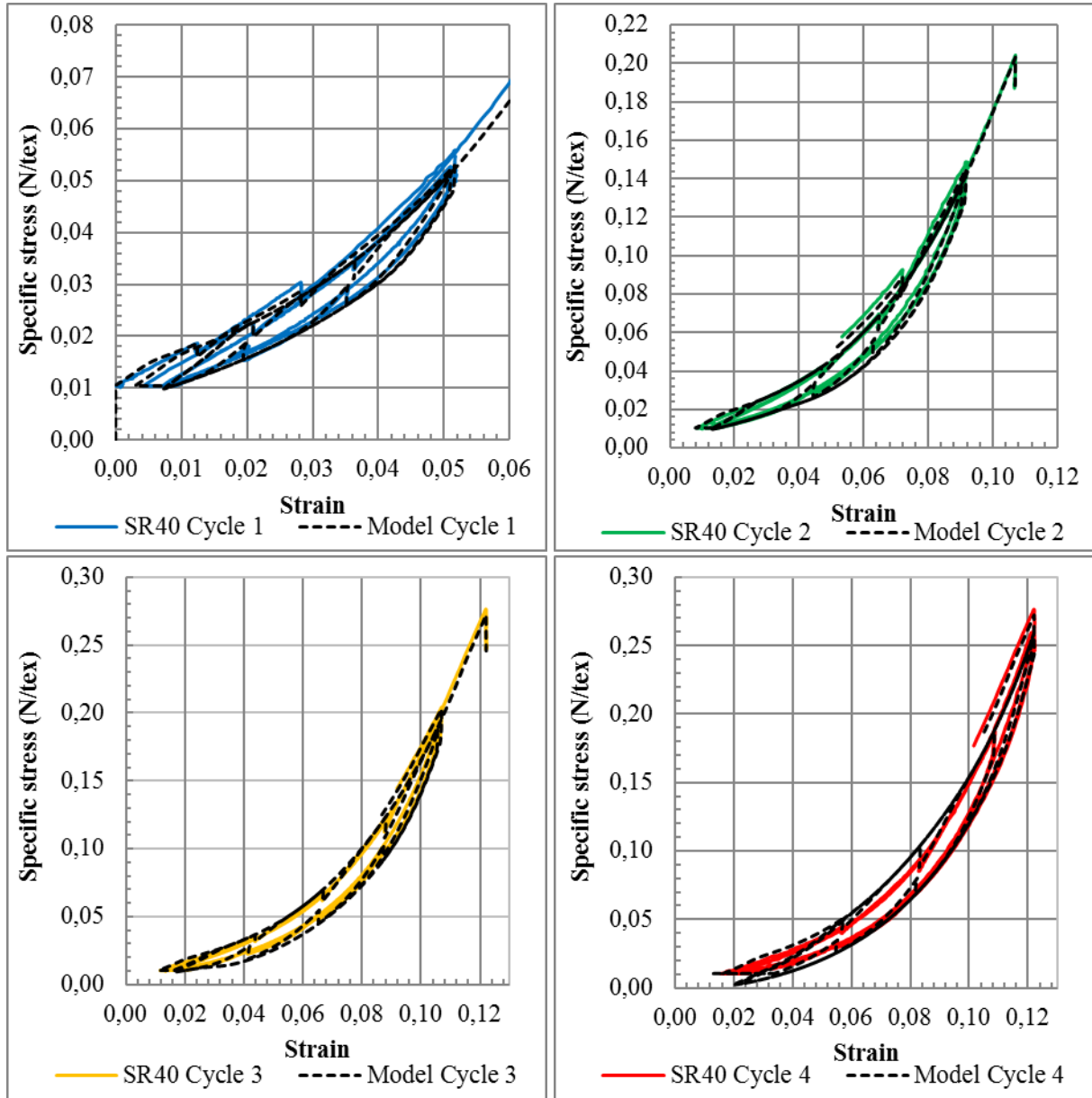


Figure 2-71. Comparison between experience and model, for the multi-relaxation test separated in 4 cycles.

The results of the model are quite close to those from the test. The fourth cycle prediction is a little worse at low load but still close enough to the test result.

So, the model seems to be working well for tests with cycle and relaxation in the load range of 0.01 to 0.25 N/tex, and strain rates around 10^{-4} s^{-1} .

It should allow to quickly determine the effect of a storm under service conditions, inducing a certain strain, allowing for a quick evaluation of the behavior.

2.8.3. Monotonous tests at different strain rates

The next step is to validate the model for different strain rates. This step allows the limits of the model to account for the strain rate to be examined. Figure 2-72 presents the evolution of the stress for 5 strain rates, as predicted by the model.

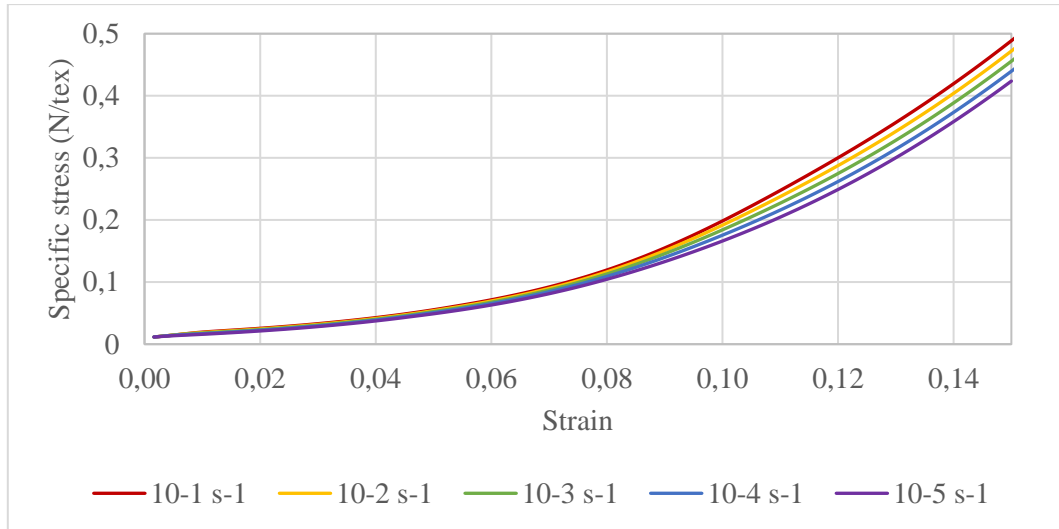


Figure 2-72. Model results in monotonous loading at five different strain rates.

Now, we can compare experimental and simulated results (Figure 2-73). As the viscosity of the model has been evaluated on the multi-relaxation tests (strain rate of 10^{-4} s^{-1}), it should be expected provide good results with a strain rate of 10^{-4} s^{-1} and below. But maybe not so good at higher strain rates if the viscous behavior is not linear.

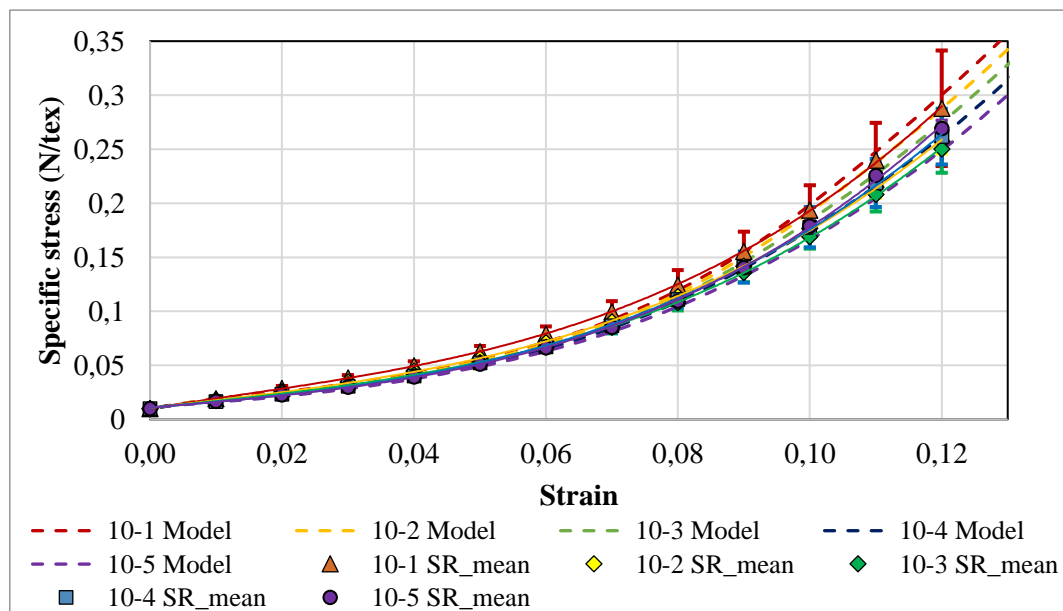


Figure 2-73. Comparison between experience and model, on monotonous loading at different strain rates.

From a large perspective, there is a good agreement between the test and the model, with most of the results within the value of standard deviation from the tensile test.

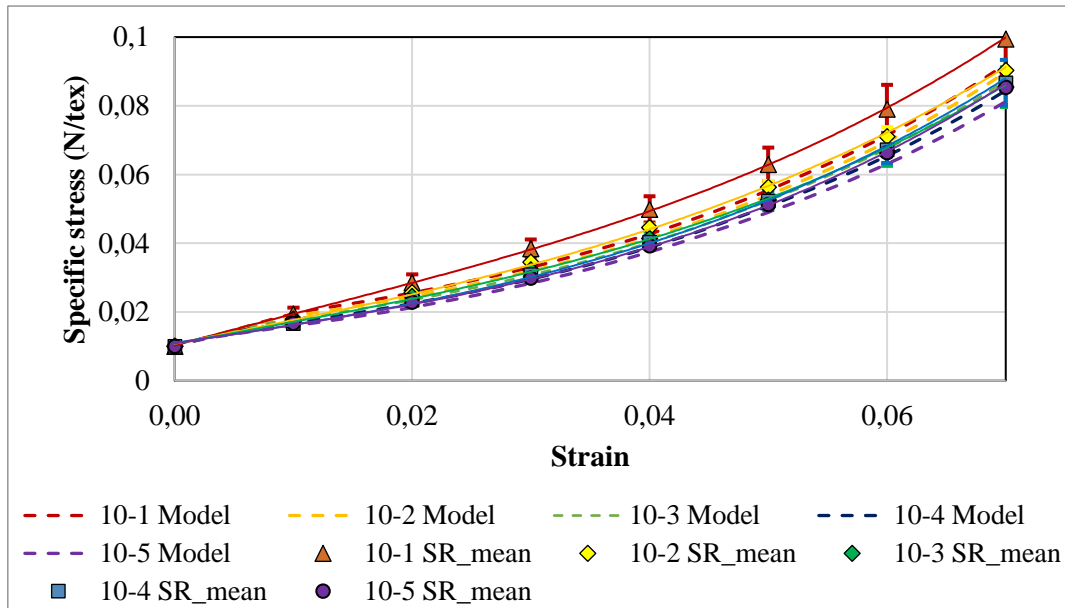


Figure 2-74. Comparison between experience and model, on monotonous loading at different strain rates; zoom at strains from 0% to 7%.

Closer examination of the data between 0 and 7 % strain where we have the lowest scatter in our experimental results (Figure 2-74), we see that the trends for the test at 10⁻¹ s⁻¹ are not described perfectly even if we still are within the scatter of the experimental tests.

If we look closer at the tests at 10⁻¹ s⁻¹ (Figure 2-75), there is an almost perfect match for one of the tests, SR30.

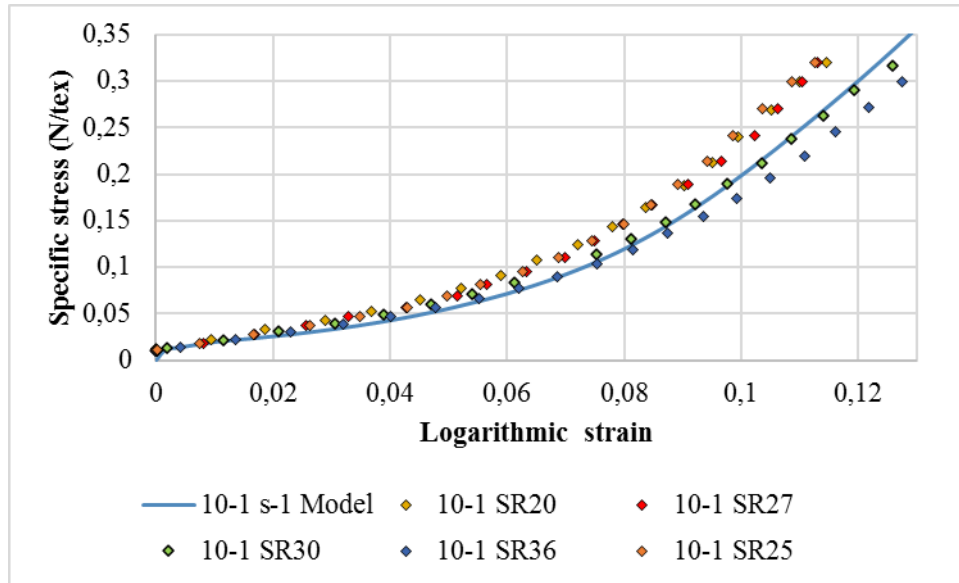


Figure 2-75. Comparison for the strain rate of 10^{-1} s-1

It should be recalled that these monotonous tests at different strain rates were not used at all for the identification of the law.

2.8.4. Cyclic test with multi-creep/recovery

The aim now is to validate the law on a loading case which is different from the relaxation stages, which were used for the identification, in order to see if the proposed constitutive law can be applied.

This test was controlled at constant stress rate, and includes creep and recovery stages. The numerical simulation is controlled in the same way (Figure 2-76) and shows that the test loading is correctly simulated.

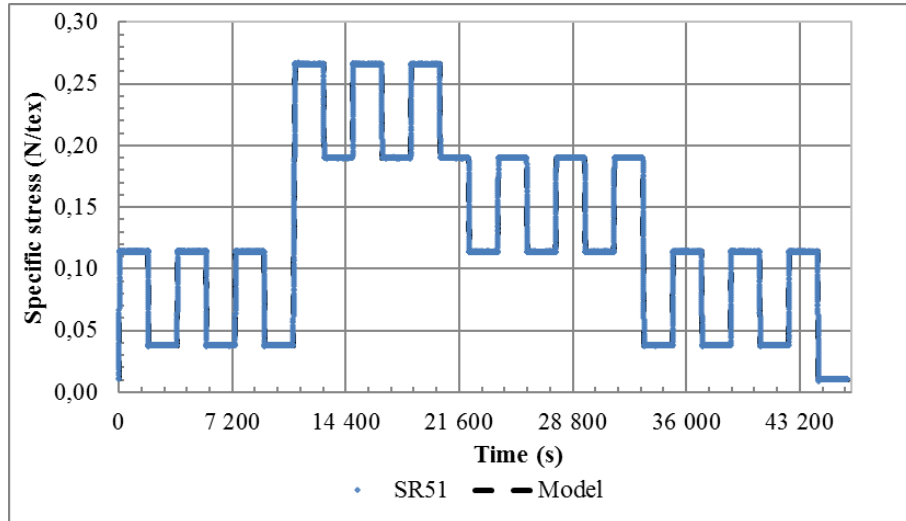


Figure 2-76. Loading sequence for the experiment and the numerical simulation of sample-SR51 test.

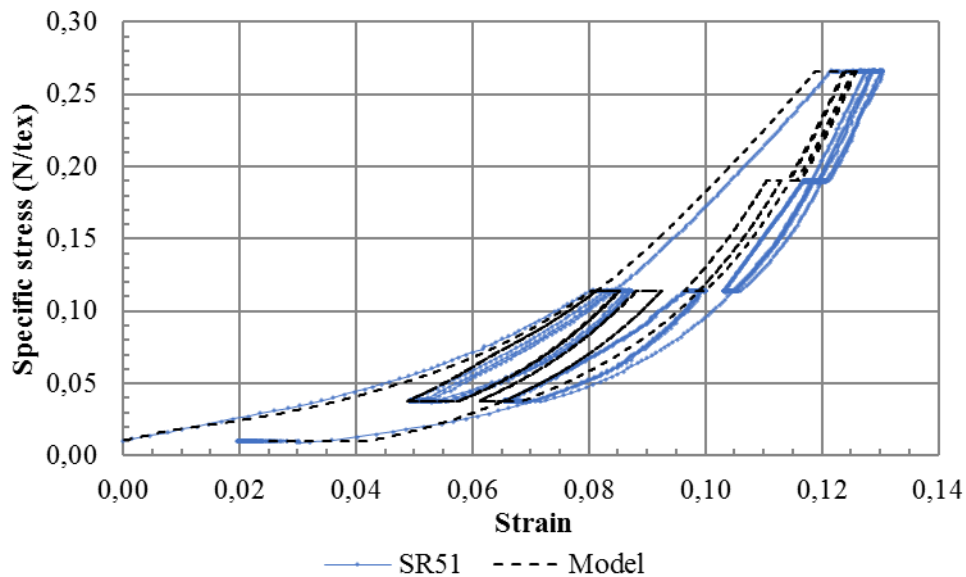


Figure 2-77. Comparison between simulation and experience for the multi-creep sample-SR51 test; stress versus strain.

The stress versus strain comparison is given in Figure 2-77. The experience-model agreement is not as good as for the multi-relaxation identification test. It seems that the combination of cycling and creep develops an additional elongation compared to the model. However, at the end of the final unloading, the experimental and simulated strains are very similar (2% of strain for the test and 2.4% for the simulation).

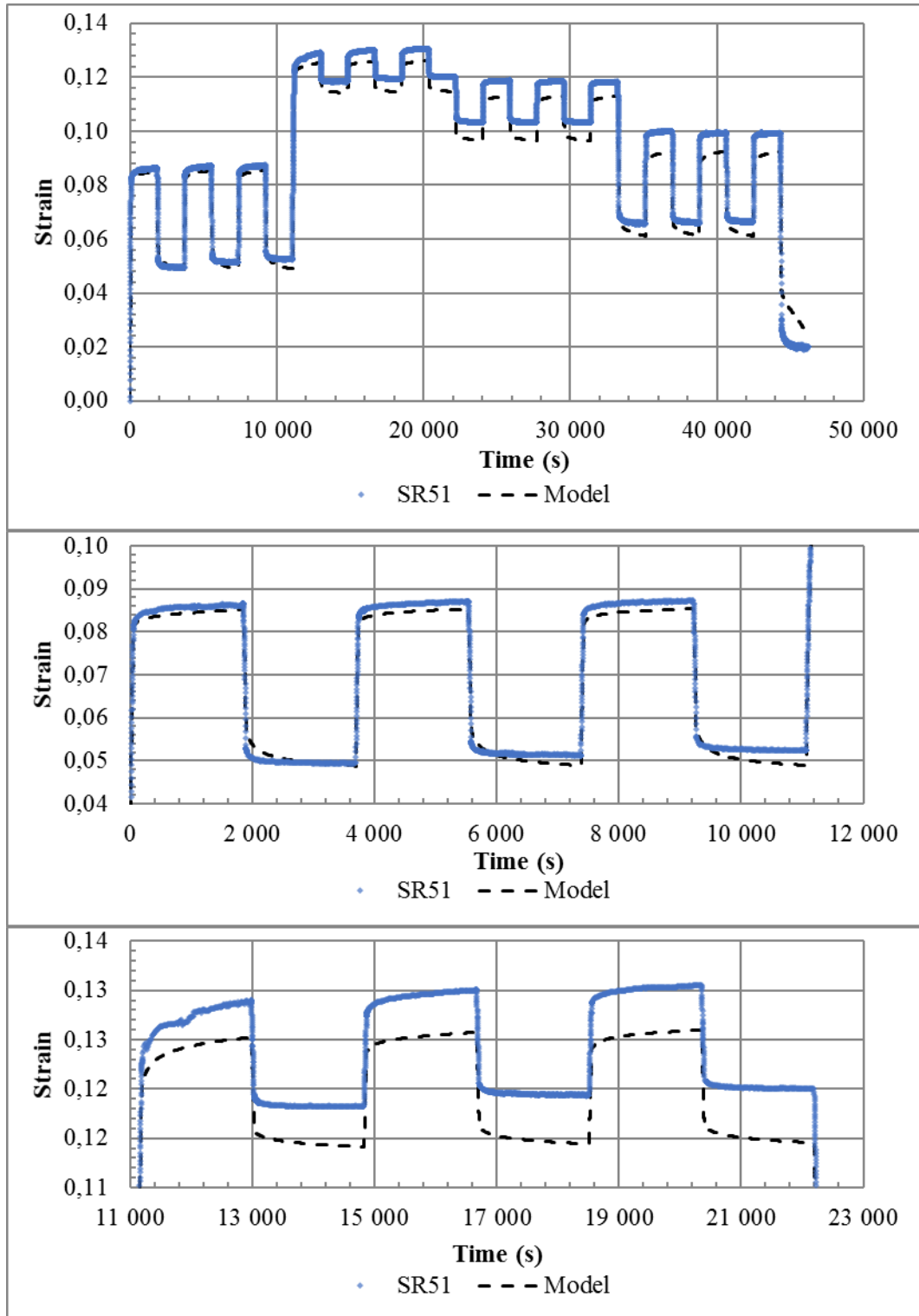


Figure 2-78. Time evolution of the strain for the simulation and experience for the multi-creep creep sample-SR51 test.

During this test the maximal stress imposed lead to an higher strain than the maximum strain used for the identification, which could explain some of the

differences. While the time evolution of the creep strain is similar to the test results, those of the strain recovery are not very good.

The same remark was made for the test with multi-relaxation. So, the constitutive law does not capture very well the polyamide sub-rope time evolution of the stress relaxation and the creep strain after a large unloading.

It should be noted that this multi-creep test was not used at all for the constitutive law identification.

2.9. Conclusion

Experimental devices have been developed in order to perform tensile tests on continuously wetted 4-ton polyamide twisted sub-ropes. Different loading paths were applied in order to reveal most of the visco-elasto-plastic features of the behavior. Different types of tensile, relaxation, and creep tests were performed, revealing the following observations:

- A non-linear stress strain behavior of the material.
- A relaxation and creep duration of 1 hour is not sufficient to stabilize the stress or the elongation of the material.
- A relative stabilization of the sub-rope length is observed after a bedding-in preloading.
- A complex strain rate sensitivity of the stress is observed; the stress does not increase monotonously with the strain rate for strains higher than 7%.

A comparison between 8-ton and 4-ton polyamide sub-ropes shows that their behaviors are similar, allowing the methods developed for the 4-ton to be applied to the 8-ton sub-rope. The stiffness of the 8-ton sub-rope is a little higher than that of the 4-ton. This is probably due to the longer lay-length of the 8-ton than the 4-ton one.

A mechanical characterization has been performed, based on the viscoelasticity theory, and previous studies (*François and Davies 2008, Bles et al. 2009, Flory 2013, Falkenberg 2018*). This has revealed:

1. A dynamic elasticity, the modulus of which is linear with the stress.
2. A time-independent behavior, the tangent modulus of which is also linear with the stress, with lower levels than the dynamic modulus.
3. A plastic or permanent elongation behavior, where the yield stress is nearly linear with the plastic strain.

Based on Flory's approach (*Flory 2013*), Bureau Veritas expertise (Michel François), and the present mechanical characterization, a phenomenological constitutive law has been proposed for polyamide 4-ton twisted sub-ropes. Its identification was made on multi-relaxation tests, by the proposal of a mostly analytical identification method in four stages:

1. Dynamic elasticity.
2. Time-independent behavior or long-term elasticity.

3. Plasticity.
4. Viscosity.

Each stage allows an assessment of the difference between the experimental data and the identified law, separately, for the four elements of the law. The multi-relaxation test, developed for the identification of the behavior law, presents some advantages as the elastic part of the model is easily determined with a robust approach. The phenomenological law is determined step by step, by analyzing each component, leading to a better knowledge of the material behavior.

Based on this evaluation, we can conclude that the 3 first points (dynamic elasticity, time independent behaviour and plasticity) are in good agreement with the experimental data, for a wide range of strain and stress. Only the viscous element should be improved for a better agreement with the experimental data. Notably, its identification was performed on a part of a multi-relaxation test and not over the whole test.

Validation of the model was made on the three types of test. The simulation of the multi-relaxation test shows very good agreement with test results, but this type of test was the one used for the identification. The simulation results, at strain rates from 10^{-5} to 10^{-1} s⁻¹, are within the scatter measured during the test, with higher differences in results for the tests at the quickest strain rate of 10^{-1} s⁻¹. However, good results were obtained for the lower strain rates. The simulation of the multi-creep test was globally in agreement with the experiments, but the time evolution during the recovery stages were different and the combination of cycles and creep results in an additional elongation compared to the model. The stress relaxation and creep strain time evolutions are captured well by the constitutive law when they are in loadings. A difference between the tests and the law is observed when the creep or the relaxation occurs after a large unloading.

The constitutive law was implemented into a commercial finite element software tool relevant for mooring line analysis. The robustness of this implementation was good. Only two internal variables are used, allowing low memory requirements for complex mooring floating body simulations. The input and output data of this implementation was agreed by the computing team of *Principia*, in charge of the implementation of this law in the commercial floating platform mooring time-simulation software tool *Deeplines*.

This phenomenological constitutive law may be improved by a viscous element with more internal variables, like a Prony series, Schapery's model or an integral-type viscoelastic law. But, in this case of viscoelastic laws, the identification process will

probably be more complicated, due to the higher complexity of viscoelastic phenomena involved. This is also their advantage over the present law.

According to the present study, it seems necessary to include more complexity in the viscoelastic modelling. Moreover, the long-term creep experimental results in chapter 3 shows that a creep duration of 9 months is not sufficient to stabilize the elongation of the 4-ton polyamide sub-rope. This will probably lead to relaxation times in the modelling of over a year. But this fact brings major difficulties for characterization and identification of a fully-relaxed or time-independent behavior.

Considering these difficulties for the viscoelasticity modelling, the present law offers an applicable and practical tool to, in the short-term, be able to simulate moored floating platforms. This law and its identification method also offer a way to characterize many aspects of the intricate visco-elasto-plastic behavior of polyamide ropes.

2.10. Reference

- Amaniampong, G., 1992. *Variability and viscoelasticity of parallel-lay ropes* (Doctoral dissertation, University of Cambridge).
- Baltussen, J.J.M. and Northolt, M.G., 2001. The viscoelastic extension of polymer fibres: creep behavior. *Polymer*, 42(8), pp.3835-3846.
- Baltussen, J.J.M. and Northolt, M.G., 2003. The viscoelastic extension of polymer fibres: complex loadings. *Polymer*, 44(6), pp.1957-1966.
- Baltussen, J.J.M. and Northolt, M.G., 2004. The Eyring reduced time model for viscoelastic and yield deformation of polymer fibres. *Polymer*, 45(5), pp.1717-1728.
- Banfield, S., Versavel, T., Snell, R.O. and Ahilan, R.V., 2000, January. Fatigue curves for polyester moorings-a state-of-the-art review. In *Offshore Technology Conference*. Offshore Technology Conference.
- Bernasconi, A., Davoli, P., Basile, A. and Filippi, A., 2007. Effect of fibre orientation on the fatigue behavior of a short glass fibre reinforced polyamide-6. *International Journal of Fatigue*, 29(2), pp.199-208.
- Bles, G., Gadaj, S.P., Guelin, P., Nowacki, W.K. and Tourabi, A., 2000. Thermomechanics of viscoplastic large strains of solid polymers. *Archives of Mechanics*, 52(3), pp.397-427.
- Bles, G., Gadaj, S.P., Nowacki, W.K. and Tourabi, A., 2002. Experimental study of a PA66 solid polymer in the case of cyclic shear loading. *Archives of Mechanics*, 54(2), pp.155-174.
- Bles, G., Nowacki, W.K. and Tourabi, A., 2009. Experimental study of the cyclic visco-elasto-plastic behavior of a polyamide fibre strap. *International Journal of Solids and Structures*, 46(13), pp.2693-2705.
- Boisot, G., 2009. *Mécanismes et modélisation mécanique de la déformation, de l'endommagement et de la rupture du PolyAmide 11 pur et renforcé choc* (Doctoral dissertation, Paris, ENMP).
- Broudin, M., Le Gac, P.Y., Le Saux, V., Champy, C., Robert, G., Charrier, P. and Marco, Y., 2015 (a). Water diffusivity in PA66: experimental characterization and modeling based on free volume theory. *European Polymer Journal*, 67, pp.326-334.
- Broudin, M., Le Saux, V., Le Gac, P.Y., Champy, C., Robert, G., Charrier, P. and Marco, Y., 2015 (b). Moisture sorption in polyamide 6.6: experimental investigation and comparison to four physical-based models. *Polymer Testing*, 43, pp.10-20.
- Chailleux E, Davies P, Modelling the Non-Linear Viscoelastic and Viscoplastic Behavior of Aramid Fibre Yarns. *Mechanics of Time-Dependent Materials*, 7, 291-303, 2003.
- Chailleux E, Davies P, A Non-Linear Viscoelastic Viscoplastic Model for the Behavior of Polyester Fibres. *Mechanics of Time-Dependent Materials*, 9, 147-160, 2005.
- Charmetant A, Vidal-Sallé E, Boisse P, Hyperelastic modelling for mesoscopic analyses of composite reinforcements, *Composites Science and Technology*, 71, 1623-1631, 2011.
- Colin, X. and Verdu, J., 2014. Humid ageing of organic matrix composites. In *Durability of composites in a marine environment* (pp. 47-114). Springer, Dordrecht.
- Davies P, Chailleux E, Bunsell A, Grosjean F, Francois M, Prediction of the long term behavior of synthetic mooring lines. Proceedings of OTC 2003, Houston Texas USA, OTC 15379, may 2003.

- Davies, P., Reaud, Y., Dussud, L. and Woerther, P., 2011. Mechanical behavior of HMPE and aramid fibre ropes for deep sea handling operations. *Ocean Engineering*, 38(17-18), pp.2208-2214.
- Davies, P., Weller, I.S. and Johannig, I.L., 2012. Testing of synthetic fibre ropes.
- Del Vecchio, C.J.M., 1992. *Light Weight Material for Deep Water Moorings* "University of Reading PhD (Doctoral dissertation, Thesis).
- Détrez, F., 2008. Nanomécanismes de déformation des polymères semicristallins. *These de doctorat. Université des Sciences et Technologie de Lille. Lille.*
- Dib W, 2014. Thèse de doctorat de l'université de Grenoble.
- Falkenberg, E., A° hjem, V., Larsen, K., Lie, H. and Kaasen, K.E., 2011, January. Global Performance of Synthetic Rope Mooring Systems: Frequency Domain Analysis. In *International Conference on Offshore Mechanics and Arctic Engineering* (Vol. 44335, pp. 507-514).
- Falkenberg, E., Yang, L. and Åhjem, V., 2018. The Syrope method for stiffness testing of polyester ropes. In *ASME 2018 37th International Conference on Ocean, Offshore and Arctic Engineering*. American Society of Mechanical Engineers Digital Collection.
- Flory, J.F., Parsey, M.R. and McKenna, H.A., 1988, February. The choice between nylon and polyester for large marine ropes. In *7th Conference on Offshore Mechanics and Arctic Engineering*.
- Fond, C. and G'sell, C., 2002. Localisation des déformations et mécanismes d'endommagements dans les polymères multiphases. *Mécanique & industries*, 3(5), pp.431-438.
- François, M. and Davies, P., 2008, January. Characterization of polyester mooring lines. In *International Conference on Offshore Mechanics and Arctic Engineering* (Vol. 48180, pp. 169-177).
- François, M. 2018. Polyamoor internal document: Load-Elongation Model - QS test.
- Hearle, J.W.S., Grosberg, P. and Backer, S., 1969. Structural mechanics of yarns and fabrics, vol. 1.
- Huang W, Liu H, Hu C, Modeling the Stress-Strain Properties of Synthetic Fiber Mooring Lines under Cyclic Loading. Proceedings of ISOPE 2014, Busan South-Korea, June 2014.
- Huang W, Liu H, Lian Y, Li L, Modeling nonlinear time-dependent behaviors of synthetic fiber ropes under cyclic loading. *Ocean Engineering*, 109, 207-216, 2015.
- Humeau, C., 2017. *Contribution to the study of coupling between moisture diffusion and mechanical stress, in high performance marine materials* (Doctoral dissertation, Nantes).
- Huntley, M. B. (2016, September). Fatigue and modulus characteristics of wire-lay nylon rope. In *OCEANS 2016 MTS/IEEE Monterey* (pp. 1-6). IEEE.
- Iwata, A., Inoue, T., Naouar, N., Boisse, P. and Lomov, S.V., 2019. Coupled meso-macro simulation of woven fabric local deformation during draping. *Composites Part A: Applied Science and Manufacturing*, 118, pp.267.
- Launay, A., Maitournam, M.H., Marco, Y., Raoult, I. and Szymtka, F., 2011. Cyclic behavior of short glass fibre reinforced polyamide: Experimental study and constitutive equations. *International Journal of Plasticity*, 27(8), pp.1267-1293.
- Launay, A., Maitournam, M.H., Marco, Y. and Raoult, I., 2013. Multiaxial fatigue models for short glass fiber reinforced polyamide—Part I: Nonlinear anisotropic constitutive behavior for cyclic response. *International Journal of Fatigue*, 47, pp.382-389.

- Lechat, C., 2007. *Comportement mécanique de fibres et d'assemblages de fibres en polyester pour câbles d'amarrage de plates-formes offshore* (Doctoral dissertation).
- Lechat, C., Bunsell, A.R. and Davies, P., 2011. Tensile and creep behavior of polyethylene terephthalate and polyethylene naphthalate fibres. *Journal of Materials Science*, 46(2), pp.528-533.
- Lim, L.T., Britt, I.J. and Tung, M.A., 1999. Sorption and transport of water vapor in nylon 6, 6 film. *Journal of applied polymer science*, 71(2), pp.197-206.
- Northolt, M.G., Baltussen, J.J.M. and Schaffers-Korff, B., 1995. Yielding and hysteresis of polymer fibres. *Polymer*, 36(18), pp.3485-3492.
- Parenteau T, 2009. Thèse de doctorat, Université de Bretagne-Sud.
- Petruska, D., Geyer, J., Macon, R., Craig, M., Ran, A. and Schulz, N., 2005. Polyester mooring for the Mad Dog spar—design issues and other considerations. *Ocean engineering*, 32(7), pp.767-782.
- Puffr, R. and Šebenda, J., 1967. On the structure and properties of polyamides. XXVII. The mechanism of water sorption in polyamides. In *Journal of Polymer Science Part C: Polymer Symposia* (Vol. 16, No. 1, pp. 79-93). New York: Wiley Subscription Services, Inc., A Wiley Company.
- Rao, Y. and Farris, R.J., 2000. A modeling and experimental study of the influence of twist on the mechanical properties of high-performance fiber yarns. *Journal of applied polymer science*, 77(9), pp.1938-1949.
- Regrain, C., Laiarinandrasana, L., Toillon, S. and Saï, K., 2009. Multi-mechanism models for semi-crystalline polymer: Constitutive relations and finite element implementation. *International Journal of Plasticity*, 25(7), pp.1253-1279
- Reuvers, N.J.W., Huinink, H.P., Fischer, H.R. and Adan, O.C.G., 2012. Quantitative water uptake study in thin nylon-6 films with NMR imaging. *Macromolecules*, 45(4), pp.1937-1945.
- Spathis, G. and Kontou, E., 1998. Experimental and theoretical description of the plastic behavior of semicrystalline polymers. *Polymer*, 39(1), pp.135-142.
- Van Dommelen, J.V., Parks, D.M., Boyce, M.C., Brekelmans, W.A.M. and Baaijens, F.P.T., 2003. Micromechanical modeling of the elasto-viscoplastic behavior of semi-crystalline polymers. *Journal of the Mechanics and Physics of Solids*, 51(3), pp.519-541.
- Vu, T.D., Durville, D. and Davies, P., 2015. Finite element simulation of the mechanical behavior of synthetic braided ropes and validation on a tensile test. *International Journal of Solids and Structures*, 58, pp.106-116.
- Weller, S.D., Davies, P., Vickers, A.W. and Johanning, L., 2014. Synthetic rope responses in the context of load history: Operational performance. *Ocean Engineering*, 83, pp.111-124.
- Weller, S.D., Davies, P., Vickers, A.W. and Johanning, L., 2015. Synthetic rope responses in the context of load history: The influence of aging. *Ocean Engineering*, 96, pp.192-204.
- Weller, S.D., Banfield, S.J. and Canedo, J., 2018, June. Parameter estimation for synthetic rope models. In *ASME 2018 37th International Conference on Ocean, Offshore and Arctic Engineering*. American Society of Mechanical Engineers Digital Collection.
- Williams, J.G., Miyase, A., Li, D. and Wang, S.S., 2002, January. Small-scale testing of damaged synthetic fiber mooring ropes. In *Offshore Technology Conference*. Offshore Technology Conference.

Chapter 3: Long term creep behavior

Under constant loading, nylon fibers and ropes show an elongation (called creep) evolving with time. This viscous behavior is strongly dependent upon load and temperature. This chapter presents first some tests to characterize the creep rate at ambient temperature and in water, to estimate creep strain evolutions of polyamide 6 yarn samples under several loads. Then long-term tests (8 months) were performed on 4-ton ropes to see if there is an effect of construction. In order to test these ropes a testing device was designed and built during the project and will be briefly presented in this chapter. Finally, a comparison will be made between results from short term and long-term tests.

Keywords: Creep, Rope, Yarn, Nylon, Mooring, Water, Long-term

Table of content

3. Long term creep behavior	105
3.1. Bibliography	105
3.2. Objectives	107
3.3. Creep tests on yarn	107
3.3.1. Material and experimental methods	107
3.3.2. Results	109
3.4. Long term creep device	113
3.4.1. Design choices.....	113
3.5. Long term creep tests.....	115
3.5.1. Material and experimental methods	115
3.5.2. Results	119
3.6. Comparison between the results on Yarns and on 4-ton ropes.....	122
3.7. Comparison with the multi-creep test.....	124
3.8. Summary.....	125
3.9. References	126

3. Long term creep behavior

In the previous section the quasi-static and mechanical behaviour of fibre materials during 1-hour relaxation and 30 minute creep loading was investigated. Nevertheless, service conditions necessarily induce stresses over the material lifetime for up to 20 years. Therefore, this evaluation may not be sufficient to predict the full long-term behaviour, and in order to get closer to the application requirement we chose to perform long creep tests on yarn and rope materials.

3.1. Bibliography

One essential brick of the project is the characterization of the behaviour at long times and at ultra-low speeds. Indeed, as seen in chapter 2, the high viscosity of these materials cannot be relaxed after one hour of creep testing, nor be removed by a slow deformation rate (10^{-5} s^{-1}). However, viscosity is one of the main parts of the loading of this type of material (*Bles, 2009*) and according to *Davies (2000)* in the case of polyester cables, it is the most difficult part to model, the rest being close to a linear viscoelasticity.

Creep that occurs at low stresses or short durations is recoverable over time under little or no load, and the same mechanisms lead to reverse stress relaxation. Creep occurring at higher stress levels and longer times is not fully recoverable. Creep failure is considered as a static damage mechanism where the rope breaks after a certain duration at a constant tension.

Creep results have been catalogued by *Mc Kenna (2004)* for different fibers (polyester, nylon), predicting very rapid failure at high load levels for Nylon (around 80% of the Minimal Breaking Load) (Figure 3-1, Figure 3-2). It is also stated that Nylon shows a greater amount of primary creep.

Table 2.5 Creep in one decade of log-time, as quoted in *Engineer's Design Guide to Deepwater Moorings*. From TTI and Noble Denton (1999)

	15% break load		30% break load	
	1–10 days	10–100 days	1–10 days	10–100 days
<i>Polyester</i>				
Diolen 855TN	0.240%	0.166%	0.093%	0.034%
Trevira 785	0.119%	0.069%	0.165%	0.009%
<i>Aramid</i>				
Kevlar 29	0.023%	0.066%	0.046%	0.021%
Kevlar 49	0.011%	0.030%	0.041%	0.009%
<i>HMPE</i>				
Spectra 900	1.7% 7/182 days*	13%	broken 0.7/4 days*	broken
Spectra 1000	1.1% 11/321 days*	6.3%	8% 1/28 days*	broken
Dyneema SK60	0.16% 70/>354 days*	0.47%	0.98% 7/123 days*	8%

*The figures in days for HMPE fibres are (time to start of rapid creep)/(time to break).

Figure 3-1. Creep testing on yarn for a wide range of materials (*Mc Kenna, 2004*).**Table 2.6** Creep rupture. The measured strength–time coefficient k for nylon is 0.08 (Meredith, 1953). The available evidence indicates that k is less than 0.05 for aramid fibres and slightly more than 0.05 for polyester fibres

k	Time to fail at percent of 1-minute break load			
	20%	30%	50%	80%
0.05	2×10^{10} yrs	2×10^8 yrs	2×10^5 yrs	200 hrs
0.08	2×10^4 yrs	1000 yrs	3 yrs	5 hrs
0.1	200 yrs	19 yrs	60 days	100 mins

Figure 3-2. Creep rupture prediction at different load ranges (*Mc Kenna, 2004*).

Studies on creep of HMPE yarn are numerous (*Chimisso, 2009*) as creep failure as been a problem for HMPE for deep and ultra deep mooring for offshore oil drilling and exploration (*da Costa Mattos, 2011*). Dry studies on braided ropes have shown that nylon ropes, while having the highest creep elongation after 5 days of loading at 32% of MBL (compared to Dyneema or Spectra and Vectran ropes) have also the highest percentage of recovery after unloading (*Pal, 2017*).

Hunt et al. (1978; 1979; 1980) studied creep of bulk Nylon 6-6 and showed that it could be modelled using rheological (*Fancey, 2005*) or thermodynamic techniques. *Humeau (2017)* investigated creep at high loads on polyamide 6 yarns for both immersed and dry conditions and show good prediction with Schapery's model for the long-term predictions. However, only two long term creep samples were tested.

The study of creep is a basic requirement for safe and economic development of floating platforms. However, the characterization of the creep phenomenon for different rope constructions can be extremely complex and costly. This means that creep tests are usually performed at a smaller scale on yarns, and this does not take into account the contribution from the construction of the rope.

3.2. Objectives

For offshore wind farms, maintenance is expensive and can reduce profits. So reducing maintenance costs is a key point for the success of offshore wind turbines. Knowing that creep is an important part of the design of polyamide mooring ropes, and that re-tensioning is a very costly operation could make the use of polyamide uneconomic, as reducing tension operations is essential.

The first point in this study is to characterise the material wet, without the effect of the rope structure. The goal is to identify creep rates at different loads for immersed fibers. Creep failure will not be investigated in this study as it happens for loads and durations exceeding the requirements of offshore mooring.

The filament level was not considered due to slippage that can appear during long tests and because degradation can occur during its extraction or manipulation. The lowest scale investigated in this chapter will therefore be yarns.

However, as yarns are quite different from the real end-use rope the second objective is to study twisted polyamide sub-ropes under realistic conditions. To allow for comparison to the results obtained in Chapter 2, the sub-rope will have the same characteristic but longer samples, to have a better strain measurement resolution.

In order to perform tests on sub-ropes it was necessary to develop a creep testing device to test sub ropes for a duration of about 1 year. The load range of interest is up to 50% of MBL with the ability to test different loads. It must also have a large stroke, to take into account the high strain in these material and long specimens. Lastly, several tests must be made in parallel because the tests last a long time.

3.3. Creep tests on yarn

3.3.1. Material and experimental methods

3.3.1.1. Samples

Before each test, the yarns are loaded with a very low tension (0.005 N/tex) and immersed in water for 4 hours.

The yarns used are coated polyamide 6 fibers made by Nexis and of average linear weight of 196.25 Tex (g/km).

3.3.1.2. Testing equipment

The creep tests on immersed yarns were studied with a testing device at Ifremer specially designed for this application, Figure 3-3. The samples were immersed in a tank filled with tap water. One end of the specimen was fixed to the test bench and at the other end, a weight was suspended. Pulleys were used to transfer the load from

the vertical to the horizontal direction. The strain variation was recorded during the test by filming markers bonded to the yarn and tracked by image analysis.

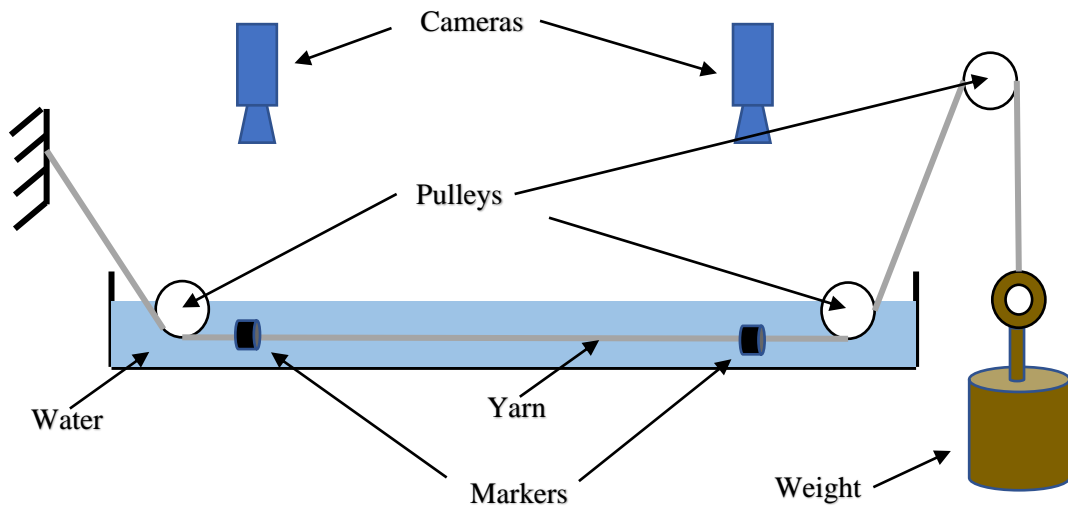


Figure 3-3. Testing device for creep test on wet yarns.

The cameras used are Logitech™ webcam C615 HD with optical correction of the lens distortion. The measurements and data treatments were made with the National Instrument Vision™ software tools.

3.3.1.3. Procedures

Before the test, each yarn is pre-tensioned at about 0.005N/tex (1 Newton), in order to put the markers on and to immerse the yarn in the water for a duration of 4 hours. The mechanical state at the end of this step serves as the reference state for the strain measurements.

Four loads were tested with two samples each (0.108; 0.161; 0.210; 0.266 N/tex), the loads are applied by hand with no precise control over the loading rate

but it takes about 10 seconds to get to the required load level. For each sample, the initial length between the markers was measured and an average value of 1250 mm was measured.

3.3.2. Results

As nylon usually shows a logarithmic visco-elasto-plastic creep behavior, we use an identification of the logarithmic creep rate : $\dot{\varepsilon}_c = \frac{\Delta\varepsilon}{\Delta \ln(\text{time})}$.

The evolution of strain with time can therefore be written:

$$\varepsilon_c = A * \ln(\text{time}) + B.$$

With A the logarithmic creep rate and B the strain after one second of creep, if the time unit is second.

To get a better idea of the logarithmic creep rate and compare it with the literature, the value of A will be presented in %/decade, using the following formula:

$$A \left(\frac{\%}{\text{decade}} \right) = (A * \ln(10)) * 100$$

Results are plotted as the evolutions of longitudinal strain versus time. Figure 3-4 presents two tests made for a stress of 0.108 N/tex, showing a creep rate of 0.122%/decade for the loading A and 0.134%/decade for the loading B. Some points in the initial part of the loading A were removed due to noise just after applying the load.

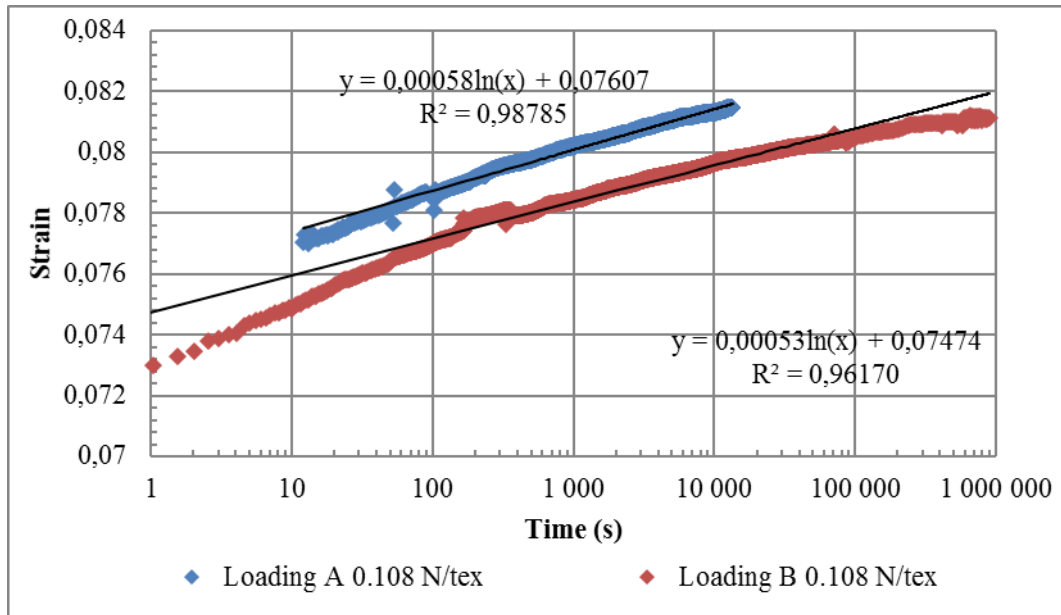


Figure 3-4. Creep test of yarn tested at 0.108 N/tex.

These two tests show a similar strain rate evolution, and the initial strain seems similar (around 7.3%). The creep strain does not follow a fully logarithmic time evolution as the logarithmic creep rate decreases with time.

Figure 3-5 presents results from two tests performed at a stress of 0.161 N/tex, showing a creep rate of 0.129%/decade for the loading A and 0.083%/decade for the loading B.

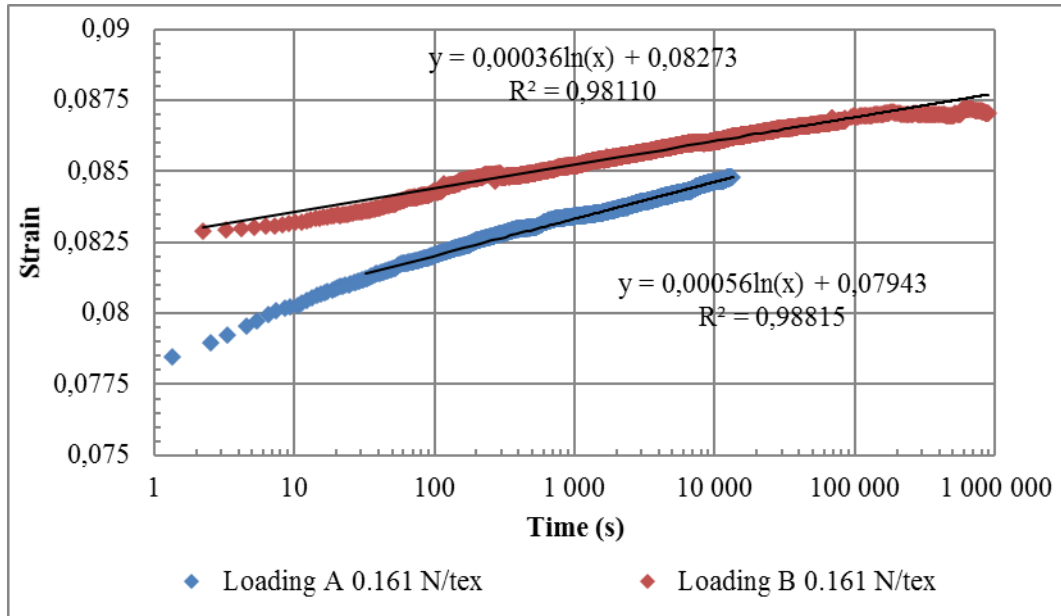


Figure 3-5. Creep test of yarn tested at 0.161 N/tex.

The evolutions of the logarithmic creep rate are similar to the one presented previously. The results from these two tests are quite scattered. The strain rate value obtained for loading B is quite low compared to other tests, even if the initial strain value is higher than for the second loading, leading to a higher strain.

Figure 3-6 presents two tests made at a stress of 0.210 N/tex, presenting a creep rate of 0.1197%/decade for the loading A and 0.1197%/decade for the loading B.

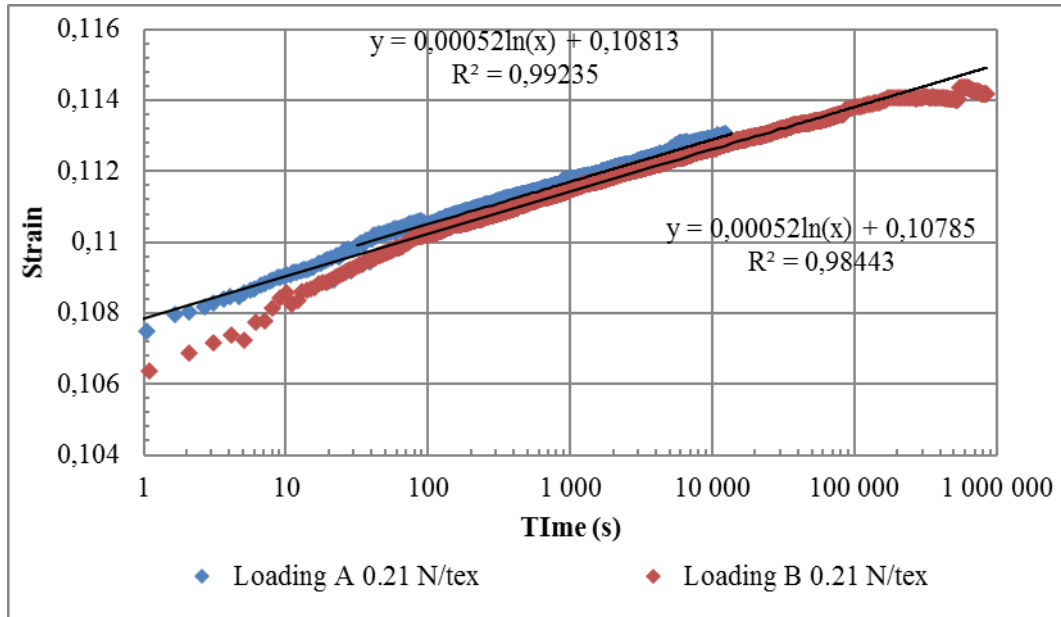


Figure 3-6. Creep test of yarn tested at 0.21N/tex.

For these two tests at higher load, a more repeatable behavior is found between the two tests, with a similar initial strain of 10.8% and the same strain rate of 0.12%/decade.

Figure 3-7 presents the test made at a stress of 0.27N/tex, presenting a creep rate of 0.134%/decade for the loading A and 0.131%/decade for the loading B. The loading B was realized with a bedding in of 1h at 0.06 N/tex before the test but with the same initial strain as the loading A.

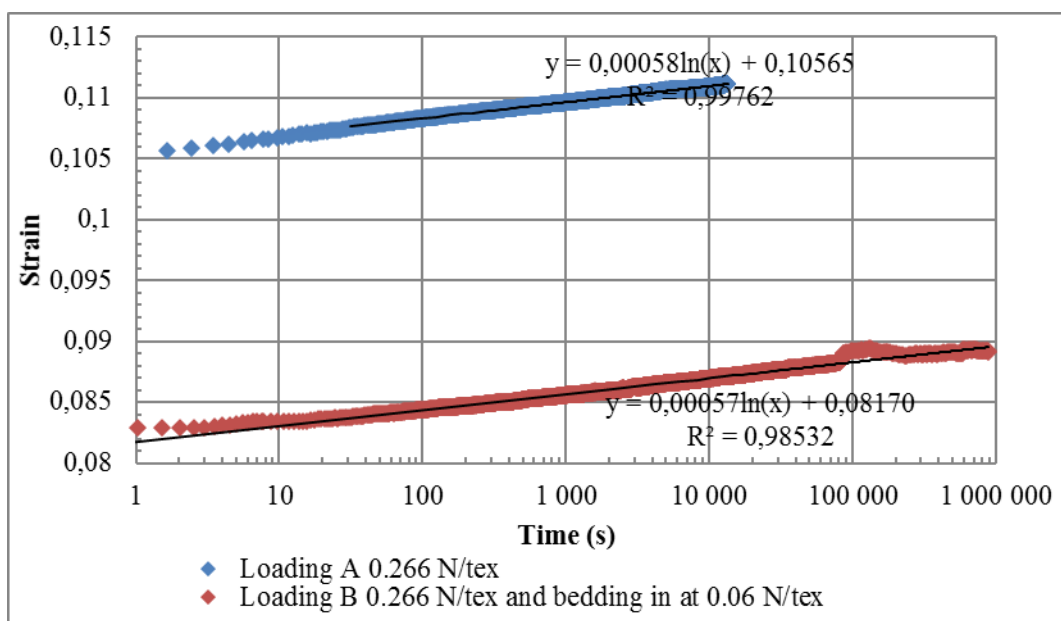


Figure 3-7. Creep test of yarn tested at 0.27N/tex.

This result shows a good repeatability for the creep rate with very similar values for the two tests. The bedding in does not seem to have not affected the creep rate but has nonetheless reduced the initial strain. The reason for this reduction of the initial strain is probably related to the change in initial stiffness due to the preliminary bedding-in.

The evolution of the logarithmic creep rate does not seem to evolve much as a function of the loading applied and remains globally constant during the campaign (Figure 3-8). However, the initial strain increases with the load level (except for the test with a preliminary bedding-in).

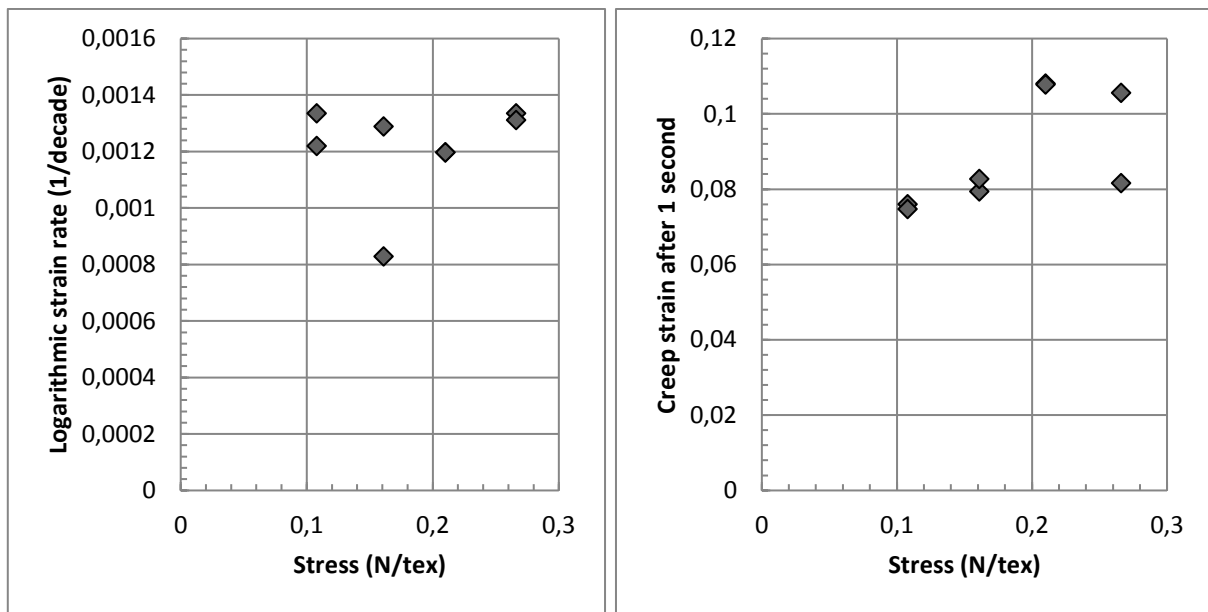


Figure 3-8. Logarithmic creep rate (left) and predicted strain after one second of creep (right) in function of creep stress on wet yarns.

3.4. Long term creep device

To characterize sub-ropes for long-term creep, a specific device needs to be designed, as standard hydraulic test machine cannot be occupied for very long durations. This led to the design and manufacture of a dedicated device to test these sub-ropes for creep of around 1 year, detail of conception can be found in the appendix.

3.4.1. Design choices

We have chosen to build a linear vertical system with a force return by pulley in order to limit the size of the masses and the floor surface area of the device. For budget reasons, we chose to make a one-piece module to test three ropes.

The pulleys impose a force on the jaws of the specimen (Figure 3-9). Under the main frame, two supports are provided to stabilize the structure laterally and distribute the load (See stress calculation).

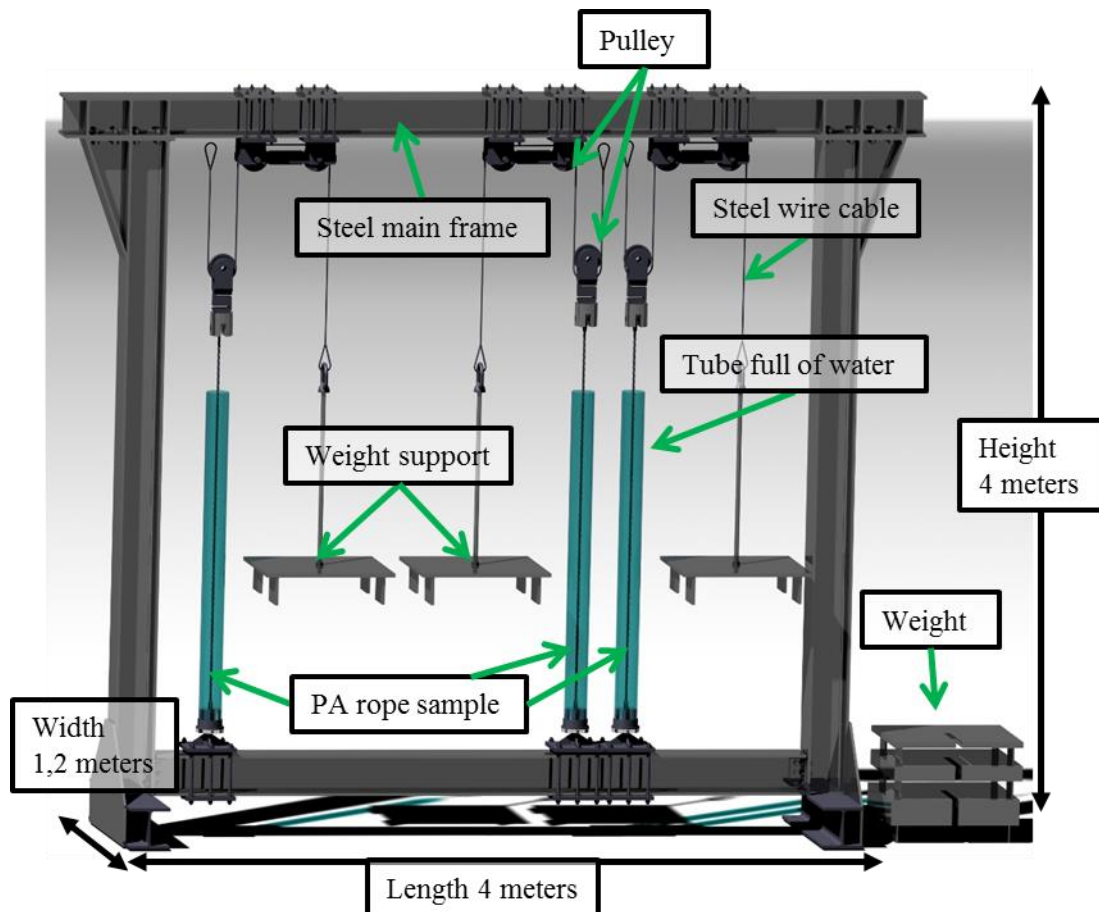


Figure 3-9. Design of the testing device for immersed creep behaviour of sub-ropes.

Different loads can be applied by the use of modular blocks that can be slide onto the supports. The tested specimens are fully immersed up to the top splice in

tubes full of tap water. The water is brought by a pump from a thermally controlled tank to a temperature around 23°C.

3.5. Long term creep tests

3.5.1. Material and experimental methods

3.5.1.1. Samples

The samples tested for the creep characterization are similar to the 4-ton sub-ropes described in Chapter 2, the length of the specimen and of the splice are quite different. The average length for these samples is 2 meters.



Figure 3-10. Long-term creep test set up.

3.5.1.2. Procedures

The creep test procedure is as follows:

- Lift the weights with a pallet truck
- Hang the cable to the jaws of the pulley in suspension.
- Attach the draw-wire displacement sensors to the central area of the rope.
- Pass the cable through the tube
- Anchor the rope in the lower jaws
- Fit the tube onto the jaw and screw it tight
- Put water into the tube
- Lower the masses with a pallet truck

- While the pallet truck is still below fix the weights and the support together

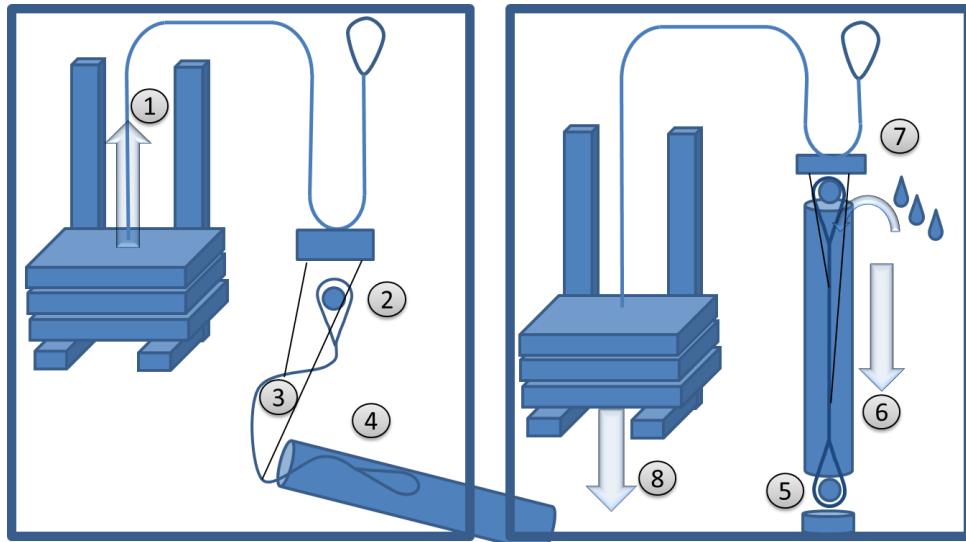


Figure 3-12. Setup of a creep test.

Before each test the rope is placed in water for 10h loaded with just weights carrying plate imposing a stress of 0.012 N/tex, which is very similar to the load at the end of bedding in of chapter 2 and close to the initial load of the yarn creep test. The strain reference is taken after the ten hours immersion.

Four creep tests were made with similar loads to yarn tests. The tests were made at stresses of 0,110, 0,175 and 0,200 N/tex. These represent approximately 25%, 38% and 50% of MBL. The duration of these tests is around half a month for SR_C01, 9 months for SR_C04B and 10 months for SR_C02 and SR_C03.

Name	Slot	Stress applied (N/Tex)	Load (in % of MBL)
SR_C01	1	0,200	50%
SR_C02	2	0.110	25%
SR_C03	3	0,175	38%
SR_C04B	1	0.062 (1h) – 0.012 (1h) – 0,200	15.5% (1h) – 3% (1h) – 50%

Table 3-1. Loading applied for the creep tests.

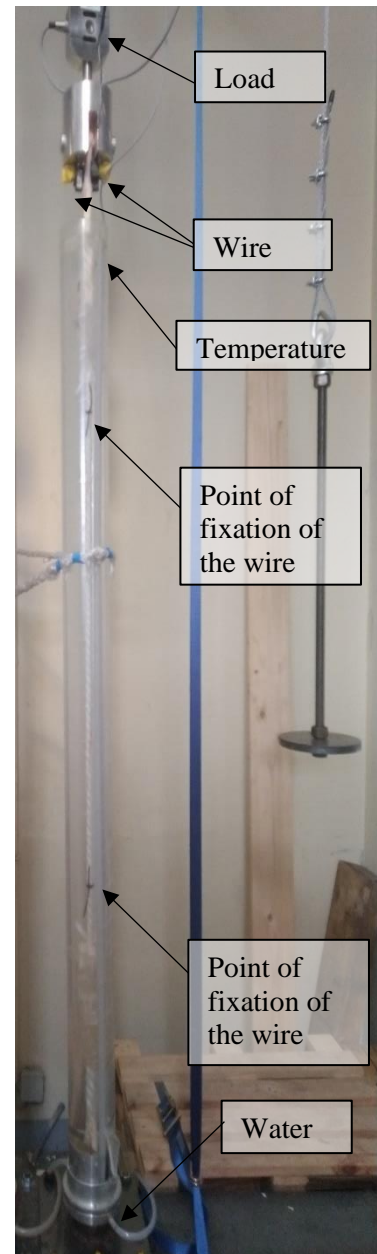


Figure 3-11. Close up of the measurement and acquisition setup.

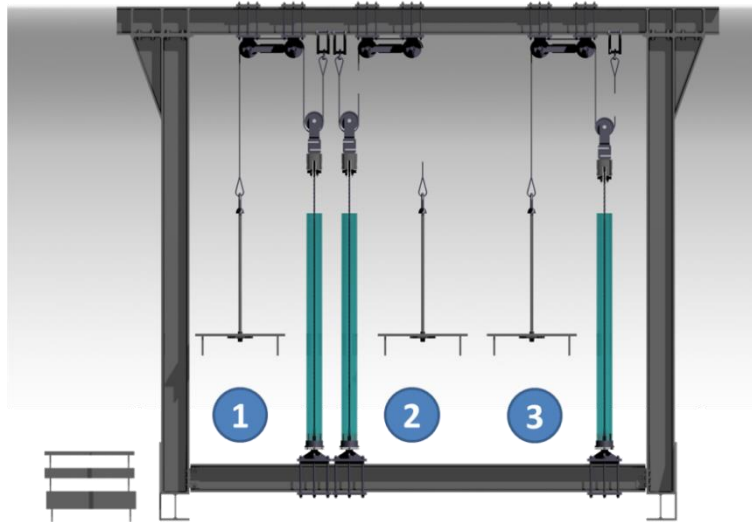


Figure 3-13. Slot position of the samples on the test bench.

The water temperature is controlled in a 150 L tank around 23°C^{+2} using three heaters (Eheim Jäger Termocontrol™ 2048 100Watt) then distributed to the three tubes. A temperature of 23°C was set as an average value for facilities in Brest for summer 2019. The temperature is measured at the top of each tube and in the main tank using A Class PT100 temperature sensors.

The stress is measured above each jaw by the load sensor (FSB251 3000 DaN from Tei technologies). Small changes occur at the start of the tests (around 3% of load) but stop evolving after a few days. The load changed once for the sample SR_Co2 in the 2nd slot when the test SR_Co4B was started on the 1st slot, provoking an increase of the load of about 2%).

The sample strains are measured by 2 wire sensors for each rope (WPS-500-MK30-P10 and WPS-750-MK30-P10) tied to the rope at two points with 2mm diameter Sandow. A minimal distance of at least 100 mm from the end of the splice was respected so as not to be affected by it. The average length between the two measurement points is around 900 mm.

The temperature evolution of the water in the tube is quite stable around 23°C as shown on the Table 3-2 and on Figure 3-14.

Temperature ($^{\circ}\text{C}$)	Mean value	Minimal	Maximal	Standard deviation
SR_C01	21,92	20,63	23,98	0,40
SR_C02	22,90	19,48	26,01	1,01
SR_C03	22,86	19,48	26,54	1,01
SR_C04B	23,36	20,62	26,06	0,94
Tank	23,02	19,71	25,85	0,96

Table 3-2. Temperature evolution in $^{\circ}\text{C}$ during creep tests.

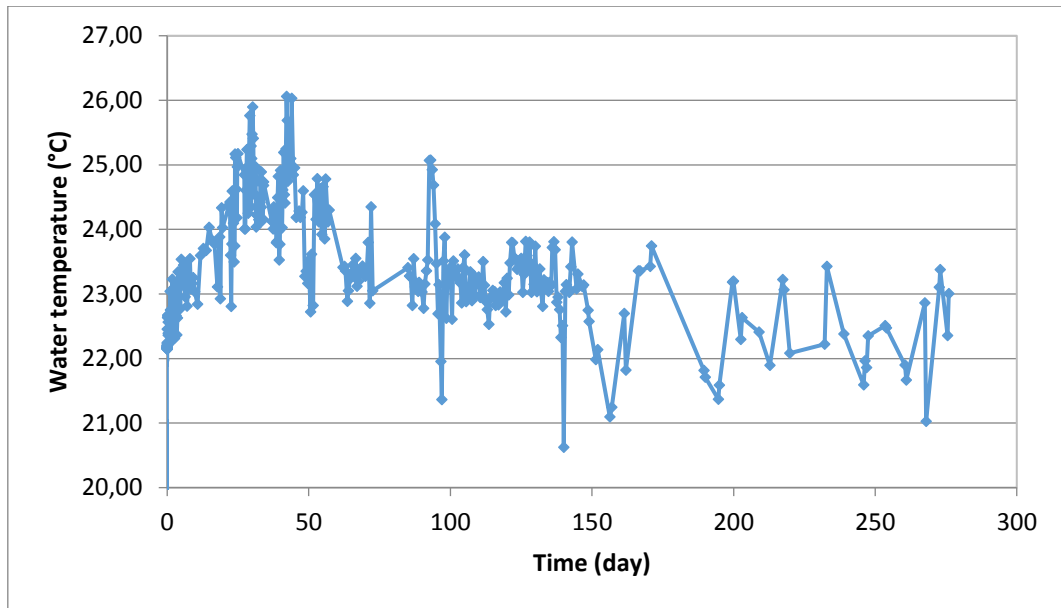


Figure 3-14. Temperature evolution of the water on top of a tube (for SR_C04B).

3.5.2. Results

Figure 3-15 shows the creep curves obtained on sub-ropes tested as described in Table 3-1.

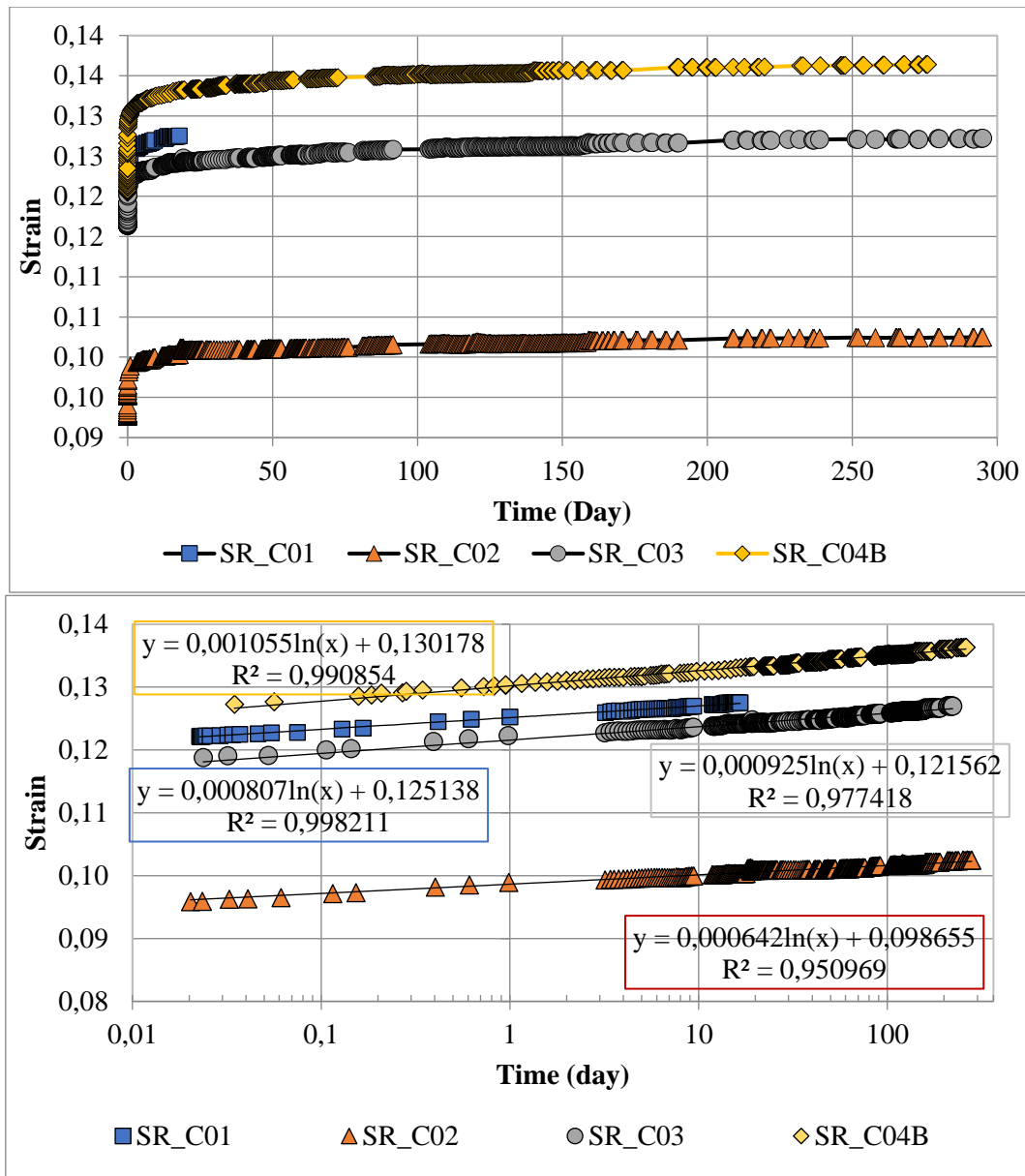


Figure 3-15. Long-term creep tests result for sub-ropes of 4-ton MBL.

The strain follows a logarithmic evolution with time, test SR_Co2 experiencing the lowest load presents the lowest creep rate at 0.156%/decade, while at higher load the creep rate is around 0.217%/decade. The difference between the test SR_Co1 and SRCo4B tested at the same load is unexpected, as the bedding in did not reduce the strain and strain rate but instead increased them (from the initial strain before bedding in).

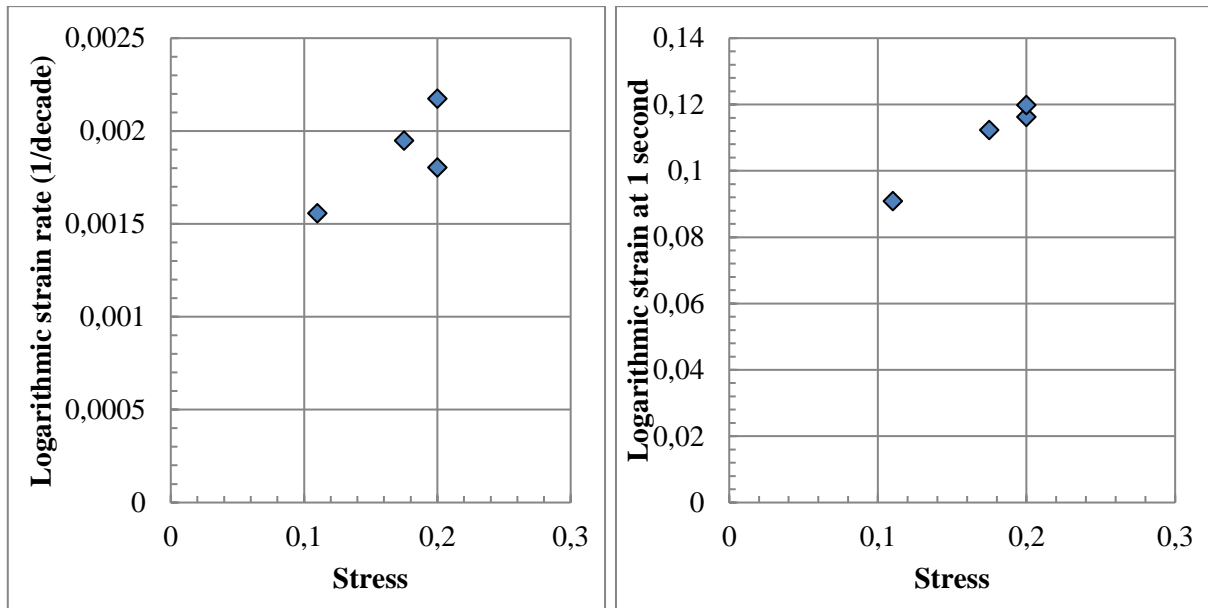


Figure 3-16. Logarithmic creep rate (left) and strain after one second of creep (right) in function of creep stress on wet sub-ropes.

For the sub-ropes, logarithmic strain rate and strain after one second both increase with stress. The evolution seems linear, but we do not have enough samples to accurately describe it.

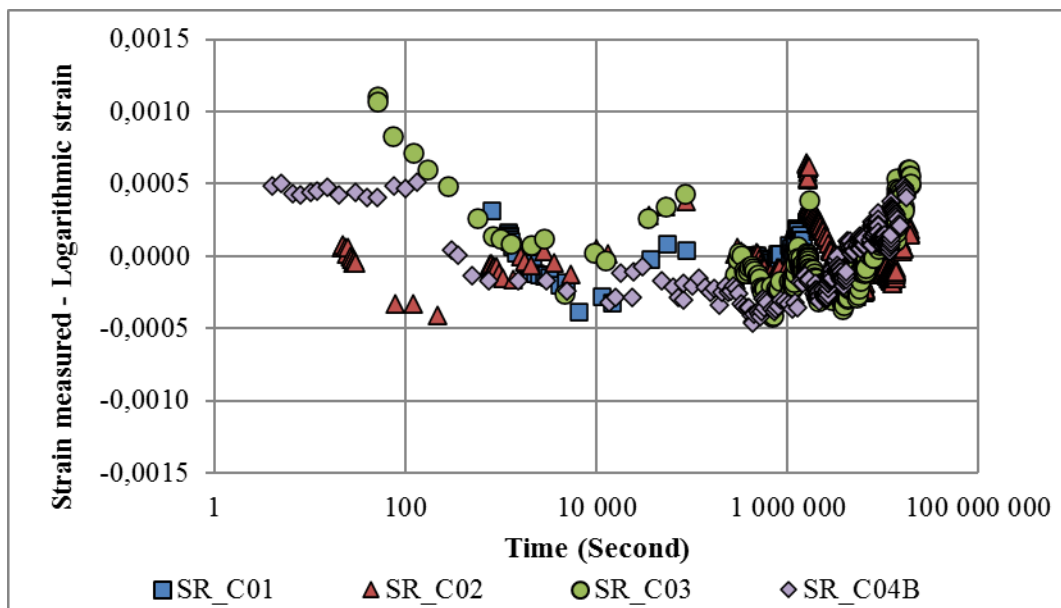


Figure 3-17. Scatter from the evaluated logarithmic strain.

The logarithmic fit shows quite a good description of the test within a scatter of 0.05% strain. Some small variability is present before 200 seconds as the first part is still influenced by the loading.

For the SR_C04B test, a similar bedding in to the one made in Chapter 2 was performed, to be able to compare the strains. Figure 3-18 presents the creep response obtained for this sample with the initial strain taken after the bedding in.

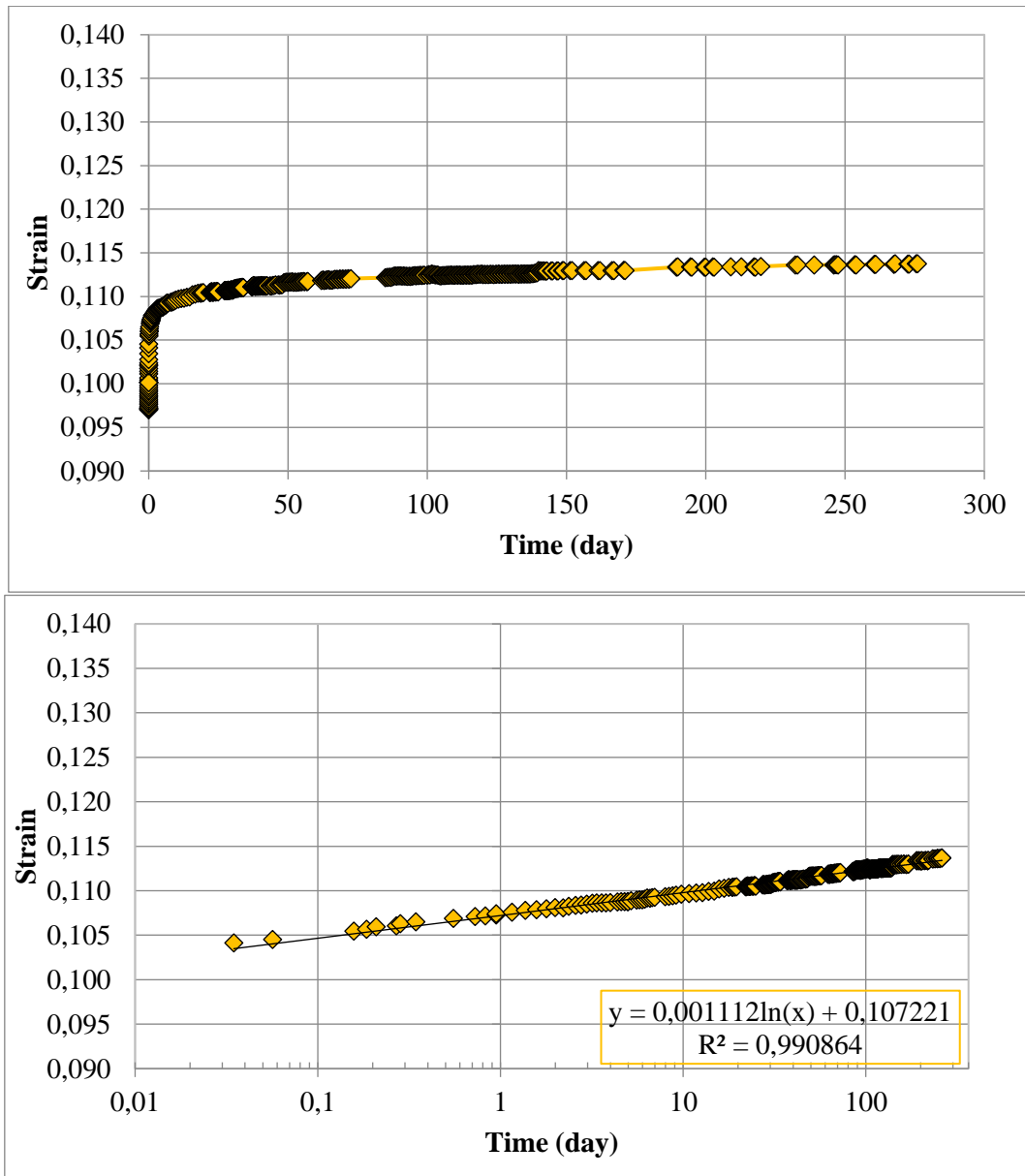


Figure 3-18. Long-term creep test result for sub-rope of 4-ton MBL for sample SR_C04B with initial strain chosen after bedding in.

By comparing the test SR_Co4B responses before and after the bedding in, we have around 2% of strain difference between the two. The creep rate evolution is similar compared to the difference with the other test SR_Co1 at the same load.

The creep tests on 4 ton sub-ropes give us an idea of the change in length of the rope as a function of the time. We saw no stabilization of the length during the hundred days' duration of these tests, however we observed a logarithmic evolution of the strain meaning that the longer the creep the less important the strain rate. These tests show a creep rate between 0.15%/decade and 0.22%/decade which is not very far from the values found on polyester at 30% of MBL being between 0.066 and 0.119%/decade (*Del Vecchio, 1992*).

3.6. Comparison between the results on Yarns and on 4-ton ropes

As the creep tests on yarns and sub-ropes were performed for similar stresses, it seems possible to compare the creep responses for the two scales (Figure 3-19, Figure 3-20, Figure 3-21).

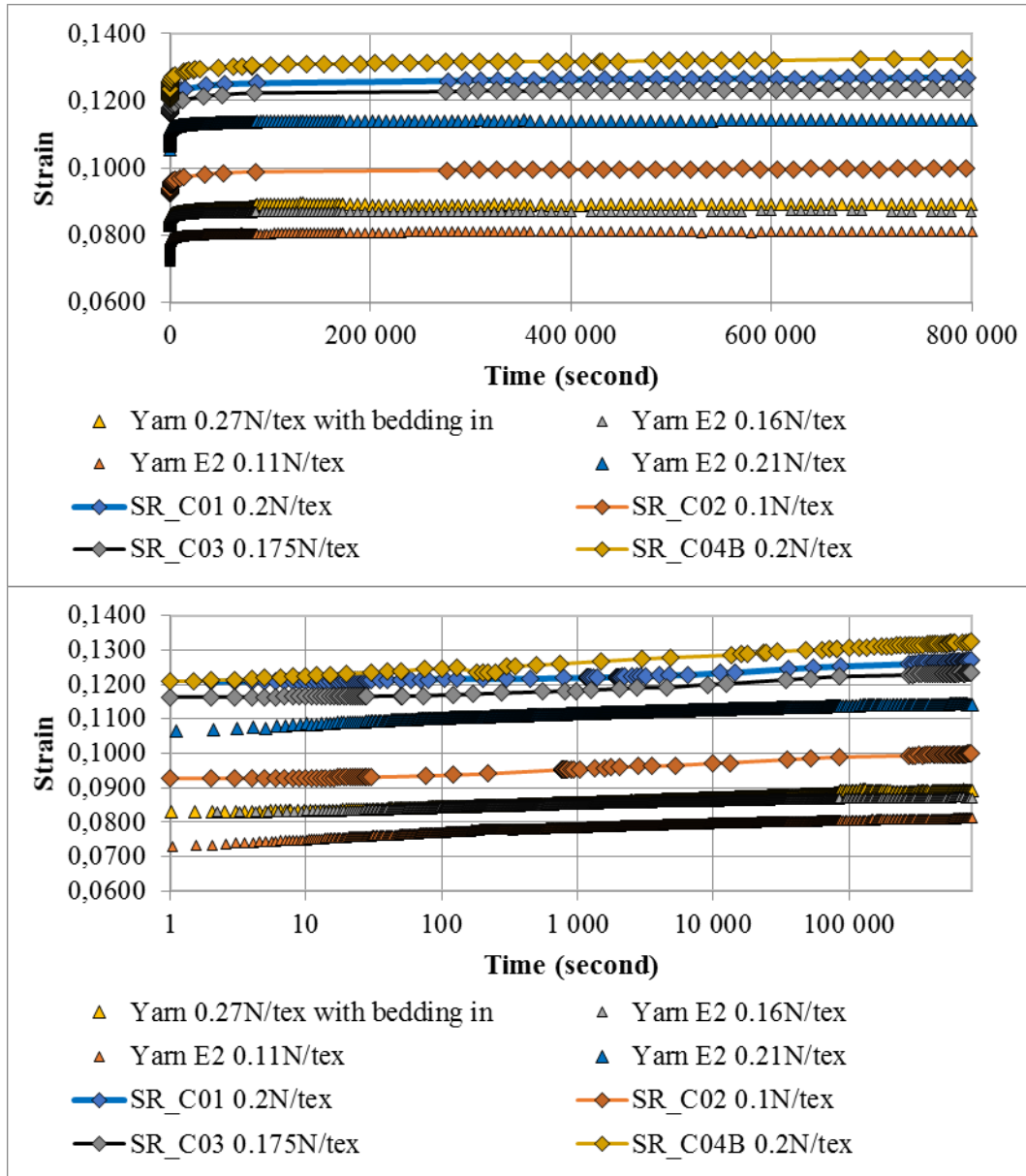


Figure 3-19. Comparison between creep tests on yarn and sub-ropes.

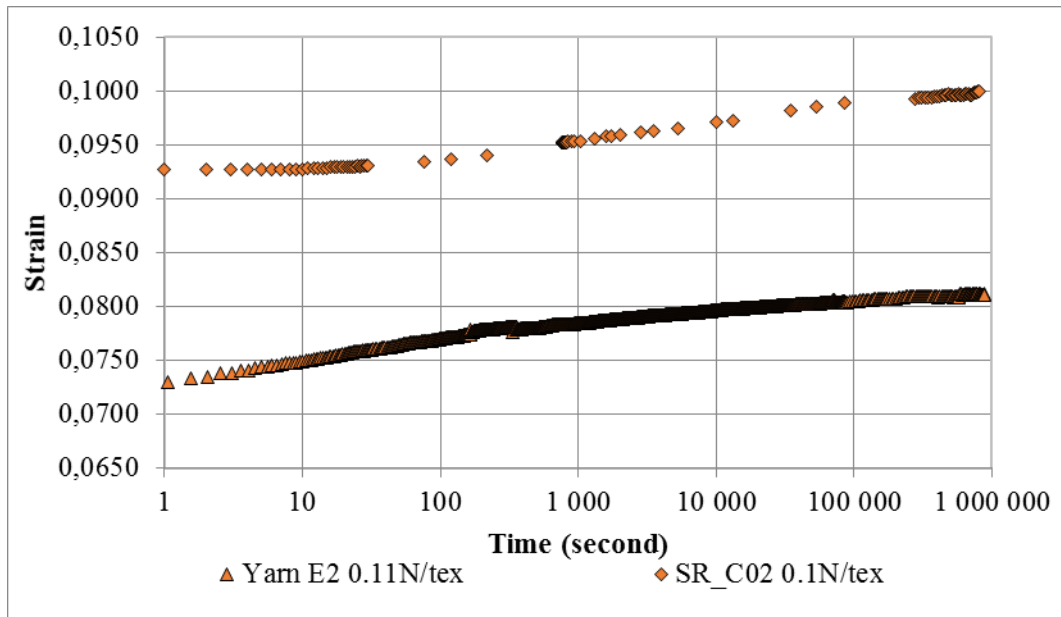


Figure 3-20. Comparison between creep tests on yarn and sub-ropes for a stress around 0.1 N/tex.

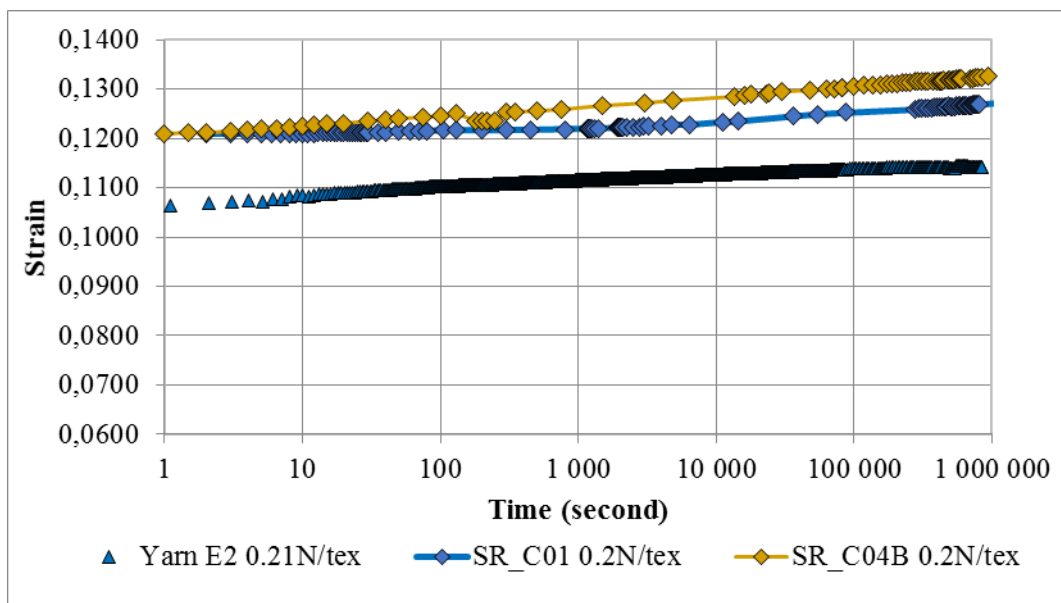


Figure 3-21. Comparison between creep tests on yarn and sub-ropes for a stress around 0.2 N/tex

From a first evaluation the total strain and creep rate is higher for sub-ropes than for yarns. This can be explained by the construction of the rope as it allows extension due to changes in its conformation, and from the fact that there are more fibers in the rope and therefore more probability that the load is not equally distributed. However, the creep rate values are in a similar range, and the value for the rope at the minimum stress is indeed close to the one of the yarn (Figure 3-22).

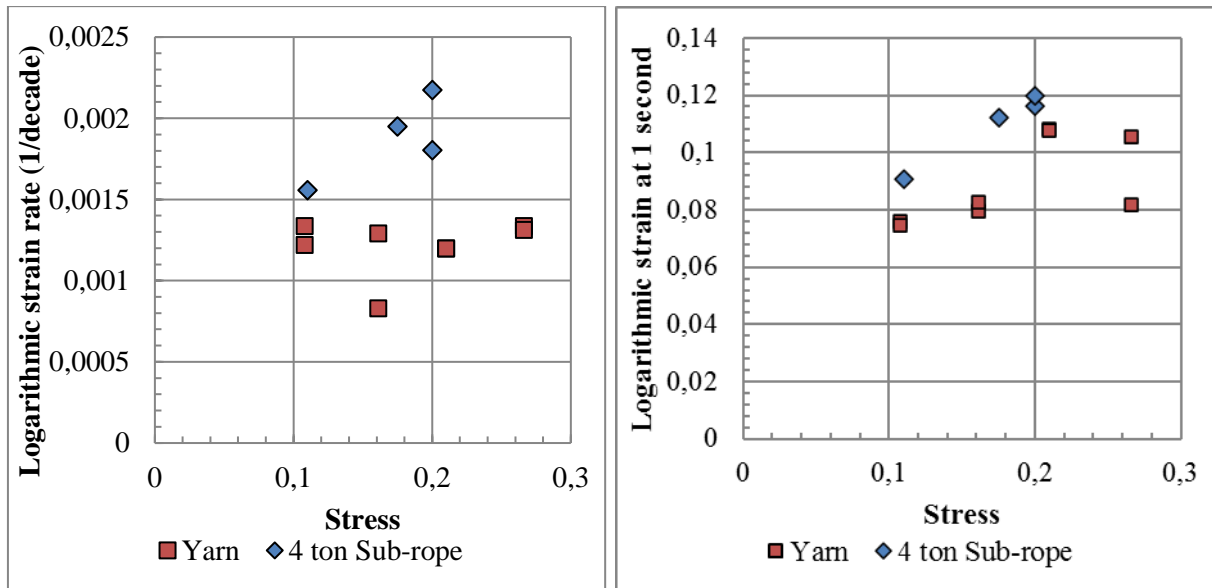


Figure 3-22. Comparison of logarithmic strain rate between creep tests on yarn and sub-ropes.

3.7. Comparison with the multi-creep test

Figure 3-23 presents two tests made for a similar load of 0.11 N/tex. The SR46 tests have however a bedding in at 0.06 N/tex presented in chapter 2, and so do not have the same reference strain.

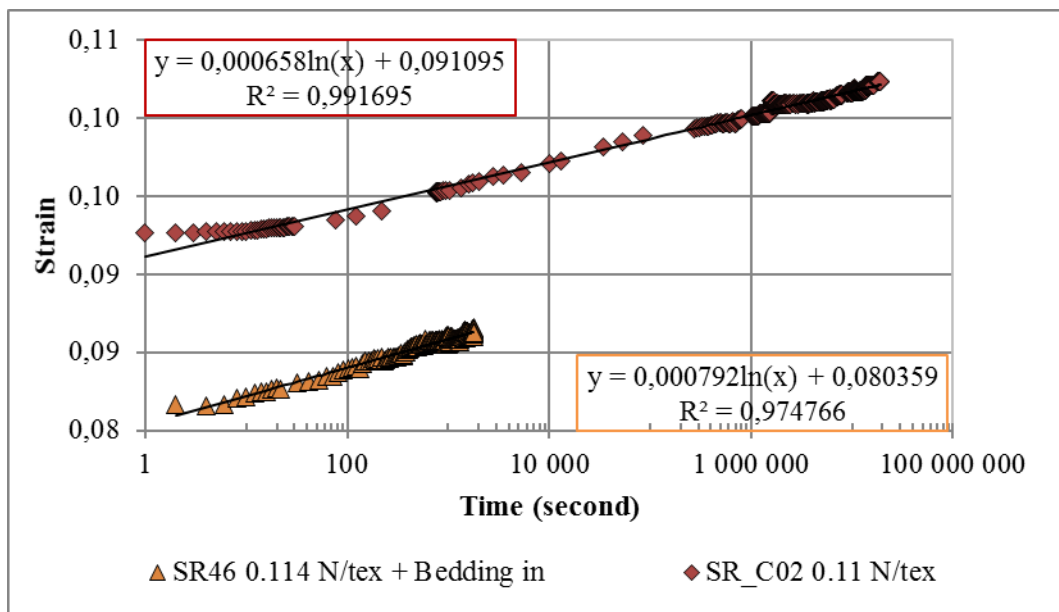


Figure 3-23. Comparison of the evolution of strain between creep test and multi-creep test.

Nevertheless, we can compare the trends of the tests. As the loading is more progressive in the multi creep tests, it is logical that the stabilization is quicker. Furthermore, the tendency is conserved during the hundred of days of the creep test.

This shows that a 30 minute test gives a good indication of the creep evolution observed for a longer period.

3.8. Summary

This chapter describes the behavior of yarns and sub-ropes subjected to long-term creep. Yarn creep tests have shown effects of the stress from 0.11 N/tex to 0.27 N/tex on the initial strain after the loading, but the stress amplitude seems to have only a small effect, if any, on the strain rate. The creep rate follows a logarithmic evolution which seems to saturate at lower load. Typical values range from 0.08%/decade to 0.13%/decade.

A long-term creep bench was designed and manufactured at Ensta Bretagne, and showed its usefulness in providing results from four tests performed on sub-ropes lasting up to 10 months.

The sub-rope creep tests have shown a logarithmic behavior of the strain rate, with values ranging from 0.13%/decade to 0.22%/decade. This creep rate is in the same range as polyester, and validates suggests that from a creep point of view these polyamide 6 ropes can be used in permanent moorings.

Comparing yarns and sub-ropes showed different creep rate behavior and underlines the fact that testing sub-ropes is necessary to obtain results closer to the in-service behaviour.

Finally, a comparison with the multi-creep test showed that short creep tests seem sufficient to predict the long-term creep evolution, which is an interesting result. However, recovery tests after a long-term creep tests would also be of interest and could be investigated in a future study.

3.9. References

- Bles, G., Nowacki, W.K. and Tourabi, A., 2009. Experimental study of the cyclic visco-elasto-plastic behaviour of a polyamide fibre strap. *International Journal of Solids and Structures*, 46(13), pp.2693-2705.
- Chimisso, F.E., 2009. Some experimental results regarding creep behavior on synthetic materials used to produce offshore mooring ropes. *Strain*, 3(3.24), pp.12-67.
- da Costa Mattos, H.S. and Chimisso, F.E.G., 2011. Modelling creep tests in HMPE fibres used in ultra-deep-sea mooring ropes. *International Journal of Solids and Structures*, 48(1), pp.144-152.
- Davies, P., Huard, G., Grosjean, F. and Francois, M., 2000, January. Creep and relaxation of polyester mooring lines. In *Offshore Technology Conference*. Offshore Technology Conference.
- Del Vecchio, C.J.M., 1992. *Light weight materials for deep water moorings* (Doctoral dissertation, University of Reading).
- de Normalización, C.E., 2005. *Eurocode 3: Design of Steel Structures. General Rules and Rules for Buildings*. Comité Europeo de Normalización.
- Document Renault, ETUDE DU COMPORTEMENT AUX CHOCS DES MATERIAUX ORGANIQUES (1990)*
https://pierre-roubinet.pagesperso-orange.fr/compositcar/etude_choc.htm
- Fancey, K.S., 2005. A mechanical model for creep, recovery and stress relaxation in polymeric materials. *Journal of materials science*, 40(18), pp.4827-4831.
- Hunt, D.G. and Darlington, M.W., 1978. Accurate measurement of creep of nylon-6, 6 at constant temperature and humidity. *Polymer*, 19(8), pp.977-983.
- Hunt, D.G. and Darlington, M.W., 1979. Prediction of creep of nylon-6, 6 at constant stress, temperature and moisture content. *Polymer*, 20(2), pp.241-246.
- Hunt, D.G. and Darlington, M.W., 1980. Creep of nylon-6, 6 during concurrent moisture changes. *Polymer*, 21(5), pp.502-508.
- Humeau, C., 2017. *Contribution to the study of coupling between moisture diffusion and mechanical stress, in high performance marine materials* (Doctoral dissertation, Nantes).
- McKenna, H.A., Hearle, J.W. and O'Hear, N., 2004. *Handbook of fibre rope technology*. Elsevier.
- Muzeau, J.P., 2012. *Constructions métalliques-Moyens d'assemblage*. Technique de l'ingénieur.
- Pal, S.K., Thakare, V.B. and Singh, G., 2007. Creep behaviour of braided cordages made of high performance fibres for aerospace applications.

Chapter 4: Durability

This part describes a study of the fatigue characterization of polyamide mooring ropes for floating wind turbines. Polyester ropes are usually favoured for offshore oil and gas platform station-keeping, but under some conditions, they are too stiff for wind turbine moorings, and polyamide may be a suitable alternative. While early studies on fatigue of braided nylon ropes showed very short lifetimes, some recent results have indicated that it is possible to significantly enhance durability performances by modifying rope construction and improving fibre coatings.

In this chapter, yarn-on-yarn abrasion testing is used first to evaluate the abrasion performance of a new yarn coating. A significant lifetime enhancement was noted. Fatigue testing of ropes was then performed on two sizes of rope. Results confirm that excellent fatigue lifetimes can be obtained, superior to those for steel chain. Finally, failed yarn and rope samples were examined by microscopy, in order to improve the understanding of the mechanisms leading to failure under fatigue.

Keywords: Fatigue, Rope, Nylon, Mooring, Water, Floating wind turbine

Table of content

4. Durability	129
4.1. Context.....	129
4.1.1. Objective	131
4.1.2. Difficulties.....	131
4.1.3. Strategy.....	132
4.2. Yarn on Yarn abrasion tests.....	133
4.2.1. Material and methods	133
4.2.2. Results	134
4.2.3. Persistence test	136
4.2.4. Summary	138
4.3. Fatigue tests	139
4.3.1. 4T sub-rope fatigue tests	139
4.3.2. 8T sub-rope fatigue tests	146
4.3.3. Fatigue test results for Heat Build up.....	154
4.3.4. Comparison between 4T and 8T sub-ropes.....	155
4.3.5. Summary	157
4.4. Yarn and rope failure mechanisms	158
4.4.1. Reference material.....	158
4.4.2. Yarn samples after Yarn on Yarn abrasion tests	158
4.4.3. Rope inspection after fatigue testing.....	159
4.5. Summary.....	161
4.6. References	162

4. Durability

4.1. Context

Polyester fibre ropes have been used for mooring deep-water offshore platforms for many years now (*De Pellegrim, 1999; Bugg, 2004; Haslum, 2005*) and extensive fatigue testing has shown that their fatigue performance is better than equivalent steel components (*Banfield, 2000*). The idea of using nylon ropes for long-term mooring lines is relatively new, as there is little available knowledge on the durability behaviour of such structures. If synthetic fibre rope mooring lines are to be used with confidence on floating wind turbines it is essential to have a better knowledge and understanding of their long term durability. Polyamide 6 (nylon) fibres are a good candidate for mooring line applications because of experience from previous use in other marine applications, low price and high breaking strain (up to 25%).

It is first instructive to examine the fatigue behaviour of individual nylon fibres. Bunsell developed a single fibre tensile test machine (*Bunsell, 1971a*), which was used in several fatigue test programmes on nylon (*Bunsell, 1971b; Ramirez, 2006; Colombar, 2006*), polyester (*Le Clerc, 2007; Lechat, 2006*) and higher stiffness (*Lafitte, 1982; Davies, 2010*) fibres. It is worth noting that the fatigue behavior mechanisms are the same for PA6.6 and Polyester fibers (*Bunsell, 2009*). Both fibres show distinctive failure morphology; fatigue cracks originate at the surface or just below it and run within the fibre in the axial direction producing long characteristic fatigue cracks. In these studies, 25-30 fibres are tested for each median value, and tests are run dry. Table 4-1 shows some published values for nylon 66 and polyester fibres obtained in the same laboratory.

Overall, the PET lifetimes appear longer, for individual test series such as those with a load range 0-75%, the median lifetimes for PET (*Le Clerc, 2004*) and nylon (*Herrera, 2004*) are very similar. It should also be underlined that any comparison between nylon and polyester is complicated by the much lower stiffness of the former. Moreover, all the tests reported in those fibre studies were run under load control; if strain control had been applied the nylon results would probably exceed those for polyester. Finally, it should be noted that it is necessary to apply very large load ranges to obtain failures, well above the usual service loads, indicating that the intrinsic fatigue strength of both kinds of fibres is high.

Load range, % break load	Polyester	Nylon 66	Source
0-70	506	-	Le Clerc (2004)
0-75	212	86	
0-80	131	-	
0-75	-	214	Herrera (2004)
0-80	-	151	
0-85	434	92	
0-90	106	-	

Table 4-1. Median lifetimes (in kcycles) for tensile fatigue tests on single fibres.

When ropes rather than single fibres are considered, studies on braided nylon 6 ropes in the 1980's (*Kenney, 1985; Mandell 1987*) have shown relatively poor fatigue performance compared to polyester, which provided little incentive for developing nylon mooring ropes. Indeed, nylon single point moorings used offshore are typically changed every one or two years. A study published by OCIMF (the Oil Companies International Marine Forum) in 1982 presented results from tests on small and large nylon rope hawsers, both new and after service. These revealed that a semi-log relationship of the type:

$$N = e^{A(100-L)}$$

could be used to represent the data, with N the cycles to failure, A an empirical parameter and L the maximum load as a percentage of break load. The empirical parameter A was found to be in the range 0.14 to 0.16 for ropes tested during that study. For a wet rope this corresponded to only a few hundred cycles at 50% of the break load.

Several other studies in the 1980's and 1990's generated fatigue data on braided nylon ropes. For example, *Seo et al. (1997)* examined wear and fatigue of nylon and polyester fibres and ropes. They obtained yarn-on-yarn (YoY) abrasion data which indicated that while nylon 66 fibres showed better durability than polyester when dry, when tests were run wet, the nylon 66 showed significant reduction in wear resistance whereas polyester did not. They also concluded that comparisons of YoY wear between nylon and polyester vary significantly with the loading condition. Nylons are superior at very high tensions whereas at low tensions polyester lifetimes exceed those of nylon. There is a widely perceived idea that polyester ropes have superior fatigue resistance to nylon ropes.

Quite recently, however, *Ridge et al. (2010; Banfield, 2017)* have shown significantly improved fatigue results for twisted nylon ropes. Those authors qualified these ropes as ideal for wave energy convertor moorings, and *Flory et al. (2016)* also discussed these applications. The two major differences compared to the earlier

fatigue works, were the use of twisted ropes with long lay lengths rather than braids, and the application of improved fibre coatings. Both can help to reduce internal abrasion, which was shown by Mandell to be a major failure mechanism during low-load, high-cycle fatigue (Mandell, 1987). At higher loads, creep rupture is the main concern, and this depends on the polymer structure rather than on the fibre interactions.

There are few other relevant and recent results for these materials, but Weller et al. (2015) examined a 44 mm diameter parallel twisted strand nylon 6 rope that had been tested at sea for 18 months on a wave energy buoy, where they showed the importance of loading history and operating conditions on nylon performance.

Indeed, as Pham et al (2019) conclude in a very recent study “a comprehensive study on the critical fatigue damage mechanisms of nylon should be the topic of future work.” It is **therefore essential to generate further data on polyamide mooring ropes, in order to validate their use for this application**. It is also of interest to see how these improved nylon rope constructions compare with the polyester ropes currently in use offshore.

4.1.1. Objective

The **goal** of this section of the present study is to provide a better knowledge and **understanding** of the **fatigue damage** of twisted polyamide ropes. The goal is also to produce a quantitative evaluation of the fatigue lifetime of this type of mooring ropes and to **compare it to other mooring line options**, in order to help designing mooring lines for floating wind turbine.

4.1.2. Difficulties

The difficulties in testing twisted nylon ropes come from the fact that they are quite stretchable with more than 25% strain at break. The long lay length also imposes long samples, due to the length of splices. This means that this type of sample needs a special test bench with a long stroke, a large overall length, high load capacity and quite fast cylinder stroke speed.

Moreover, fatigue tests are long to perform, particularly when the cycling period is that of waves, around 10 seconds. As a result, equipment availability is also an issue.

Nylon behavior and abrasion resistance are more sensitive to water than polyester, so a water system should be put in place to keep the sample fully saturated during the duration of the test, to be relevant for service conditions.

4.1.3. Strategy

First, the influence of fibre coating is evaluated, by yarn-on-yarn abrasion tests. This coating was selected by our Polyamoor partner BEXCO. This test enables the coating to be studied on small samples to see if it improves abrasion resistance, or if we need to change it. If the test shows good results, we can pursue to the next step with quasi-static tests on ropes, to get an idea of the load range we will need for fatigue testing. Once we have these values, a first test at high load range is to be performed as a comparison to the results of *Ridge (2010)* in order to validate the construction of the rope. If the result is satisfactory, a complete fatigue characterization is to be started. Finally, to confirm that abrasion is indeed the main failure mechanism for fatigue loading, optical and SEM (Scanning Electron Microscopy) examinations are carried out on broken samples.

4.2. Yarn on Yarn abrasion tests

4.2.1. Material and methods

The YoY abrasion test was developed by an Oil Companies International Marine Forum (OCIMF) study following failures on large single point mooring hawsers in the early 1980s. Tests have shown that internal abrasion was the principal cause of strength loss and failure in these fiber ropes in cyclic load tension. This led to the adoption of the test as a standard test method by the OCIMF, Cordage Institute (CI) and ASTM, this method is also referenced in other industry guidelines. The CI then established a definition and guideline for marine grade yarn for use in mooring and towing hawsers, represented by a minimum value of cycles to be respected at a given load.

Yarn-on-yarn abrasion tests were performed as described in the *CI (Cordage Institute) requirements (2009; Flory, 2013)* and *ASTM D 6611 (2007)*. This test is the standard method for testing inter-yarn abrasion of synthetic fibers and provides a qualitative value of the abrasion resistance. The only difference from the standard test procedure was that tests were performed in natural sea water here, rather than the tap water defined in the standards.

These tests were carried out with the configuration presented in Figure 4-1. A yarn is twisted with itself (by turning it by 3.5 turns) between three pulleys. At one end of the yarn a weight is attached to apply a constant tension, and at the other end a motor drives the cable back and forth with a 1 Hz frequency. The test runs until the yarn breaks due to abrasion in the twisted region. Different weights are applied to vary the applied tension.

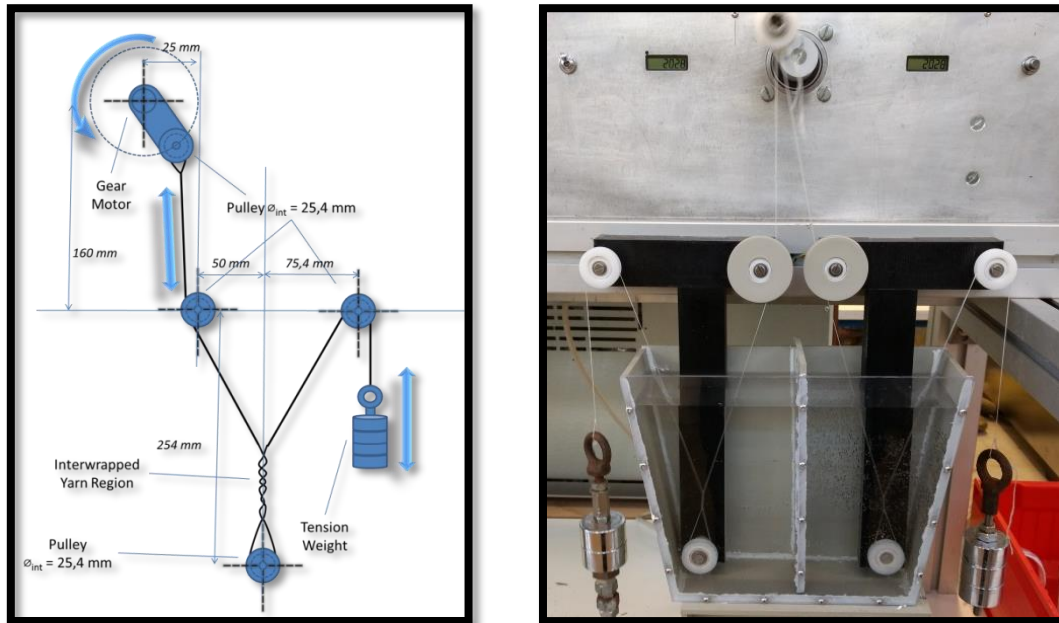


Figure 4-1. Yarn on yarn test set-up (left) and picture (right).

The inter-wrapped region is kept in filtered sea water throughout the test until failure. The yarns used are made by Nexis fibers with a linear weight of 188 tex (g/km), provided with and without a proprietary coating. Hence two types of specimens have been tested with this test:

- yarn without coating.
- yarn with a special marine finish applied by the ropemaker.

4.2.2. Results

Results are given as cycles to failure versus the load or specific stress, expressed in grams per tex. Contrary to the standard fatigue graph, the classical yarn on yarn results are presented with stress on the X-axis and the number of cycles to failure on the Y-axis.

Yarn on yarn abrasion tests were performed up to failure, which occurred in the inter-wrapped section of the yarn in all cases reported on Figure 4-2. On this curve, each point represents 3 to 8 tests for each applied stress level. The error bars represent the minimum and maximum numbers of cycles found at each load. The dashed lines show a linear best fit on the semi-log scale. The continuous red line corresponds to a limit given by a Cordage Institute guidance document (2009), which recommends a minimum lifetime for each stress level for offshore hawsers.

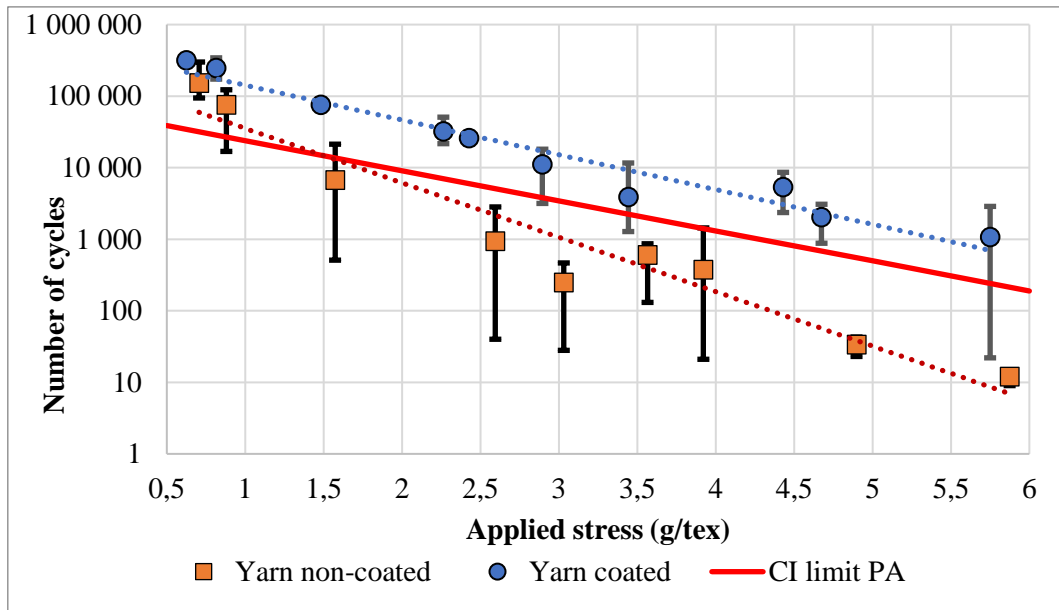


Figure 4-2. Yarn on yarn results for uncoated and coated polyamide 6 yarns.

Cycles to failure are significantly higher for coated yarn samples, with a reduced scatter compared to uncoated yarns. The coating is therefore necessary in order to satisfy the criterion given by the CI document (2009) for nylon yarn, for fiber usage in permanent mooring applications.

A set of yarn-on-yarn abrasion tests was also performed on a 220-tex polyester fibre yarn with a marine finish, currently used in offshore mooring line applications. Figure 4-3 shows the comparison between the polyester and the nylon. These tests were all performed on the same test machine, in natural seawater, following the same test procedure. It is apparent that the yarn-on-yarn abrasion lifetimes of the coated nylon yarn are similar to those of this polyester yarn.

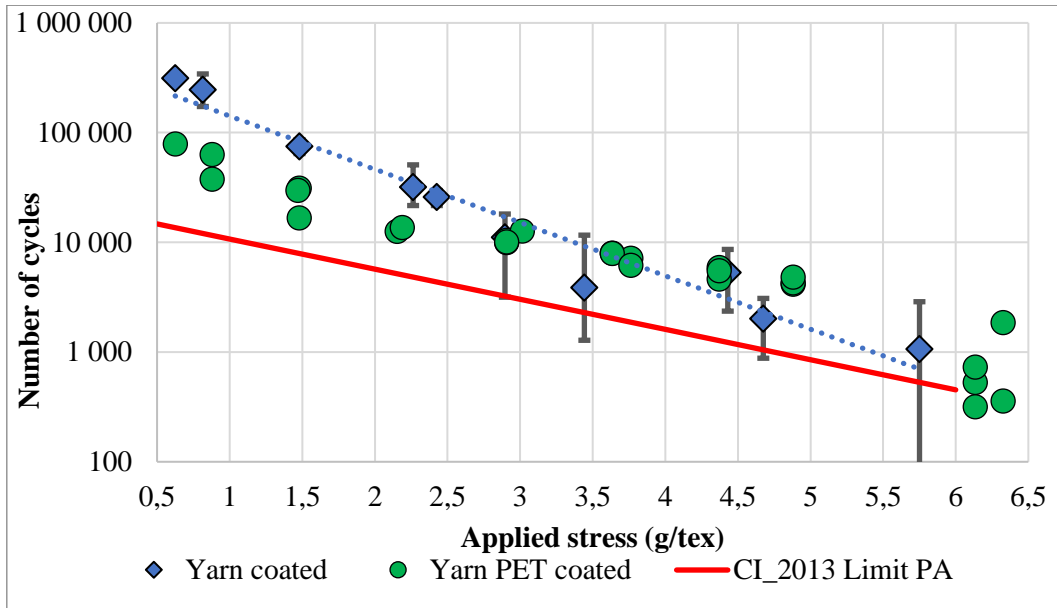


Figure 4-3. Comparison between YoY abrasion test results for nylon 6 and polyester (PET) yarns.

4.2.3. Persistence test

Some coating persistence tests were also performed, following the suggestion of Michel François (Bureau Veritas). This test is being studied within the ISO working group.

The aim of this study is to evaluate the ability of the coating to remain on the fiber surface during the service lifetime of a synthetic rope. To do so, a washing process is proposed to simulate, in an accelerated way, the effect of the environment that should remove the coating.

The proposed method is based on a water-bath ultrasonic cleaner; it involves the following steps:

- Wash the polyamide yarn in an ultrasonic cleaner with demineralized water for 8 hours.
- No other samples should be put in the same bath and the fibre should be in direct contact with the water. The test frequency should be 40 kHz or lower. The water bath should be degassed prior to the test for 5 -10 minutes. Also, measures should be taken to prevent the water temperature increasing more than 20°C during the test.
- Then the yarn should be tested in accordance with ASTM D 6611.

The results from these tests are shown on Figure 4-4 below.

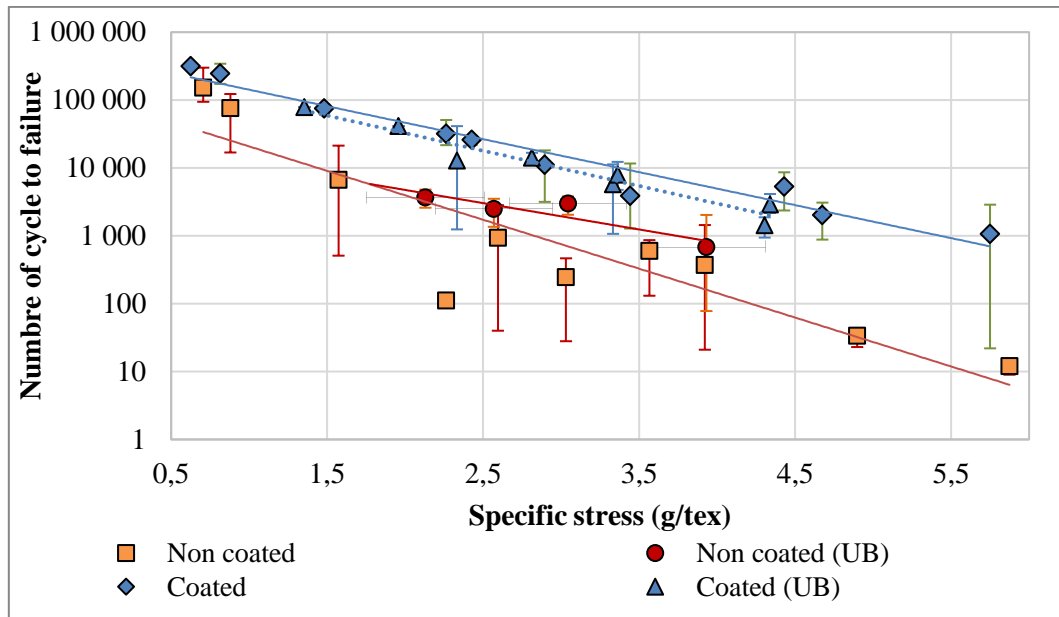


Figure 4-4. Comparison between YoY abrasion test results for nylon 6 before (non-coated and coated) and after ultrasonic bath (non-coated (UB) and coated (UB), respectively).

We see no effect of this washing treatment on the coated yarn as the tendencies stay the same (coated and coated (UB) on Figure 4-4). There appears to be a small effect on the non-coated sample as there is a slight increase in lifetime for these samples (non-coated and non-coated (UB) on Figure 4-4).

The reason for this effect may come from the fact that when the non-coated samples are placed in the ultrasonic bath, they tend to curl and retract on themselves, changing their conformation. The yarn in the ultrasonic bath is shown below in Figure 4-5, and it may be this physical change which affects the abrasion resistance after washing.



Figure 4-5. Non-coated yarn after the ultrasonic bath after drying (a) and in water (b).

4.2.4. Summary

The main conclusion from these test results is that addition of this special BEXCO's coating to yarns results in an increase in lifetime by one or two decades. The coating enables this yarn to pass from below to above the CI limit and to achieve similar performance to those of a polyester yarn with marine finish. Given this promising improvement, a set of rope specimens was then prepared from these coated yarns.

The washing tests show no degradation of the coating, suggesting that it is well bonded to the fibres.

4.3. Fatigue tests

4.3.1. 4T sub-rope fatigue tests

4.3.1.1. Experiments

4.3.1.1.1. Samples

The 4T samples used for fatigue tests are almost the same as the PA6 sub-ropes used for the model characterisation in chapter 2.4.1, with the parameters shown in Figure 4-6 below. The only difference is in the splicing procedure, as a longer splice with a smoother decrease of size from the splice to the useful length was employed for the fatigue cyclic tests.

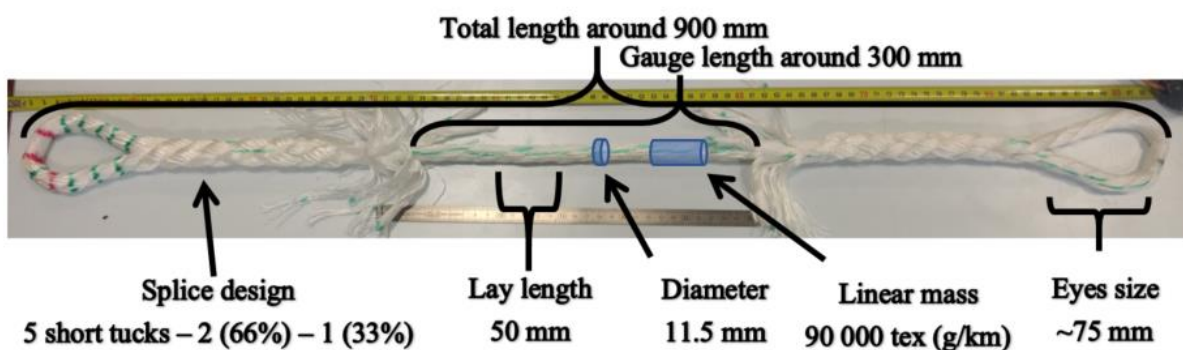


Figure 4-6. Sample dimensions for fatigue testing on 4-ton sub-ropes (sample called SR39).

4.3.1.1.2. Test equipment

As for the 4T samples tested in the chapter 2, the specimens were tested on a Servotest™ hydraulic machine with a cylinder stroke of 600 mm, and a maximal quasi-static speed of 100 mm/s. No strain has been measured during the test due to the presence of a plastic cylinder around the rope to allow infrared temperature measurement (Figure 4-7) presented in chapter 5. The loading pin diameter was 35 mm.



Figure 4-7. 4-tons sub-rope during a fatigue test.

4.3.1.1.3. Protocols

The cycle amplitude was between $0.01N/tex$ and the maximum value, this results in an R ratio around 0.035. The full loading cycles for each specimen are described in section 5.3.1.3.

The frequencies are similar to those of waves, around 0.1 Hz. At the start of the test around 10 cycles are needed for the machine control program to get to the set value, (Figure 4-8).

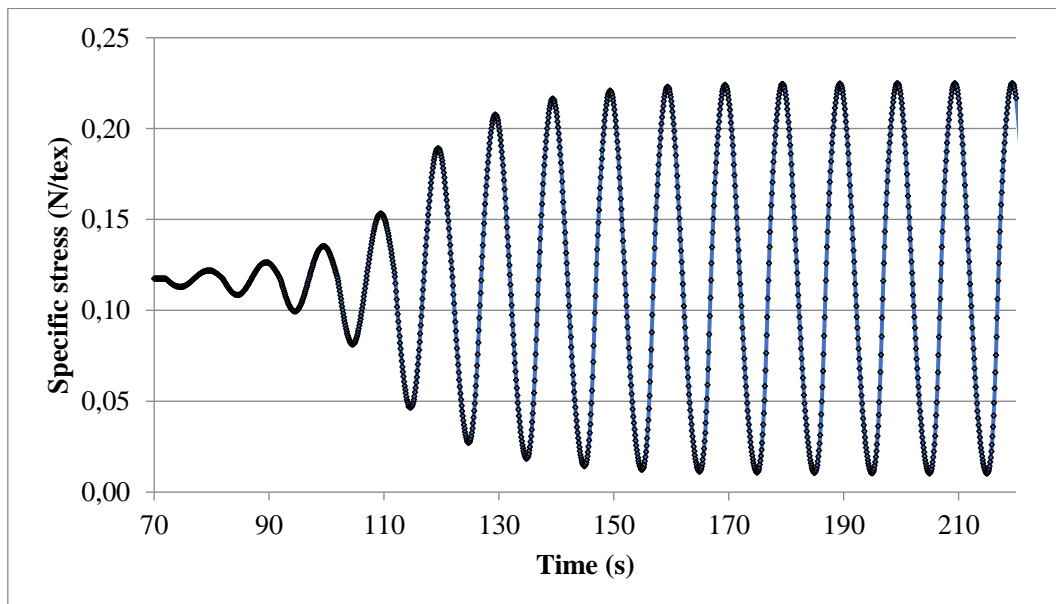


Figure 4-8. Evolution of the first cycles.

It is well known that polyamides are sensitive to water, and moisture has been shown to affect the long term behaviour of polyamide 6 fibres (*ISO18692, 2007; Miri, 2009; Hunt, 1980; Humeau, 2018*). So, it is essential to perform tests in the wet state. As for the test described in chapter 3.4, the rope has been placed unloaded in tap water for 10 hours, then mounted onto the test bench in flowing water throughout the test.

We can see on the sample and on the curves in Figure 4-9 that slipping is occurring in the splices; in fact due to the short length of our samples the splices are not long enough and usually contract on the eyes.

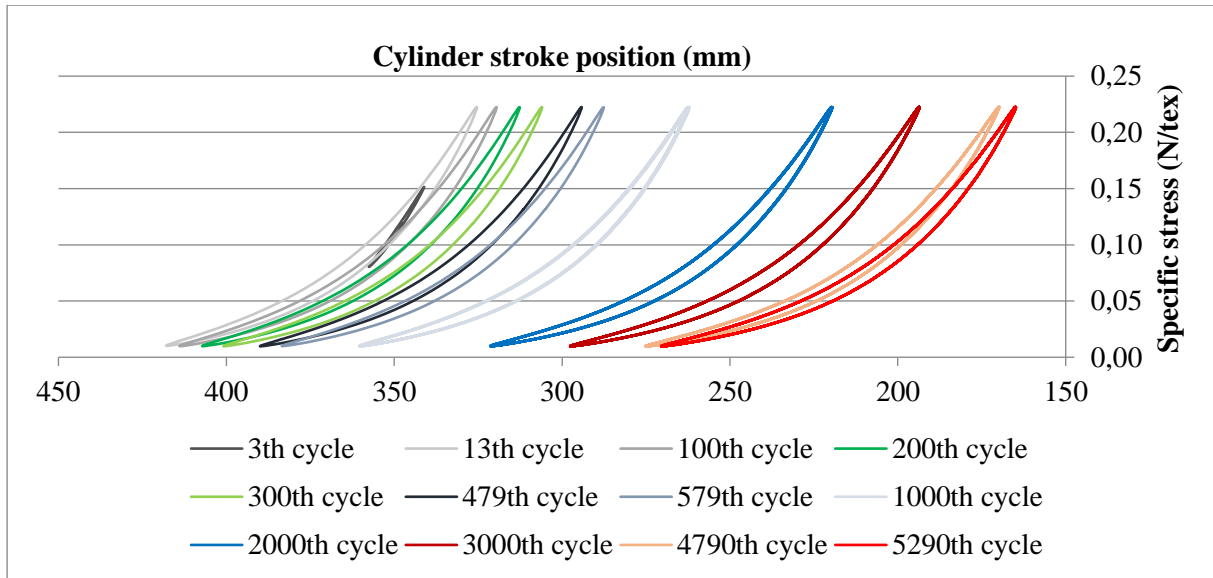


Figure 4-9. Examples of stress-displacement response obtained for several numbers of cycles during a cyclic test performed on sample SR41 with number of cycles to breakage of 5754 cycles and a maximal load of 50% of MBL.

From these data we can calculate a relative hysteresis energy density correlated with the anelastic energy dissipated or stored by the material during a cycle. Usually the equation can be given by $W_h = \int_{cycle} \sigma * d\varepsilon$, however as we do not measure the strain between splices during our fatigue test, we will follow the evolution from the displacement of the cylinder stroke, as shown in Figure 4-10.

$$W_{h\ relative} = \int_{cycle} \sigma(t) * d\ Position(t)$$

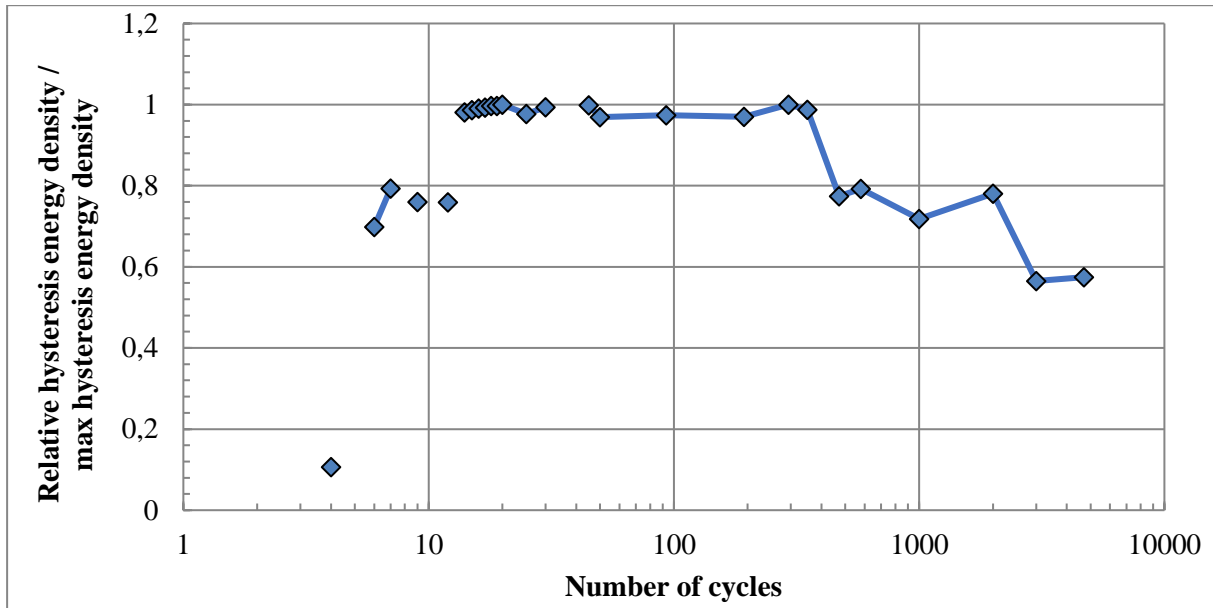


Figure 4-10. Hysteresis energy densities on sample SR41: Energetic response versus cycles.

During the first 10 cycles we have the program stabilization showing an increase of the hysteresis energy, then after around 400 cycles, we note a decrease of the energy by about 20 %. This effect can come from various phenomena, located along the whole sample length, as we only base our measure on the overall displacement measured. One possible reason is the slippage of the splices contracting around the pins, as once the eye is contracted around the pin the slippage should stop and reduce the amplitude of displacement.

4.3.1.1.4. Results

We defined the lifetime when one or more strand from our sub-ropes break, provoking the unwinding of the rope and reducing the load to zero.

Usually for fatigue testing on ropes, one does not keep results from tests which fail anywhere other than in the central part of the sample or at the end of the splices. However, for the 4T sub-ropes specimens, the specimens are short and a good control over the breakage point was not obtained. So, we choose to present first all specimen results with their breakage location, then only the valid results are shown, and finally to compare all the different results. Table 4-2 provides a brief description of the samples tested at which load, number of cycles and breaking location for these ropes.







Name	Load range (N/tex)	Load range (% of MBL)	Number of cycles to failure	Breakage zone
SR22	0.301	67,75	72	Bottom splice eye 
SR39	0.257	57,75	640	Bottom eye / near the end of the top splice: 
SR42	0.234	52,75	2908	Top splice / top splice near the eye: 
SR41	0.212	47,75	5754	Middle of the bottom splice / bottom splice: 
SR43	0.257	57,75	1241	End of the top splice: 
SR44	0.257	57,75	2215	Top splice near the eye (part without water): 

Table 4-2. Fatigue result for each samples and breaking zone.

Here only SR39, SR41 and SR43 have valid failure zones. The results for these three tests have been plotted in terms of load range (in % of Minimal Breaking Load or N/tex) in Figure 4-11:

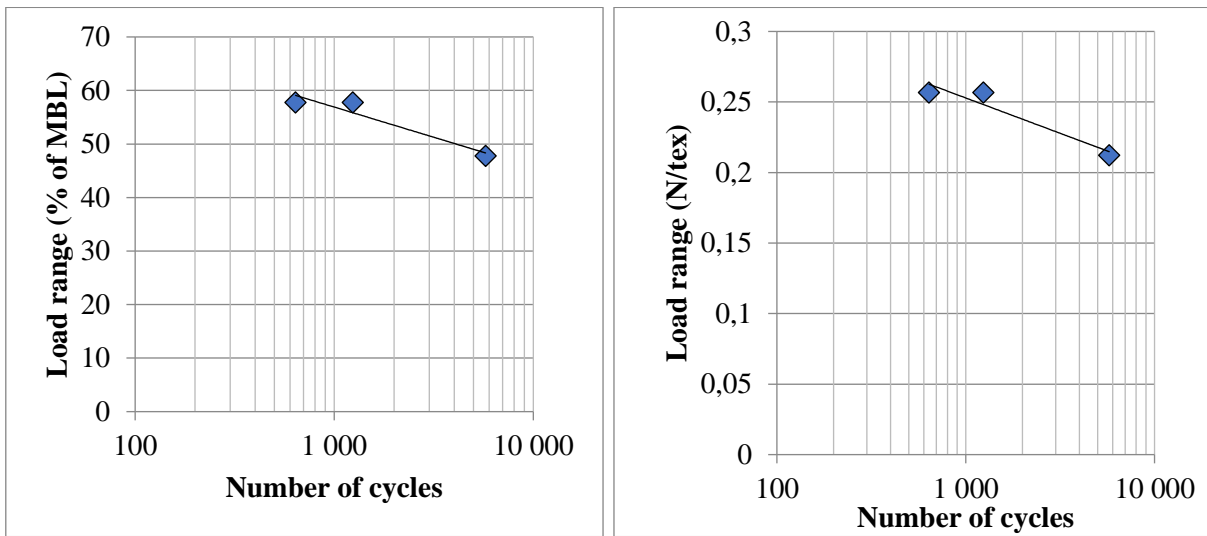


Figure 4-11. Fatigue test results for 4T sub-rope samples. (a) Load range expressed as percentages of break load (40 kN), (b) Load range in specific stress.

Then if we add the results from the three other samples we can observe in Figure 4-12 that the results from those tests are consistent and even superior to the previous points.

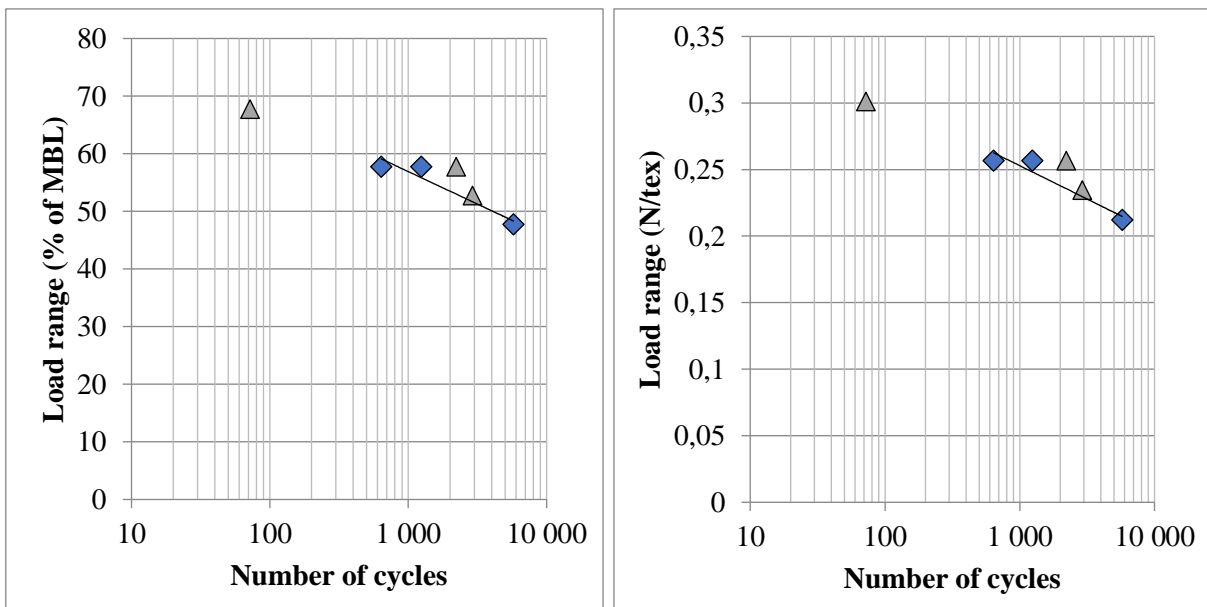


Figure 4-12. Fatigue test results for 4T sub-rope samples, with the non-valid breakage point in grey triangle. (left) Load range expressed as percentages of break load (40 kN), (right) Load range in specific stress.

In a first analysis, we will therefore use all our test results to describe the fatigue characteristic of the 4-tons sub-ropes.

4.3.1.1.5. Analysis

The early stages of failure are not always simple to evaluate after the break because the rope releases energy, and recoils and slippage may occur. However, from testing on longer samples on the testing machine at Ifremer, we know that usually when the breakage occurs, the three strands break at the same time, in the central section near the end of the splice. This suggests that the splices are too short here, but unfortunately, we are already at the maximal size for our specimen due to fixed limitations on the Servotest machine stroke and thus we cannot increase the splice length any further.

Figure 4-13 compares these results with published data.

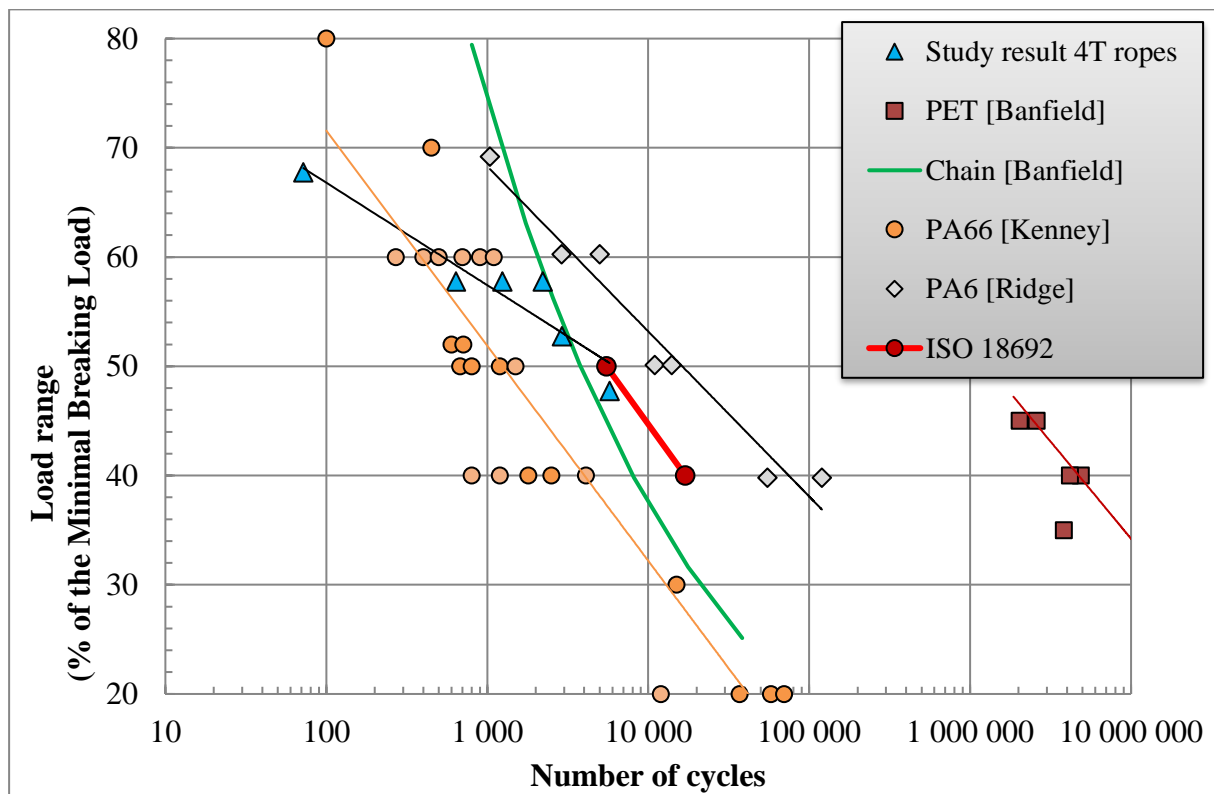


Figure 4-13. Overview of fatigue results for 4-tons sub-ropes, compared to previous tests on nylon and steel chain.

The values found are similar to those found by *Kenney (1985)* around 60% of MBL (with an average value of 645 cycles at 60% for the Kenney test and an average value at 1365 cycles at 57% for ours) with a scatter of about 1000 cycles. However, at lower load level (below 55% break load), we are quite close to results for chain and the *ISO 18692* guidelines. The slope for the evolution of the lifetime seems to be similar to Ridge's result not taking into the result at high load. The slope of the result

is not entirely determined by the material, but also by the coating and lay length. This comparison shows that even with a small number of imperfect samples, we obtain a result coherent with other tests and materials.

4.3.2. 8T sub-rope fatigue tests

4.3.2.1. Experiments

4.3.2.1.1. Samples

The second set of samples tested in fatigue are the same as the PA6 sub-rope of 8T breaking strength described previously in chapter 2. The sample geometry is shown on Figure 4-14.

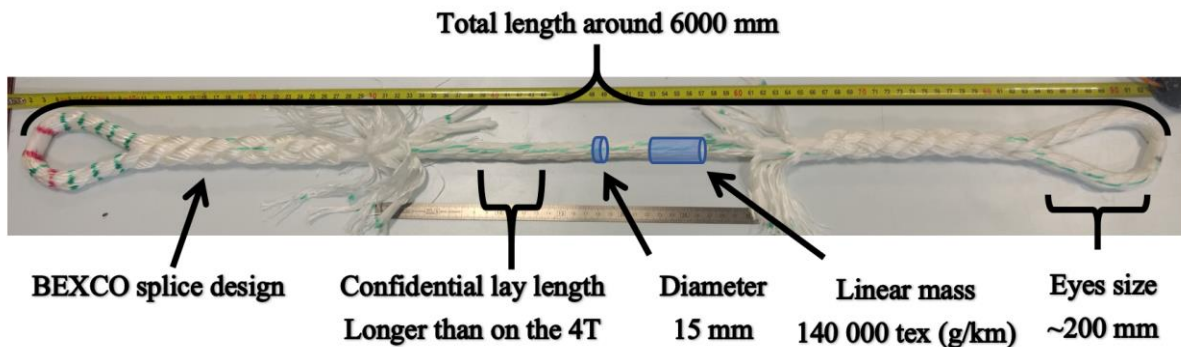


Figure 4-14. Sample dimensions for fatigue testing on 8-tons sub-ropes (but picture of a 4-tons sub-ropes).

4.3.2.2. Procedures

Quasi-static and fatigue testing have been performed on a servo-hydraulic test machine at the IFREMER Marine Structures Laboratory in Brest. This machine has a load capacity of 300 kN and a piston stroke of 3 meters. Load was introduced to the eye splices through steel pins of 100 mm diameter.

As with the 4-tons sub-rope, the watering of the rope is important, so before each test, the rope sample was fully immersed in tap water for at least 4 hours on the testing machine without load. It was then continuously sprinkled with tap water throughout the test, as shown in Figure 4-15.

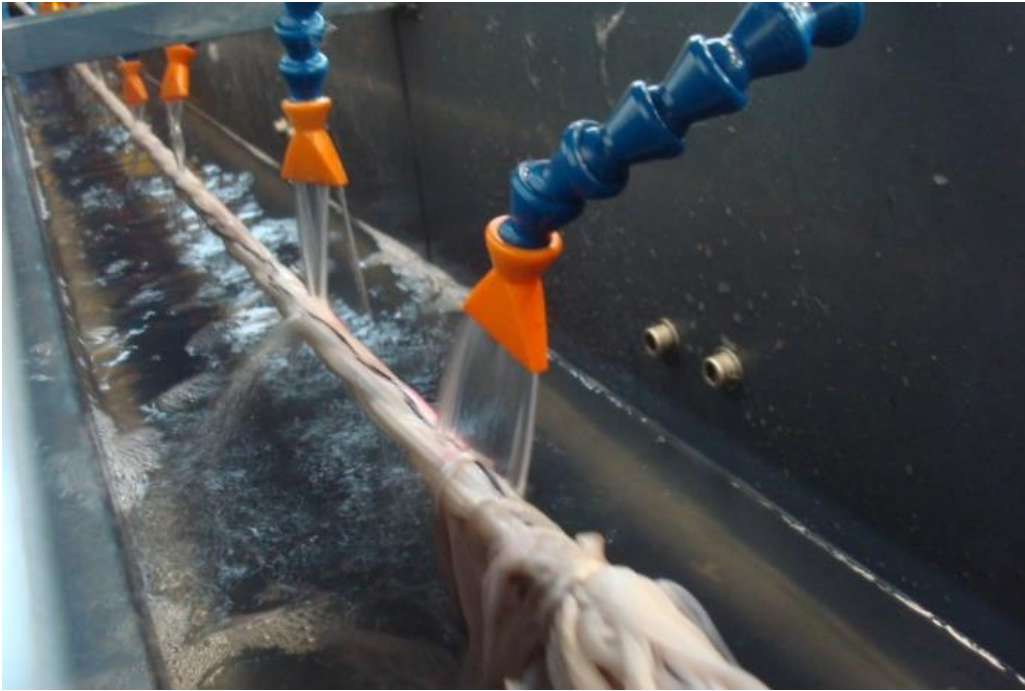


Figure 4-15. 8-tons sub-rope during a fatigue test on the IFREMER testing machine.

The fatigue test results presented here were obtained with a mean-load of 40% of nominal break load, and at a cycling frequency of 0.1 Hz. Sinusoidal cyclic loading was applied around this mean value. Before each test, a pre-cycling “bedding in” protocol was applied. This bedding-in consisted of five load-unload cycles from 2 to 50% of nominal break load, with each loading and unloading ramp lasting 2.5 minutes and hold periods of 5 minutes at 2 and 50% (see Figure 4-16).

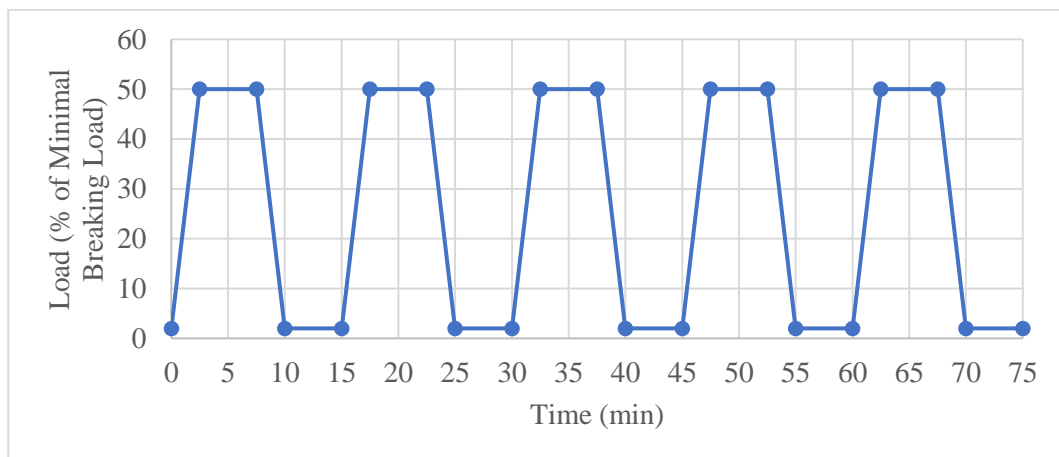


Figure 4-16. Sequence used for the 8T sub-rope bedding-in.

The ropes were delivered in two batches with nominally the same process parameters (i.e. manufacturing procedure, coating amount). These parameters are confidential and will not be given in this manuscript.

Six other tests were performed with a **different loading** to compare the result with the ones obtained for the 4-ton rope fatigue tests. These tests were also used for **heat build-up tests** (described later). The loading was set between 2% of nominal break load and a maximal value. This will also allow us to see if there is a creep effect in our rope by comparing different R-ratios. Indeed, the R-ratio is around 0.04 for the heat build-up fatigue tests while standard fatigue test at the same load range present an R-ratio of 0.15. Results from these tests are shown in section 0.

4.3.2.3. Rope quasi-static break tests

Wet and dry break tests were performed first, to check nominal reference strength values. On wet samples the strain to failure was measured by fixing an (expendable) wire transducer gauge to the central section between splices. Figure 4-17 shows the load-strain plot for the wet break test. This rope sample was subjected to cycles whose maximum loads were 20, 40, 60 and 80% of the nominal break load. The load-strain response is very non-linear as it has been noted in previous studies.

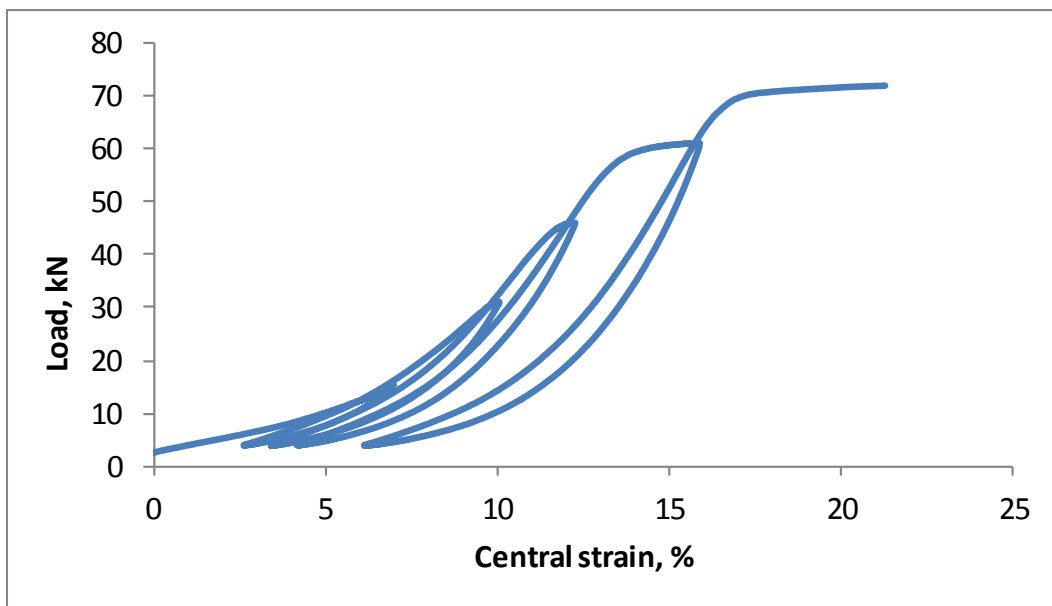


Figure 4-17. Example of experimental result in the case of wet quasi-static test to failure.

Six samples were loaded monotonically to failure at a rate of 20% break load/minute without strain measurements. Table 4-3 shows the results from these six tests.

Condition	Break loads, kN
Dry	75, 78, 77
Wet	72, 73, 71

Table 4-3. Rope break loads

4.3.2.4. ISO cyclic tests

In order to compare the behaviour of the improved nylon rope with the polyester used today for offshore moorings, two tests were run following the ISO18692 (2007) procedure for offshore station-keeping. The rope was cycled between 5% and 55% of breaking strength, i.e. a load range of 50%. 10 000 cycles were applied followed by a residual break test. In fact, the ISO test requires the number of cycles, N, to be only 5500 cycles for this load range so the tests performed here were more severe than the specified conditions. Table 4-4 shows the results.

Sample	Cycles applied	Residual strength after cycling, kN	Nominal value, kN
1 Tested dry	10 000	75	77
2 Tested wet	10 000	72	72

Table 4-4. Results from ISO 18692 cyclic loading tests on improved nylon rope.

The residual strengths are very close to 100% of the measured dry and wet strengths (see Table 4-2 and Table 4-4). This suggests that the cyclic performance of these ropes satisfies the ISO fatigue requirement for permanent offshore moorings.

4.3.2.5. Fatigue tests result

Twenty-five rope specimens were then tested wet in fatigue, at different load levels, with continuous cycling up to failure at 0.1 Hz. The longest test lasted around 320 000 cycles (37 days).

Results are shown first in the traditional S-N format in Figure 4-18, with cycles to failure plotted versus maximum load (a) and load range (b), both normalized by break load. For all tests reported here failure occurred in the central section of the rope, initiating near the transition between the end of a splice and the central section, with complete separation of the specimen into two parts. A small number of samples

failed in the eye splice region at the sample end, and these have been removed from the dataset. Figure 4-19 shows an example of a broken specimen.

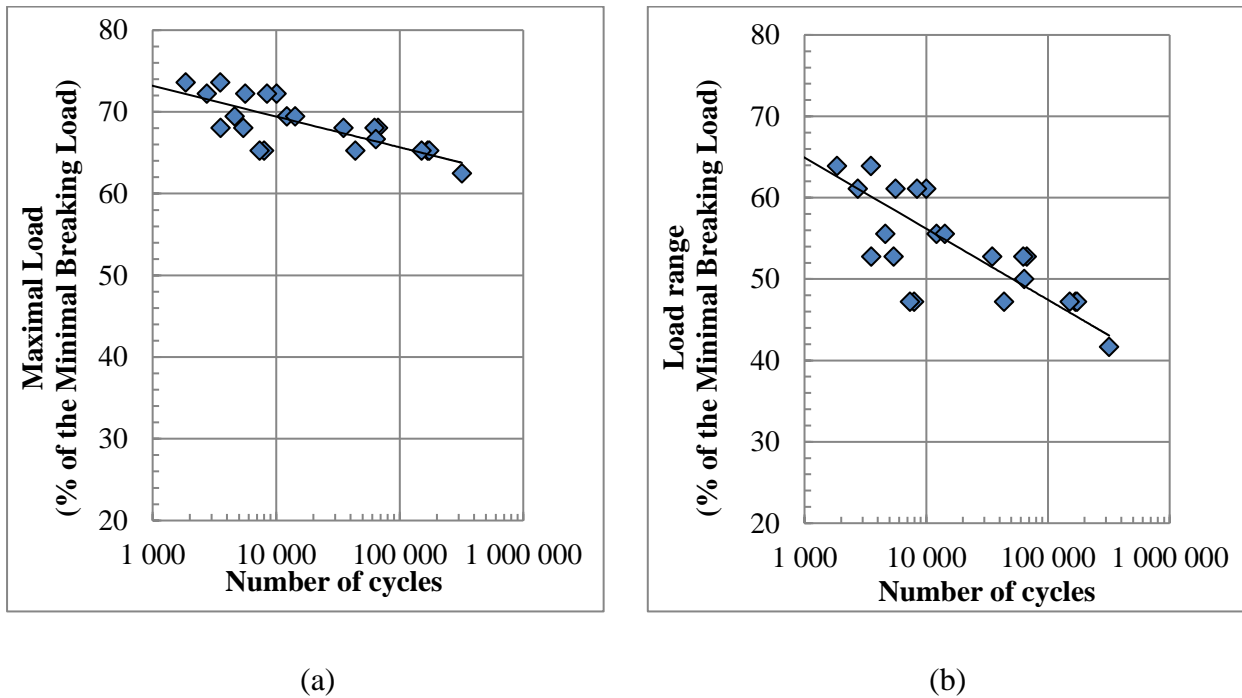


Figure 4-18. Fatigue test results for 8-tons sub-rope samples. (a) Maximum applied load, (b) Load range, both expressed as percentages of wet break load (72 kN). Dashed lines show linear regressions.



Figure 4-19. Failed 8-tons sub-rope sample after test, showing two broken parts superposed.

4.3.2.6. Fatigue tests analysis

A detailed analysis of the results shown in Figure 4-20 revealed two populations. Indeed, when the results are plotted according to their batches, it is apparent that the final batch provide significantly higher fatigue lives and lower variability than the initial batch.

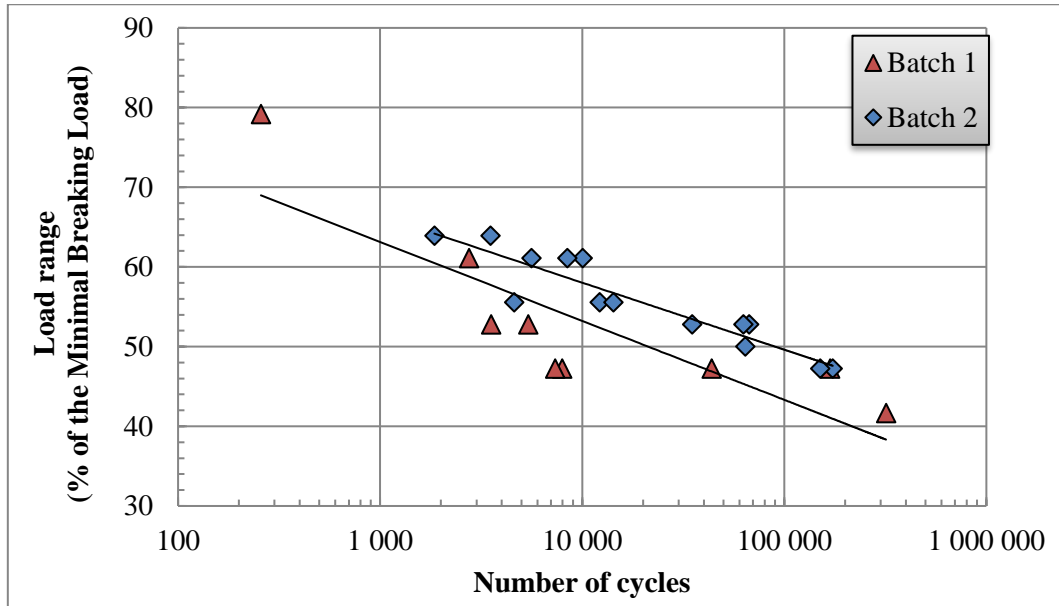


Figure 4-20. Fatigue test results separated according to batches, initial and final (8-tons sub-rope).

The results from the two batches show that there is a difference in lifetimes of almost one decade, highlighting the importance of the manufacturing process. This difference may be related to coating parameters, but further work is underway to confirm this.

The fatigue data points are shown in Figure 4-21, in order to be compared with the data published by *Ridge et al. (2010)*. Here the load range for our result is normalized by the wet break load (72 kN).

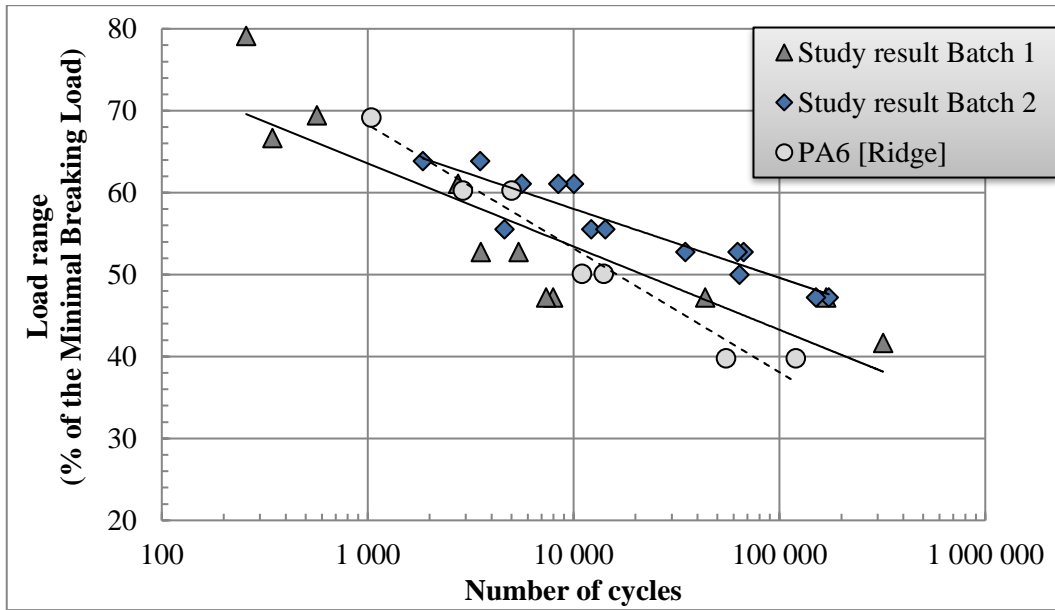


Figure 4-21. Fatigue test results for 8-tons sub-rope samples and comparison with published data from Ridge et al. (2010), shown as dashed line.

The dashed line in Figure 4-21 shows the trend line for the results from *Ridge et al. (2010)* on their improved polyamide rope for long term mooring of wave energy converters. The results for the rope from the present study, from a different rope manufacturer, are grouped around those previous results.

Figure 4-22 shows a summary of the results from the two batches of nylon 8-tons sub-ropes and compares them with published results for Nylon (*Kenney, 1985; Ridge, 2010*) and Polyester ropes (*Banfield, 2000*). A curve is also included which corresponds to S-N behaviour of steel chain (*Banfield, 2000*).

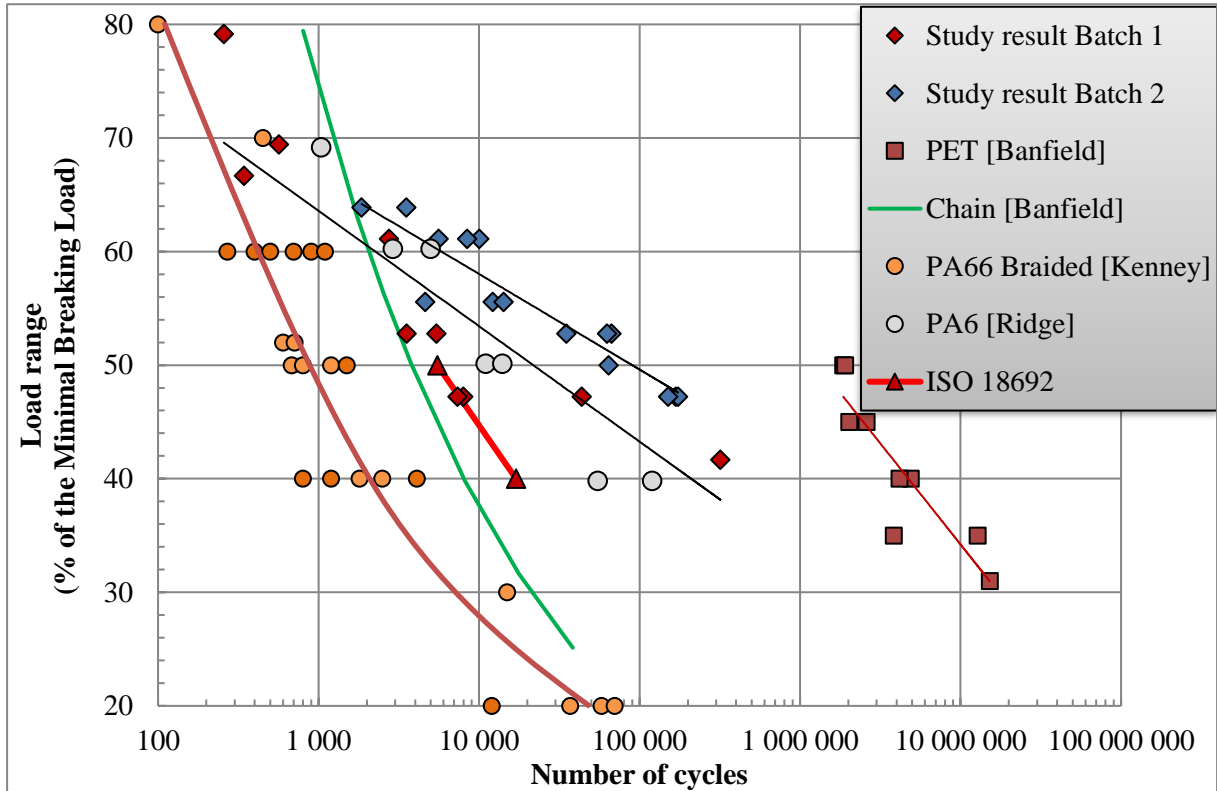


Figure 4-22. Overview of fatigue results, compared to previous tests on nylon, polyester and steel chain.

The coated nylon 8-tons sub-ropes studied here provides considerably better fatigue lifetimes than the early values for double braided ropes (*Kenney, 1985*) and a little better than recently published values on coated twisted ropes (*Ridge, 2010*). Values are still a little lower than measured polyester offshore rope values but these nylon values exceed the minimum ISO requirement (thick red line), confirming the ISO test results noted previously in Table 4-4. The fatigue lifetimes of these improved ropes are also considerably better than chain values.

These results reinforce the idea that provided that appropriate rope constructions and coatings are adopted, **nylon fatigue may no longer be an issue for mooring lines for marine renewable energy applications.**

4.3.3. Fatigue test results for Heat Build up

Six additional 8T sub-rope specimens were tested wet in fatigue with different load levels than previously. A continuous cycling up to failure at 0.1 Hz with a load ratio of around 0.04 was imposed. We can observe from the results in Figure 4-23 that when plotted in terms of maximal load the results do not match closely.

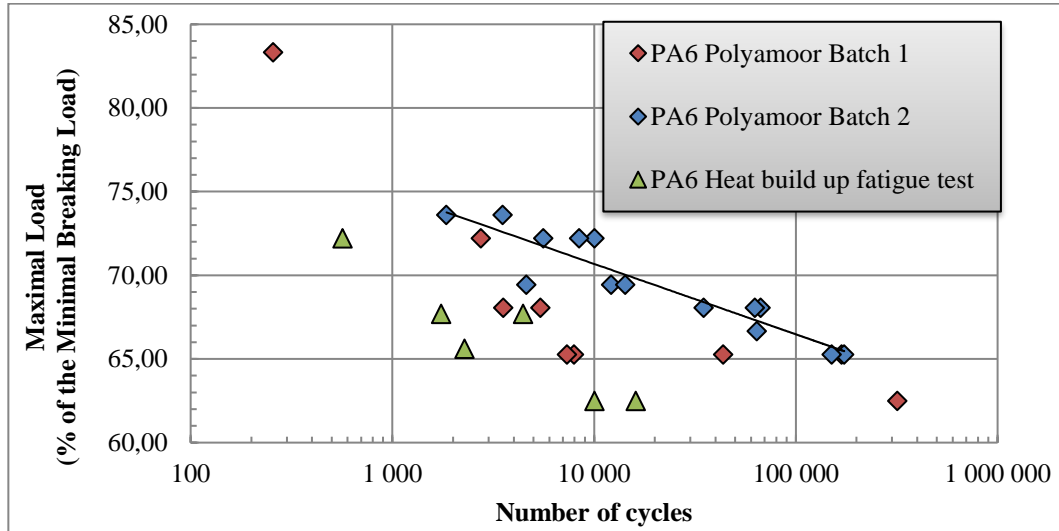


Figure 4-23. Fatigue test results separated according to batches and test conditions in function of maximal load.

However, when load range is plotted, Figure 4-24, there is a good correlation between the two sets of data.

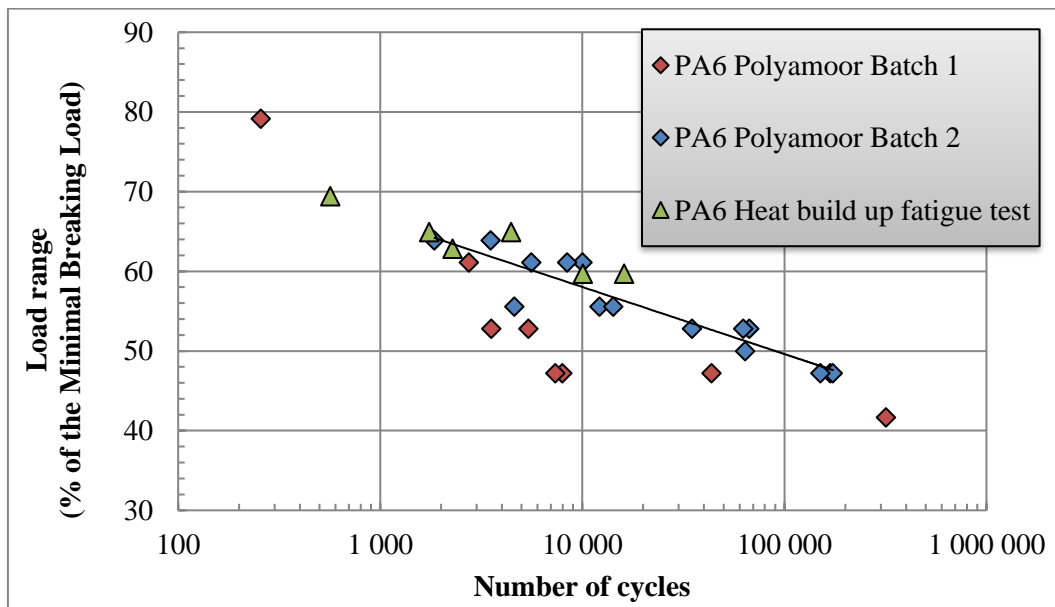


Figure 4-24. Fatigue test results separated according to batches and test conditions in function of the load range.

The fact that our results match in load range, with different R-ratios (0.04 and 0.15) could mean that the effect of creep is not a major component in failure below 70 % MBL.

4.3.4. Comparison between 4T and 8T sub-ropes

When we take the two results from fatigue tests performed with the same R ratio around 0,04 (cycling between a minimal value of around 2% of MBL and a maximal value) we have similar slopes for the curves in terms of maximal load in N/tex (as seen in Figure 4-25, a). In % of MBL however when we compare the relative amplitude to static failure, the slopes are clearly different, but the results are closer (i.e. Figure 4-25, b).

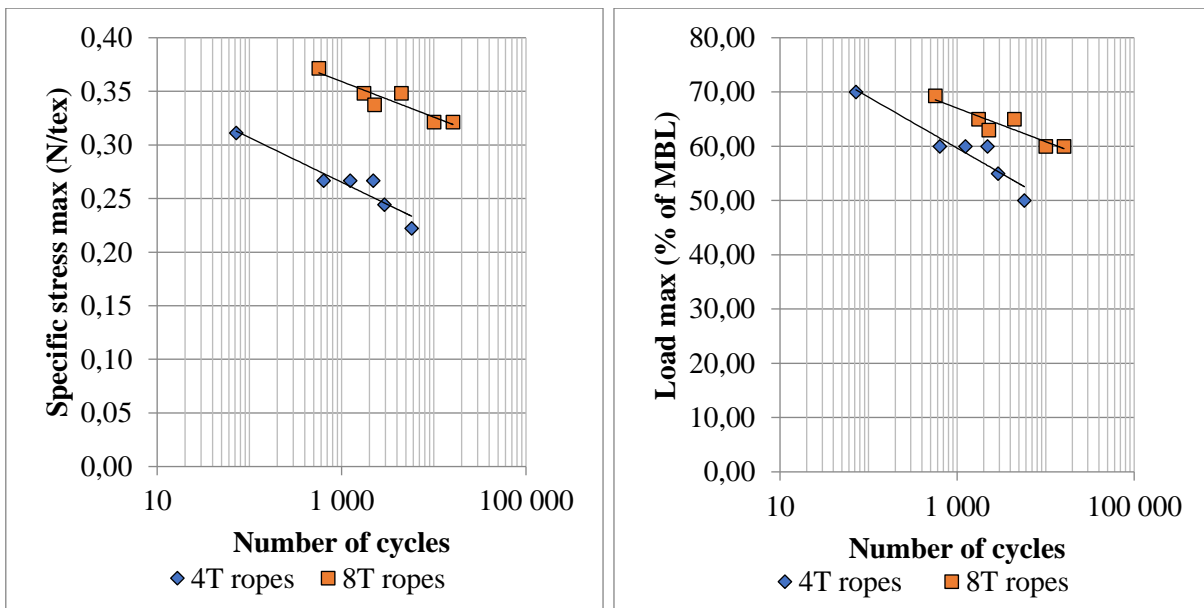


Figure 4-25. Fatigue test results separated according to sub-rope dimension.

It is clear that, with a shorter lay length, splices, and with breakage outside the central part, as expected, we have a shorter lifetime with the 4-ton ropes. The difference is around 10% in % of MBL and 0.1 N/tex.

Figure 4-26 presents all fatigue results from the different loading sequences and sizes of ropes. As noted above, creep is not a predominant factor in failure here and so a load range presentation may be more appropriate.

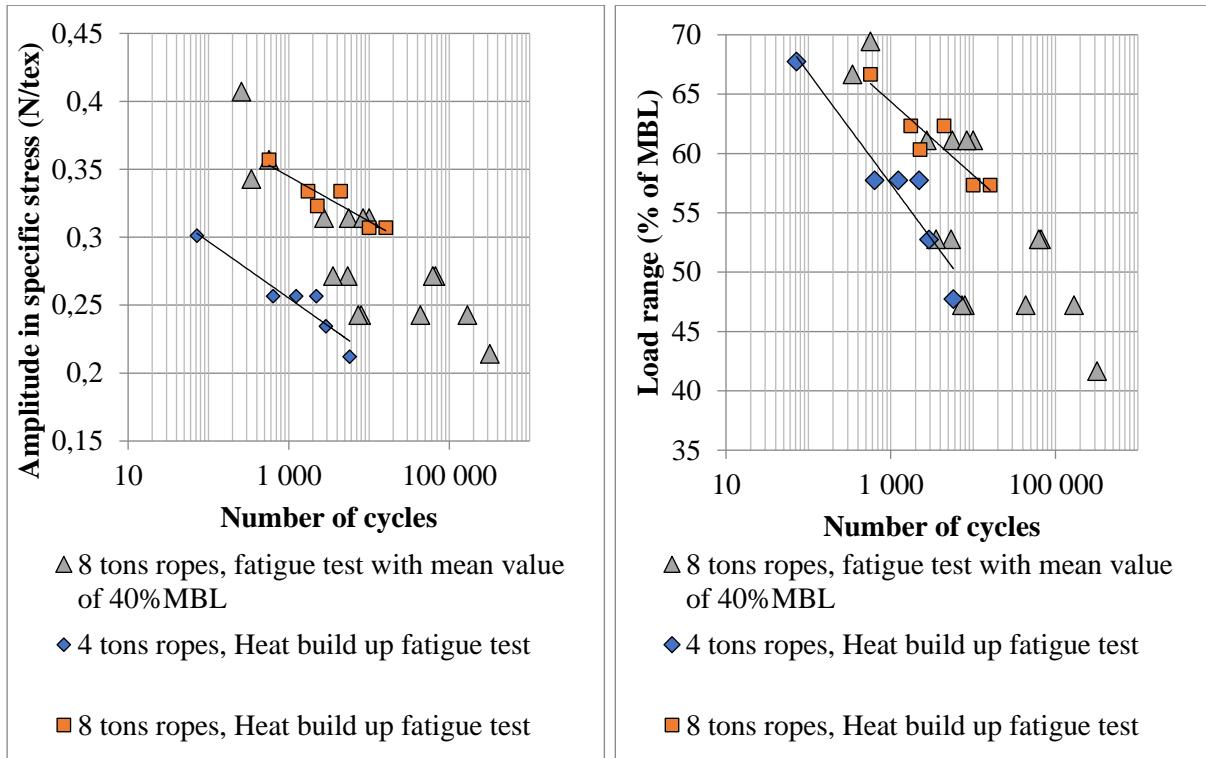


Figure 4-26. Fatigue test results separated according to sub-rope dimension and test conditions.

When we compare lifetimes from the heat build-up tests with an R-ratio around 0.04 (see Figure 4-26) to from those standard fatigue tests with an R-ratio around 0.15, the results are quite close, even between the 4-ton and the 8-ton sub-ropes. In terms of specific stress, there are similar tendencies for each tests, even if the lifetime is much longer on the 8t ropes, which is as predicted (based on the shorter lay length and lower splice quality of the 4T samples). In load range in % of MBL, the gaps between each rope type are reduced, and the 4-ton sub-ropes coincide with the worst batch of 8T below 55%. The heat build-up result will be discussed further in the next chapter of the manuscript.

4.3.5. Summary

The first objective here was to assess the fatigue performance of our polyamide 6 ropes with the same construction as the full-size sub-rope. For this purpose, 18 tests have been performed with the same loading condition as those adopted for the most recent study by TTI (*Ridge, 2010; Banfield, 2017; Flory, 2016*) in order to compare our results. Results from fatigue tests on the 8-tons nylon rope are very promising. They show a clear improvement compared to early published results for this material and are comparable, if not better (batch 2), to the results published more recently by TTI with a different rope manufacturer. We have also a superior lifetime value than steel chain, and the rope passes the ISO test for polyester rope. Published polyester values remain superior, but the slope of the nylon fatigue curve seems lower than that of the polyester and may join it at low loads. This suggests that polyamide 6 fibre ropes are good candidates for near-coast mooring of floating wind turbines.

As we tested smaller scale sub-rope than those of the real rope, the effect of size is present in our study. However, due to testing machine limitations, the smaller scale sub-rope of 4t has different characteristics than the 8t sub-ropes. Shorter lay length and splice length lead to lower fatigue lifetimes. However, the evolution of the lifetime shows similar tendencies to the 8T sub-ropes. Due to their short length and the small number of specimens tested the fatigue lifetime values obtained on the 4 tons sub-ropes have limited value for design, but they were useful in the heat build-up study presented in the following chapter.

The manufacturing parameters may have an effect on the lifetime. To confirm that two batches of ropes have been tested, and we observe a different fatigue result between the two batches. This suggests that the fibre coating conditions can significantly affect fatigue performance and must be carefully controlled, but this aspect requires further study.

As for abrasion, creep is a failure mechanism in synthetic ropes and can influence the lifetime. In order to examine the effect of creep, fatigue tests with a different loading ratio have been tested. These tests show similar load range dependency with the previous tests, and do not seem to be governed by the maximal load. Hence, the creep may not be predominant at the load range tested, which is already much higher than the loads seen in service by the rope.

4.4. Yarn and rope failure mechanisms

Optical microscopy and Scanning Electron Microscopy SEM (Quanta 200, FEI) were both used to assess the main phenomena involved in fatigue failure and to determine if the yarn-on-yarn test samples show the same damage mechanisms as those in rope fatigue testing.

4.4.1. Reference material

First, Figure 4-27 presents images of the coated and non-coated yarns before yarn on yarn testing, in order to show the virgin material state.

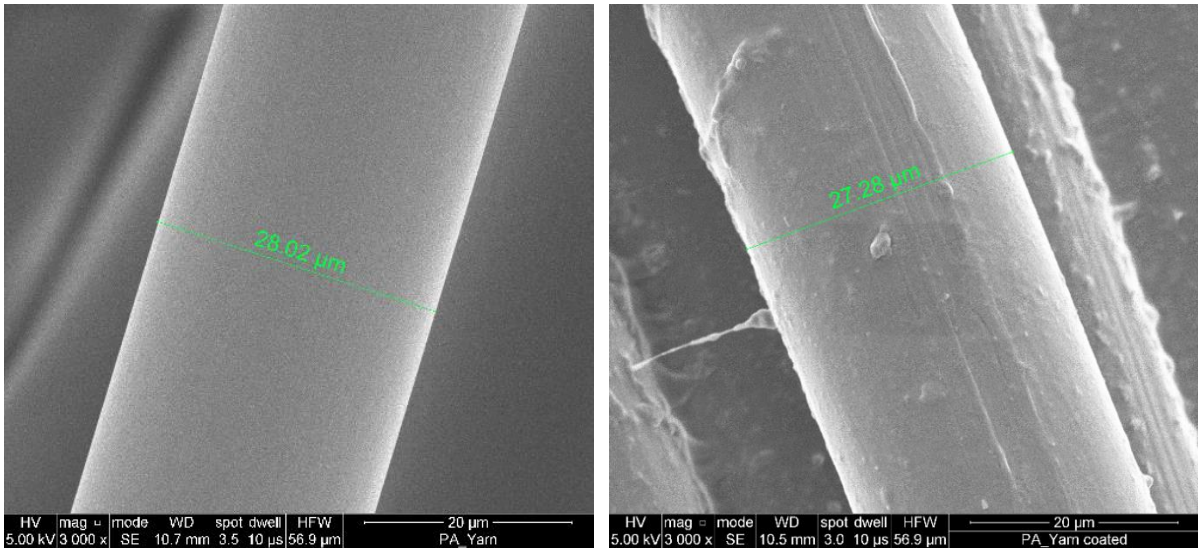


Figure 4-27. Examples of fibers non coated (a), coated (b)

The filaments are about 28 μm diameter, very smooth for the non-coated specimen and rougher when coated.

4.4.2. Yarn samples after Yarn on Yarn abrasion tests

Specimens were analysed after yarn-on-yarn tests. Even for moderate loads some marks are observed on broken fibers, which suggest a peeling mechanism may be acting. Examples are shown in Figure 4-28. It should be noted that melted fibers were not observed on yarn samples.

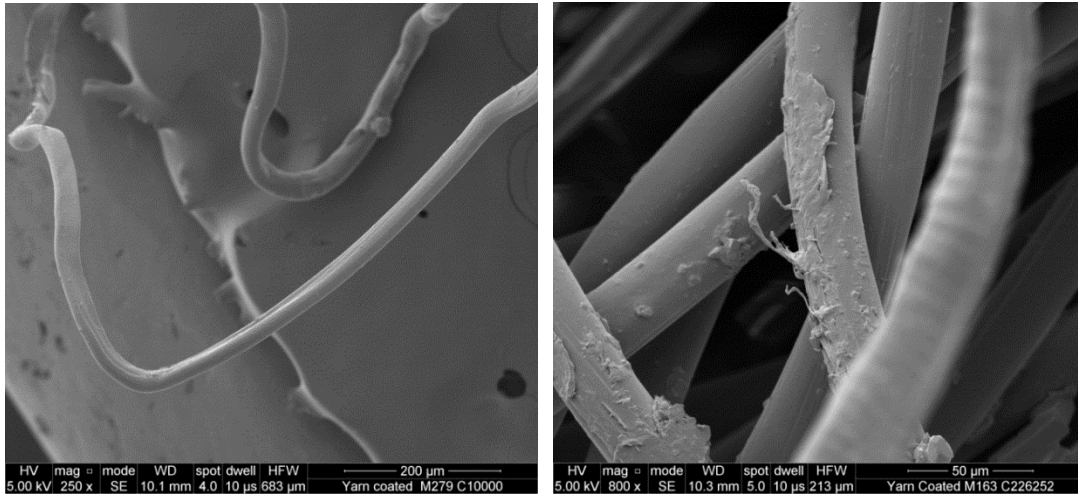


Figure 4-28. Examples of damage to fibres after yarn on yarn testing (coated yarn).

4.4.3. Rope inspection after fatigue testing

The results discussed by *Mandell (1987)* suggest that two failure mechanisms dominate cyclic response of nylon ropes. At high loads, creep rupture is the main failure mode, while at low loads abrasion can cause failure, either external abrasion on bollards or internal abrasion between fibres. However, it should be noted that there is not a distinct cut-off between these two mechanisms, both may occur if loading amplitude (and hence relative internal movement within the rope elements) is sufficient. As coatings are improved, one would also expect the abrasion mechanism to be shifted to higher numbers of cycles. Samples were taken from broken ropes at 200 mm from the final failure zone. Observations on samples from tests interrupted before final failure, and from areas of failed samples away from the break region, revealed significant areas of abrasion in the contact areas between the rope strands, Figure 4-29. The outer surfaces of the strands are intact but the inner surfaces in contact reveal broken fibres.



Figure 4-29. Example of internal abrasion in rope sample.

More detailed examination revealed areas of surface peeling, similar to those seen in yarn-on-yarn tests (Figure 4-30), similar features were documented by *Hearle (1998)*.

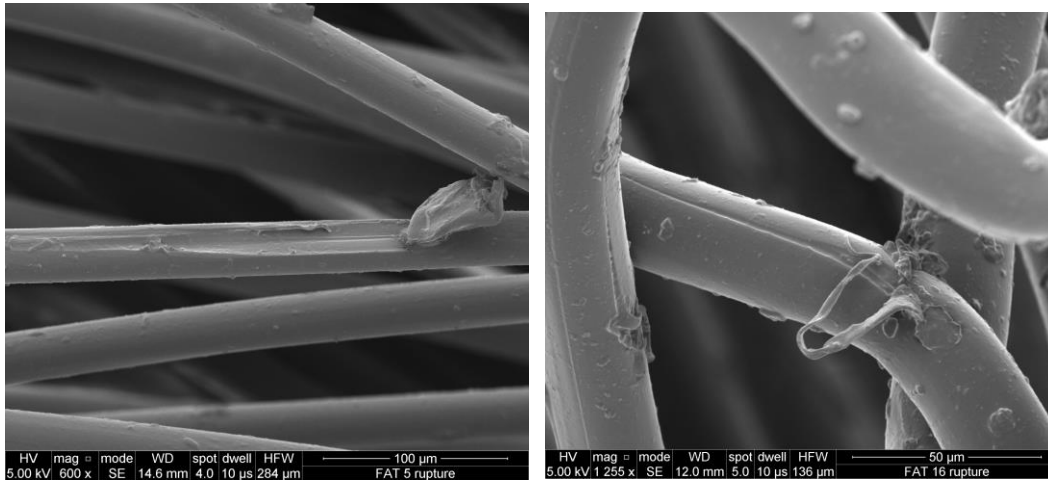


Figure 4-30. Examples of peeled zones on fibres taken from two rope specimens after fatigue tests to failure with a range of 52% of break load (coated yarn).

A third significant feature in observations of broken ropes in fatigue is the presence of highly compacted and melted fibres (Figure 4-31); this probably occurs during the final separation of the rope, when all the stored elastic energy is released.

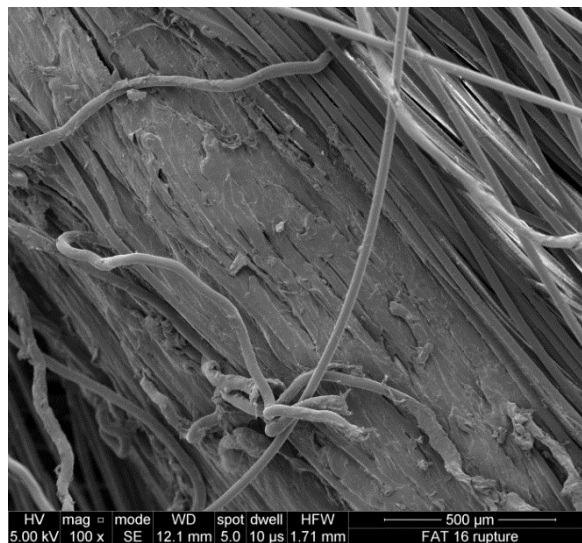


Figure 4-31. Examples of compacted zone in a sample taken from failure region of coated rope tested to failure with a range of 52% of break load.

4.5. Summary

The first point studied here was the fiber performance in abrasion and the effect of coating. The results from yarn-on-yarn loading abrasion tests show a significant increase in abrasion resistance by the addition of a specially developed coating. The lifetime of the coated yarn is superior to the value chosen by the Cordage Institute as a limitation for choosing fiber for permanent mooring.

Once we validated the quality of our yarn, the following goal was to assess the behavior of polyamide rope with the same construction as the full size sub-rope. For that, the lifetime of two batches of 8T sub-rope was evaluated with load ranges from 40 to 70 % of MBL. The lifetime is clearly superior to results published for nylon ropes in the 1990's, and similar, if not superior for batch 2, to that demonstrated recently for another rope product by TTI (*Ridge, 2010; Banfield, 2017; Flory, 2016*). Fatigue lifetimes are also superior to steel chain and to the ISO test for polyester rope. Even if the polyester values remain higher, the slope of the nylon fatigue curve seems lower than the polyester and may join it at low loads. These results, and the favourable comparison with polyester ropes currently being used for offshore platform station keeping, suggest that, provided appropriate coatings are applied to fibres, **fatigue lifetime should not be a limiting factor for mooring floating wind turbines with nylon fibre ropes.**

An outstanding question is the influence of size and scale effects on rope behavior. Lay-length has an impact on fatigue; the tested 4-T sub-ropes with a shorter lay-length have shown shorter fatigue lifetimes than 8-T sub-ropes. However, as many parameters were changed between the two sub-ropes, it is difficult to say to which extent. Similar slopes are noted in the evolution of the lifetime in amplitude of the specific stress, but there are few results from the 4T samples. So, more tests should be performed to investigate this further.

The last point concerns the failure mechanisms of the nylon sub-rope in fatigue. SEM observations show two particular failure mechanisms in ropes; the first and most visible is melted fibres, usually over a large area of the size of a yarn. The second mechanism is the peeling of individual fibres; this is probably indicative of abrasion, as similar features were observed on broken fibres from the yarn on yarn test samples.

4.6. References

- ASTM D 6611, 2007. Standard Test Method for Wet and Dry Yarn-on-Yarn Abrasion Resistance, ASTM, West Conshohocken, PA.
- Banfield SJ, Versavel T, Snell RO, Ahilan RV, 2000. Fatigue curves for polyester moorings – A state of the art review, OTC 12175.
- Banfield SJ, Ridge IML, 2017. Fatigue durability of nylon rope for permanent mooring design, Proc. OCEANS 2017, IEEE publication.
- Bugg DL, Vickers DT, Dorchak CJ, 2004. Mad Dog project: Regulatory approval process for the new technology of synthetic (polyester) moorings in the Gulf of Mexico, OTC 16089.
- Bunsell AR, Hearle JWS, Hunter RD, 1971a, An apparatus for fatigue-testing of fibres, *Journal of Physics E: Scientific Instruments J. Phys. E: Sci. Instrum.* 4, 868-872.
- Bunsell AR, Hearle JWS, 1971b, A mechanism of fatigue failure in nylon fibres, *Journal of Materials Science*, 6, 1303-1311.
- Bunsell AR, 2009. Tensile fatigue of thermoplastic fibres, chapter 11 in *Handbook of tensile properties of textile and technical fibres*, Editor Bunsell AR, Woodhead publishing.
- Colomban P, Herrera Ramirez JM, Paquin R, Marcellan A, Bunsell A, 2006. Micro-Raman study of the fatigue and fracture behaviour of single PA66 fibres: Comparison with single PET and PP fibres, *Eng Fract Mech*, 73, 2463–2475.
- Cordage institute Guidline 2009P, “Performance Requirements for Marine Grade Polyester Yarn for Fiber Rope”.
- Davies P, Chailleux E, Bunsell AR, 2010. Tensile fatigue behaviour of PBO fibres, *Journal of Materials Science Letters*, 45:6395–6400.
- De Pellegrin I, 1999. Manmade fiber ropes in deepwater mooring applications, OTC 10907.
- Flory, J. F., 2013. Cordage Institute guidelines for marine grade nylon and polyester rope-making yarns. In Proc. Oceans-San Diego, (pp. 1-6). IEEE. (2013, September).
- Flory J. F. et al., 2016. "Mooring systems for marine energy converters," OCEANS 2016 MTS/IEEE Monterey, Monterey, CA, pp. 1-13.
- Haslum HA, Tule J, Huntley M, Jatar S, 2005. Red Hawk polyester mooring system design and verification, OTC 17247.
- Hearle, J. W., Lomas, B., & Cooke, W. D., 1998. *Atlas of fibre fracture and damage to textiles*. Elsevier.
- Herrera Ramirez JM, 2004. Fatigue mechanisms in thermoplastic fibres, PhD thesis Ecole des mines de Paris, in French, available at: <https://pastel.archives-ouvertes.fr/tel-00161491/document>
- Humeau C, Davies P, LeGac P-Y, Jacquemin F, 2018. Influence of water on the short and long term mechanical behaviour of polyamide 6 (nylon) fibres, *J. Multiscale and Multidisciplinary Modeling*, Experiments and Design, 1, 317-327.
- Hunt DG, Darlington MW, 1980. Creep of nylon-6,6 during concurrent moisture changes. *Polymer* 21(5):502–508
- International Organization for Standardization, 2007. “Fibre ropes for offshore station keeping – Polyester”, ISO standard 18692.
- Kenney, M. C., Mandell, J. F., & McGarry, F. J., 1985. Fatigue behaviour of synthetic fibres, yarns, and ropes. *Journal of Materials Science*, 20(6), 2045-2059.
- Lafitte MH, Bunsell AR, 1982. The fatigue behaviour of Kevlar-29 fibres, *Journal of Materials Science*, 17, 8, 2391–2397.

-
- Lechat C, Bunsell AR, Davies P, Piant A, 2006. Mechanical behaviour of polyethylene terephthalate & polyethylene naphthalate fibres under cyclic loading, *Journal of Materials Science*, Vol. 41, pp1745-1756.
- Le Clerc C, 2004. Microstructural mechanisms involved in fatigue of thermoplastic fibres, PhD thesis Ecole des mines de Paris, in French, available at: <https://pastel.archives-ouvertes.fr/tel-00164759/document>.
- Le Clerc C, Monasse B, Bunsell AR, 2007. Influence of temperature on fracture initiation in PET and PA66 fibres under cyclic loading, *Journal of Materials Science*, 42, 22, 9276-9283.
- Mandell JF, 1987. Modelling of marine rope fatigue behavior, *Textile Research Journal*, 318-330.
- Miri V, Persyn O, Lefebvre J-M, Seguela R, 2009. Effect of water absorption on the plastic deformation behavior of nylon 6. *Eur Polym J* 45(3):757-762
- OCIMF, 1982. Hawser test report, Data on large synthetic ropes in the used condition.
- Pham H-D, Cartraud P, Schoefs F, Soulard T, Berhault C, 2019. Dynamic modeling of nylon mooring lines for a floating wind turbine, *Appl Ocean Res*, 87, 1-8.
- Ramirez J.M.H., Bunsell A.R. & Colomban P., 2006. Microstructural mechanisms governing the fatigue failure of polyamide 66 fibres, *Journal of Materials Science*, 41: 7261.
- Ridge, I. M. L., Banfield, S. J., & Mackay, J., 2010. Nylon fibre rope moorings for wave energy converters. In Proceedings OCEANS 2010, IEEE publication.
- Seo M, Wu HC, Chen J, Toomey CS, Backer S, 1997. Wear and fatigue of nylon and polyester mooring lines, *Textile Res. J.*, 67 (7), 467-480.
- Weller, S. D., Johanning, L., Davies, P., & Banfield, S. J., 2015. Synthetic mooring ropes for marine renewable energy applications. *Renewable Energy*, 83, 1268-1278.
- Weller, S. D., Davies, P., Vickers, A. W., & Johanning, L., 2015. Synthetic rope responses in the context of load history: The influence of aging. *Ocean Engineering*, 96, 192-204.

Chapter 5: An attempt to use a heat build-up measurement protocol to evaluate the fatigue properties of ropes rapidly

This chapter describes a study of the rapid fatigue characterization of wet polyamide mooring ropes for floating wind turbines. As conventional fatigue test on ropes are very long and expensive, due to the use of special machines and low frequencies, we tried to apply a heat build up analysis method on ropes, using an Infrared camera for the thermal measurements. The basic idea is to use the dissipated energy evaluated from temperature measurements to predict the fatigue properties of our ropes. The approach is based here on a graphical evaluation and on the identification of an energy-based fatigue criterion.

First, the protocol has been developed and the approach applied on 4-tons subropes with a vertical setup, where we had good control of the wetting of the rope. Then the same approach has been applied on 8-ton sub-ropes on a horizontal testing machine; this is more difficult due to intermittent wetting conditions. Finally, comparison with classical fatigue results is presented, and a good agreement is found for both kinds of ropes. The comparison between results for the two ropes shows a similar trend in the heat build-up curves, even if a quantitative comparison is not directly possible due to the scale change.

Keywords: Fatigue, Heat build-up, Rope, Nylon, Water, IR camera

Table of contents

5. An attempt to use a heat build-up measurement protocol to evaluate the fatigue properties of ropes rapidly.....	167
5.1. Introduction	167
5.1.1. Context, difficulties and objectives	167
5.1.2. An approach to measure dissipated energy.	169
5.1.3. Establishing the link between self-heating and fatigue	170
5.1.4. Comparing the results obtained for the two rope scales.....	171
5.1.5. Plan.....	172
5.2. Evaluating the cyclic dissipated energy from thermal measurement	173
5.3. Heat build-up tests on 4T sub rope	176
5.3.1. Material and methods	176
5.3.1. Reliability of the experimental protocol.....	179
5.3.2. Prediction of the Wöhler curve and qualification of the analysis	181
5.4. Heat build-up tests on 8T sub rope	186
5.4.1. Material and methods	186
5.4.1. Reliability of the experimental protocol.....	188
5.4.2. Prediction of the Wöhler curve and qualification of the analysis	190
5.5. Comparison between the 4T and 8T sub-ropes	194
5.6. Summary.....	196
5.7. Reference	197

5. An attempt to use a heat build-up measurement protocol to evaluate the fatigue properties of ropes rapidly

5.1. Introduction

5.1.1. Context, difficulties and objectives

1) Complexity of design against fatigue

Synthetic ropes are complex materials that are subjected to a wide range of load ratios with various failure mechanisms: abrasion, creep, tension and axial compression. Ropes are produced with a range of constructions, dimensions, and coatings, making their design and the prediction of their fatigue properties very difficult, and it is almost impossible to test every design. Even more so for permanent applications like mooring, where the lifetime is expected to be around 60 million cycles.

2) Experimental difficulties

To characterise synthetic mooring ropes in fatigue is indeed a long and expensive process. It requires numerous samples, very long test durations with low frequencies (0,1 Hz) and specialized machines allowing very long specimens (and hence very large displacements). As a result testing parameters are usually limited to 1 or 2 conditions, and the tests are performed at very high loads, well above the service conditions (usually around 20% of MBL). Speeding up the fatigue characterisation is therefore crucial in order to characterise several rope candidates and investigate more design parameters.

3) Difficulties for incremental methods

In order to define a fatigue criterion rapidly, two methods may be used. The first one is an incremental method, where a variable is followed with time (usually a variable related to damage). To accelerate a test, we may increase the testing frequency, however these materials are highly dissipative (introducing strong heat build-up modifying the mechanical and fatigue properties) and also show very large strains making it difficult for the test bench to follow the high frequency (in terms of cylinder speed and PID control).

4) Difficulties for steady-state methods

A second method consists of considering that the constitutive response under fatigue conditions reaches a stationary state within a limited number of cycles. It is

often possible to relate a material parameter (such as the secant modulus, cyclic or elastic strain) to the fatigue lifetime but this is quite complicated here, as our material is quite complex. We can use local strain measurement but may miss some parameters as we do not have a clear definition of the stress (as the rope section contains voids between fibers). Additional difficulties are also present: friction, rotation of the rope can make measurement of the strain difficult, slipping in the splices on smaller samples makes it difficult to follow the cylinder stroke position ... Hence, it is difficult to define a global parameter to correlate the loading to the lifetime of the material.

5) Thermal measurements and access to dissipated energy

However, by using the cyclic thermomechanical response of our sample under different load amplitudes, we can assess a global value of the elevation of temperature that we can measure and try to link to the dissipated cyclic energy. This global evaluation is interesting for many reasons, as there is no contact with the specimen and we obtain a mean value for the full section of the specimen. However, as our material is complex (voids) and immersed in water, we will not be able to determine the material physical constants (as for standard bulk materials) to translate directly the temperature into dissipative energy.

6) Protocol of heat build-up for a quick fatigue evaluation

Moreover, a protocol of heat build-up for a rapid fatigue evaluation must be defined as we cannot link directly a number of cycles to a given thermomechanical parameter, especially for low amplitude where the signal is weak. We need to identify the evolution for several loading amplitudes to identify a change in dissipation that could be related to the activation of the fatigue failure mechanisms and thus to a given fatigue lifetimes (*La Rosa, 2000*). This kind of approach has been used on metallic materials with great success (*Doudard, 2005*) linking changes of dissipated energy to microplasticity and identifying an energetic criterion (*Morrow, 1965*). Some more recent studies have shown the feasibility for materials with more complex dissipative energy contribution like short-fiber reinforced composite (*Jegou, 2013; Abello, 2014*), elastomeric materials (*Marco, 2017*) and even 3D textile composites (*Navrátil, 2019*).

One other point that makes our study difficult is that we have several dissipative phenomena coming from the material and from the rope structure inducing friction. An important point to be checked is that the damage mechanism should be linked to the main thermal dissipation in our material. As seen in Chapter 4, abrasion seems to be the main failure mechanism in the load range tested here, so we hope that the induced heat is not masked by the viscous dissipation generated by this material (like visco-plasticity, visco-elasticity, crystallization and so on). More importantly being able to separate the two phenomena, would allow the values of the respective

mechanisms to be compared. However, within the present study we have not had enough time to use our constitutive model to improve our approach.

7) Size effect

Comparing the effect of the size of the rope and construction on the dissipative energy evolution and on fatigue is interesting, as the samples tested here are smaller than the full-scale ropes used for the mooring system. The latter is of the same construction as the 8-tons subropes and has a different lay-length to the 4-ton subropes. As we would like to be able to describe the fatigue of a larger sample, and even with a different lay length, it is therefore important to see what the effect of rope size on the results is.

8) Objectives

The objectives of the study are detailed below:

- The first objective is to set up a procedure to evaluate the dissipated energy. Controlling the thermal response of polyamide ropes has been done in some previous studies (*Parsey, 1983; Seo, 1997*) but mostly as a control over the specimen to ensure its mechanical stability. The idea of this study is to obtain a thermomechanical value defining the steady state of the material under cyclic loading.
- The second point is to try to evaluate the fatigue properties rapidly, based on the heat build-up curve and using a minimum number of samples, in order to assess the mean fatigue properties of a rope in less than two days.
- The third objective is to compare the results obtained for the two subrope scales, 4T and 8T. The subropes tested in our study are small scale samples compared to the real mooring lines. Understanding the scale factor could allow us to predict the fatigue properties for larger scale ropes.

5.1.2. An approach to measure dissipated energy.

5.1.2.1. Available options and technical precautions

The analysis of the dissipated energy can be based either on a stationary state (*Le Saux, 2010; 2013; Marco, 2013*) or an adiabatic hypothesis (*Marco, 2014; Masquelier, 2015*).

A first question for these multi-scale samples is: Should we look to the strand, rope-yarn or a mean zone on the subrope?

The emissivity of our sample must be as close to 1 as possible because the flux captured by the infrared camera depends directly on it. Hence the closer to a black body condition we are, the more signal we get, as real bodies emit much less radiation

than black bodies for a given temperature, regardless of wavelength. Reducing reflection is also important, so as not to be affected by external radiation like the sunlight or even coming from the sample thermal emission.

Finally, the environment is also a key point for our experiment. Water plays a major effect on the material behavior (see Chapter 1) and acts as a lubricant for friction. However, it also reduces the InfraRed radiation of our sample and limits the temperature rise.

5.1.2.2. Chosen approach

First of all, the rope lifetime has to be defined, and it can come from different elements like inter-strand friction, creep or other. The criterion we choose for our study is the breakage of one or more strands of our rope. This is quite easy and clear to define and is a global response of the rope.

Now that the lifetime is defined, we have to make sure that we work in a volume representative of the breakage of these strands, which means we have to base our analysis on the whole rope.

We will base the analysis of the dissipated energy on the stationary state. The stationary state was selected for multiple reasons: first and foremost the first loading cycles in our tests are not stabilized before ten cycles due to the large displacement and non-linear behavior of our rope; secondly it is easier to control the stabilised temperature than to ensure good conditions for the adiabatic hypothesis.

The idea is to validate whether the heat build-up method can be applied on fully structured materials, such as ropes, and in a wet environment. We need an experimental setup which is reproducible, with control over both the environment (wetting of the rope and reflection), and the mechanical loading. Water is the most important effect influencing our material behavior, the strength of the structure (lubrication) and the measured temperature. For this reason, the first tests were performed on smaller 4-tons subropes, allowing us to test our specimen using a vertical configuration, because this leads to a controlled film of water around our rope.

Finally, we need to check a full set of hypotheses: stabilized mechanical cycles, repeatability, transition from heat build-up test to fatigue ones, ...

5.1.3. Establishing the link between self-heating and fatigue

Verification of several hypotheses is needed to validate the link between the self-heating and the fatigue lifetime.

First, the repeatability of our tests must be checked. The material exhibits a noticeable scatter in fatigue, which might also be the case for the heat build-up tests.

Applying different loading sequences should not affect the energetic response of the different steps of the heat build-up curve. Blocks are made of a small number of cycles and are supposed to generate no significant damage in the specimen, leading to a limited change in the dissipative energy of the other steps.

It is interesting to modify the test frequency, to check if our energetic analysis relating the temperature to the dissipated energy is physically consistent. Indeed, if frequency obviously has an effect on the stabilized temperature, a reasonable increase of the testing frequencies (avoiding any thermal coupling) should have no impact on the per-cycle dissipated energy.

The final verification is to check that an evaluation performed over a limited number of cycles is representative of the full fatigue test. This was not investigated in this study but it will be studied in a following project. For this study, we will consider that the mechanical cyclic response is stabilized within each heat build-up step.

5.1.4. Comparing the results obtained for the two rope scales.

How and where can we compare the fatigue and dissipative results for ropes of different capacities? It is in fact difficult to directly compare our two types of samples because there are several parameters changing between the two samples.

However, we kept the same type of construction with the same number of strands. The difference between the ropes includes lay-length, splice length and size of the strands.

The two tables below show the main characteristics of the two tests and the differences between the two types of ropes.

8 ton sub-ropes test	+	-
	Existing testing machine Literature data and more fatigue tests Size closer to the service rope Breakage zone of the rope controlled	Limited control of the loading sequences Less-homogeneous horizontal watering system

Table 5-1. Advantages and disadvantages of the heat build up test on 8T sub-ropes.

4 tons sub-ropes test	+	-
	<p>Complex loading sequence available</p> <p>More-homogeneous vertical watering system</p>	<p>Limited availability and hence limited number of tests</p> <p>Test setup and protocols not existing</p> <p>Small samples, with short splices and limited control over the breaking zone</p>

Table 5-2. Advantages and disadvantages of the heat build up test on 4T sub-ropes.

5.1.5. Plan

This chapter starts with a section explaining how we can evaluate the dissipative energy from the thermal measurements made with the infrared camera.

Test on the 4 ton sub-rope samples are presented, with a presentation of the results found for the dissipated energy and validations of the protocol that has been listed in paragraph 5.1.3. Then a first evaluation of a fatigue limit from the heat build-up curve is obtained, followed by a quick evaluation of the mean fatigue curve using a criterion based on the dissipated energy.

After validating that the heat build-up method can be applied on the 4 ton sub-ropes, tests on a classical testing bench on 8 ton sub-ropes were performed. The goal is to see if the method can be directly applied to classic ropes characterisation setup, and if the size of the rope is an important parameter as we only measure surface information. During this experimental campaign we check the repeatability, and the effects of load sequences, and frequencies. Then, as for the 4 ton samples, we analyse the heat build-up curve and find a relation between the dissipated energy and the number of cycles to failure.

Then the comparison between the 4T and the 8T will be presented in terms of heat build-up curve and fatigue prediction results.

5.2. Evaluating the cyclic dissipated energy from thermal measurement

The main idea is to evaluate the dissipated energy from the temperature measurements by an infrared camera and to correlate these values to the number of cycles to failure. In order to do that, we need to identify a way to get the dissipated energy from the temperature measurements.

In the following paragraph, we shall resolve a thermo-mechanical problem to estimate the dissipation source. The hypotheses used to identify the thermal sources are described in the next paragraphs, using the heat equation below (*Doudard, 2005; Chrysochoos, 2000*):

$$\rho c \dot{T} + \text{div}(\vec{q}) = \rho c S_t = \Delta + r + \rho T * \frac{\partial^2 \Psi}{\partial V_k \partial T} * \dot{V}_k + \rho T * \frac{\partial^2 \Psi}{\partial \varepsilon^e \partial T} : \dot{\varepsilon}^e$$

ρ	mass density	$\rho c \dot{T}$	temporal evolution
c	specific heat capacity	$\text{div}(\vec{q})$	thermal exchange and diffusion
T	temperature	Δ	intrinsic dissipation
S_t	thermal sources	r	external heat supply
Δ	intrinsic dissipation	$\rho T * \frac{\partial^2 \Psi}{\partial V_k \partial T} * \dot{V}_k$	coupling between V_k and the temperature
r	external heat supply	$\rho T * \frac{\partial^2 \Psi}{\partial \varepsilon^e \partial T} : \dot{\varepsilon}^e$	thermo-elastic coupling
Ψ	Helmholtz free energy		
V_k	constants		
ε^e	elastic strain tensor		

Table 5-3. Description of each parameters of the heat equation.

From that equation we can apply some usual hypotheses: The external heat supply is not time-dependent and as the temperature variation (under 10°C in the following experiment for the 8 ton ropes, 2°C for the 4 ton) is low, the variations of ρc can be neglected, as for the coupling between temperature and internal variables (other than the elastic variable). This leads to the following equation with \mathbf{k} as the thermoelastic tensor and λ the conductivity tensor, considered isotropic ($\lambda = \lambda \mathbf{1}$) and using Fourier's law:

$$\rho c \dot{T} - \lambda \Delta T = \Delta + r + \rho T \mathbf{k} : \dot{\varepsilon}^e$$

Additionally, the external heat supply is considered constant over the test duration and as the thermo-elastic coupling terms compensate over a mechanical cycle, the equation reduces to:

$$\rho c \dot{T} - \lambda \Delta T = \Delta = f_r * \Delta^*$$

With Δ^* the intrinsic dissipation over a cycle, and f_r the frequency.

The thermal measurements are made using a tube of 40 mm diameter (see Figure 4-5 and Figure 5-14). Mean temperature values for the specimen are calculated on the blue rectangle (18x5 mm) and for the mean “ambient” temperature, on the red rectangle (8x4 mm). Both areas are shown in the rectangle zoom in Figure 5-1.

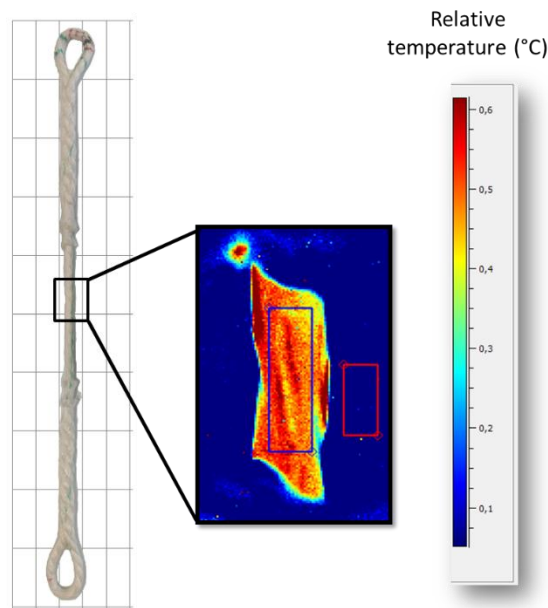


Figure 5-1. Zone of observation for thermal analysis.

This equation can then be written as:

$$\dot{\theta} + \frac{\theta}{\tau_{eq}} = \frac{f_r \Delta^*}{\rho c}$$

with τ_{eq} the characteristic time (which depend on the sample geometry, thermal boundary conditions and wetting of the samples).

To link the average surface temperature to the average cyclic dissipation, we need to evaluate τ_{eq} . On a general basis, we use a cooling period between two cyclic blocks to determine it, as for the 4 ton sub-ropes, by fitting the equation below (5). This is mainly used because the sample is stabilized (no thermo-elastic coupling, no mechanical dissipation). However, on the 8 ton sub-ropes, as the water is applied by

jets at specific regions and the water film is not continuous it is not effective when the rope does not move, so the identification was made on the loading stage.

$$\theta = \theta_0 * \exp\left(-\frac{t}{\tau_{eq}}\right)$$

with θ_0 the temperature at the beginning of the cooling step.

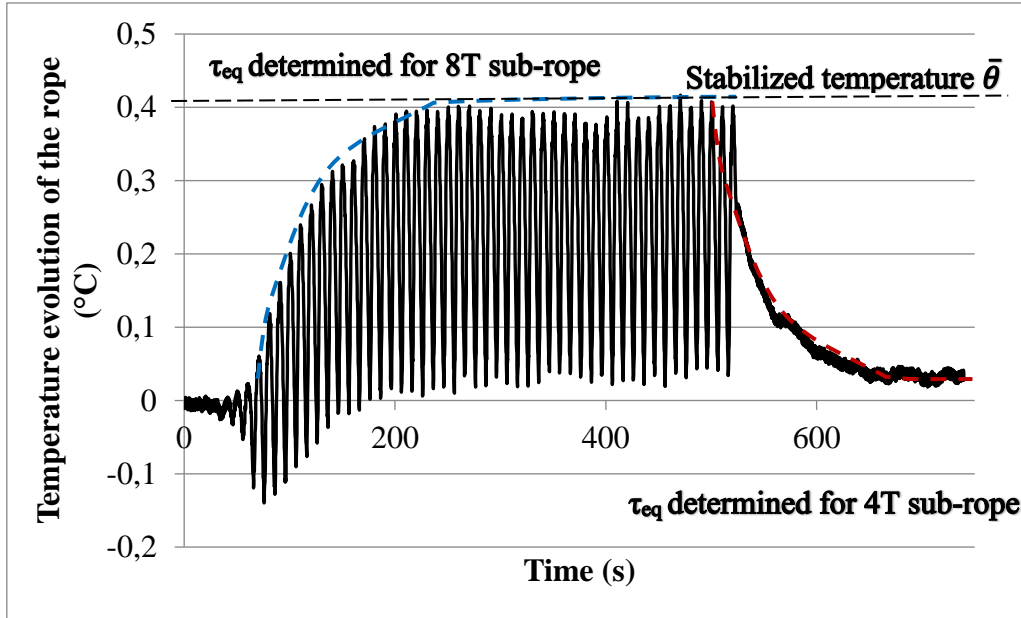


Figure 5-2. Example of a thermal acquisition for one cycle block (SR44, 50% of MBL).

The previous equation leads to the following expression:

$$\theta = \frac{f_r * \tau_{eq} * \Delta^*}{\rho c} * \left[1 - \exp\left(-\frac{t}{\tau_{eq}}\right) \right]$$

The average cyclic dissipation therefore writes:

$$\Delta^* = \frac{\rho c \bar{\theta}}{f_r * \tau_{eq}}$$

With $\bar{\theta}$ the stabilized temperature at the end of each loading step.

On our materials, the value of the density ρ and the specific heat c are unknown due to the complex structure and the presence of water. This means that the dissipated energy Δ^* , that we obtain is not an intrinsic parameter and depends on the wetting protocols.

5.3. Heat build-up tests on 4T sub rope

5.3.1. Material and methods

5.3.1.1. Samples

The six samples tested for the characterization presented here are the same PA6 sub-ropes as the ones used for the fatigue tests (see chapter 5.3.1). Figure 5-3 recalls the characteristics of these ropes.

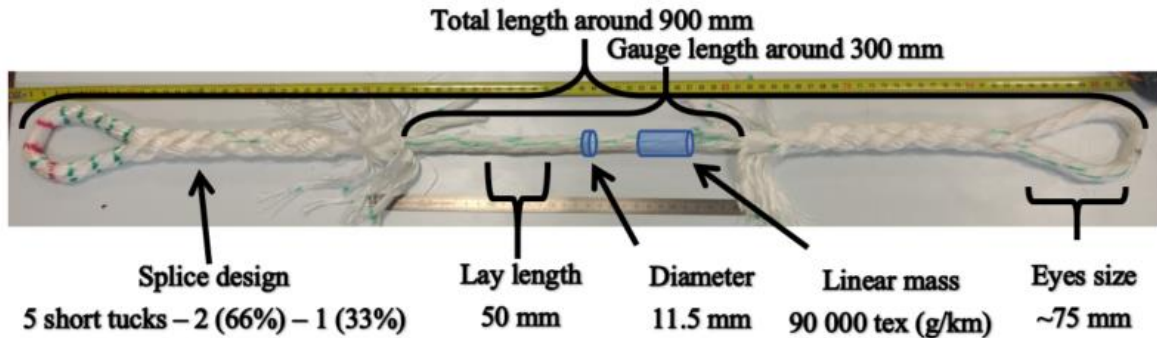


Figure 5-3. Sample dimension for fatigue testing on 4 ton sub-ropes (here SR39).

For this test, the surface of the sample is painted black over the gauge length with an acrylic paint, in order to get an emissivity value as close as possible to 1.

5.3.1.2. Equipment

The same hydraulic machine (load range 50 kN, cylinder stroke 600 mm) as used in the fatigue and characterisation tests on 4 ton sub-ropes, was used.

The environment affects the measurements, so the sample is surrounded by a blackened tube and covered from the top by a sheet, to limit any reflections, as shown in Figure 5-4.

The infrared camera used is a Flir Systems camera (reference Phoenix SC7600-BB) with a Stirling-cycle cooled Indium Antimonide (InSb) Focal Plane Array (FPA). The FPA is a 512×640 array of detectors digitized in 14 bits, sensitive in the $1.5 \mu\text{m}$ to $5.1 \mu\text{m}$ spectral band. A calibration operation allows the conversion of the thermo-signal (proportional to the thermal radiation) into a temperature in Celsius degree ($^{\circ}\text{C}$). The optical lens used is called “G1”, with a focal distance of 300 mm, and a pixel size of $15 \mu\text{m}$. The integration time is set to 1800 μs . After calibration, a precision of about 40 mK is obtained from differential measurement.

The tests were analysed using in-house software Belenos (*Le Saux, 2017*). This software allows us to work directly on the film taken from the camera, calibrating it, making mean value measurements and using fonctions to determine the τ_{eq} .

One drawback of this technology is that only surface measurements can be performed, however we assume that working with the stabilized temperature state will enable the temperature seen by the camera through the film of water to be related to the heating of the rope over the full section.

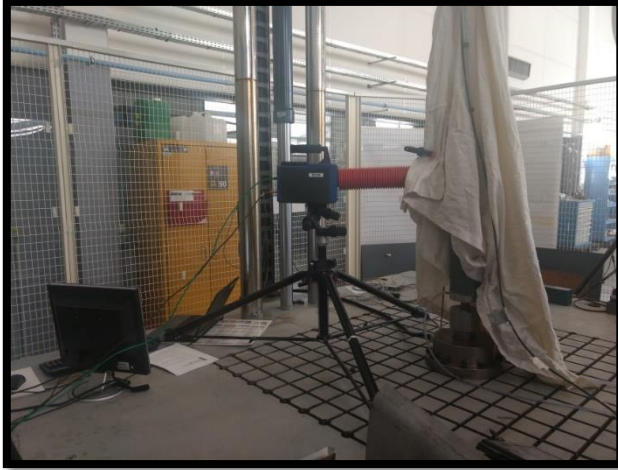


Figure 5-4. Pictures of the experimental setup for the 4 ton rope heat build-up test.

5.3.1.3. Procedures

Before the test and after the specimen was painted, the rope is put in tap water for a duration of 10 hours. Then it is mounted in the test machine where the sample is kept watered as presented in chapter 2 (see Figure 2-10) and 4 (see Figure 4-7).

The test consists of applying several cycle blocks of increasing load. Each block consists of cycling between 2% of the nominal load and a maximal load chosen. The frequency for the cycles of each block is 0.1 Hz. This frequency was chosen to be the same as the one used to perform the fatigue tests, in order to be as representative as possible for the evaluation of the fatigue lifetime.

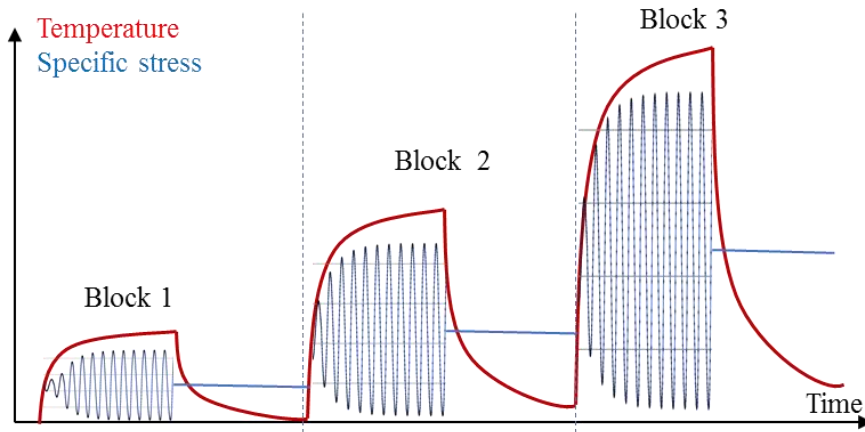


Figure 5-5. Schematic view of the heat build-up sequence.

The last step of the heat build-up protocol is chosen to lead to a limited ($<10^4$) number of cycles. After an evaluation of the dissipated energy over the first cycles, the test is left running to failure for this loading amplitude.

The number of cycles used for each loading condition is the number of cycles needed for the temperature to stabilize (usually around 50 cycles for the 4 ton sub-ropes). We have two aims in running a small number of cycles. First, the less cycles the quicker the test, allowing more steps to be tested. Second, the less cycles the lower the damage in our specimen before the last step.

We assume that over 50 cycles at 0.1 Hz (500 seconds) we have enough time to obtain a stabilized temperature. For the τ_{eq} value evaluated during our test (around 50s), the time ratio of 10 is sufficient to get a value very close to the stabilized temperature. After cycling, a cooling sequence of about the same duration as the cycling, 500 seconds, is applied in order to assess the characteristic time τ_{eq} .

Table 5-4 presents the different test cycle blocks with the different maximal loads.

Test	Blocks (maximal loads in % of MBL)
SR22	30 – 35 – 40 – 45 – 50 – 50 – 55 – 60 – 65 – 67,5 – 70 %
SR39	20 – 25 – 30 – 35 – 40 – 45 – 50 – 55 – 57 – 60 %
SR42	15 – 20 – 25 – 30 – 35 – 40 – 45 – 50 – 55 %
SR41	12,5 – 17,5 – 32,5 – 37,5 – 42,5 – 45 – 50 %
SR44	17,5 – 22,5 – 27,5 – 32,5 – 37,5 – 40 – 45 – 50 – 60 %
SR43	60 %

Table 5-4. Loading sequences of cycle blocks for heat build-up on 4 ton sub-ropes.

More information on the shape of the loading (cyclic evolution...) can be found in chapter 4.5.1.

5.3.1. Reliability of the experimental protocol

In this section, the reliability of the heat build-up protocol is discussed. Three aspects are tested: the repeatability in terms of dissipated energy, the effect of the steps in terms of dissipated energy and the consistency with the fatigue tests.

5.3.1.1. Repeatability

Figure 5-6 presents the results for three different samples (SR22, SR39, SR42) with similar loading sequences, in order to assess the repeatability of the test. The curve is plotted in load range (in % of MBL, a conventional approach for rope testing) versus the dissipated energy Δ^* .

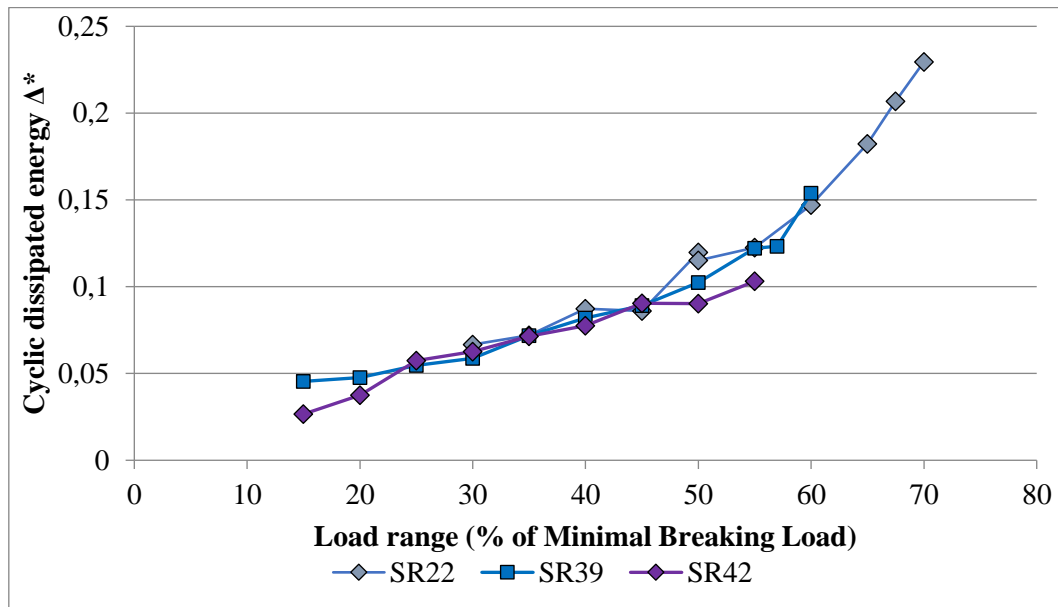


Figure 5-6. Heat build-up curve for 4 tons sub-ropes, checking repeatability.

A good repeatability can be seen between the tests, with a scatter between 1% to 15%. It should be underlined that below 15% of MBL the values are more scattered due to the lack of thermal resolution (heat build-up below 0.2°C in this range).

5.3.1.2. Influence of block sequences

Figure 5-7 presents the same curve as on Figure 5-6 with two more samples (SR41, SR44), tested with a different loading sequence.

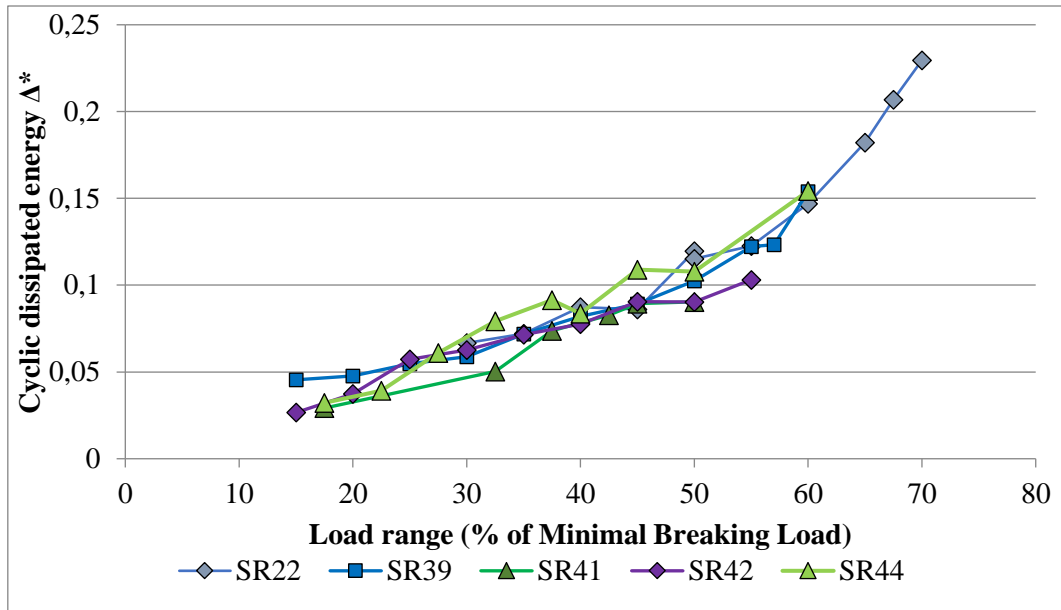


Figure 5-7. Heat build-up curve for 4 ton sub-ropes, checking effect of step sequences.

It appears that the loading sequence does not affect the results, that remain within a reasonable scatter (less than $\pm 17\%$).

5.3.1.3. Consistency with fatigue test

Figure 5-8 displays each test previously shown, with one more test (SR43) made with only one cycle block. This test was performed like a standard fatigue test and allows us to see if there is an effect of the heat build-up protocol on the dissipative energy measured.

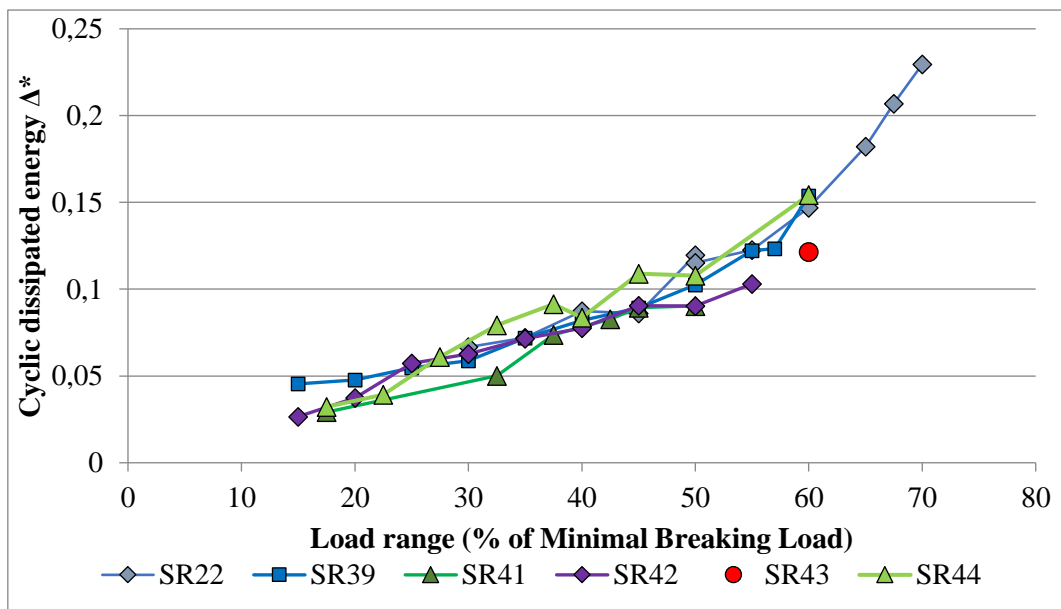


Figure 5-8. Heat build-up curve for 4 ton sub-ropes, checking loading step effect.

The value for the cyclic dissipated energy of the test is not fully unified but is still within the scatter of the other tests, around 17%, showing no noticeable effect of the step sequences on the data evaluated during the heat build-up test.

The fatigue result of the test matches perfectly the two other fatigue tests made after a heat build-up protocol for the same load. The number of cycles for SR43 is well between two other tests at the same load range of 60% of MBL (The 1241 cycles for the SR43 compared to 640 (SR39) and 2215 cycles (SR44)). Confirming that the previous step sequence does not induce significant damage to our specimen.

5.3.2. Prediction of the Wöhler curve and qualification of the analysis

5.3.2.1. Identification of the regimes

Figure 5-9 presents the mean value of the tests presented in the reliability section. The heat build-up curve plots the evolution of the dissipated energy as a function of the load range. This value does not represent an intrinsic measurement, in contrary to the expression in N/Tex, but can be converted as will be shown in the comparison section. The error bar represents the standard deviation for multiple results.

From a graphical evaluation of the shape of the curve, three regimes can usually be identified by straight lines on the heat build-up curves (*Serrano, 2017; Marco, 2017; Leveuf, 2018*). Evaluation is usually made starting from the third regime down to the first one.

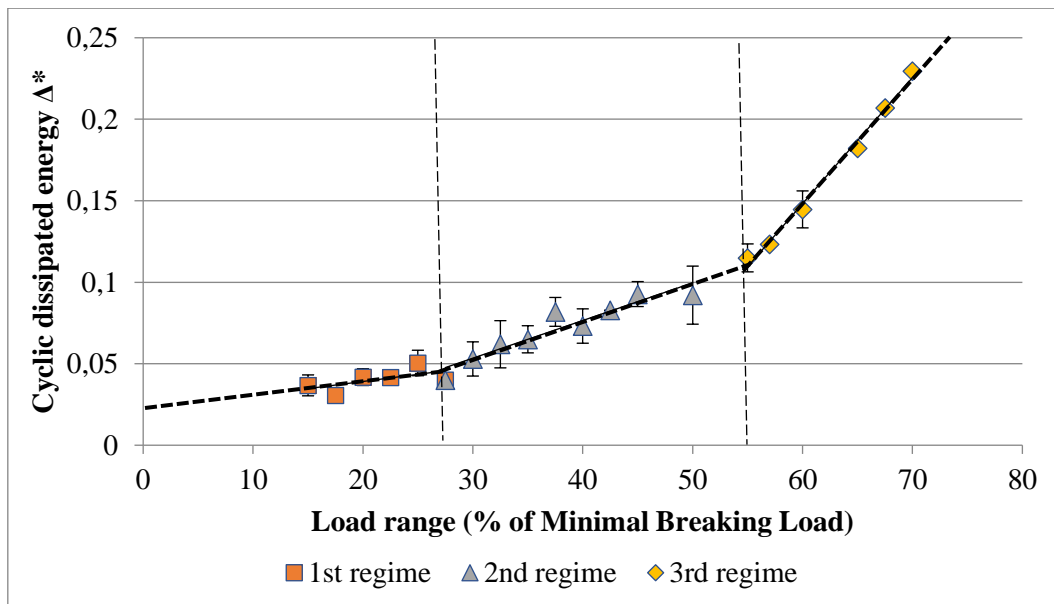


Figure 5-9. Heat build-up curve for 4-ton sub-ropes and linear fit of three regime (dashed lines).

From Figure 5-9, the transitions from regime 1 to regime 2 can be found around 27,5 % of MBL and from regime 2 to regime 3 around 55%.

In order to relate thermal measurements to fatigue characterisation some hypotheses must be made. First of all, we suppose that our material reaches a stationary state in a small number of cycles in order to speed up the process.

Secondly, a rough analysis can be provided by considering that the change of shape of the heat build-up curve could be related to a change of the intensity of the dissipation mechanisms. For several materials, this change can be related to the acceleration of the fatigue mechanisms, leading to a very reasonable evaluation of a given fatigue lifetime. The first change in slope is supposed to lead to a lifetime of 10^6 cycles. It is a big assumption as no clear fatigue limit exists for polymeric materials. Nevertheless, studies on composites with PA and PEEK matrix have shown very good predictions (*Abello, 2014; Leveuf, 2018*) of the mean fatigue curve within one day and on one sample.

For now, we cannot confirm the value of 10^6 , as very high numbers of cycles are too difficult to provide (as they require unreasonably long campaigns). Even if we get a reasonable evaluation, scatter is higher on long fatigue lifetimes, so it is difficult to assess the accuracy. Moreover, the resolution is generally good enough to be around 10^6 but would need a better resolution of the shape to get up to 10^7 cycles. These results need to be confirmed for our ropes fully immersed and with sprinkler watering.

At this stage of the study, we can use an empirical analysis as performed on metals or thermo-plastics (*Doudard, 2005; Marco, 2017*). The key point of the heat build-up-based analysis is related to the analysis of the shape of the curve. As explained earlier, friction is indeed a key parameter of both fatigue and dissipative phenomena (*Leech, 2002*), but the dissipative mechanisms are very numerous (visco-elasticity of the material, friction at several scales in the rope construction) and an accurate understanding and therefore analysis of the heat build-up curve requires much deeper investigation. Even more so, given that or wet PA6 we are above the glass transition temperature (*Launay, 2011*) which triggers a wide range of dissipative phenomena in PA6, and that a fatigue limit does not seem to exist for polyamide fiber rope.

Nevertheless, this evaluation is applied to the curve obtained, as illustrated on Figure 5-9. The force evaluated is around 27,5 % of MBL and used to plot a horizontal line on the same graph as the fatigue tests (see Figure 5-10).

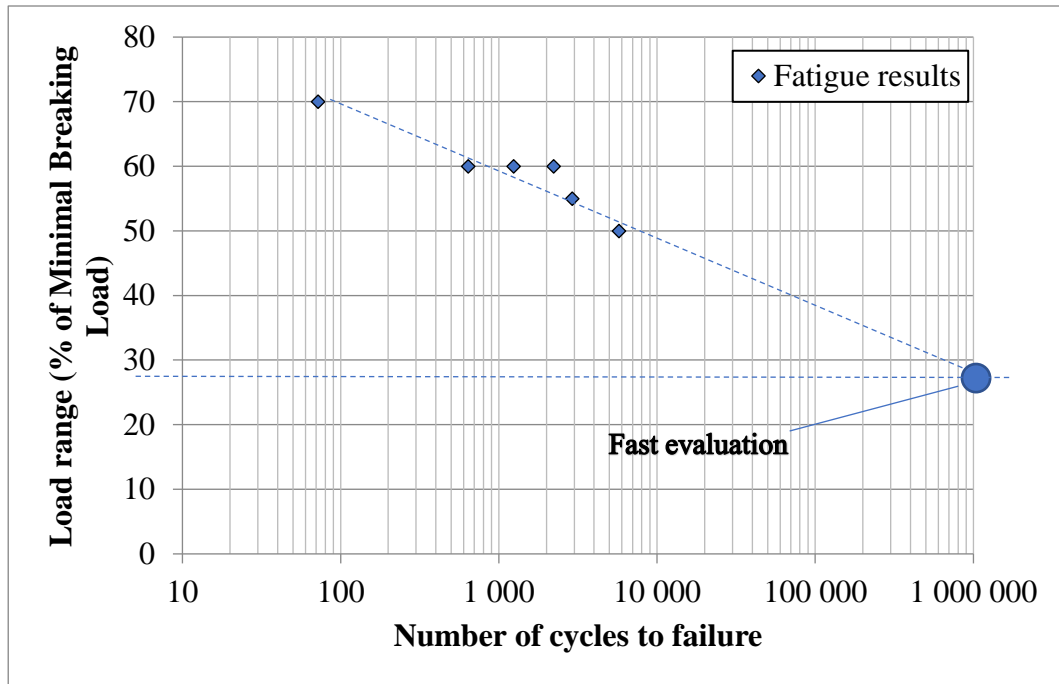


Figure 5-10. Fatigue curve for the 4 ton sub-ropes with preliminary prediction from the heat build-up.

One can conclude that this evaluation seems consistent with classic fatigue test results and that the application of the heat build-up approach to these ropes deserves a closer look.

5.3.2.2. Energy criterion

In this chapter, we describe the identification of the parameters of the energetic criterion in order to describe the full mean fatigue curve. The energetic criterion aims at relating the number of cycles leading to failure N , to the dissipated energy during the stabilized cycle Δ^* . The relation based on the work of (*Morrow, 1965*) has been used with success on metallic (*Doudard, 2005*), elastomeric (*Marco, 2017*) and composite materials (*Jégou, 2013*), and can be written as (8):

$$\Delta^* * N^b = C$$

With b and C , the model parameters that need to be identified.

To identify the two parameters b and C , two pairs of (Δ^* and N) are necessary. The first pair is quite straightforward as taken from the last test block kept running until the failure of the ropes. We will call these two parameters (Δr^* and N_r). The second pair is more difficult to determine precisely as it is at lower load range, and is purely empirical, taken from the shape of the curve.

Figure 5-10 illustrates that the graphical evaluation of the stress amplitude leading to 10^6 cycles was supported by our fatigue results even if the campaign is

limited. Moreover, as this identification was also found to be relevant in other publications (*La Rosa, 2000; Jégou, 2013; Marco, 2017*), it can be assumed that this evaluation gives a reasonable value of the stress amplitude leading to 10^6 cycles.

Two couples of data (Δ^* , N) can then be obtained for the heat build-up test. Knowing these two couples, the parameters b and C of the energetic criterion can be identified analytically. The values obtained for the SR39 samples are $b = 0.176$ and $C = 1.876 \text{ J/m}^3$.

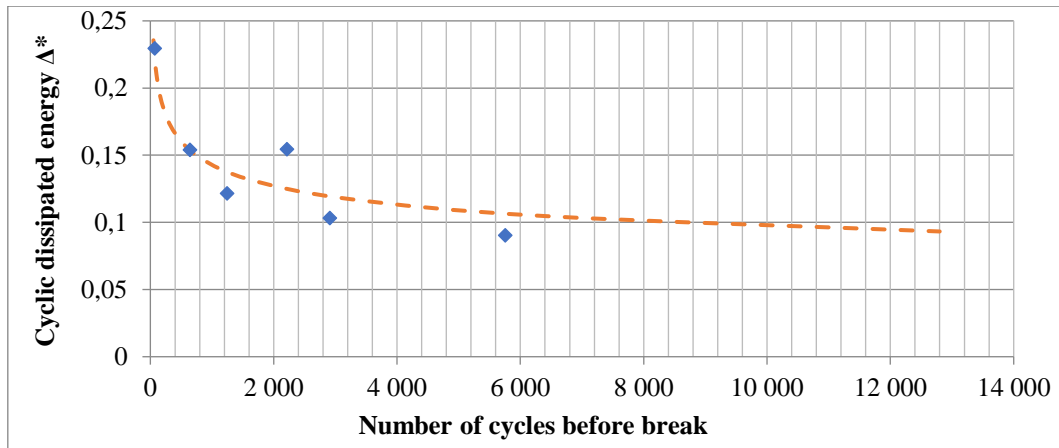


Figure 5-11. Evaluation of an energy based criterion.

From the criterion, we have a relation between the number of cycles and the dissipated energy. Using a fit of the heat build-up curve with the three line (shown on Figure 5-9) to link the stress amplitude to the dissipated energy and the identified energetic criterion to predict the number of cycles to failure, it is possible to predict the fatigue curve. As illustrated in Figure 5-12, with the fatigue results shown as blue hexagons and the prediction as the blue line. A very good agreement is observed between the experimental data and the predicted curve.

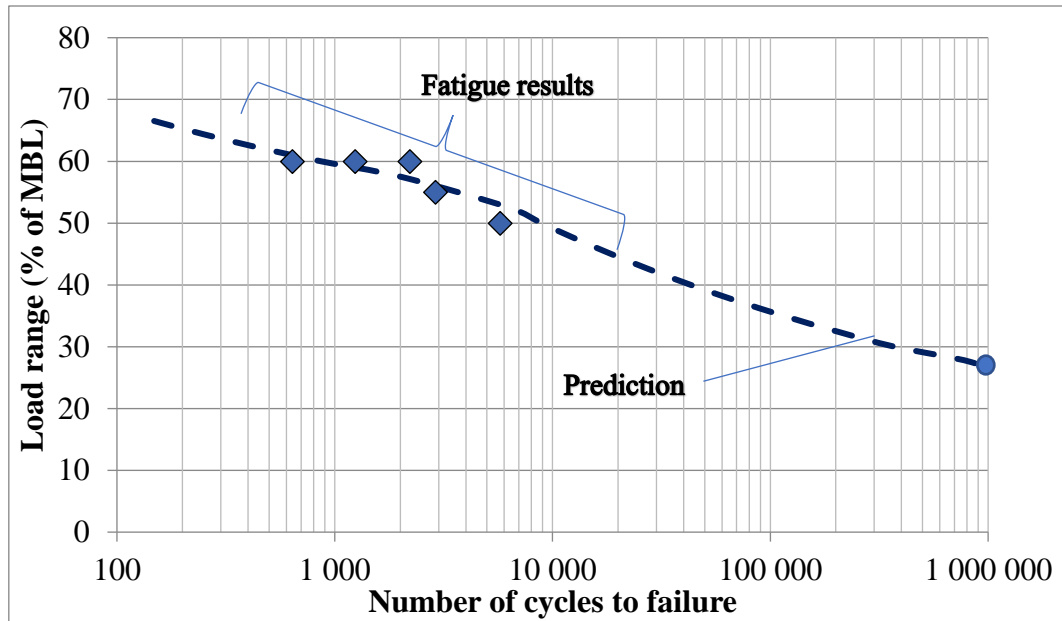


Figure 5-12. Prediction of the fatigue curve for 4 ton sub-ropes by means of the heat build-up method.

This result shows that the heat build-up curve can probably be used in a very efficient manner to provide a good prediction of the deterministic Wöhler curve, through an energetic fatigue criterion. More fatigue tests are needed to clearly validate this result, in particular for high cycle fatigue, but it is a promising result that may allow accelerated characterization of the fatigue properties of fiber ropes, using only one sample and with a test lasting less than 2 days.

5.4. Heat build-up tests on 8T sub rope

The aim of the 8T sub-rope test was to validate the result found on the 4T sub-rope and to evaluate if the heat build-up method could be applied in a less controlled wetting environment.

5.4.1. Material and methods

5.4.1.1. Samples

We use the same samples as presented in chapter 4. The only difference is that we put a small amount of black paint onto the rope in order to improve emissivity over the gauge length.

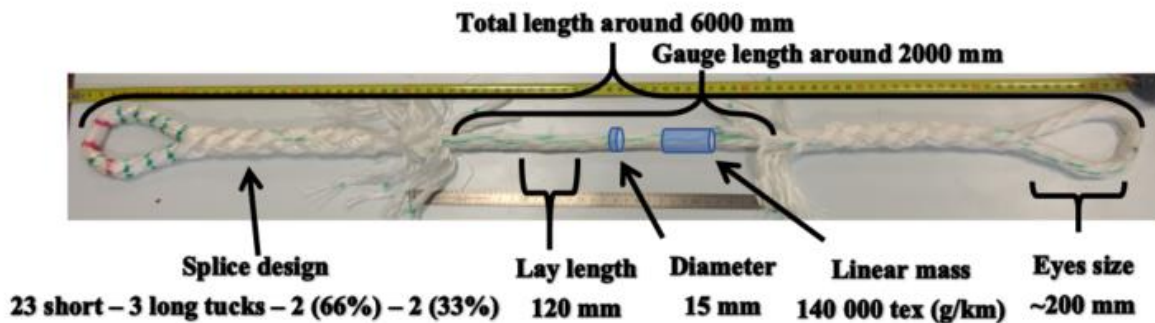


Figure 5-13. Sample dimensions for fatigue testing on 8 ton sub-ropes (image of a 4 ton sub-rope).

5.4.1.2. Equipment and procedures

The 8T fatigue tests were performed at IFREMER on the same machine that was described previously in Chapter 4. As a reminder it is a servo-hydraulic test machine with a load capacity of 300 kN and a piston stroke of 3 meters. Load was applied to the eye splices through 100mm diameter steel pins.



Figure 5-14. Pictures of the experimental setup for the 8 tons heat build-up test.

The camera used for the thermal acquisition is a Flir Systems camera (reference Phoenix SC7600-BB) and the software used to process the results are the same as those used on the 4 ton sub-ropes in chapter 5.3.1.

For the test on 8 ton sub-ropes, when the paint is dry the rope is put in water for 4h before the test. The rope goes through a T shaped pipe with the camera observing the rope through one branch of the tube, each part of the interior of the tube is blackened, either with duct tape or paint (Figure 5-15). The system is then covered with a curtain, to protect the experiment from the sunlight and possible reflections.

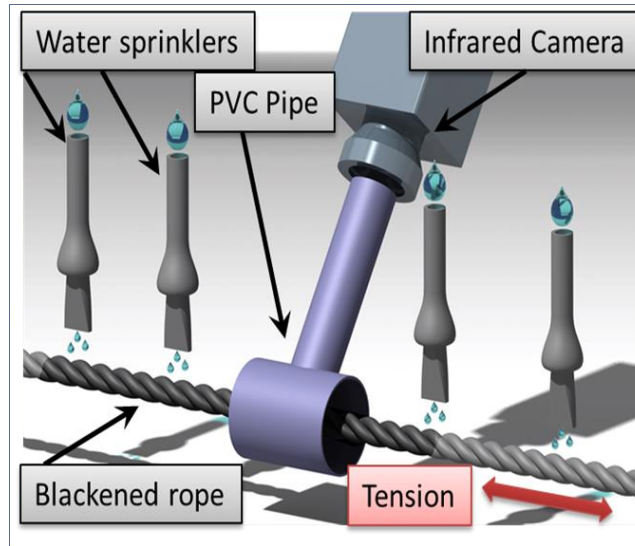


Figure 5-15. Schematic view of the heat build-up test on 8 ton sub-rope.

As for the 4 ton sub-rope tests presented in Figure 5-5, the machine takes a certain number of cycles in order to get to the target value, and more important, here wetting is not continuous along the rope. Some cycles are needed in order to get the rope in a stabilized state during each block and the stabilized temperature is studied here. All the characteristic times are evaluated from the temperature rise because it was not possible to get them from the cooling step due to the local wetting system (leading to significant variations along the rope when the rope is not moving).

Table 5-5 presents a list of the different tests with the different maximum loads, with a minimum load fixed at 2 kN, and a frequency of 0.1 Hertz as for the 4 ton sub-ropes. Each block contains 150 cycles due to a higher characteristic time (around 400 seconds).

Name	Sequence of cycle blocks (Load maximal in % of MBL)
2-1	10 – 15 – 20 – 20 – 25 – 32 – 37 – 47 – 52 %
2-2	20 – 30 – 35 – 40 – 45 – 50 %
3-8	30 – 40 – 50 – 55 – 60 – 60 – 60 %
4-3	15 – 25 – 35 – 40 – 60 %

Table 5-5. Loading sequence of cycle blocks for heat build-up on 8 tons sub-ropes at 0,1 hertz.

We performed another test with two frequencies, to challenge the fact that the dissipated energy evaluation should be intrinsic to the cable and therefore not dependant on the test frequency.

Name	Sequence of cycle blocks (Load maximal in % of MBL)
4-2	63 (0.05 Hertz) – 63 % (0.1 Hertz) – 63% (0.1 Hertz)

Table 5-6. Loading sequence of cycle blocks for heat build-up on 8 tons sub-ropes at different frequencies.

5.4.1. Reliability of the experimental protocol

In this section, repeatability of the heat build-up protocol is discussed for the 8 ton sub-ropes. For these specimens four questions are investigated: the repeatability in terms of dissipated energy, the effect of loading sequences in terms of dissipated energy, the fatigue result, and lastly the influence of frequency.

5.4.1.1. Repeatability

Figure 5-16 presents the result obtained on four samples of 8 ton sub-ropes. Results are quite scattered. Furthermore, we observed during the test different wetting conditions due to the sprinklers precise locations, and it clearly influenced most of our tests and the repeatability of the results. This is clearly shown on sample 4-3, that presents the same tendencies as the sample 2-1 but for much higher dissipated energy.

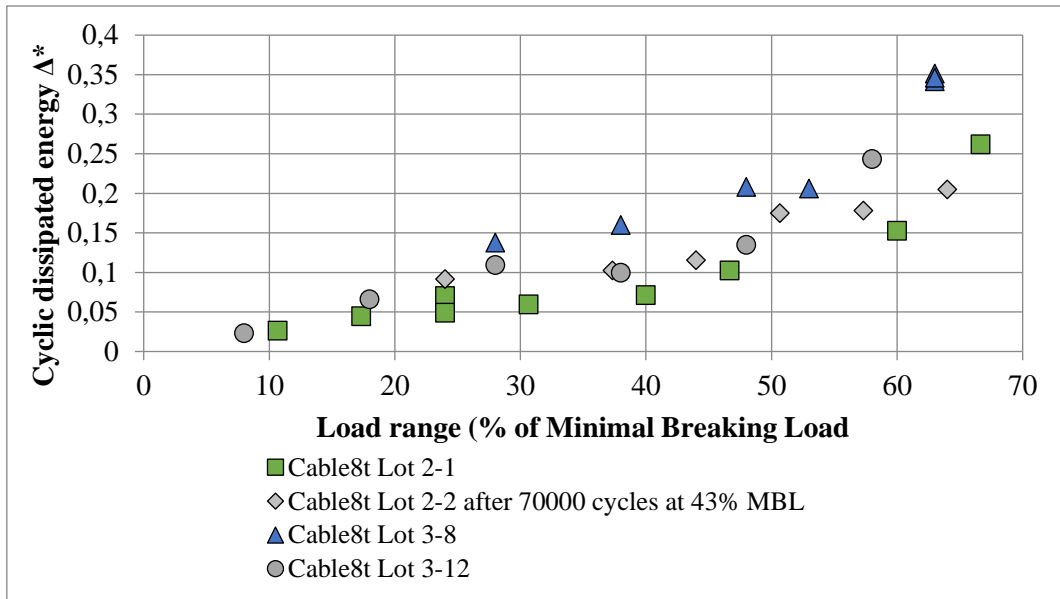


Figure 5-16. Heat build-up curve for 8 tons sub-ropes.

The repeatability for the heat build-up seems quite poor, with differences in term of absolute values and sometime even in shape at higher load range. As noted previously, the τ_{eq} (thermal constant) evolves in this test much more than for the 4T test. This change in τ_{eq} indicates that the sprinkler is not the best wetting method, as its position influences the amount of water on the rope at the observation points. This leads to scatter in the measurements of dissipative energy. This raises the question of which curve should we base our analysis on, so we must keep one full test in one sequence with a good control of water and a consequent number of steps. For all these reasons, analysis will be performed on the test made on sample 2-1.

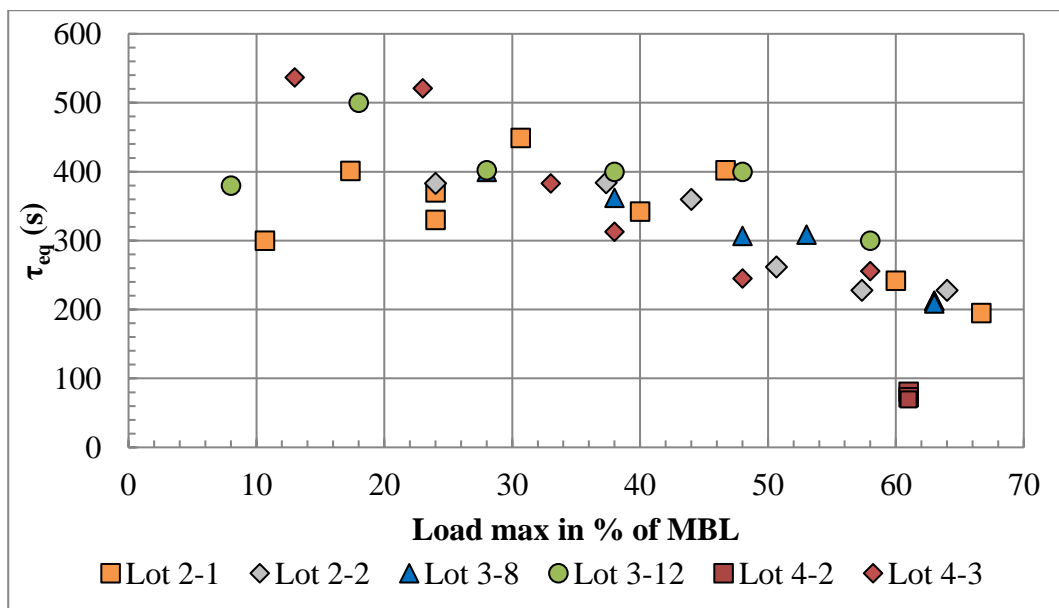


Figure 5-17. Evolution of the characteristic time as a function of the load range.

5.4.1.1.1. Influence of the frequency and of the loading history

Figure 5-18 presents results for one sample (4-2) tested at the same load with different frequencies. For this test, a heat build-up cycle block has been applied at a frequency of 0.05 Hz. Then as previously, a block has been applied at 0.1 Hertz (twice) then the sample was broken in fatigue at the same load range of 60% of MBL. This result confirms a good repeatability of the dissipated energy, as the differences between the different frequencies are lower than between two tests at the same frequency, indicating that evaluation of the dissipated energy leads to intrinsic measures.

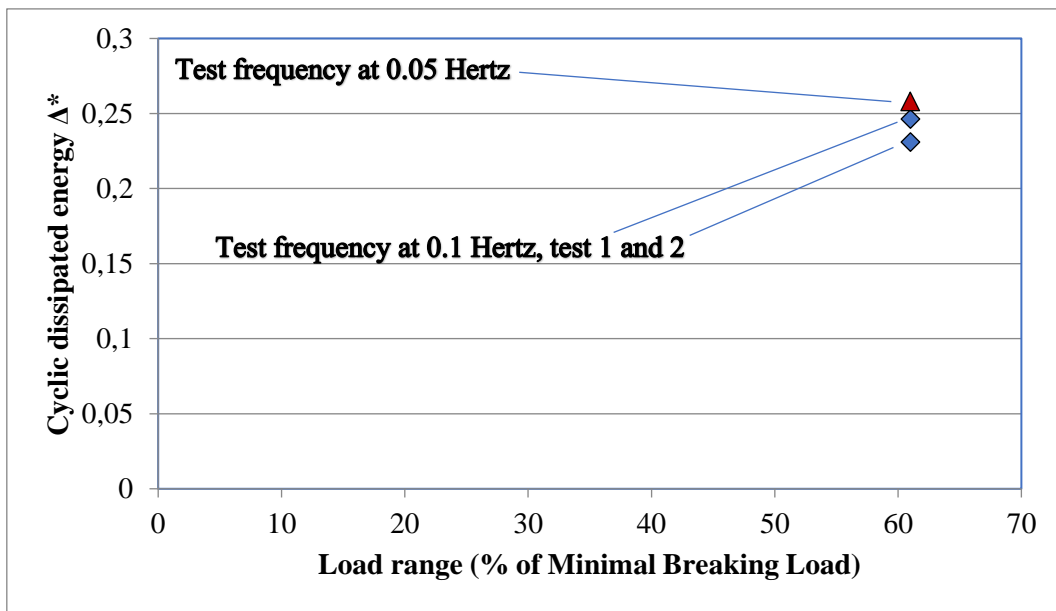


Figure 5-18. Heat build-up curve for 8 ton sub-ropes, influence of frequency (specimen 4-2).

It also seems that the number of cycles obtained for the last block is consistent with the other fatigue results. The lifetime of 2277 cycles for 61% of MBL is similar to results from other samples broken after a heat build-up sequence at a close load range of 63% of MBL (1745 cycles and 4446 cycles).

5.4.2. Prediction of the Wöhler curve and qualification of the analysis

5.4.2.1. Identification of regimes

Figure 5-19 presents the analysis made on sample 2-1 as this test has the highest number of steps and as no change due to wetting was observed on this test. As for the 4 ton sub-ropes, we can suggest 3 regimes, identified by straight lines (*Serrano, 2017; Marco, 2017; Leveuf, 2018*). Even if the last regime is not well identified as we have

only two points this does not matter as we will not use it for the analysis (as the load range higher than 60% will not be used in service). This time, we find a transition between regime 1 and regime 2 around 37.5% for the 8 ton sub-ropes and a transition between regime 2 and regime 3 around a load range of 56% of MBL.

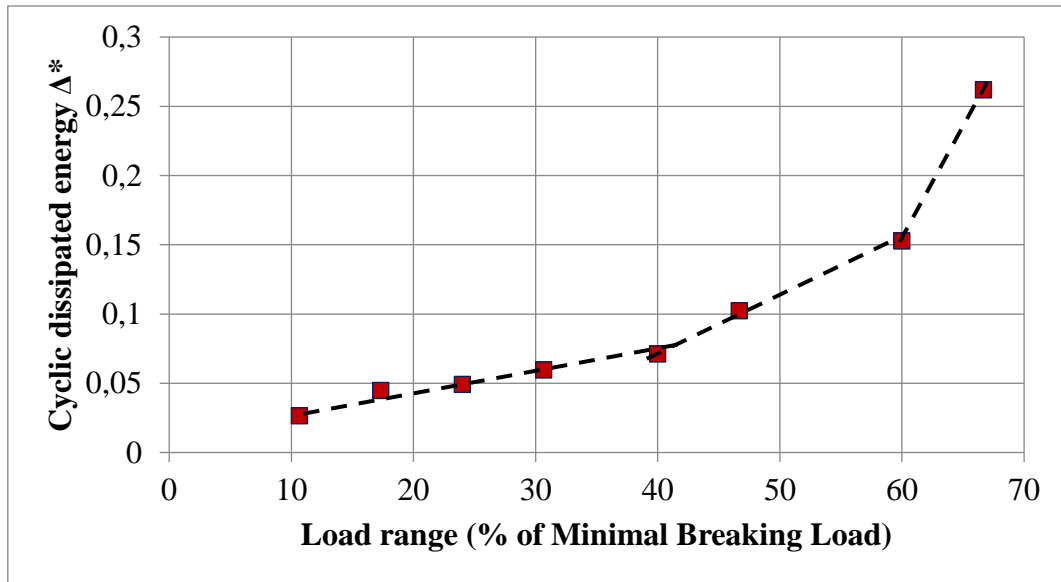


Figure 5-19. Heat build-up curve for 8-ton sub-ropes (specimen 2-1) and fit of the heat build-up curve for the evaluation of the dissipated energy.

5.4.2.1. Fatigue criteria

As for the 4 ton ropes, we use equation (8) presented in chapter 5.3.2.2.

We take two couples of data (Δ^* , N) in order to evaluate parameters b and C of the fatigue criteria. For this criteria, the same sample (2-1) is used, with the point of failure (0,262; 639) and the change between regime 1 and 2 (0,0713; 10^6). The identified values are $b = 0.176$ and $C = 1.876 \text{ J/m}^3$.

As we do not have test samples with a long lifetime (around 10^6 cycles), we cannot validate our model on these lifetimes. However with the fatigue tests we have a quite good description of the fatigue curve between the two evaluated points, so we will verify if the non-linearity of the curve is well described in Figure 5-20.

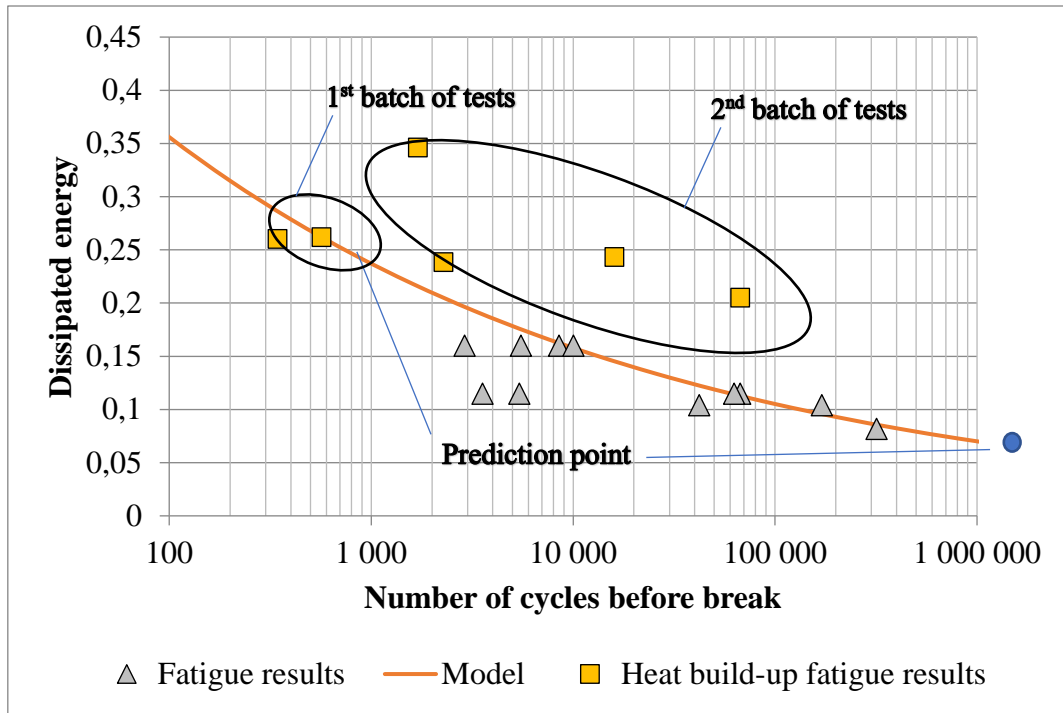


Figure 5-20. Cyclic dissipated energy in function of the number of cycles comparison with fatigue result based on the heat build-up curve of sample 2-1.

This curve shows a reasonable agreement with the prediction of the model over the range used for the determination of the parameters b and c . We can also observe quite a high scatter in the dissipated energy results for the different heat build-up tests. This change between the different batches may be caused by the experimental setup of the water sprinklers, as these tests were made on a different date.

Figure 5-21 presents the final analysis made in fatigue with the heat build-up curve on one sample (2-1). This curve presents the model identified with the two parameters b and C and compares them to the fatigue results obtained in chapter 4.

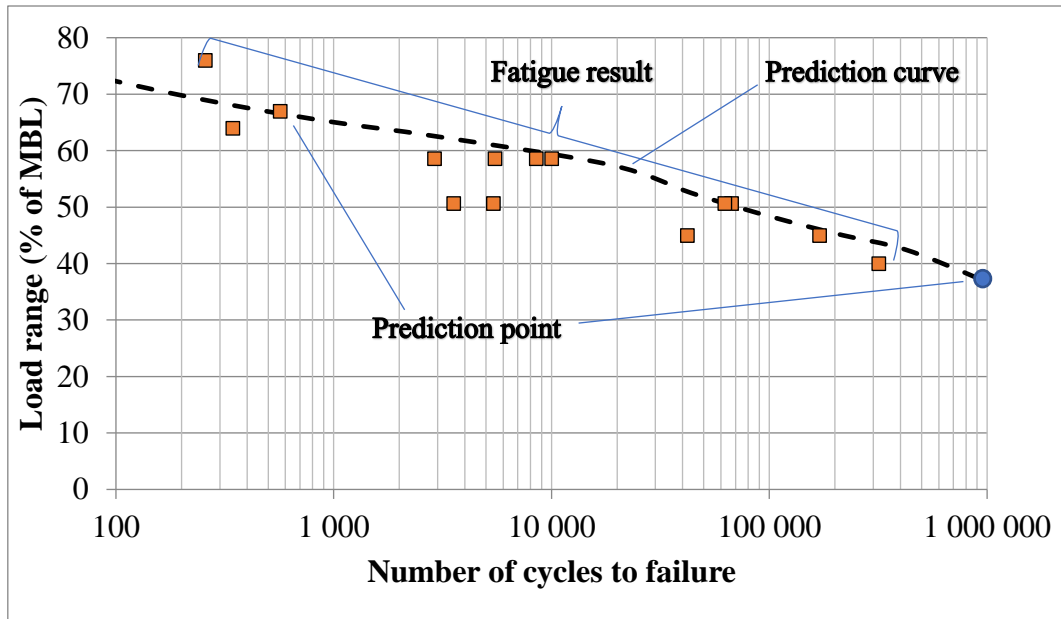


Figure 5-21. Prediction of the fatigue curve for 8 tons sub-ropes by means of the heat build-up method.

The correlation between the Wohler curve obtained using classic fatigue tests and the one predicted by the self-heating criterion appears reasonable. However, the predicted curve is higher than most of the fatigue results. Indeed, our observation of the rope is made in the central part of the specimen and not where the failure happens near the end of the splice, so this may reflect the stress concentrations of the splice ends.

5.5. Comparison between the 4T and 8T sub-ropes

In this section, we will compare the heat build-up method applied on the 4T and 8T sub-ropes, bearing in mind that these were performed on a vertical and a horizontal testing machine respectively. However, as we have different wetting methods in the two cases, the global Rho and Cp differ. So, we do not have the true dissipated energy Δ^* , and we should only compare the trends of the curve.

However, we have a similar twisted construction, in a similar environment. To compare them, we can plot the results in N/TeX , Figure 5-22 (a). We discern a change from regime 1 to regime 2 at a higher load range which is consistent with the fatigue results, as explained in chapter 4. Comparing now the two results in % of breaking load, Figure 5-22 (b) shows that the heat build-up curves are very close to each other.

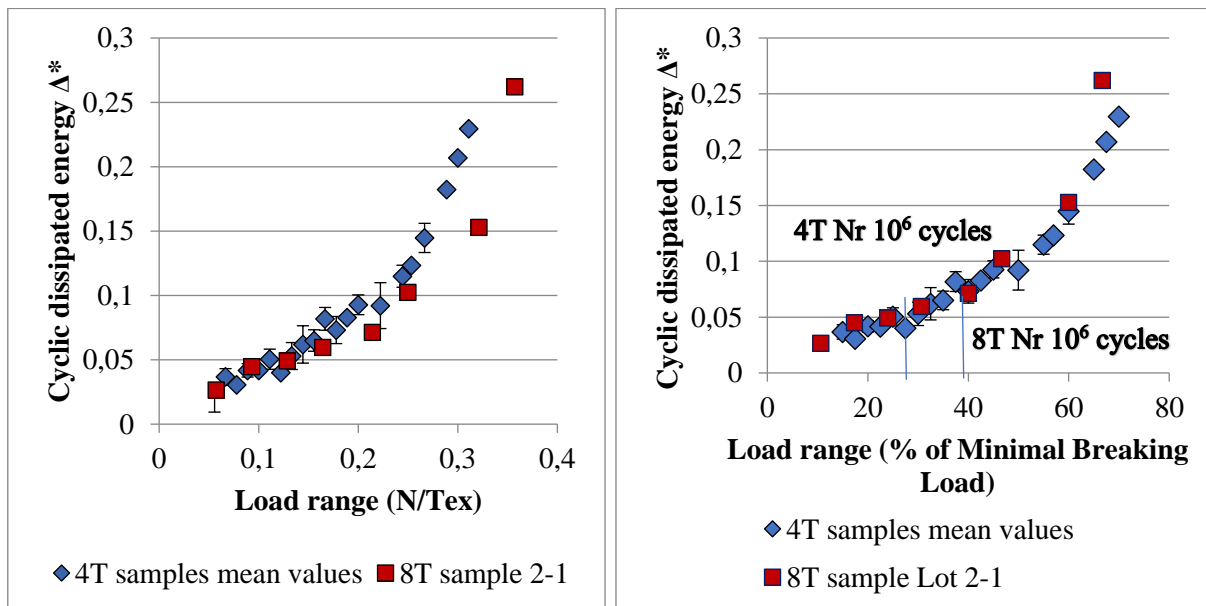


Figure 5-22. Heat build-up curve comparison between 4T and 8T in N/tex (a) and % of MBL (b).

Considering now the fatigue results, we can clearly observe the effect of the lay-length when comparing the two sample types in terms of specific stress (Figure 5-23). This effect is consistent with the change of regime on the heat build-up curves (Figure 5-22), as the 4T samples have a lay-length of about 50 mm for a fatigue lifetime of 10^6 cycles at 0.12 N/tex and the longer 8T lay-length for a fatigue lifetime of 10^6 cycles at 0.21 N/tex . The results plotted in % of MBL are much closer to each other; with values almost superposing up to the last block.

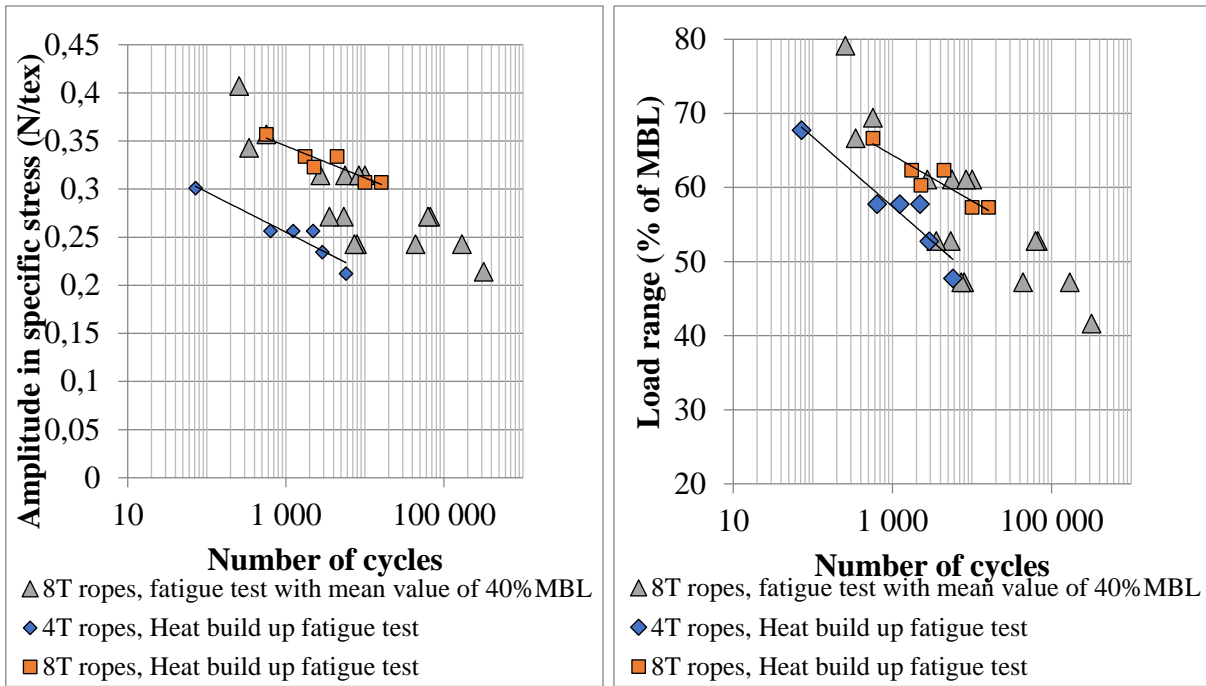


Figure 5-23. Fatigue result comparison between the different tests.

Comparing the two mean failure predictions in Figure 5-24 using a normalized parameter (% of MBL), we observe that the results are close, even if the tendency of smaller lifetimes for the 4 ton compared to 8 ton is still usable and well described by the heat build-up prediction.

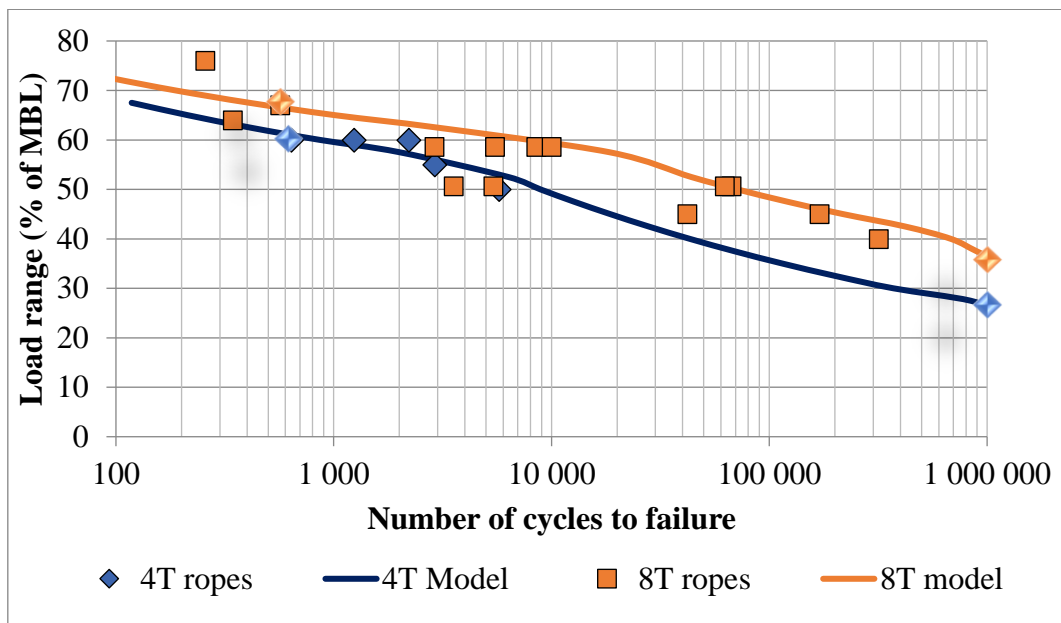


Figure 5-24. Predicted fatigue plots based on the energetic criteria and the two data points used to construct the prediction curve.

5.6. Summary

The objective of the study was threefold. The first aim was to define an experimental set up and a protocol to evaluate the dissipated energy from temperature measurements, for ropes immersed in water. The second objective was to define a rapid evaluation method to obtain fatigue properties of ropes based on the heat build-up curve. Then the last objective was to compare the results from tests at two scales, 4 tons and 8 tons break load, for heat build-up and fatigue.

First an evaluation of an apparent dissipated energy was generated from temperature measurements. Then the heat build-up curve was generated from 6 specimens for the 4 ton sub-ropes and 5 specimens for the 8 ton sub-ropes. Reliability tests were performed on these samples to challenge the validity of the protocol. Secondly, the fatigue curve was predicted from the heat build-up curve, first by a graphical evaluation, then by identifying an energy based criterion to relate the number of cycles to failure to the dissipated energy.

The application of a protocol for the fast determination of the fatigue properties has been assessed on 4T sub-ropes. It shows promising results, and clear trends for fatigue lifetimes which are in agreement with classic fatigue test results. This now needs further validation at lower load ranges such as the tests made on the 8T sub-ropes. Such tests have been validated on 8T sub-rope, but the test setup was not optimal, as the water sprinklers produce less continuous wetting, so the results are more difficult to analyse. Nevertheless, results are similar to those for the 4T sub-rope. This is promising for the application on bigger sub-ropes. Comparison between the ropes shows similar heat build-up behavior, however a quantitative comparison is not yet possible, due to unknown parameters in the evaluation of the dissipated energy.

In summary, an apparent dissipated energy was measured but not related to the structure of the ropes. An evaluation of the dissipative energy using the linear density and the apparent section of the rope would be interesting in order to compare the two kinds of specimens. Testing different ropes with only one parameter change would help assessing the accuracy of the method. A rapid evaluation of the fatigue properties was performed in a one/two day test, and provides convincing results, but low load fatigue results (long lifetimes) are now needed to confirm our evaluation at 10^6 cycles.

5.7. Reference

- Abello, L.S., Marco, Y., Le Saux, V., Robert, G. and Charrier, P., 2014, June. Fast prediction of the fatigue behavior from heat build-up measurements: application to short fiber reinforced thermoplastics under various loading conditions. In *Proceedings of the 16th European Conference on Composite Materials* (pp. 22-26).
- Chrysochoos, A., & Louche, H. (2000). An infrared image processing to analyse the calorific effects accompanying strain localisation. *International journal of engineering science*, 38(16), 1759-1788.
- Doudard, C., Calloch, S., Cugy, P., Galtier, A., & Hild, F. (2005). A probabilistic two-scale model for high-cycle fatigue life predictions. *Fatigue & Fracture of Engineering Materials & Structures*, 28(3), 279-288.
- Jegou, L., Marco, Y., Le Saux, V., & Calloch, S. (2013). Fast prediction of the Wöhler curve from heat build-up measurements on Short Fiber Reinforced Plastic. *International Journal of fatigue*, 47, 259-267.
- La Rosa, G. and Risitano, A., 2000. Thermographic methodology for rapid determination of the fatigue limit of materials and mechanical components. *International journal of fatigue*, 22(1), pp.65-73.
- Launay, A., Maitournam, M. H., Marco, Y., Raoult, I., & Szmytka, F. (2011). Cyclic behaviour of short glass fibre reinforced polyamide: Experimental study and constitutive equations. *International Journal of Plasticity*, 27(8), 1267-1293.
- Leech, C.M., 2002. The modelling of friction in polymer fibre ropes. *International Journal of Mechanical Sciences*, 44(3), pp.621-643.
- Leveuf, L., Marco, Y., Le Saux, V., Navrátil, L., Leclercq, S. and Olhagaray, J., 2018. Fast screening of the fatigue properties of thermoplastics reinforced with short carbon fibers based on thermal measurements. *Polymer Testing*, 68, pp.19-26.
- Le Saux, V., Marco, Y., Calloch, S., Doudard, C. and Charrier, P., 2010. Fast evaluation of the fatigue lifetime of rubber-like materials based on a heat build-up protocol and micro-tomography measurements. *International Journal of Fatigue*, 32(10), pp.1582-1590.
- Le Saux, V., Marco, Y., Calloch, S., Charrier, P. and Taveau, D., 2013. Heat build-up of rubber under cyclic loadings: Validation of an efficient demarch to predict the temperature fields. *Rubber Chemistry and Technology*, 86(1), pp.38-56.
- Le Saux, V., 2017. Belenos users manual. *Internal report, ENSTA Bretagne*.
- Marco, Y., Masquelier, I., Le Saux, V., Calloch, S., Huneau, B. and Charrier, P., 2013. Contributions of IR thermography and X-ray tomography to the fatigue characterization of elastomeric materials. *Constitutive Models for Rubber VIII*, pp.25-28.
- Marco, Y., Le Saux, V., Jégou, L., Launay, A., Serrano, L., Raoult, I. and Calloch, S., 2014. Dissipation analysis in SFRP structural samples: Thermomechanical analysis and comparison to numerical simulations. *International journal of fatigue*, 67, pp.142-150.
- Marco, Y., Masquelier, I., Le Saux, V. and Charrier, P., 2017. Fast prediction of the wöhler curve from thermal measurements for a wide range of nr and sbr compounds. *Rubber Chemistry and technology*, 90(3), pp.487-507.
- Masquelier, I., Marco, Y., Le Saux, V., Calloch, S. and Charrier, P., 2015. Determination of dissipated energy fields from temperature mappings on a rubber-like structural sample: Experiments and comparison to numerical simulations. *Mechanics of Materials*, 80, pp.113-123.
- Morrow, J., 1965. Cyclic plastic strain energy and fatigue of metals. In *Internal friction, damping, and cyclic plasticity*. ASTM International.

Navrátil, L., Marco, Y., Le Saux, V., Leclercq, S. and Carrère, N., 2019, July. Investigation thermomécanique pour le dimensionnement en fatigue des composites tissés 3D. In *21ème Journées Nationales sur les Composites*.

Parsey, M.R., 1983. *The fatigue resistance and hysteresis of man-made fibre ropes*, Proc. Offshore Europe, September 1983, SPE-11908-MS, Society of Petroleum Engineers, .

Seo, M., Wu, H.C., Chen, J., Toomey, C.S. and Backer, S., 1997. Wear and fatigue of nylon and polyester mooring lines. *Textile research journal*, 67(7), pp.467-480.

Serrano, L., Marco, Y., Le Saux, V., Robert, G. and Charrier, P., 2017. Fast prediction of the fatigue behavior of short-fiber-reinforced thermoplastics based on heat build-up measurements: application to heterogeneous cases. *Continuum Mechanics and Thermodynamics*, 29(5), pp.1113-1133.

Chapter 6: Conclusions and further work

Table of contents

6. Conclusions and further work	200
6.1. Conclusions	200
6.2. Further work	203

6. Conclusions and further work

6.1. Conclusions

This PhD work investigated the mechanical behavior and the fatigue properties of Polyamide 6 mooring sub-ropes for floating offshore wind turbines under relevant loading and environmental conditions. These investigations focussed on a design approach to assess the mechanical behaviour and the durability of these polyamide ropes, for near shore mooring application.

The main outcomes and conclusions of this work are the following:

1) A first objective of this project was to characterize the constitutive response under cyclic loading of the ropes and to provide, identify and challenge a constitutive model. Several additional constraints needed to be considered, on experimental conditions (material in a wet state) as well on modelling (simple enough to be implemented in industrial softwares). A wide characterization campaign has been achieved on water-saturated 4-ton MBL sub-ropes, which were kept underwater during tests that may last up to two days. This campaign is original in the literature and therefore provides an interesting database for model identification and validation. Based on the literature models and on the experience of the project partners, a phenomenological model has been suggested. The identification of the model parameters is achieved using a step-by-step direct procedure and is based on a complex cyclic test using several cyclic loadings interrupted with relaxation steps. The model involves 12 parameters but is using only two internal variables (viscous strain and plastic strain), which limits its numerical cost. A numerical implementation was done and the comparison of the model predictions to experimental results was performed on monotonous tests at different strain rates and cyclic tests with multi-creep/recovery. It appears that the three main features of the constitutive response (dynamic elasticity, time independent behaviour and plasticity) are in good agreement with the experimental data and this for a wide range of strain and stress. Nevertheless, the viscous behaviour is too simple to catch creep or relaxation effects after large unloading or for very long times. Improvement could be easily made from a modeling point of view by adding more characteristic times, but it will also lead to a much more complex identification procedure.

As a conclusion on these aspects, this constitutive law and the identification method offer a way to characterize most of the aspects of the intricate visco-elasto-plastic behavior of polyamide ropes and provide an applicable and practical tool to be integrated in commercial software to design moored floating platforms.

2) A second objective was to characterize long-term creep response both for yarns and 4-ton MBL sub-ropes. Tests on the latter scale are indeed not so common and a specific testing device was entirely designed and manufactured in ENSTA Bretagne during this project. Four sub-ropes samples have been tested for durations up to 8 months. The results showed logarithmic strain rates of around 0.12%/decade for yarns and around 0.19%/decade for sub-ropes. This appears to indicate the necessity for long term creep testing. However, a comparison with multi-creep test results for sub-ropes showed that these short creep tests (30-minute-long) provide a reasonable prediction of the long-term creep evolution.

3) A third objective was to investigate the durability properties of nylon ropes. A yarn coating was selected, based on yarn on yarn abrasion tests which showed a significant improvement compared with non-coated yarns. Then, fatigue tests were performed with a load range between 40 to 70 % of MBL on 4-tons and 8-tons sub-ropes. To do so and to master the watering conditions, specific machines were used both in Ifremer and ENSTA Bretagne, and experimental set-ups developed when needed. When compared to published results for other mooring systems, fatigue lifetimes were found to be superior to steel chain and similar to the ISO test results for polyester rope. One of the main conclusion of the project is therefore that the ropes developed by BEXCO in this project should exhibit appropriate durability for fatigue requirements for a long-term marine use. The comparison between 4-tons and 8-tons sub-ropes reveals that because of a shorter lay length, lifetime is shorter for 4-tons ropes, even if the fatigue properties remain similar in tendencies and order of magnitude. The difference is around 0.1 N/tex and 10% when plotted in % of MBL.

4) The last objective was to evaluate the potential of a technique based on heat build-up measurements to evaluate quickly the fatigue performances of the ropes. There were several challenges, with dissipation sources coming both from the thermoplastic material and from the friction between the ropes elements, and the need to characterize the ropes immersed in water. Once again, specific experimental set-ups were designed and validated for 4-tons and 8-tons sub-ropes. In both cases, it was possible to generate the heat build-up curves, relating the load to the evolution of dissipated energy, even if the results were more repeatable for 4 tons sub-ropes, which were tested with a better controlled vertical watering system. For both scales, it was possible to quickly evaluate the fatigue mean curve based on the evolution of the dissipated energy. Indeed, a fairly good prediction of the fatigue mean curve can be obtained from the heat build up technique on synthetic ropes, leading to the prediction of a fatigue curve in less than 2 days. The next step will be to perform longer fatigue tests to assess the prediction of the technique for large number of cycles.

The results from this project will be able to help industrial companies to design a polyamide 6 mooring line for long-term service with more accuracy in terms of modeling, fatigue, long-term property predictions and possibly on choice of the rope structure, based on the quick fatigue evaluation. However, as the project was studying a wide range of properties, not all the results can be directly transferred to industrial application. Some suggestions for further developments are presented in the paragraph below.

6.2. Further work

For the different parts of the study the following future work could be performed:

1) For the constitutive response and behavior law, three points can be considered. First a better characterisation of the viscosity could be made, based not only on the first loading but also on the reloading and unloading phases. Second, characterization should be realized on the full size sub-ropes to determine the model parameters for the real application, or at least by tests on samples with the right lay length should be performed. Third, an additional damper representing the long term creep could be used for very long term prediction, but for now, we do not yet know to what extent the creep evolution based on our tests is recoverable, so this should be a priority.

2) For this reason, recovery after creep should be envisaged after the one year creep test on our sub-ropes, to evaluate how much permanent strain was accumulated and to examine the recovery kinetics. Residual strength testing would then also be of interest.

3) For fatigue study, the different fatigue performance between batches is quite intriguing, and finding the cause should be the focus of further study, as no parameters were changed between the batches. Fundamental studies of the changes of polymer fibre microstructure and yarn coating with time should enable these differences to be understood and lead to improved industrial products.

4) One other important point for permanent mooring lines is long-term loading at low load. However, in this (and most other) fatigue programme tests were performed at fairly high loads in order to achieve results within the available time frame. This means that it was not possible to approach even 10^6 cycles. It therefore limits the validation for longer tests, leading to around 10^6 cycles. To do so, a possible way in this load range would be to increase test frequencies, which could be investigated on some of our devices and calls for further tests.

In addition to these specific points there are many other topics of interest related to mooring of MRE structures. One which is particularly urgent is the need to know the state of mooring lines in service, so that maintenance can be programmed. This relies on a thorough understanding of rope behaviour so that appropriate measurement devices are developed, and the results from the present project will be the basis for a new FEM/ANR project which has just started on monitoring of mooring lines.

Chapter 7: Appendix

7. Appendix

7.1. Long term creep device

7.1.1. Design specifications

The specifications of the creep bench are summarized in the following Table 7-1.

Function	Characterization of functions	
	Criterion	Level
FC1: Adapt to the sample	No stress concentration	–
	Consideration of fibre elongation during loading	maximum 30% total strain
	Consideration of fibre elongation during creep	
	Loop axis diameter	25 to 75 mm
FC2: Number of specimens	Perform several tests at the same time	3 to 4
FC3: Avoid transverse forces in the fibres	Blocking of cable rotation (intrinsic torque)	–
	No force return on the cable (pulley,...)	20 Newton
FC4: Monitor the elongation state of the rope	Frequency of elongation measurement during loading	10 Hz
	Frequency of elongation measurement during creep	2 to 3 per day after a certain time
	Accuracy of local elongation measurement	0,01 % of ϵ
FC5: Perform the immersed	Submerged cable length	Minimum 500 mm

creep test on a controlled and homogeneous part	Immersion liquid	Tap water
	Immersion liquid temperature	Measured or kept constant near 20°C
FC6: Adapt to the load to be applied	No indentation effect of the attachment of the fibres to the load	–
	Ease of loading protocol	–
	Easy access for the loading of the structure	–
FC7: Resist the applied load	Safety factor	3 for the main structure
	Deformations of the structure do not affect the elongation measurement	Strain < 0,01% de ϵ
	Controlled buckling	–
FC8: Adjust the applied load	Knowing the applied mass, load sensor	-
	Mass decomposed into separable blocks	150, 360, 500 kg mass
	Maximum load applied at the same time	20 kN on three samples or 30 kN on two samples.
FC9: Resist the ambient environment	Samples protected from the sun	–
FC10: Respect the environment	No polluting materials	–
FC11: Adapt to the available energy	Type of energy available	Standard current EDF - 220 Volt
FC12: To fit into the space allocated in the mechanical laboratory	Floor space requirement	4 m x 1,5 m
	Maximum height	4 m
	Can be dismantled (storage after/between uses)	Bolted assembly preferred
FC13: Safety standard of the mechanical laboratory	No risk of tipping over	Fixing to the wall
	Observe the maximum stress on the ground	10 kN/m ²
FC14: Ensure operator safety	Protection of sensitive parts of the machine (whipping effect in case of sample breakage)	Tube around the sample
	Marked-off area around the creep machine	1.5 meters
FC15: Monitoring of the test	Accessibility of the measurement	–
FC16 : Cost	Within the project budget	Max 30 000 €

Table 7-1. Functional specifications of the creep test machine.

7.1.1. Static resistance

The Euler–Bernoulli beam theory allows for quick and reliable design and thickness choice of the main structure.

The initial conditions are as follows. Y-shaped movement blocked for the base and fixing of each end in the XZ plane. Three 3-tonne forces are distributed in the central area of the upper structure representing applied loads, knowing that in reality the force will be distributed over some part of the beam due to the upper bracket. Three forces of 2 tons at the bottom represent the cable forces.

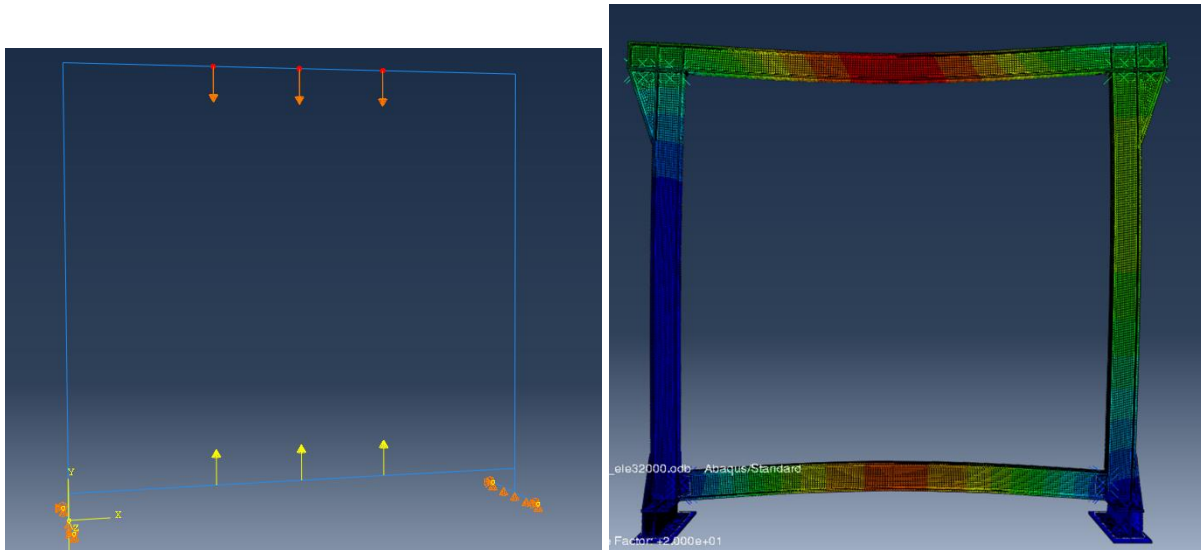


Figure 7-1. Beam stress simulation of the maximal loading of the testing machine.

For the main component of the structure, a safety coefficient of 3 was taken, as people may be close to the creep testing machine. The second criterion for the structure is its deformation, as we do not want too much displacement between the beams which could affect the displacement measurements. From the simulation, at full capacity we only have a 3 mm displacement, which is reasonable, considering that the length of the ropes tested are 2000 mm.

7.1.1.1. Soil loading

Classic values for concrete strength are around 20 MPa in compression. If we consider that the load is fully distributed we find that the stress imposed by the gantry is:

$$\frac{\text{Weigth}}{\text{Foot surface}} = \frac{4000 \cdot 9.81 \text{ Newton}}{0.22 \cdot 1.2 + 0.22 \cdot 1.2 \text{ m}^2} = 0.074 \text{ MPa.}$$

Even, if we consider that our effort is only propagated under the column the effort remains largely admissible: $\frac{4000 \cdot 9.81}{0.22 \cdot 0.22 \cdot 2} = 0.4 \text{ MPa}$

7.1.1.2. Buckling

The two lateral beams are subjected to a bending moment from the base which will facilitate buckling, so we needed to quantify the load needed for buckling. A finite element model was run with *RDM6 Le mans*, and a final analysis was performed using *Abaqus* for the main beams with the maximal loading of 2 tons on each rope. The results obtained lead to a security factor well above 3.

Mode	Values
1	12.88
2	-13.307 (Not happening)
3	15.165
4	-17.992 (Not happening)

Table 7-2. Bucking results for the long-term creep device.

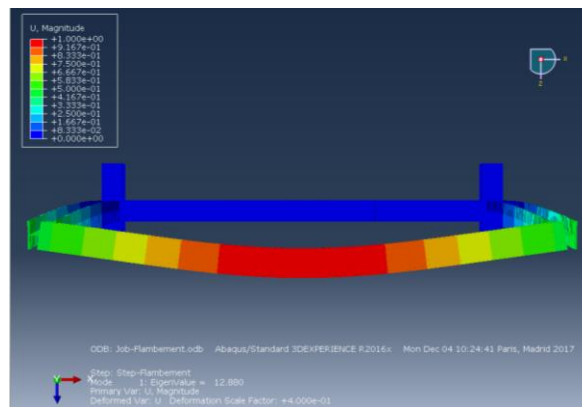


Figure 7-2. First buckling mode of the long-term creep device (view from above).

7.1.1.3. Eigen frequency analysis

The last point evaluated for the main frame is the modal analysis and the determination of the eigenfrequencies. Simulation of an elastic model with *Abaqus* gives the following eigen frequencies:

Mode	Frequency (Hz)
1	6.3882
2	8.8790
3	14.527
4	29.47

Table 7-3. Eigen frequency of the long-term creep device.

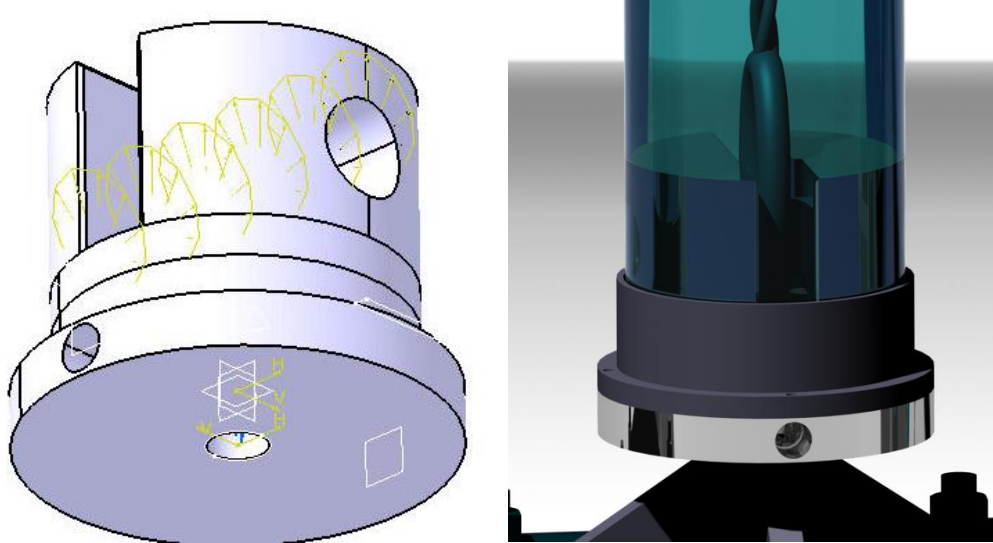


Figure 7-4. Lower jaw design.

7.1.1.6.1. Lower bracket

The lower bracket is the part directly connected to the jaws, and will be subjected to a three ton maximal load when the rope is loaded at its highest capacity (Figure 7-5). The steel used for this part is a standard construction steel S235.

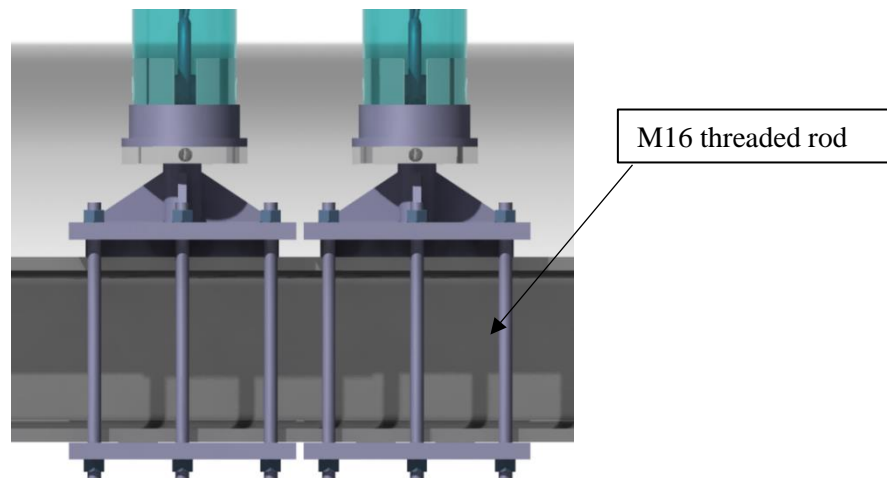


Figure 7-5. Lower bracket design.

Numerical evaluation of the stress in each rod and the welds was performed according to the Eurocode 3 calculation rules. Finally, an elastic simulation was made to ensure no critical stresses are induced, with a safety coefficient of 2.

7.1.1.6.2. Upper bracket

The top bracket is composed of three parts: the first part is attached to the HEB beam, with a clevis and an axis. The second part is the pulley, purchased from Berra Marine for the right steel rope dimension, with an ultimate operating load of $3T$. The third part is a beam between the two pulleys, that withstands the horizontal component of the force.

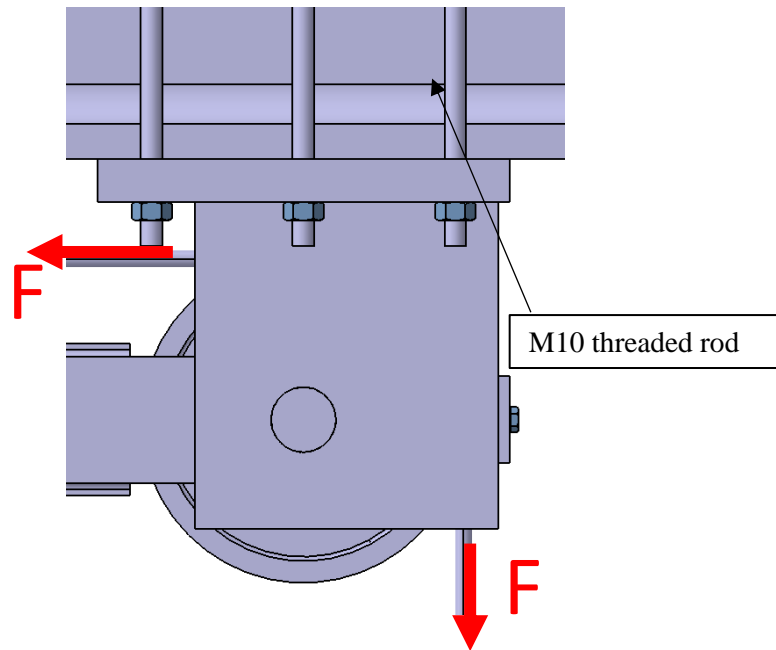


Figure 7-6. Higher bracket.

A similar procedure was used to design the lower bracket. A calculation of the average stress present in the threaded rods was made, then of the weld and of the contact of the cylinder on the hole, followed by three simulations for each part of the structure, to ensure a safety coefficient of 2. Buckling was also evaluated on the beam between the pulley and a safety factor of around 9 was found.

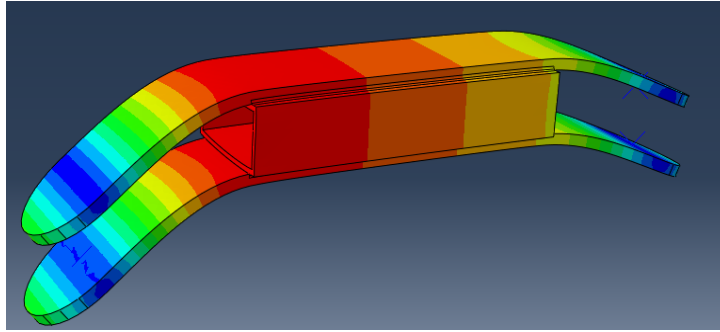


Figure 7-7. Buckling of the central part of the higher bracket.

7.1.1.7. Pulley

Ball bearing pulleys were chosen because it is necessary to accommodate the main frame deformation as smoothly as possible during loading of specimens.

7.1.1.8. Damping in case of rope breakage

The tests are not intended to go up to breakage, however if the rope should happen to break, the fact that the weight (Figure 7-8) will fall should not provoke any breakage of the structure, soil or adjacent equipment.



Figure 7-8. Weight of the long-term creep machine.

Several solutions have been considered, from sand, to safety ropes, and steel shock absorber similar to cars. However, all these proposals have some shortcomings: the sand

is heavy and bulky, the lifeline is connected directly to the structure, and the effectiveness of the bumpers depends on the drop height. The use of a panel of EPS polymer foam was finally preferred, as it allows easy installation of the protection and does not interfere with the setting up of the test. More details can be found in the Appendix.

7.1.2. Long term creep device manufacturing

7.1.2.1. Main frame

The welding of the main frame was performed in-house at Ensta Bretagne. The structure was assembled directly in the building because the size of the apparatus was too high to go through the door (Figure 7-9).



Figure 7-9. Installation of the long-term creep frame.

All other components were also made at Ensta Bretagne either manufactured or welded, only the pulleys, load sensor and HEB claws were purchased for the structure. Some pictures of the making of parts shown bellow.

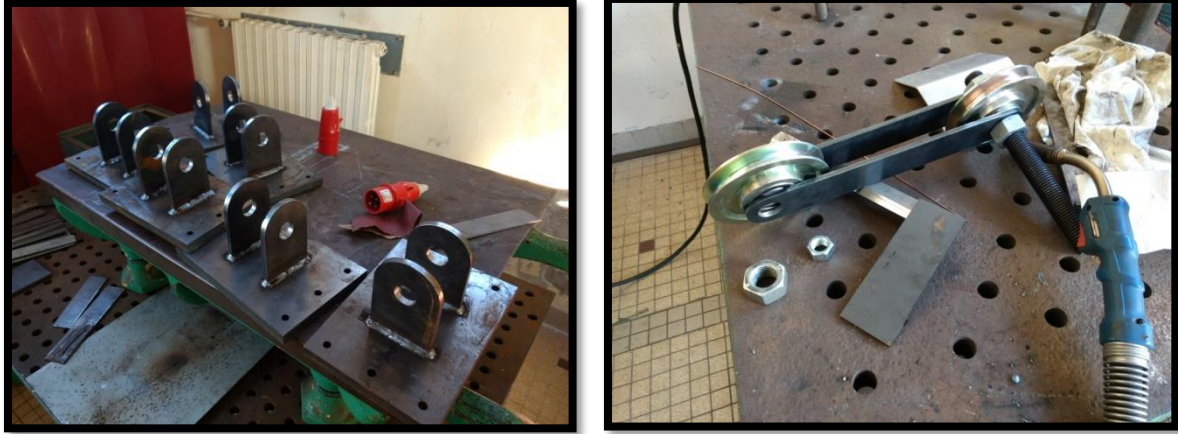


Figure 7-10. Making of the top bracket.



Figure 7-11. Watertightness test of the tube (a) and installing the top bracket (b).

7.1.2.1. Measurement and data acquisition

During the tests, three types of sensor were used: wire-sensor for measuring the strain, load sensor for the force and PT100 thermocouples for the temperature. For the acquisition a CompactRIO allowed the data to be saved directly on a computer or an USB key. One of the risks of a long-term study is related to the measurement drift of the equipment. For this reason, a sequenced acquisition leading to shorter operation time of the electronic system and allowing operation between sequences was used.

With a LabVIEW program it is possible to switch from a manual acquisition program to an automatic program, starting all electrical components for 1 hour for stabilization purposes then recording for a 10-minute duration. The acquisition is usually made 5 times a day in order to account for the evolution of temperature.

7.1.3. Damping in case of rope breakage

With respect to the type of foam, there are three possibilities:

- Elastomer plate absorbs little energy, and is mainly useful for vibrations.
- PU foam, PVC, and PP have a medium damping but are reusable.
- EPS foam, not reusable but high damping and a lightweight material.

Moreover, at the end of the shock depending of the material used, there might be a rebound.

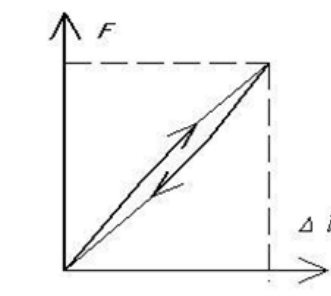
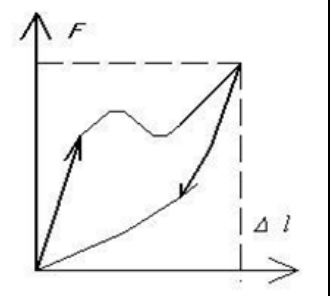
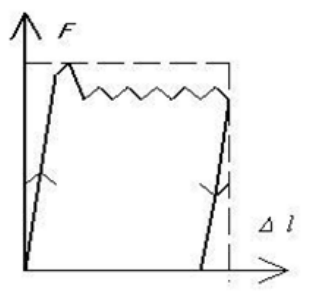
		
Elastic material	Damping material	Brittle material
(Elastomers)	(Foam: PVC, PP; Compressive-buckling: bumper...)	(Foam: phenolic, rigid polyurethane, EPS ...; Malleable material: Honeycomb, aluminium)
Efficiency <0.5	Efficiency between 0.55 to 0.65	Efficiency ~1

Table 7-4. Renault Document (1990).

A first evaluation equation for the shock absorption is the following (Renault Document, 1990):

$$\frac{W}{V} = \frac{F}{S} * Rd * \frac{Dl}{L}$$

With W the energy, V the volume of the damping part, F the load applied, S the contact area, Rd the efficiency, Dl the compressed length, and L the total length.

As failure is not expected, and we do not plan to reuse the safety system, the optimal choice is a brittle material, and the most cost-effective material is EPS foam. Used in insulation applications it is widely available, cheap and easy to cut with a metal wire and an electrical current.

Data from *Techniques de l'ingénieur* and *Kemisol* can be used for designing the damping part. As the heavy block is quite heavy, a dense foam is required but with a large plastic zone to absorb as much energy as possible with the smallest thickness possible. A 30 kg/m³ foam was selected as it has the best ratio between the two and is available easily (Figure 7-12).

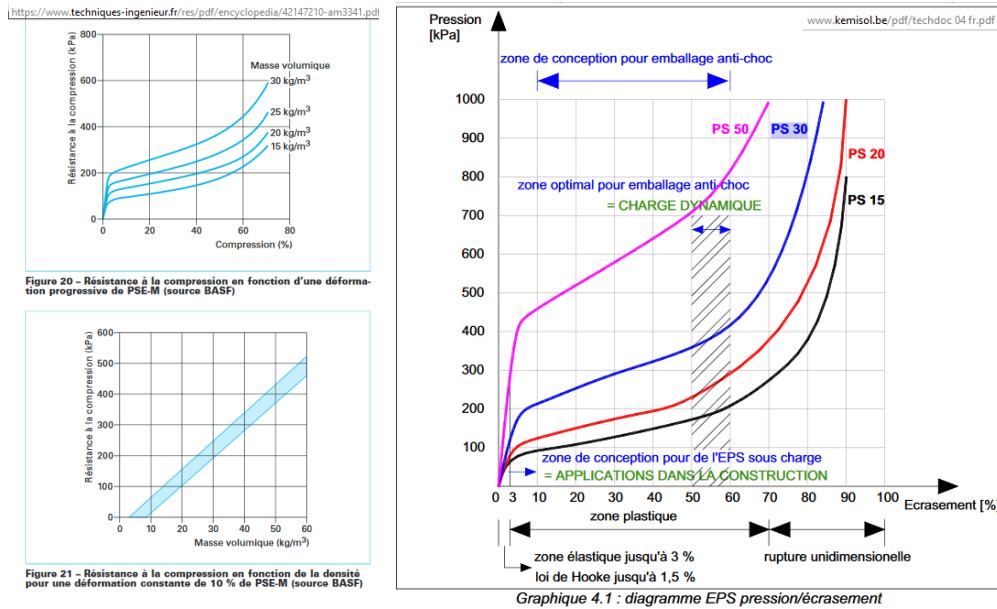


Tableau 2 – Résistances mécaniques pour différentes masses volumiques apparentes de PSE moulé (valeurs pour différents Styropor®, transmises par BASF)				
Résistance	Masse volumique			Normes
	15 kg/m ³	20 kg/m ³	30 kg/m ³	
Compression pour une déformation de 10 %..... (kPa)	65 à 100	110 à 140	200 à 250	NF-EN 826
Rupture en flexion (kPa)	150 à 230	250 à 310	430 à 490	NF-EN 12089
Rupture en traction..... (kPa)	160 à 260	230 à 330	380 à 400	NF-EN 1608

Figure 7-12. Data for impact energy absorption of polystyrene foam (*Techniques de l'ingénieur; Kemisol*).

The part to be damped has the following characteristics at full capacity: it is composed of 4 stacked masses and a support with a surface area of 0.49 m², with the maximum weight of the masses equal to 1500 kg. However, the minimum contact surface between the support and the foam, 0.39 m², can be the worst case.

The next step is to determine the energy produced by the mass drop. In the most critical case, the mass falls from a height of 500 mm leading to a potential energy of 7,360 J or N*m.

From the chart of Figure 7-12, we can extrapolate the minimal energy absorbed by the panels. Using the shock equation formula for a strain of 10%, and an efficiency for EPS foam taken at 0.9, we found the following graph.

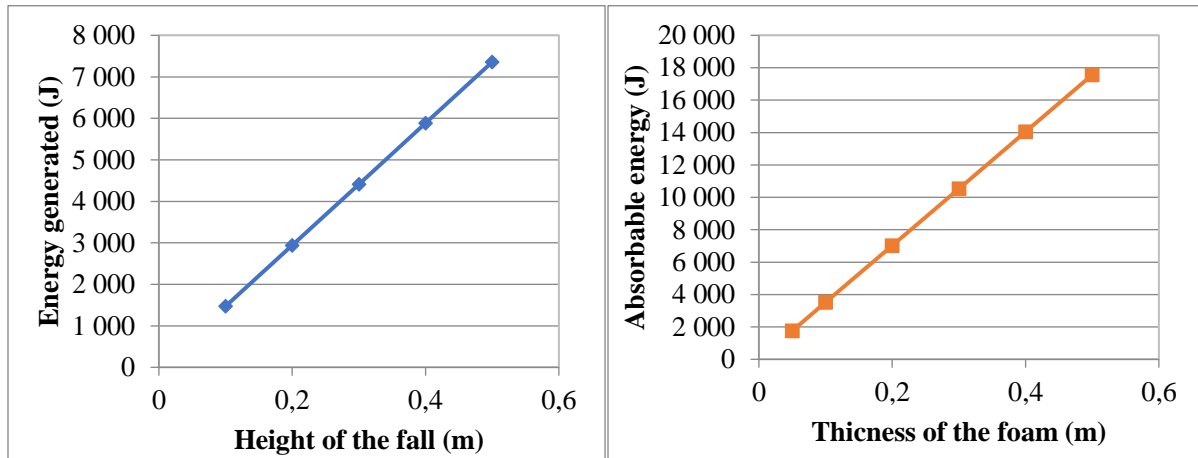


Table 7-5. Energy generated by the weight fall (a), and absorbable energy by the foam protection.

Expanded polystyrene at 30 kg/m^3 allows us to absorb a mass drop only once, but in a particularly effective way. Indeed, a thickness of half the falling distance allows a damping of the mass energy for a compaction (deformation) of 50%.

To have a satisfactory safety factor, a foam thickness of at least 150 mm, and a maximum distance of 200 mm between the foam and the support must be conserved.

Titre : Caractérisation du comportement mécanique à long terme et de la durabilité des câbles d'ancrage en polyamide pour les éoliennes flottantes.

Mots clés : Cable synthétique, Durabilité, Loi de comportement, Polyamide 6, Caractérisation, Eau.

Résumé :

La base de données scientifiques concernant les cordages d'amarrage en nylon est encore très limitée. Le déploiement de ces fibres pour l'ancrage permanent est donc actuellement impossible en raison du manque de données sur leurs propriétés mécaniques. Un des objectifs de cette étude est donc de fournir une meilleure compréhension du comportement mécanique et de l'endommagement par fatigue de ces cordes en polyamide, afin d'aider à la conception de lignes d'amarrage d'éoliennes flottantes.

La présente étude comprend la caractérisation mécanique, la modélisation et la validation de celle-ci.

La première partie étudiée est la modélisation du cordage. La caractérisation sur des sous-cordages de 4 tonnes implique une charge cyclique avec relaxation, permettant la caractérisation du câble avec un seul test. A partir de ce test, il est possible d'identifier chaque partie du modèle et de le valider sur différents tests, avant de le comparer aux résultats des tests effectués sur des sous-cordages de 8 tonnes. Ceci a conduit à un modèle simple 1D visco-élasto-plastique assez proche du comportement du câble.

La deuxième partie concerne les essais de fluage à long terme. Tout d'abord, une brève explication de la conception et de la construction de la machine d'essai sera faite. Ensuite, les résultats de 3 essais d'un an sur des sous-cordages de 4 tonnes seront présentés et comparés à d'autres résultats. Les résultats montrent des valeurs de fluage similaires à celles du polyester et peuvent être utilisés pour prédire si une remise en tension de la corde sera nécessaire.

Dans la troisième partie, la durabilité du câble en polyamide sera évaluée. Tout d'abord, des tests d'abrasion ont été réalisés, afin de s'assurer que le revêtement utilisé est suffisant pour valider la résistance à l'abrasion sur des mèches de fils. Ensuite, des tests de fatigue standard ont confirmé que les durées de vie des cordages en polyamide sont largement suffisantes pour un amarrage permanent, avec une durée de vie supérieure à celle de la chaîne en acier même si un peu inférieure à celle du polyester.

Enfin, une évaluation rapide de la fatigue par des tests d'auto-échauffement a été réalisée. Un résultat prometteur basé sur la mesure thermique de l'énergie dissipée du câble a permis de prédire sa durée de vie en fatigue en moins de deux jours.

Title : Characterization of the long-term mechanical behavior and the durability of polyamide mooring ropes for floating wind turbines.

Keywords : Rope, Durability, Constitutive law, Polyamide 6, Mooring, Characterization.

Abstract:

The scientific database for mooring nylon rope is still very limited, thus the deployment of these fibres for permanent mooring is currently impossible due to the lack of data on their mechanical properties. One of the goals of this study is therefore to provide a better understanding of the mechanical behavior and the fatigue damage of these polyamide ropes, in order to help designing floating wind turbine mooring lines.

The present study involves mechanical characterization, modeling and its validation.

The first part investigated is the modeling of the rope. The characterization on 4 tons sub-ropes involves cyclic loading with relaxation, allowing characterization of the rope with only one test. From this test one can identify each part of the model and validate it on different tests, before comparing to results from tests made on 8 tons sub-ropes. This has led to a simple 1D visco-elasto-plastic model quite close to the behavior of the rope.

The second part involves long term creep tests. First, a brief explanation of the design and the building of the test machine will be made. Then results from 3 one year long tests on 4-ton sub-ropes will be presented and compared with other results. The results show similar creep values to those for polyester and they can be used to predict if re-tensioning of the rope will be needed.

In the third part, the durability of polyamide rope will be assessed, first abrasion tests were employed, to ensure that the coating used is sufficient to validate the abrasion resistance on yarn. Then standard fatigue tests have confirmed that polyamide rope lifetimes are largely sufficient for permanent mooring, with a lifetime superior to steel chain even if a little shorter than those of polyester.

Lastly, quick fatigue evaluation by heat build-up tests was realized. Showing promising result based on thermal measurement of the dissipated energy of the rope to predict its fatigue lifetime in less than two days.